Study of the Laminar Burning Velocities and Instabilities of Premixed Producer Gas-Air/O_2 Mixtures at Elevated Pressures

A thesis submitted in partial fulfilment of the requirements for the award of the degree of

Doctor of Philosophy

by

Muniraja Tippa

Roll No.: 166151104

School of Energy Science and Engineering

Indian Institute of Technology Guwahati

August 2022

School of Energy Science and Engineering

Indian Institute of Technology Guwahati

Guwahati-781039

DECLARATION

I hereby certify that the work presented in this thesis entitled "**Study of the Laminar Burning Velocities and Instabilities of Premixed Producer gas-Air/O_2 Mixtures at Elevated Pressures**" is the outcome of my original research work carried out at the School of Energy Science and Engineering, Indian Institute of Technology Guwahati, under the supervision of **Prof. Senthilmurugan Subbiah** and **Dr. Prathap Chockalingam**. The results documented in this thesis are not submitted to any other university or institute for the award of any degree or diploma. Due acknowledgment has been made wherever the work described is based on the findings of investigations of others with supporting references.

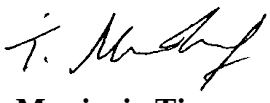

Muniraja Tippa

Roll No.166151104

School of Energy Science and Engineering

Indian Institute of Technology Guwahati

Guwahati-781039, Assam, India

School of Energy Science and Engineering

Indian Institute of Technology Guwahati

Guwahati-781039

CERTIFICATE

This is to certify that the work contained in this thesis entitled "**Study of the Laminar Burning Velocities and Instabilities of Premixed Producer gas-Air/O_2 Mixtures at Elevated Pressures**" is being submitted by **Muniraja Tippa** (**Roll No.166151104**), for the award of Ph.D. degree, is a record of bonafide original research carried out by him at the School of Energy Science and Engineering, Indian Institute of Technology Guwahati, under our guidance and supervision. The work embodied in this thesis has not been submitted to any other University or Institute for the award of any other degree or diploma.

Prof. Senthilmurugan Subbiah

Professor
Department of Chemical Engineering
Indian Institute of Technology Guwahati (IITG)
Guwahati, Assam, India.

Dr. Prathap Chockalingam

Associate Professor
Department of Aerospace Engineering
Indian Institute of Space Science and Technology (IIST)
Thiruvananthapuram, Kerala, India.

Abstract

Research on power generation and adaptation of existing traditional fossil fuel-based engines/infrastructure to run on renewable gaseous fuels such as producer gas (PG) is gaining pace. PG is a multicomponent fuel mixture with combustible species such as H_2, CH_4, and CO and non-combustible species such as H_2O, CO_2, and N_2. Chemical composition and physical form of biomass, choice of the gasifier, catalysts, oxidizing agent, moisture content, processing temperature, and pressure, working fluid path in the gasifier, location of gas collection in the gasifier, and time of collection after the onset of gasification affect the final composition of PG mixture substantially. The producer gas mixtures are relatively less explored due to (a) the lower calorific content, because of the presence of higher levels of non-combustible components, and (b) the varying calorific profile due to inconsistent composition. Producer gas-based internal combustion engine was operated and tested in the literature and recommended fuel refinement to lower the non-combustible components.

Refining PG is one of the most effective ways to increase the heating value of fuel; for example, membrane technology isolates CO_2 from other gas mixtures. Combustion characteristics depend on multiple factors such as fuel composition, choice of oxidizer, fuel-oxidizer mixing proportion, operating pressure, temperature, etc. In domestic and industrial applications, there are several applications in which combustion occurs at high pressures, such as Spark Ignition Engine, Compression Ignition Engine, Jet Engine, Rocket Engine, etc. Hence, it is essential to understand the variation in PG composition and initial pressure on combustion characteristics at conditions within the limits/ranges of practical importance. A representative composition of PG was obtained from an exhaustive literature review in this work. The combustible and non-combustible components were varied. Their effect on laminar burning velocity and the onset of thermo-diffusive and hydrodynamic instabilities at elevated pressure conditions was thoroughly investigated.

In this research, a comprehensive literature survey was undertaken to identify the extent of H_2, CO, CH_4, N_2, and CO_2 variation in a multicomponent producer gas fuel. 800 diverse compositions (different research groups, feedstock, gasifier, oxidizers, operating and collecting conditions) from recent literature (2001 -2019) were compiled. After obtaining the realistic range of all the important species of PG from a detailed literature survey, the study was conducted in two different ways.

The PG was considered with combustible and non-combustible components in the first strategy. It was burnt with oxygen to avoid the effect of nitrogen present in ambient air. Combustible components (CC) and Non-combustible components (NCC) species were systematically varied. Forty-five different PG compositions were investigated to understand their impact on unstretched laminar burning velocity (*LBV*) and flame stability at 1 bar, 300 K, and an equivalence ratio of 0.8. In this study, the composition of PG was considered as Z% CC+(100-*Z*)% NCC, where *Z* was varied at 25, 35, and 45. It was referred to as the Inter-CC-NCC study. CC was considered ($25CH_4$:$25CO$:$25H_2$:25Y), where *Y* represented rich combustible species CH_4/CO/H_2 and referred to as an intra-CC study. NCC was *P*%CO_2+(100-*P*)%N_2, where *P* was varied from 0- 100 (by volume) at 25%.

In the second strategy, the PG was considered without any non-combustible components, and it was termed as Refined Producer Gas (RPG). It reacted with air (21%O_2 and 79%N_2 by volume). Twelve different RPG compositions where the CC was again systematically varied to realize its effect on unstretched *LBV* and flame stability at 1-4 bar, 300 K, and equivalence ratio of 0.8-1.2. In this study, the composition of RPG was considered as 50%*A*+(*X*)%*B*+(50-*X*)%*C*, where *A*: CH_4/H_2/CO, *B*: H_2/CO/CH_4, *C*: CO/CH_4/H_2, and *X*: 00:50 in steps of 12.5%.

The freely expanding spherical flame method was used to measure *LBV* and flame stability. All experimental operating conditions were simulated using a one-dimensional freely propagating planar flame model in Ansys Chemkin using GRI Mech 3.0 (Gas Research Institute Mechanism version 3.0), USC Mech 2.0 (University of Southern California Mechanism version 2.0), and FFCM-1 (Foundational Fuel Chemistry Model version 1.0) chemical kinetic schemes. One dimensional expanding spherical flame model in Cosilab was also used to predict *LBV* for few operating conditions using GRI Mech 3.0.

Significant findings are: Higher volume fraction of fuel/inert species in combustible/non-combustible components commands the combustion characteristics of PG. PG with higher mole fractions of hydrogen, carbon monoxide, and nitrogen and relatively lesser amounts of methane and carbon dioxide resulted in stable flames with respect to preferential diffusion. It had better resilience towards minor deviation/fluctuations in composition. Combustion properties of intermediate compositions can be well estimated for mixtures having non-combustible components, CO_2:N_2, in the range of 50:50 to 00:100. The presence of higher levels nitrogen than CO2 enhanced the stability of the mixtures toward the preferential diffusion effects.

The *LBV* of RPG-air mixtures followed a decreasing order with respect to the rich/ higher mole fractions (50% vol) of H_2, followed by CO and CH_4 in the mixture due to the individual variation in the flame temperature and thermal & mass diffusivities. The non-linear variation of *LBV* with equivalence ratio at any given RPG-air composition increased with an increase in the mole fraction of CH_4 in the mixture due to a shift in the peak *LBV* towards the stoichiometric condition. The simulated values obtained using GRI Mech 3.0 were consistently higher in magnitude than those obtained using FFCM-1 at all the conditions.

From the burned gas Markstein length and effective Lewis number analysis, CO added resilience to the mixtures against thermo-diffusive instabilities while supported by CH_4 and opposed by H_2. The onset of hydrodynamic instability is strongly dependent on critical radius and flame thickness. From the newly presented exclusive susceptibility score/ranking system related to the onset of hydrodynamic instability, the composition H_2:CO:CH_4 = 0:1:1 (0:4:4) was found to have the highest resilience. The increase in the content of H_2 in the presence of CO favoured the onset of hydrodynamic instability, while the presence of CH_4 favoured the onset of thermo-diffusive instability. Increment in the mole fraction of CH_4 suppressed the susceptibility to hydrodynamic instability, while a rise in the mole fraction of CO suppressed the thermo-diffusive instability. Combustible mixtures having lower values of *LBV* promoted thermo-diffusive effects, and the higher values resulted in earlier onset of hydrodynamic instability.

Keywords: *Spherical flame, Producer gas, Laminar burning velocity, Thermo-diffusive instability, Hydrodynamic instability, Refined producer gas, Premixed multicomponent gas, Premixed combustion.*

Acknowledgements

I have met several people during this journey, but when I look back, the first two persons that come to mind are my supervisors, Prof. Senthilmurugan S and Dr. Prathap C. I sincerely thank them for providing the opportunity and resources required to complete this research stint. Beyond that, they have extended their support at all possible times and levels. This journey under their mentorship has helped me develop a new perspective on research and working with a diverse research group.

I thank my doctoral committee chairman, Prof. U K Saha, for his constructive inputs on improving my report writing skills. I also thank my previous and present members of the doctoral committee, Prof. Senthilvelan S, Dr. Nagaeswara Rao Peela, and Dr. Harsha Kota, for sharing meaningful insights and enduring my unconventional presentations all way.

I had a wonderful opportunity to be part of two different research groups in two different institutes. I initially became part of Water and Energy Nexus group, Department of Chemical Engineering, IIT Guwahati. I cherished many beautiful moments with them. I tried to mention a few overhere but realized after writing a page that I had many with them which will be difficult to consolidate. I would like to take this opportunity to thank Dr. Vishal, Dr. Vignesh, Dr. Habtom, Dr. Aanisha, Dr. Nivedhitha, Dr. Viswanth, Dr. Arun, Mr. Senthil, Ms. Ananya, Mr. Bala, Mr. Dinesh, Mr. Naveen, Ms. Neelam, Mr. Priyamjeet, Mr. Sureandhar, Ms. Seema and Mr. Bharat. Mr. Kranthi had left us in between for his heavenly abode leaving a deep impact. Missed you brother at multiple occasions. I couldn't interact much with recently joined members and some past members who stayed for brief time but still had some memories with them such as Ms. Deepika, Ms. Udaratta, Mr. Manish, Mr. Shanmugam, Mr. Bijoyendra, Mr. Venkatesh, Ms. Bonita, Mr. Sachin, Mr. Sanjay, Mr. Rohan, Mr. Kartheek and Mr. Maharshi. Our beloved Mr. Banajith and Mr. Bishnu for keeping lab space tidy all the time.

Outside our own research group in the Department of Chemical Engineering, I had very fond memories with many such as Mr. Hanumanth, Dr. Bharath, Mr. Ameer, Ms. Sarmistha, Dr. Devipriya, Dr. Alam, Mr. Rambabu, Dr. Vamsi, Mr. Shubam, Dr. Deepthi,

Mr. Anweshan, Mrs. Swarna, Mrs. Soumi, Ms. Shivani, Ms. Sayani, Mr. Vishnu and Mr. Ajeeth.

Similarly with my friends from Energy Science and Engineering such as Mr. Ojing, Mrs. Sunita, Dr. Mrinal, Dr. Anil, Mrs. Ankita, Mr. Samar, Mr. Bhaskar, Mr. Sukumar and Mr. Abebe. From other departments and hostel such as Mr. Shafique, Mr. Manvendra, Dr. Anji, Dr. Suresh, Dr. Venkatesh, Dr. Vinay, Mr. Subbu, Mr. KC, Mr. Surya, Ms. Anamika, Mr. Yashavanth, Ms. Aishwarya, Mr. Muthu, Mr. Basu, Ms. Sangeetha, Mr. Mohith, Mr. Rahul, Mr. Prasad, Ms. Prathiba, Mr. Arun, Dr. Kaushik, Ms. Sofi, Mr. Mukesh, Ms. Simran, Ms. Nishi, Ms. Aditi, Ms. Thara and Mr. Aryan.

I thank the following people for serving good food during my stay: Mr. Dipjyoti and Mr. Monu for Baskin Robbin's ice creams, Mr. Raju for Biryani and Dosa, Mr. Jatin for fruit salads & juices, Mr. Ranjith for Maggies and lemon tea, Core-3 & 5 canteens, Ganesh stall, Mr. Vikram’s Manasha -OH shop, Nepali shop for our Sunday evening chai sessions, Mr. Shobit and Mr. Guru for Khokha eats and Shri Chaitanya Das Prabhu for amazing food from Hare Krishna Movement Temple.

I thank Capt. Ajay, Capt. Rudrakanth, Capt. Puneet, HMT Surendhar from 621 EME Battalion, Indian Army for arranging and accompanying three amazing trips to conduct experiments at exotic locations of Arunachal Pradesh.

I thank my combustion group members at the Department of Aerospace Engineering, Indian Institute of Space Science and Technology for their amazing support. They helped me building a whole new test facility, explore combustion and beautiful parts of Kerala. As I mentioned, I had multiple memorable interactions with them and was difficult to consolidate. I thank Mr. Rajesh, Mr. Dinesh, Mr. Bipin, Mr. Meghsham and Mr. Akash. Past members Mr. Akash Gupta, Ms. Khirabdi, Mr. Madhav, Mr. Rakesh, Mr. Bihara, Mr. Keshav, Mrs. Rishitha, Mr. Vijay, Ms. Sreya, Mr. Shrey and Mr. Rishab.

I also thank my friends from other departments and hostel: Ms. Ashita, Mrs. Reena, Mrs. Anuja, Ms. Swathi, Mr. Sumeet, Mr. Arun, Ms. Risha, Mr. Sarath, Dr. Aryadutt, Mr. Dheeraj, Dr. Gyaneshwar, Dr. Jogender, Mr. Kirhsna Thej, Mr. Manohar, Dr. Vinod, Dr. Sudhanshu, Mr. Danish and Dr. Dhanesh.

I would like to thank Mr. Prakash and his workshop team, Mr. Satish and Mr. Vineel for helping me build test facility and conducting Laser experiments.

I thank Binu chettan shop, Aerospace department canteen, Institute hostel canteen, eateries at 16th stone junction and Nedumangad for serving amazing food, especially during odd hours which helped me to carry out experiments.

I thank my vendors for taking up the orders and supplying the much-needed scientific equipment to complete my research work. I thank the Ministry of Education and other funding agencies for the very essential financial support.

I thank my friends from kgp; Mr. Anurag, Mr. Teja, Mr. Sandeep, Mr. Mourya, Mr. Prashanth, Mr. Vamsi, Mr. Abhinav, Mr. Bhatta, Mr. Bharadwaj, Mr. Tejas, Mr. Sasi, Mr. Hanish, Mr. Thasir and Mr. Rithin for their support at crucial moments and reminding the amazing moments spent back at kgp.

I specially thank Mr. Saket and Mr. Bnbn who stood by for the past 10 years. The time spent with them, endless discussions and crazy trips are to be acknowledged. I also would like to thank Mrs. Durga, Mrs. Jenny, Ms. Sharmila, Ms. Bhavana and Ms. Trishala for being there. I thank Puppy for the support provided at much-needed time. I sincerely thank Bujji and Dobby for coming into my life who kept me sane and gave vibrant colourful memories. I thank Barak hostel's pack of dogs for their love & affection. Brownie, Kaalu, Mommy dog, Tharku, Parvo, Sheep dog and brown twin dogs. 5months dog and her pups too.

I might have definitely missed mentioning someone. I thank everybody for their direct and indirect contributions.

I thank my teachers for helping me to navigate through formal education.

I sincerely thank my parents for their support from my very first breath, without which I wouldn't have come this far.

Lastly, I want to thank myself for gathering the courage to start PhD journey during the most fragile phase of life, rebuilding myself, staying back, and completing the degree.

Table of contents

List of Tables

List of Figures

Chapter 1 Introduction

1.1 General Introduction

Research on power generation and adaptation of existing traditional fossil fuel-based engines/infrastructure to run on renewable gaseous fuels such as producer gas (PG) is gaining pace[1–9]. PG is a multicomponent fuel mixture with combustible species such as H_2, CH_4, and CO and non-combustible species such as H_2O, CO_2, and N_2 [10]. Chemical composition and physical form of biomass, choice of the gasifier, catalysts, oxidizing agent, moisture content, processing temperature, and pressure, working fluid path in the gasifier, location of gas collection in the gasifier, and time of collection after the onset of gasification affect the final composition of PG mixture substantially [11–15].

The producer gas mixtures are relatively less explored due to (a) the lower calorific content, because of the presence of higher levels of non-combustible components [16–18], and (b) varying calorific profile due to inconsistent composition. Producer gas-based IC engine was operated and tested in the literature and recommended fuel refinement to lower the non-combustible components [19–24]. Refining PG is one of the most effective ways to increase the heating value of fuel; for example, membrane technology isolates CO_2 from other gas mixtures [12,25–31]. A detailed survey of the suitable cleaning technologies for natural gas [13] is available in the literature; Similar approaches may be implemented to clean PG to obtain better heating values.

Emission protocols, operating conditions for maintaining synchronization among different system units, and dynamic power demand bring in further constraints on the variation of the fuel composition. But the performance of any refining module is inherently prone to decline with time, and replacing an entire unit within a short period is not an economically viable option. The replacement cycle can be increased if the dwindling operational unit can achieve the desired outcome. A decline in performance eventually leads to possible scenarios such as 1) Drop-in absolute refining efficiency and 2) Differential refinement, *i.e.,* the difference in the removal rate of CO_2 and N_2. This variation in the composition will impact the performance of end applications *viz.,* burners, combustion chambers, internal combustion engines, and gas turbines. These are further affected by different volume fractions of combustible components, H_2, CO, and CH_4.

There are several applications in which combustion occurs at high pressures, such as Spark Ignition Engine, Compression Ignition Engine, Jet Engine, Rocket Engine, etc. Apart from domestic and industrial applications at atmospheric conditions, Natural gas is also used in internal combustion engines (~60 atm) and stationary power generation gas turbine engines (~30 atm). At elevated pressures, the specific volume decreases; collision frequency and the reaction rate increase. Combustor/reactor size depends on the parameters, *viz*., reaction rate and residence time to attain complete combustion. Mixtures with high reactivity require less residence time. Thus, pressurizing the reactant mixture leads to smaller combustors/reactors with a high flow rate. In addition, the surface area susceptible to thermal loss decreases as well. The pressurization further will result in an increase in core temperature, which will accelerate the reaction rate.

Gas-based power generators are of two types based on the drive *viz.*, Gas engine and Gas turbine. Gas engine-driven generators are typically opted for small-scale power generation projects, while gas turbine-driven generators are for large-scale projects. In both cases, the combustion occurs at elevated/high-pressure conditions due to the compression stage. Combustion characteristics depend on multiple factors such as fuel composition, choice of oxidizer, fuel-oxidizer mixing proportion, operating pressure, temperature, etc. Hence, it is essential to understand the variation in PG composition and initial pressure on combustion characteristics at conditions within the limits/ranges of practical importance. In this thesis work, an attempt has been made to understand the variation of combustible and non-combustible components in PG composition in practice, the effects of composition variation on premixed combustion characteristics such as laminar burning velocity, and the onset of thermo-diffusive and hydrodynamic instabilities at elevated pressure conditions.

1.2 Combustion characteristics - fundamental concepts and definitions

All essential concepts related to combustion characteristics in the scope of this thesis are introduced in this section. The exact mathematical models and procedures to obtain the parameters are presented in Chapter-3, while the explanation below is limited to introducing the concepts.

1.2.1 Combustion

Combustion is a rapid oxidation process of fuel to form equilibrium products releasing large amounts of heat with or without light emission. The species that undergo oxidation is called fuel, while the species undergoing reduction is called an oxidizer. Generally, the mixture comprising fuel, oxidizer, and other inerts are called reactants. The release of heat from the reactants at a standard temperature and pressure is due to the difference in the heat of formation between the reactants and the products. Based on the state-of-mixedness of the fuel and the oxidizer, the combustion is classified as (a) premixed and (b) non-premixed combustion. In non-premixed combustion, the fuel and the oxidizer move from opposite directions, meet at the reaction zone, undergo mixing, and react. A candle flame is a classic example of a diffusion flame. The fuel and oxidizer are thoroughly mixed to the molecular level in premixed combustion, resulting in a homogeneous mixture before the reaction zone. Both combustion modes exist in the real world and are chosen according to necessity and feasibility. Premixed combustion is commonly preferred in many applications, as it provides an inherent control advantage over the end temperature and composition of products to achieve clean combustion. As shown in Figure 1-1, a modern LPG gas stove is an exemplary application of premixed flame that replaced the inefficient open-wood stack stoves. Present research work falls under the premixed combustion category.

Figure 1-1 A modern LPG gas stove with a premixed flame mode

1.2.2 Stoichiometric mixture and Equivalence ratio

A stoichiometric mixture is an exact composition of fuel and oxidizer components for achieving complete combustion without any excess/shortage of reactants. Equivalence ratio (ϕ) is a non-dimensional variable to characterize the composition of a premixed combustible mixture. It is defined as the ratio of stoichiometric oxidizer to fuel ratio to the actual oxidizer to fuel ratio as $\phi = \frac{\left(\frac{Oxidizer}{Fuel}\right)_{Stoichiometric}}{\left(\frac{Oxidizer}{Fuel}\right)_{Actual}}$. In this definition, both the oxidizer to fuel ratios should have the same units, and they can be either volume or mass. If ϕ equals unity, it is called a stoichiometric mixture; $\phi < 1$ refers to a fuel-lean mixture, and $\phi > 1$ refers to a fuel-rich mixture.

1.2.3 Equilibrium temperature

The temperature of flame or products is an essential intensive thermodynamic property of the combustion process. It is a crucial design variable in the development of a combustion application. It is necessary to provide adequate residence time to the combustion process, assumed to be adiabatic with the surroundings, to generate products at equilibrium composition and temperature. The equilibrium composition and temperature of the products are estimated for a given set of reactants considering the equivalence ratio, initial pressure, initial temperature, and prescribed/expected product species. These are achieved by minimizing the Gibbs free energy approach and solving the energy equation. In this work, the equilibrium composition and the temperature are estimated using the equilibrium model in Ansys Chemkin software.

1.2.4 Laminar burning velocity

Unstretched adiabatic laminar burning velocity (*LBV* or S_u^0) of a premixed combustible mixture is defined as the relative velocity of unburned reactants propagating normal to the adiabatic planar flame front, as shown in Figure 1-2. *LBV* provides a piece of first-hand information on the reactive intensity of the combustible mixture. It is a critical parameter in calculating and assessing complex phenomena like ignition, quenching, flashback, flame stabilization, etc. A generic combustor design starts from the information of *LBV* of the chosen fuel-oxidizer mixture and its associated initial

thermodynamic and flow conditions. It is one of the standard parameters used for validating and updating the existing and new chemical kinetic schemes.

Figure 1-2 shows the structure of a planar flame front in a flame coordinate system depicting the propagation of the unburned mixture into the flame at a velocity identical to that of laminar burning velocity. The products from the flame hot and light. A slight pressure drop occurs, which is a characteristic feature of deflagrations resulting in acceleration of the products. The adiabatic planar flame consists of two zones, preheat and reaction zone, as shown in Figure 1-2.

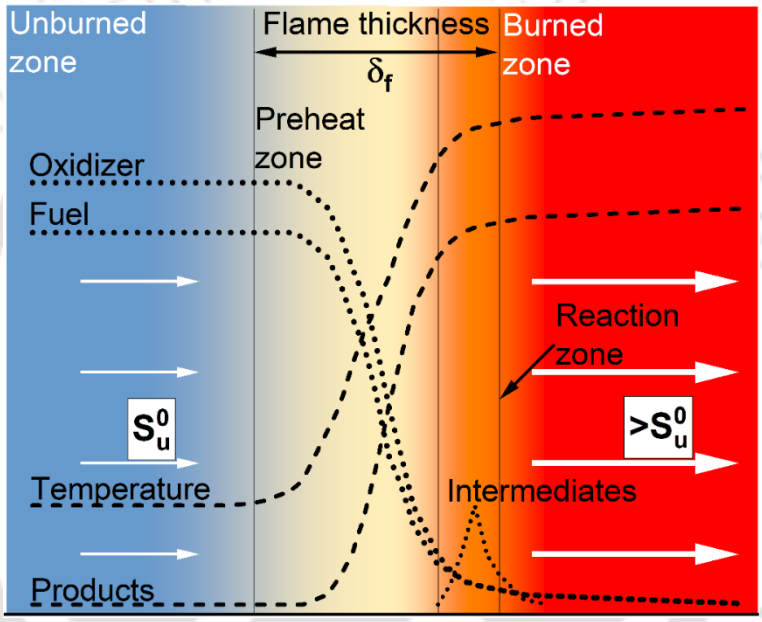

Figure 1-2 Schematic representation of the premixed flame structure in a flame coordinate system

The heat diffusion from the reaction zone to the preheat zone raises the temperature of the reactants to the cross-over temperature due to the presence of a temperature gradient resulting in spontaneity in the reactivity. These preheated reactants oxidize in the reaction zone to attain equilibrium composition and temperature. These two zones together are called a flame, and their width is referred to as flame thickness (δ_f). Several factors that affect the flame structure and propagation rate are mass diffusivity, thermal diffusivity, initial pressure, initial temperature, fuel type, oxidizer type, mixture composition, and reaction rate. In any combustion application, the flame ultimately has to anchor in a

position/location where the convection and diffusion of reactants into the flame balance the consumption rate of reactants in the flame.

1.2.5 Stretch

LBV is defined for an adiabatic planar flame, as displayed in Figure 1-2, whose area will remain constant, and a uniform flow of unburned gases always flow normal to it. Such an optimum situation occurs only in carefully anchored laboratory-level flames. In real-life applications, unburned gases may flow non-uniform and non-orthogonal towards the flame front. Due to the non-uniform flow conditions, the balance/alignment between convection, diffusion, and reaction gets affected, eventually leading to perturbation of the flame. This flame front adjusts to establish a new balance/equilibrium by becoming flexible (wrinkling/bending from planar) and/or elongated depending on the conditions. This phenomenon is called flame stretch and is typically correlated with the change in the surface area. Three typical cases of the flame stretch are presented in Figure 1-3. A conical flame is anchored in case-A, where the reactants flow towards the stationary flame front. At the tip, the flame is curved, tending to close in/collapse, resulting in a negatively-stretched flame (compression).

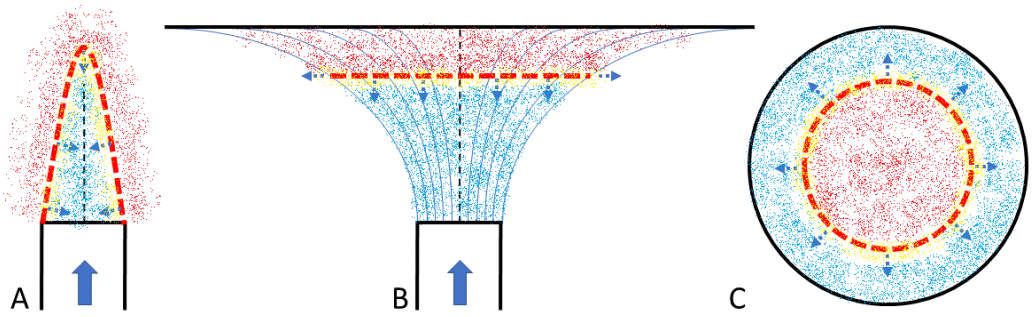

Figure 1-3 A) Conical flame-Negatively stretched flame B) Wall stabilized stagnation flame-Positively stretched flame and C) Spherical flame- Outward (inward) propagation results in positively (negatively) stretched flame

In case-B, a stagnation flame is established by injecting the reactants against a solid adiabatic surface. The established flame extends the boundary/surface resulting in a positively-stretched flame. The above cases fall under the stationary flame category but still exhibit two different types of stretch. In case-C, a freely expanding spherical flame is presented. By nature, at any instant, the flame cannot be considered to be stretched, but

it is stretched during its outward or inward propagation. In a freely expanding spherical flame propagation, the unburned gases always flow normal to it, but the flame surface area and the associated curvature change during its propagation, resulting in a positive flame stretch.

1.2.6 Intrinsic instabilities

Establishing a stable flame with a constant consumption rate is the ultimate objective in any combustion application. Despite damping the external contributing/triggering factors, the flames are still prone to intrinsic instabilities such as thermo-diffusive and hydrodynamic (or Darrieus–Landau). These instabilities lead to the formation of cells, which increase the surface area, leading to a sudden change in consumption rate. The occurrence of instabilities in positively stretched spherical flames is shown in Figure 1-4.

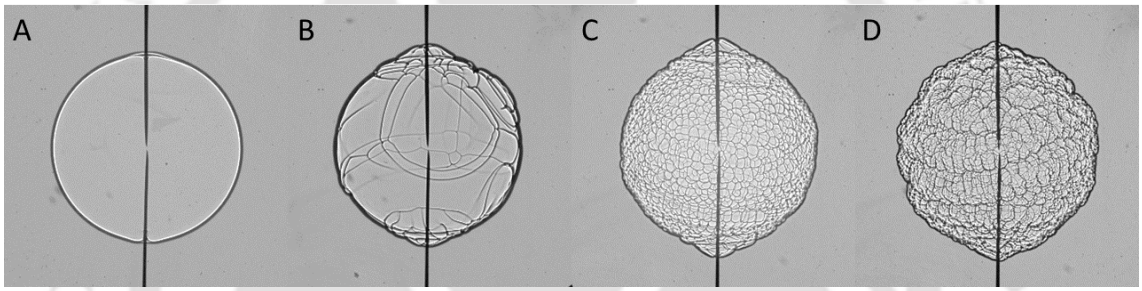

Figure 1-4 (a) Stable flame (b) Thermo-diffusive instability (c) Hydrodynamic instability (d) Both thermo-diffusive and hydrodynamic instability

1.2.6.1 Thermo-diffusive instabilities

A stretched flame generated in a reacting mixture with an imbalance in thermal and mass diffusivities leads to thermo-diffusive instabilities. Lewis number (*Le*) is often associated with the onset and characterization of this instability which is the ratio of thermal to the mass diffusivity of the mixture. If a stretched flame is generated in a mixture having: (a) *Le* as unity lead to thermo-diffusive stable flame, (b) $Le > 1$, the heat diffusion dominates than mass diffusion, resulting in again, thermo-diffusive stable flame, (c) $Le < 1$, and if the deficient reactant is more diffusive, it results in thermo-diffusive unstable flame due to change in the local equivalence ratio. If a stretched flame is subjected to a perturbation, and if the diffusional effects hinder/accelerate its growth, it results in a stable/unstable flame towards thermo-diffusion. Instability generates cells, cusps, and crests on the flame surface. These create locally low and high-temperature spots leading to extinction and

reignition, further triggering other flow and thermo-acoustic fluctuations. These local temperature and mass distribution irregularities affect the final composition of products and temperature. Cells of non-uniform sizes and spatial distribution are the characteristic feature of these instabilities.

1.2.6.2 Hydrodynamic instabilities

Uniform small cells occurring evenly on the entire surface of the flame is a unique characteristic feature of hydrodynamic (or Darrieus-Landau) instability. Density jump across the flame front, which is usually linked with thermal expansion ratio (σ) (or unburned-to-burned density ratio), is one of the significant factors contributing to this instability. This type of instability increases the flame surface area resulting in self-acceleration leading to sudden pressure rise inside a confined environment. An increase in initial pressure further enhances or prepones the occurrence of this instability. Expanding spherical flames in a confined chamber, where the lighter products (flame) propagate into a denser reactant mixture, are prone to hydrodynamic instability. This instability affects all the spherical flames anchored in a combustion chamber irrespective of the type of fuel, oxidizer, and initial conditions. But the onset of this instability is strongly dependent on the type of fuel, oxidizer, and initial conditions. A combination of both thermo-diffusive and hydrodynamic instabilities will significantly enhance the flame propagation rate.

1.3 Organization of thesis

The content of the thesis is distributed and organized into five chapters. In addition to the above few appendices are added to explain the presented content further.

- Chapter-1: The general background and motivation behind the work are introduced in the simplest terms. Later, the necessary fundamental concepts of the current work are discussed, followed by the organization of the thesis.
- Chapter-2: The literature review of the associated topics of interest is presented and summarized. The research gaps are carefully articulated, and primary objectives are discussed.
- Chapter-3: The methods adopted to obtain the required parameters are discussed in this chapter. The experimental test facility, the theory behind it, the post-

processing procedure, design of experiments, and uncertainty analysis are primarily presented.

- Chapter-4: The consolidated results of conducted analysis and corresponding discussions are presented in this chapter. The results are further segregated into multiple divisions along with the conclusions for a coherent flow of understanding.
- Chapter-5: The summary of conclusions from the above study is presented, followed by the associated application potential and future scope.
- References: All the referred sources in the above-discussed chapters are consolidated.
- Appendix-1: The state-of-the-art literature review of 800 producer gas compositions is presented in this section.
- Appendix-2: The complete development of the test facility from framing the design objectives and constraints, conceptual, preliminary & detailed design, execution, and commission.
- Appendix-3: The adopted uncertainty analysis of the considered parameters is discussed.

Chapter 2 Literature Review

2.1 General introduction

Laminar burning velocity is the relative velocity of reactants propagating normally to an adiabatic planar flame. It is a physicochemical property and gives information on the reactivity, exothermicity, and diffusivity of the mixture. Thermo-diffusive instabilities occur due to the considerable disparity/competition between mass (species) and thermal diffusivity at a local region in the flame. Tangential velocity strain and curvature normal to the propagation surface result in stretching of the flame surface, which escalates the thermo-diffusive instabilities.

In contrast, another category of instabilities originates due to the thermal expansion jump across the propagating flame, referred to as hydrodynamic (or Darrius-Landau) instability. This instability leads to the formation of uniform cell structures resulting in the self-acceleration of flame due to an increase in the surface area. These instabilities are important at elevated pressure combustion conditions as the flame thickness reduces significantly with an increase in the initial pressure.

2.2 Flame measurement techniques

Today, several techniques are available for accurately measuring the laminar burning velocity of gaseous mixtures at a wide range of initial pressure, temperature and composition conditions. Some popular and widely explored techniques are Flame tube, Soap bubble, Bunsen burner, Slot burner, Flat flame, Heat flux, expanding spherical flame, Stagnation flame, Counter-flow flame, Diverging channel method, etc. In the following sections, certain contemporary flame measurement methods are briefly discussed.

2.2.1 Burner method

This method falls in the category of stationary flames. Bunsen burner, nozzle/orifice burner, and slot burner are popular variants that anchor a conical flame to measure *LBV*. This technique has been widely adopted for quite a long time owing to its simplicity. The main challenge is to anchor the flame for: (a) mixtures having high burning velocity at

laminar flow conditions, (b) ultra-lean/rich mixtures may result in buoyancy affected flames or blow-off, and (c) mixtures at elevated pressures result in very short flames at high flow rates. Other common challenges are heat loss from the flame to the burner rim, flame interaction with ambient air, flame stretch effects leading to tip opening, etc.

A burner, flow regulator, and gas cylinders constitute the main essential elements of a generic burner setup, as presented in Figure 2-1. Gas is supplied to the burner with the help of a booster pump from the storage cylinder. A digital flow regulator is placed between the gas reservoir and burner to achieve desired flow rate to maintain the mixture composition. An exclusive mixer is used for attaining multicomponent mixtures depending on the requirement. The measured values of the flow rate and the surface area of the flame front are used to calculate the laminar burning velocity. It is very helpful in obtaining first-hand information on the *LBV* of any combustible mixture.

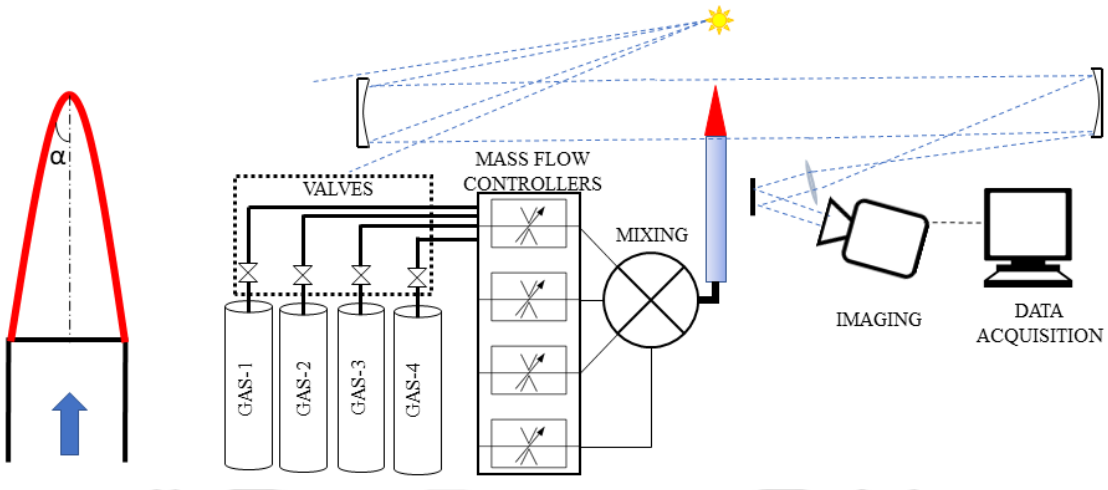

Figure 2-1 Schematic diagram of Bunsen burner setup and burning velocity definition based on the half cone angle

Advantages:

- The test rig is relatively inexpensive due to its simple configuration and experimental procedure.
- Less post-processing time.
- Effective real-time control over the flame.

Challenges:

- Flame anchoring.
- Accurate determination of flame structure, cone angle, and surface area.
- Heat loss to surroundings and burner rim are significant at the bottom of the flame.
- Tip of the flame prone to stretch and thermo-diffusional effect.
- To achieve initial elevated pressure and temperature conditions.

2.2.2 Planar flame method

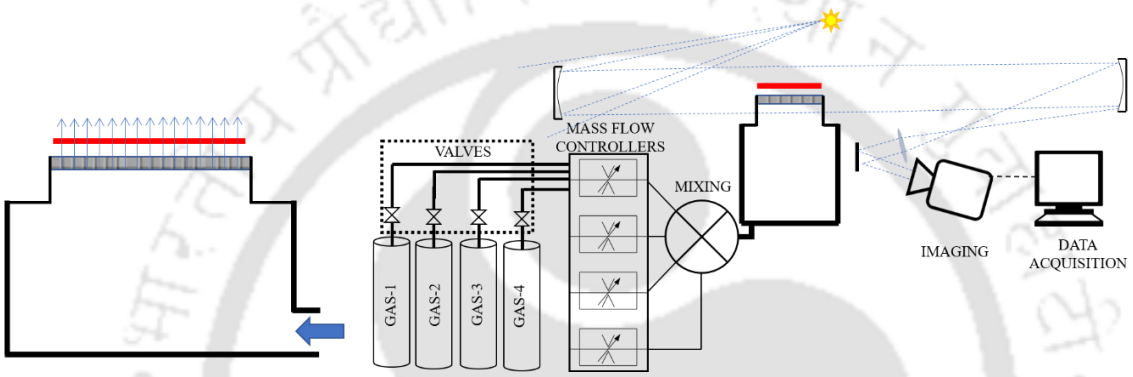

Figure 2-2 Schematic diagram of Flat flame burner setup

One dimensional planar flame is achieved using a flat flame burner, as shown in Figure 2-2. It is also referred to as the heat flux method. The burner plate design plays a crucial role in anchoring the flat flame over the burner plate. Uniform flow of premixed combustible mixture at the upstream of burner plate is obtained by allowing the gases to pass through flow straighteners such as honeycomb structure. In this method, a special heating provision in the plenum chamber preheats the unburned gases before reaching the burner plate. The key feature is to supply thermal energy by preheating the unburned gases to compensate for the heat loss from the flame to the burner. Later, using an interpolation technique, the *LBV* of an adiabatic flame is measured in this method. The post-processing is simple compared to other techniques.

Advantages:

- One dimensional flame anchored normal to the unburned gas mixture.
- Significant reduction in heat loss from the flame to burner plate.
- Free from the flame stretch.

- Provision for probe intrusion for collecting chemical samples under special conditions.

Challenges:

- Fabrication of burner plate is challenging.
- Flame anchoring.
- To achieve laminar flow conditions at high pressures.
- Testing of liquid fuel mixtures.

2.2.3 Stagnation flame method

In this method, a premixed air-fuel mixture is passed through a nozzle at velocities higher than the expected laminar burning velocity for that particular mixture. The flow is directed towards a stagnation plate where the mixture flow decelerates to a stagnation regime upon reaching the plate surface. The counter-flow flame method is a special case of the stagnation flame method. A stagnation plate is replaced with a jet of similar flow characteristics and mixture composition. It impinges on the already established jet, and as a result, two planar flames are formed, as shown in Figure 2-3. This will create an adiabatic flame condition omitting the necessity of a hot plate and the associated wall reactions. At a specific height from the nozzle, the flame front gets stabilized. Here, the particle image velocimetry technique is popularly used to measure the unburned gas velocity fields, and from that, the strain rate and *LBV* are estimated.

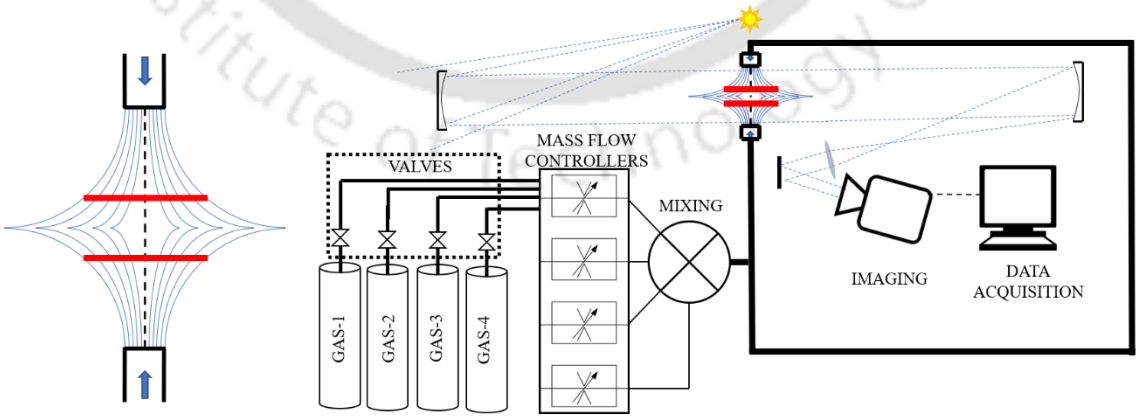

Figure 2-3 Schematic diagram of Stagnation flame burner setup

Advantages:

- Nearly one-dimensional planar flame is anchored.
- High flame speed mixtures can be tested.
- Measurements at elevated pressures and temperatures are possible.

Challenges:

- Fuel-air mixture in large volume is necessary for an experimental run.
- Flame experiences a positive stretch.
- Achieving two similar jets with identical flow properties.
- Complicated measurement techniques such as particle image velocimetry or Laser Doppler velocimetry are needed to measure the unburned gas velocity.
- Uncertainties associated with post-processing methods.

2.2.4 Spherically expanding flame method

In this method, air and fuel components are filled into a chamber sequentially and left ideal for achieving quiescent conditions. Two high voltage electrodes with a minimum gap are typically used to generate a spark to establish a flame kernel that propagates outwardly, consuming the fresh reactants. It extinguishes once it reaches the inner surface of the chamber. The pressure development inside the chamber and radial propagation of flame are captured. High-speed imaging techniques such as shadowgraph, etc., capture the flame front propagation. Pressure-time and radius-time data are processed to obtain laminar burning velocity using mathematical models developed based on underlying physics. Depending on the facility, the vessel used in this method can be operated in constant-volume or constant-pressure mode. Constant-pressure mode facilitates combustion at high initial pressure conditions. Typical test facility connections and propagating flame images can be seen in Figure 2-4 and Figure 2-5.

Advantages:

- A small quantity of fuel is sufficient for a single experimental run, given that the chamber size is relatively small. Liquid and gaseous fuels can be tested.
- Measurements at higher initial temperatures and pressures can be performed.

Challenges:

- A sudden spike in chamber pressure during combustion in constant-volume mode.
- Prone to multiple flame instabilities, including buoyancy, thermo-diffusive, hydrodynamic, acoustic, etc.

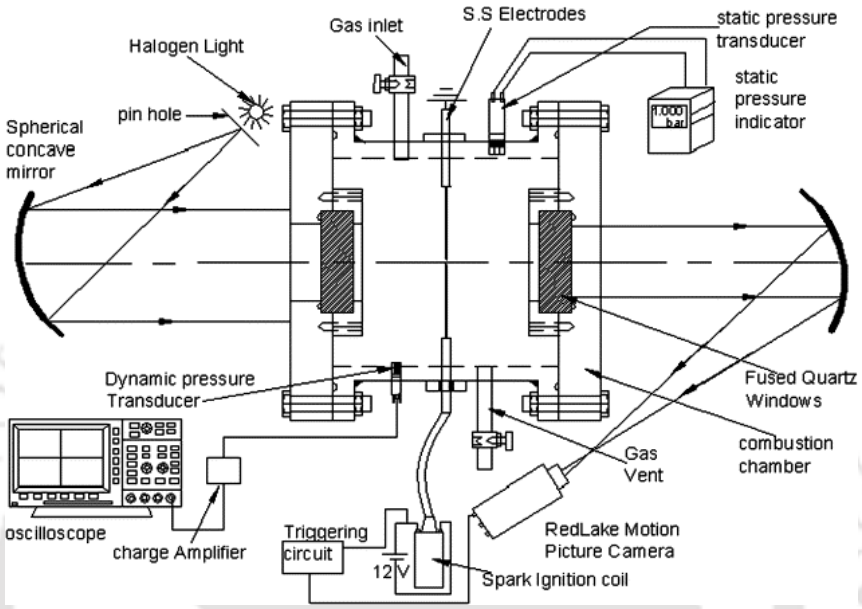

Figure 2-4 Schematic diagram of Spherically expanding flame setup [32]

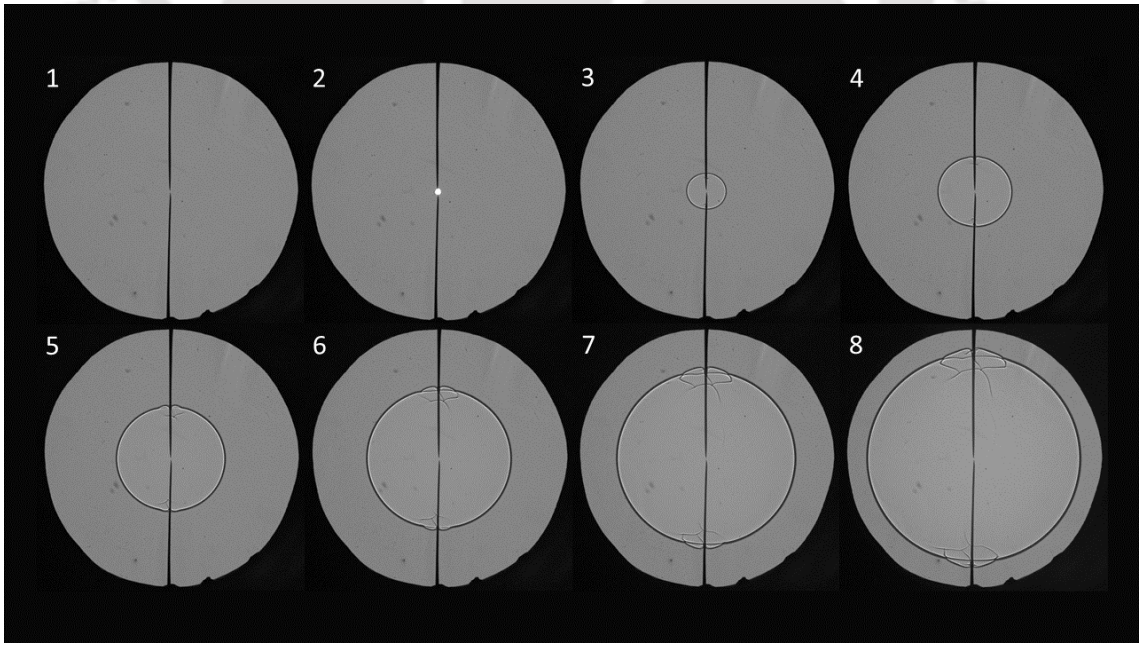

Figure 2-5 Shadowgraph images of expanding flame from a spark generated flame kernel

2.2.5 Summary of Flame measurement techniques

The most common experimental techniques used for flame propagation measurements are the conical flame burner, stagnation/counter-flow flame, heat flux burner, and spherical flame methods. Each method comes with a set of merits and challenges. The steady flow systems (stagnation, heat flux, Bunsen) can achieve higher initial temperatures, as these systems can easily control residence time and temperature. However, these devices are typically limited to pressures below 5, 10, and 15 atmospheres for stagnation flames [33], heat flux burners [34], and Bunsen burners [35]. In contrast, the spherical flame method is most suited for higher pressure measurements up to 71 atm [36]. The other systems require a steady flow with a relatively large volume of gas at high pressures. Burning rates typically increase with pressure, leading to high Reynolds number and flow instabilities in these systems and difficulty in cooling the burner and associated equipment. For these reasons, the outwardly propagating spherical flame is the best suitable method for laminar burning velocity studies at high pressure [33].

2.3 Spherical flame combustion test facilities

Measurement of laminar burning velocities, flame stretch interaction, hydrodynamic instabilities of premixed combustible mixtures, etc can be studied using outwardly propagating spherical flame method. This method also facilitates to condcut at elevated initial pressure, and temperature conditions in constant volume or pressure configuration. Single and double chamber concept test facilities are typically adopted to achieve the elevated initial pressure conditions in constant pressure mode. The mixtures are prepared inside the chamber in single-chamber rigs and ignited. The post-combustion pressure increase substantially, restricting it to a range of elevated initial pressures subjected to the designed structural integrity. Various test facilities operated in constant pressure configuration using a single chamber are presented in Table 2-1.

In a dual-chamber rig, after ignition, the volume of the chamber will be adjusted (increased) to accommodate the rise in post-combustion chamber pressure. Some of the dual chamber test facilities are reported in Table 2-2. A typical double chamber test facility is shown in Figure 2-6.

Dual-chamber rigs are typically comprised of an inner and outer chamber. Both chambers have dedicated optical accesses. From the literature, the volume of the outer chamber is selected such that the annular volume between the inner and the outer chambers varied 10-25 times than that of the volume of the inner chamber. The inner chamber is initially filled with the combustible mixture to the desired initial pressure and temperature. The outer chamber will be filled with inert gases at the same thermodynamic conditions as the inner chamber. The chambers are then left ideal to achieve quiescent conditions, and a central spark is generated at the center of the inner chamber. The gas release mechanism synchronously disengages and allows the combustible mixture to flow into the outer chamber. The combustible mixture flowing into the outer chamber gets diluted with inert gases and does not react. As a result, only 10-12% of the combustible mixture in the inner chamber will be burnt, depending on the mechanism and time of engagement (gas release mechanism engagement). Because of this mechanism, the peak post-combustion pressures will typically reach 1-2% of the initial pressure of the inner chamber[37]. This design concept facilitates conducting experiments at high initial pressure and temperature conditions.

Table 2-1 Selected single chamber test rigs with different chamber volumes

Sl.No.	Group	Volume(L)	Geometry	References
1	Razus et al.	0.5	Spherical	[48]
2	Keshava Murthy et al.	1	Spherical	[49]
3	Omari et al.	1	Spherical	[50]
4	Xiouris et al.	4.4	Spherical	[51]
5	Bradley et al.	28.7	Spherical	[52]
6	Prathap et al.	43.7	Cylindrical with unity aspect ratio	[53]

Table 2-2 Overview of Double Chamber combustion rig development from literature

Year	Group	Chamber geometry	volume ratio	Max P(atm)	Regime and variation	Imaging technique
2000	Tse et al. [38]	Inner-Cylindrical Outer-Cylindrical	25:1	60	Laminar (Pressure)	Schlieren Shadowgraph
2005	Qin et al. [39]	Inner-Cylindrical Outer-Cylindrical	10:1	30	Laminar	Schlieren
2009	Kelley et al. [40]	Inner-Cylindrical Outer-Cylindrical	12:1	30	Laminar (Pressure & Temperature)	Schlieren
2011	Liu et al. [41]	Inner- Cruciform Cylindrical Outer-Cylindrical	-NA-	10	Laminar & Turbulent (Pressure and Reynolds number)	Schlieren Direct Imaging Particle Image Velocimetry Laser Doppler Velocimetry
2012	Chaudhuri et al. [42]	Inner-Cylindrical Outer-Cylindrical	12:1	30	Turbulent	Schlieren Particle Image Velocimetry Laser Mie-Scattering
2013	Santner et al. [43]	Inner-Spherical Outer-Cylindrical	12:1	30	Laminar	Schlieren
2013	Nassouri et al. [44]	Inner-Cylindrical Outer-Octagonal	10:1	118.4	Laminar (Pressure & Temperature)	Shadowgraph Laser tomography
2014	Ai et al. [45]	Inner-Cylindrical Outer-Cylindrical	-NA-	39.5	Laminar	Schlieren
2015	Thimothée et al. [46]	Inner-Spherical Outer-Octagonal	9.2:1	118.4	Laminar (Pressure & Temperature)	Shadowgraph Laser tomography
2016	Jiang et al. [47]	Inner- Cruciform Cylindrical Outer-Cylindrical	-NA-	10	Laminar & Turbulent (Pressure and Reynolds number)	Schlieren Direct Imaging Particle Image Velocimetry Laser Doppler Velocimetry

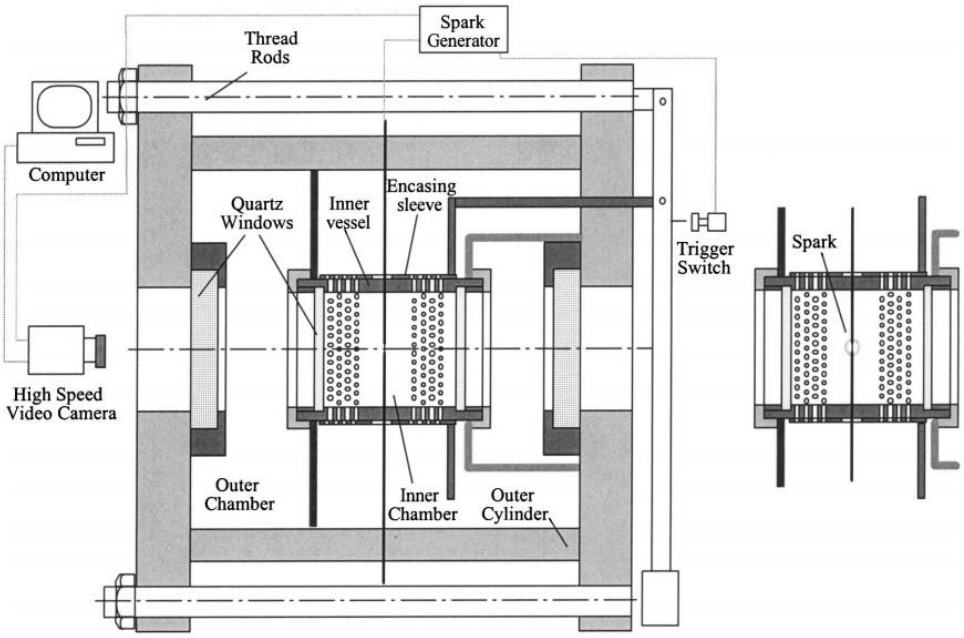

Figure 2-6 Schematic diagram of a typical double/dual-chamber test facility [37]

2.4 Summary of Spherical flame combustion test facilities

Both single and double chamber test facilities were predominantly used for exploring the combustion characteristics at elevated pressure conditions. Each variant/test facility was associated with both operational advantages and drawbacks. A hybrid test facility that can be operated in single and double chamber mode would be more appropriate to maximize the benefits. The mode can be selected based on the requirement of the initial pressure. A test facility chamber with the following characteristics will address many of the above-discussed challenges

- Spherical inner chamber with optical access to monitor flame front evolution.
- Flat surface for accommodating the instrumentation and pressure release systems.
- Gas pressure release mechanism with a minimum number of moving parts, less complex, replaceable, reliable, and provision for synchronous operation.
- Non-exclusive, detachable, and spherical chambers with minimum required volume.
- Simple heating mechanism with less warm-up time and with better active control.
- Small maintenance cycle, provision for sample collection, and reuse of inert gases.

2.5 Producer gas

As mentioned in the previous chapter, the producer gas is chiefly generated from biomass gasification. Due to a significant volume fraction of non-combustible gaseous components, it has a low heating value. It is unsuitable for a wide range of applications due to the relatively low flame temperature and laminar burning velocity. A large volume of the gas has to be stored for the same energy content compared to a pure combustible gaseous mixture. The share of non-combustible components has to be decreased to increase the energy per unit volume, flame temperature, and laminar burning velocity. It is crucial to analyze the variation in the composition and its effects on the laminar burning velocity and onset of intrinsic instabilities.

2.5.1 Composition variation

Eight hundred diverse compositions (different research groups, feedstocks, gasifiers, oxidizers, operating and collecting conditions) from recent literature (2001-2019) were considered to understand the PG composition variation. These included compositions of gases obtained at the middle/end of any gasification process and simulated gas (a mixture created from individual gas cylinders) based on other experimental data and/or with theoretical justifications. The model estimated compositions were omitted. A detailed list of about 800 compositions with references has been presented in the Appendix section, and an abridged summary is in Table 2-3. To avoid ambiguity upon using individual absolute values, the percentage volume fraction (mole fraction) of individual components was segregated into combustible components (CC) ($CH_4 + H_2 + CO$) and non-combustible components (NCC) ($N_2 + CO_2$) categories and then normalized. The other volatile components were ignored in the current work due to the negligible fraction and their presence exclusive only to certain feedstocks and operating conditions. Moisture was one of the important NCC species that was not considered, as in most production plants, the PG was dried out to minimize moisture.

Table 2-3 Abridged summary of producer gas composition from different sources

Year	CO_2	N_2	CH_4	H_2	CO	Source	Data Extraction	Reference
2001	6.2666	43.2408	0.9145	20.7936	28.8706	Unspecified Wood	Digitized	Zainal et al. [61]
2004	10	55.1	1.9	14	19	Keekar Wood	Absolute	Uma et al. [62]
2005	14.44	na	4.19	5.84	15.77	Seed Corn	Absolute	Zhang et al. [63]
2006	18.93	55.63	1.51	12.03	11.9	Cashew Nut Shells	Absolute	Singh et al. [64]
2007	na	51.471	1.864	14.083	14.049	Jatropha Seed Husk	Absolute	Vyas et al. [65]
2008	42.48	na	6.73	26.68	22.79	Olive Kernels	Absolute	Skoulou et al. [66]
2009	16.8	45.3	1.9	13.7	22.3	Simulated Gas	Absolute	Mohon Roy et al. [67]
2010	19.43	28.2	2.54	20.71	29.13	Coal+Pine Sawdust+Rice Straw	Absolute	Alauddin et al. [68]
2011	19.72	55.02	3.15	5.04	17.07	Cashew Nut Shells	Absolute	Tippayawong et al. [69]
2012	12	47	2	19	20	Simulated Gas	Absolute	Street et al. [70]
2013	15	53	3	13	16	Modified-Municipal Sewage Sludge	Absolute	Szwaja et al. [71]
2014	9.5	47.5	2	18.5	19.5	Unspecified Wood Chips	Averaged	Vera et al. [72]
2015	22.48	38.11	8.2	3.13	25.8	Rubber Wood Sawdust	Absolute	Simanjuntak et al. [73]
2016	9	50	3	17	20	Babul wood	Averaged	Yaliwal et al. [16]
2017	15	45	5	15	20	Simulated Gas	Absolute	Warsita et al. [74]
2018	20.5	0	15.5	42.8	21.2	Simulated Gas	Absolute	Wang et al. [75]
2019	11.9	45.9	1.5	19.7	21	Bamboo	Absolute	T. Piemsinlapakunchon et al. [76]

2.5.2 Laminar burning velocity and intrinsic instabilities

A large database on laminar burning velocities of H_2-air, C_1-C_5 hydrocarbons-air, liquid fuels (n-Heptane, iso-octane, and n-decane)-air spanning over the last three decades was presented by Konnov et al. [54] for a broader range of equivalence ratios (ϕ) and thermodynamic conditions. Similarly, *LBV* data were available for the H_2-CO-air system with respect to different H_2/CO ratios, equivalence ratios, initial temperatures, and pressures with/without N_2/CO_2 dilution [55–60]. Vu et al. [77] studied the delay in the onset of hydrodynamic instabilities in an equimolar mixture of H_2 and CO by adding hydrocarbon (such as CH_4/C_3H_8/C_4H_{10} from 0 to 10%) at 1-3 bar and 298 ± 3 K by using the spherical flame method. The addition of methane did not alter the critical radius at which the onset of hydrodynamic instabilities was observed, whereas C_3H_8/C_4H_{10} delayed the same to a much larger critical radius. Other than methane, Yan et al. [14] reported *LBV* of PG (H_2/CO/CH_4/CO_2/N_2)-air mixtures using a flat flame method at 1 atm and 298-358 K. In their study, three variants of PG derived from a gasification unit were considered.

The co-firing of PG with methane provided higher *LBV* than pure methane-air mixtures, and the prediction of respective *LBV* at measurement conditions by GRI Mech 3.0 was not satisfactory. Similarly, He et al. [78] studied 14 variants of PG-air mixture at 1 atm and 298 K to understand the impact of variation of CO in the considered fuel. It was reported that augmentation/reduction in *LBV* due to an increase in CO in the absence/presence of H_2 depended on the viability of chain propagation elementary reaction of OH + CO ↔ CO_2 + H.

Lapalme et al. [79] used the Bunsen burner method and the chemiluminescence technique to measure *LBV* of syngas mixtures with H_2/CO ratio kept as unity, and methane was varied between 0-40% by volume in the fuel, which resulted in reduced *LBV*. But in another aspect, Kolekar et al. [80] studied syngas having H_2/CO ratio of 0.75 with 5% CH_4 and 65% (CO_2:N_2) burning in the air using a diverging channel method at 1 bar and up to 650 K, and reported that the addition of CH_4 enhanced *LBV* of the mixture as methane was only added replacing the diluents in the fuel. Varghese et al. [81] studied nine variants of PG-air mixtures using a diverging channel method at 300-650 K and 1-5 bar. The effect of replacing the non-combustible components with combustible components was also studied. A new power law-based correlation was proposed to

estimate the *LBV* of PG air mixtures as a function of equivalence ratio, initial temperature, and pressure for a wide range of operating conditions. The level of variation in each component of PG considered in the study was inadequate compared to the substantial variation in the PG reported in the literature.

Zhou et al. [82] investigated *LBV* and L_b of fuel ($40H_2$: 40CO: $20CH_4$)-air mixtures with different proportions of diluent (N_2/CO_2) by using the freely expanding spherical flame method in a cylindrical chamber at 0.1 MPa, 300 K and ϕ = 0.6-1.5. It was mentioned that the addition of diluents in syngas decreased *LBV* and promoted the diffusional-thermal instability, but it delayed the onset of hydrodynamic instabilities. Hence, dilution with CO_2 had a pronounced effect in suppressing or delaying hydrodynamic instabilities than N_2. Li et al. [83] mechanism was used (21 species, 84 reactions). A deviation was reported between experiments and simulations at higher percentages of N_2/CO_2. Using the spherical flame method, Lapalme et al. [84] investigated the onset of thermo-diffusive/hydrodynamic instability for syngas fuels (H_2:CO) at 1 bar, and 300 K. CH_4/CO_2 was also added to syngas and studied the effect on the instabilities. It was mentioned that the controlling parameters were Lewis number, flame thickness, and density ratio of reactants to products. It was reported that the addition of methane did not delay the onset of instabilities. Recently, Oliveira et al. [85] reported *LBV* of synthetic gas ($H_2/CO/CH_4/CO_2/N_2$) representing composition from downdraft gasifier at 950 mbar, 298 K, ϕ = 0.88-1.74 using the Bunsen burner method equipped with OH-PLIF technique.

Cheng et al. [86,87] measured the *LBV* of the Refined Producer gas (RPG) -Air mixtures by the opposed-jet flames method. *LBV* increased with the addition of H_2 due to a chemical effect (an increase in the mole fraction of active species) than thermal effect (increase in equilibrium flame temperature). Abe et al. [1] measured the *LBV* of RPG (xCH_4:yCO:zH_2)-air mixtures in proportions x:y:z = 1:1:1 to 1:2:2 using the nozzle burner method at different initial temperatures, T = 323-573 K, with and without N_2/CO_2 dilution. A linear increment in the *LBV* with the increase in temperature was reported. Morovatiyan et al. [9] explored *LBV*, flame morphology, and pressure history of CH_4:CO:H_2 mixtures (100:00:00, 80:10:10 & 60:20:20) in a cylindrical constant volume vessel using spherically expanding flame method at P = 1 bar and T = 298 K. CH_4:CO:H_2 (60:20:20) mixture observed to had wider flammability and higher *LBV*. Lapalme et al. [79] measured the *LBV* of H_2:CO mixtures mixed with CO_2/CH_4 using the Bunsen burner

method at different initial temperatures (295-450 K) and compositions (ϕ: 0.8-2.2). The addition of CH_4 reduced the *LBV* of RPG mixture compositions such as CH_4:CO:H_2 = 5:47.5:47.5, 20:40:40, and 40:30:30 and shifted the peak *LBV* towards the stoichiometric mixture. The USC Mech II or GRI Mech 3.0 could not predict the shift. Xie et al. [88], Liu et al. [8], Zhou et al. [89], etc. studied the flame morphology, pressure history, effect of dilution, etc. on RPG mixtures at different conditions.

Apart from *LBV* measurement, Lapalme et al. [84] quantified the occurrence of thermo-diffusive and hydrodynamic instabilities in the CO:H_2 mixtures mixed with CO_2/CH_4 using an expanding spherical flame method. The ratio of the stretched burning velocity at the critical radius, and the normalized critical *LBV* $\left(S_{u,cr}/S_u^0\right)$, and its variation with self-acceleration coefficient (α) were used to determine and distinguish the two instabilities as compared to the critical radius (R_{cr}) as a function of α. A new correlation of critical Peclet number (Pe_{cr}) in terms of both instabilities (hydrodynamic: Prandtl number (Pr) & unburnt-burnt density ratio (σ), thermo-diffusive: Lewis (Le) and Zeldovich (Ze) numbers) was proposed [84] based on experimental data and a correlation proposed by Jomaas et al. [90]. Further studies on these instabilities can be found here [19–30].

2.5.3 Summary of Producer gas combustion characteristics

The preceding discussion pointed out that most of the studies involved very specific PG composition-air mixtures or a slight variation, which are insufficient to map the composition variations expected in real biomass gasifiers. In addition, most of the dilution effect studies are reported either with CO_2 or N_2 but not a combination of both, which is inevitable in practical PG compositions. The burner method was chiefly employed by most of the studies, and the flame stability aspect was not discussed in detail. Comprehensive treatment of intrinsic instabilities and a systematic approach to understanding the effect of change in composition under the testing conditions of practical importance are missing in the available related literature. Hence, a systematic study of the variation of each species in PG on its combustion characteristics and flame stability using one of the accurate methods, the freely expanding spherical flame method, is required. A comprehensive and systematic treatment of intrinsic instabilities is also necessary.

2.6 Objectives

1. Addressing the design, development, and execution challenges associated with elevated pressure single chamber test facility with all essential provisions to upgrade to a double chamber test facility.

   • Effect of chamber geometry, volume, thermodynamic model, and post-processing data range selection by analyzing the raw measured data from different test rigs.

   • Conception of design solutions for the listed challenges and development of a combustion rig based on the outcomes to facilitate freely expanding spherical flame combustion at elevated initial pressure conditions.

   • Development of robust post-processing algorithms to detect flame edges, and the onset of cell formation on the spherical flame fronts.
2. Identification of standard representative producer gas composition from a detailed literature review.
3. Effect of non-combustible components (N_2 and CO_2) on the *LBV* and instability due to preferential diffusion effects of producer gas-oxygen mixtures.
4. Effect of combustible components (H_2, CO, and CH_4) on the *LBV* and stability of mixture towards preferential diffusion effects of producer gas-oxygen mixtures.
5. Effect of initial pressure on the *LBV* and preferential diffusion instability of refined producer gas (H_2, CO, and CH_4) - air mixtures.

2.7 Design of experiments

The experiments were conducted in two different phases to understand the effect of various constituents on combustion characteristics at different initial thermodynamic conditions. The variation in the compositions and conditions were selected based on the discussed literature gaps.

2.7.1 Effect of Non-combustible components

The mole fraction of CC for all the 800 compositions is presented in Figure *2-7*, and the variation of X_{CC} typically varied around 25-45% in most cases. The extent of variation in mole fractions of H_2, CO, and CH_4 in the combustible components is reported in Figure 2-8. The above figure clearly shows that the mole fraction of CH_4 among all combustible species is relatively low, and it varied in the range of 0-20% with few exceptions like

51.6%. The mole fractions of H_2 and CO have comparable values of 25-65%, with an average of around 45%.

Compositions of PG from a batch type pyrolysis plant in India which was developed and operated by Chandrasekaran et al. [102] were obtained. Air was used as the oxidizer and Casuarina wood, Prosopis Juliflora twigs (from small branches), logs (from the trunk), roots (bigger ones) and coconut shells as feedstock. The measured compositions (major species only) of generated PG from Prosopis Juliflora wood feedstock at different temperatures (measured at the exit of the bed) for an experimental run are summarized in Table 2-4.

Table 2-4: The typical component formation at different temperatures in a pyrolysis unit for Prosopis Juliflora wood feedstock

	Temperature at the exit of the bed (°C)						
Contents	**27-100**	**100-150**	**150-300**	**300**	**400**	**500**	**600**
Water Vapour	Small	Significant	Significant	-	-	-	-
CH_4 (%)	-	-	-	1.32	4.98	8.74	12.46
H_2 (%)	-	-	-	1.58	5.74	9.38	15.52
CO (%)	-	-	Small	30.56	34.22	36.34	35.10
Diluents (%)	-	-	-	66.54	55.06	45.54	36.92

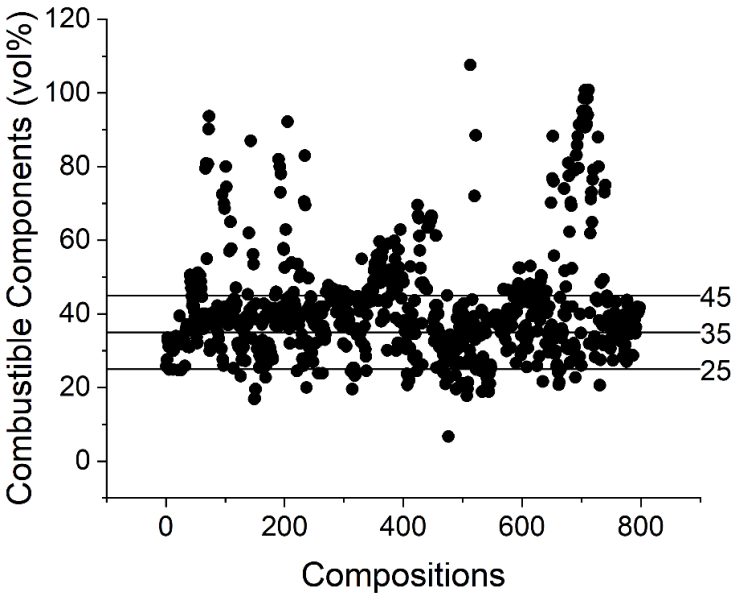

Figure 2-7 Mole fraction of combustible components for various compositions of producer gas reported in literature.

Additional data corresponding to PG compositions based on different feedstock (not presented here) by Chandrasekaran et al. [102] was also considered. A plant operating at an equivalent condition to 400-600°C (at the exit of the bed) or above led to a similar range of variation of H_2, CO & CH_4 (Figure 2-8).

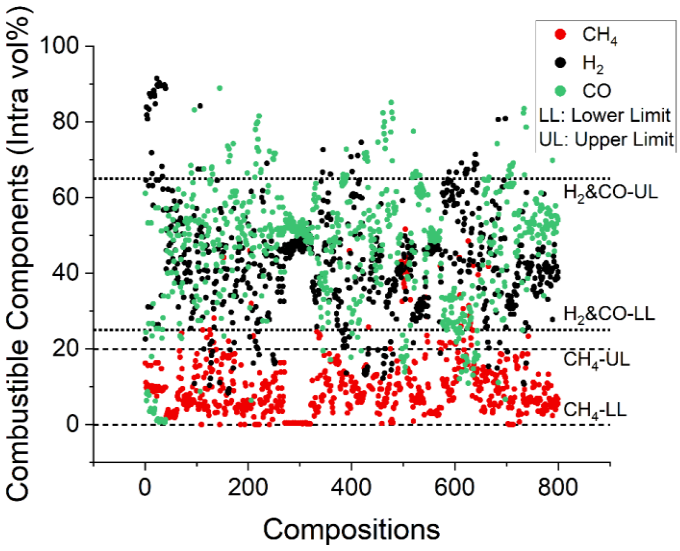

Figure 2-8 Normalized variation of intra-combustible components in producer gas.

2.7.1.1 Intra-NCC-Variation

Identical to the intra-CC study, the intra-NCC compositions are calculated and reported in Figure 2-9. The CO_2 and N_2 have a narrow variation band with average values around 25% and 75% (by volume), respectively, unlike the combustible components.

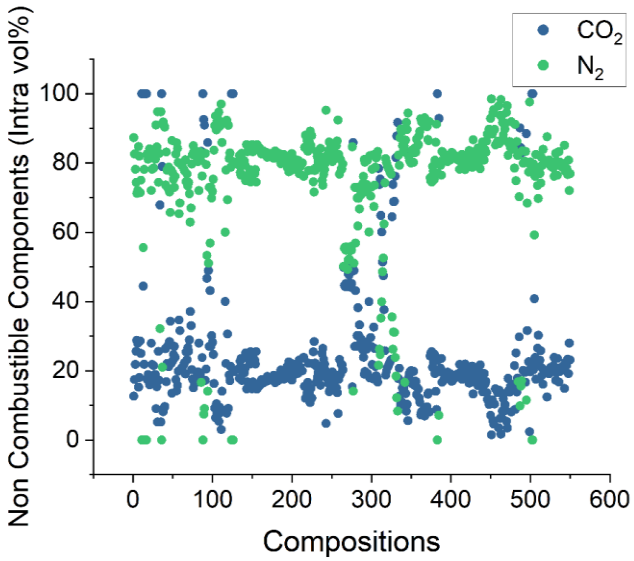

Figure 2-9 Normalized variation of intra-non-combustible components in producer gas

2.7.1.2 Present PG composition matrix

The composition of PG is considered as *Z*% CC+(100-*Z*)% NCC where *Z* is varied at 25, 35, and 45 as presented in Figure 2-7. It is referred to as the inter-CC-NCC study. CC is considered as 25CH_4:25CO:25H_2:25Y, where *Y* represents rich combustible species, which may be CH_4 or CO or H_2, and referred to as the intra-CC study.

Hence, a fuel with more CH_4/CO/H_2 is called CH_4/CO/H_2-rich PG fuel. In the Intra-CC study, each fuel species is varied between 25-50%. This variation is in line with the variations shown in Figure 2-8 for H_2/CO species. 25% CH_4 in CC corresponds to the higher limit of the average shown in Figure 2-8. For CH_4, a few exceptional cases are reported with higher values; around 50% is considered than the lower proportions. As mentioned earlier, refining inert from PG may lead to higher mole fractions of all combustible species. Also, no studies are available for PG having higher volume fractions of CH_4. A similar approach is followed for NCC as *P*% CO_2 + (100-*P*)% N_2 where *P* is varied from 0-100 (by volume) and referred to as Intra-NCC study. To mimic the differential refining process, the mole fraction of CO_2 in NCC is also varied from 0 - 100% identical to that of N_2. Forty-five variants of PG were tested in the present work to understand the effect of each species in detail while it was reacting with pure oxygen. Figure 2-10 shows all the studied compositions of PG (CH_4-rich set) in the present work graphically.

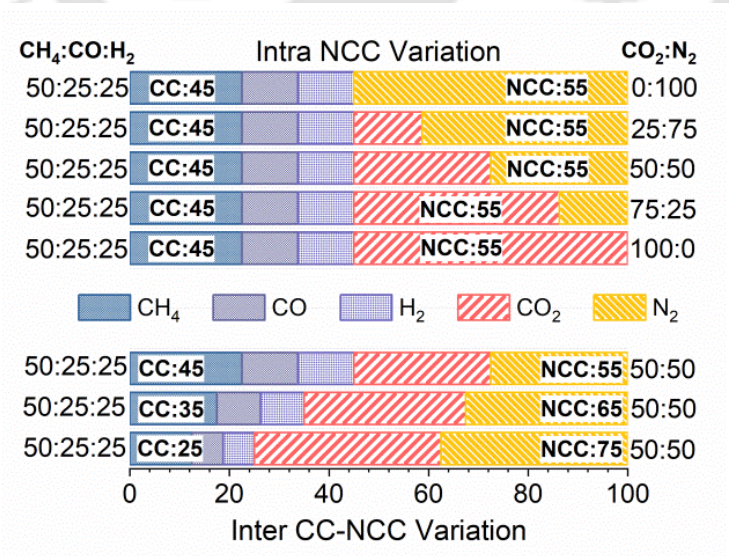

Figure 2-10 Producer gas compositions studied in the present work (CH_4-rich set)

2.7.2 Effect of Combustible components

The composition of refined producer gas (RPG) is considered as 50%*A*+ *X*%*B* + (50-*X*)%*C* where *A*: $CH_4/H_2/CO$, *B*: $H_2/CO/CH_4$, *C*: $CO/CH_4/H_2$, and *X*: 0:50 in steps of 12.5%. Table 2-5 and Figure 2-11 shows the compositions considered for the combustible composition variation study.

Table 2-5 Refined producer gas composition variation

Refined Producer Gas (RPG) Composition (vol%)				
Case	**H_2**	**CO**	**CH_4**	**H_2: CO: CH_4**
1	50	0	50	**4**:0:4
2	50	12.5	37.5	**4**:1:3
3	50	25	25	**4**:2:2
4	50	37.5	12.5	**4**:3:1
5	50	50	0	**4**:**4**:0
6	37.5	50	12.5	3:**4**:1
7	25	50	25	2:**4**:2
8	12.5	50	37.5	1:**4**:3
9	0	50	50	0:**4**:**4**
10	12.5	37.5	50	1:3:**4**
11	25	25	50	2:2:**4**
12	37.5	12.5	50	3:1:**4**
1*	50	0	50	4:0:**4**

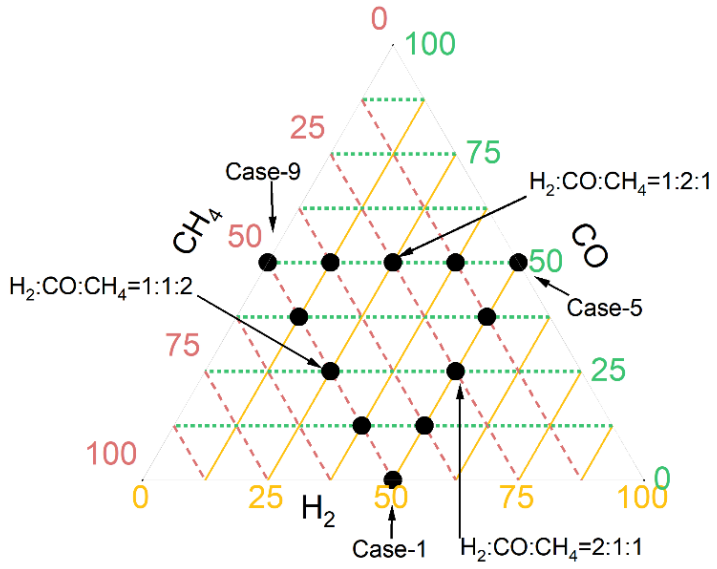

Figure 2-11 Producer gas compositions studied for combustible component variation study

2.7.3 Effect of Initial pressure

All the compositions discussed in section 2.7.2 were considered at 300 ± 3 K and 1, 2, and 4 bar to study the effect of initial pressure.

Chapter 3 Experimental setup and Methodology

The design of the experimental rig, experimental operating conditions, experimental procedure, and post-processing methodology are discussed in this chapter.

3.1 Design of single-chamber test rig

According to the regular engineering practice, the test facility development of the design was carried out in three stages. The requirements, essential features, and different designs of core parts were discussed in the conceptual design phase. A particular design concept was selected based on desired requirements and practical feasibility. The primary design parameters were defined, and other subsystems were identified with essential information during the preliminary design phase. The entire list of design parameters was prepared in detail and updated to achieve an optimized setup during the detailed design phase. After concluding this phase, the execution, redesign, and refinement were carried out. The chamber diameter (shape: spherical) was considered at least 20 cm with at least 10 cm optical visibility based on volume effect analysis [103] and other physical constraints, as discussed in the previous chapter. The vertical alignment of heating cartridges was preferred. Non-magnetic grades of stainless steel were explored, which can withstand a ceiling working pressure of 100 bar and a body temperature up to 500 K. Standard ½" BSP threaded ports were considered. Several models were designed and iterated to include features based on these primary design constraints, as shown in Figure 3-1.

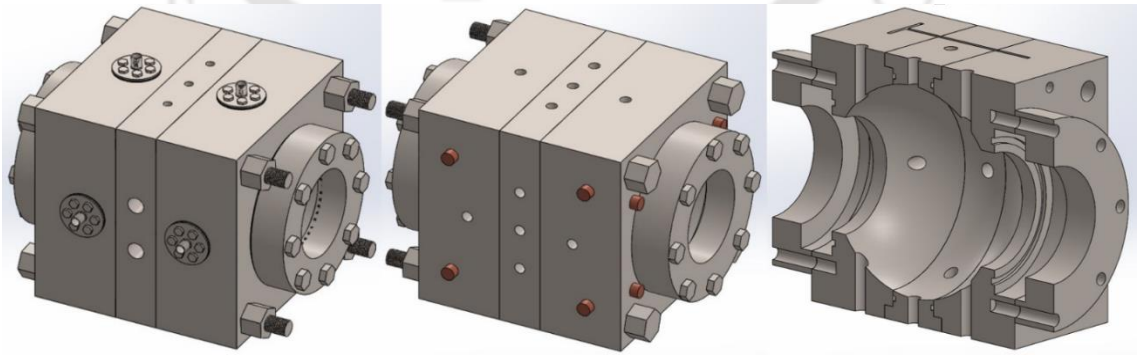

Figure 3-1 Design of the chamber at the end of the 4th iteration

3.2 Design Specifications of Developed Chamber

The test rig design was developed to facilitate double chamber related diverse operations, as presented in Table 3-1.

Table 3-1 A summary of the subsystems and their operation

Sl.No	List of processes	Functionality
1	Purging	To purge the chamber with air after the combustion to replace the burned gases and bring down the chamber temperature.
2	Evacuating	To evacuate the leftover gases from the chamber after combustion & purging before creating a vacuum to refill with fresh gases.
3	Filling	To channel the high purity fresh gases from cylinders to the chamber to fill it with the desired combustible mixture.
4	2nd chamber	To collect the gases from the core chamber with active control during/at the end of the spherical flame propagation.
5	Heating	To achieve a stable and uniform set temperature in the core chamber with minimum warm-up time.
6	Ignition	To generate a spark of specific energy and duration at the center of the chamber upon triggering.
7	Imaging	To capture the propagating flame with an excellent resolution to facilitate edge and cracks detection.
8	Triggering	To send the trigger signals to the various devices/systems depending on the response times in synchronization with ignition.
9	Data Acquisition	To acquire, monitor, and store the data of important parameters.

After several design iterations upon including all required subsystems of specific operations, the final design was concluded with the design specifications mentioned in Table 3-2. The detailed procedure for arriving at the design specifications is explained in the Appendix. The developed test facility under operation is shown in Figure 3-2.

Figure 3-2 Elevated Pressure combustion test facility under operation

Table 3-2 Summary of final design specifications

Sl. No.	**Design parameter**	**value**
1	Design Pressure	100 bar
2	Temperature	500 K
3	MOC – Central body and flanges	SS321
4	MOC – Studs	SS304
5	Inner volume of the chamber	~4.5 L
6	Inner shape of chamber	Spherical
7	Outer shape of the chamber	Cube
8	Inner major dimensions	Diameter = 200 mm
9	Outer major dimensions	250 mm × 250 mm × 250 mm
10	Minimum thickness	25 mm
11	Weight	100+ kgs
12	Clear Aperture dimension	110 mm
13	No. of Optical access	2
14	Diameter of studs	20 mm
15	Diameter of flange holes	12 mm
16	No. of Bolts used for flanges	8
17	Minimum thread engagement	25 mm
18	No. of holes (after assembling)	18 (threaded & through)
19	Sealing	O-ring
20	No. of ports	15

3.3 Experimental Procedure

A new spherical chamber having an inner diameter of 20 cm was designed to withstand 10 MPa and 500 K in compliance with ASME standards and fabricated. Two quartz windows with 110 mm clear aperture were mounted to the chamber to facilitate the imaging of flame propagation. KELLER LEO 3 (0-4bar, ±0.1% FS accuracy) and KISTLER 7061C pressure transducers were used to measure absolute and unsteady pressure in the spherical chamber. A standard LED white light source, two spherical concave mirrors of 6” diameter and 60” focal length, and a high-speed camera (PHANTOM v1210) were used to establish the high-speed shadowgraph imaging system. A schematic representation of the test facility is presented in Figure 3-3.

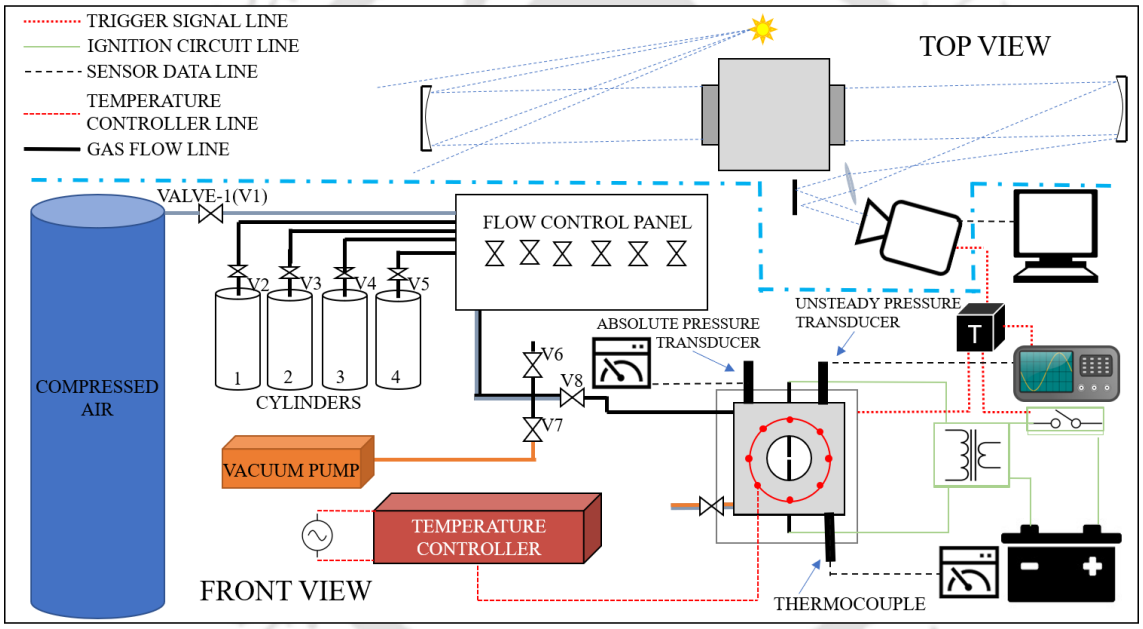

Figure 3-3 Schematic diagram of the combustion test facility in constant volume configuration

Ignition was achieved by an electronic spark ignition system using extended thin steel electrodes which were pointed near the tip. Electrodes were positioned vertically with a 1mm gap between them. A pulse generator was used to trigger the camera, ignition system, and data acquisition system simultaneously to initiate the experiment and record the essential data.

A K-type thermocouple was used to measure the temperature of the reactants in the chamber. The gases of purity level H_2 (99.99%), CO (99.95%), CO_2 (99.99%), CH_4 (99.999%), O_2 (99.999%), and N_2 (99.9997%) were used in the current study. The chamber was purged with dry (de-humidified) air supplied by the lab compressor, bringing the core temperature to around 300 ± 5 K, and then evacuated. The gases were filled from lower to higher volume fractions through the partial pressure method. Needle valves and an absolute pressure transducer were used to precisely fill the gases. The system was left idle for 10-15 mins to achieve quiescent and well-mixed conditions inside the chamber. Ignition was then achieved by supplying slightly higher than minimum ignition energy. The flame propagation and pressure development were recorded using a high-speed camera and an unsteady pressure transducer. The chamber was then evacuated and later purged to remove post-combustion products and ultimately lowered the temperature to normal. The constant pressure period was identified from pressure-time data, and images corresponding to that period were used for processing. An image processing algorithm and Image Processing Toolbox in MATLAB software platform were used to obtain the radius data from recorded images. The radius-time data corresponding to constant pressure period and free from cells, distortions, buoyancy, etc., were considered for the following parameter calculations.

3.4 Data Processing

As mentioned in the earlier section, two data sets were recorded in the expanding spherical flame experiments under constant volume configuration. Depending on the type of data, the method was selected. The unsteady pressure-time data-based method was referred to as the confined flame method, while the radius-time data-driven method was called the unconfined flame method.

3.4.1 Confined flame method (Unsteady pressure-time data-driven)

In this method, unsteady pressure-time *(P-t)* data was solely required to estimate laminar burning velocity. The main advantage of this method was the ability to calculate the *LBV* at all possible conditions between initial and end thermodynamic conditions. As a result, thermodynamic conditions at elevated levels can be obtained. The primary thermodynamic model used to calculate the burning velocity was presented in Eq. 3.1.

The assumptions were:

- The total mass and volume of the vessel contents were conserved.
- The unburned premixed combustible gas mixture was initially at rest.
- The pressure remained spatially uniform during combustion.
- External heat input, heat losses, and buoyancy were negligible.
- The flame front was spherical and infinitely thin.
- The effect of flame stretch was negligible.
- The unburned gas was compressed isentropically.
- There was no heat transfer between the burned and unburned gas zones.

$$S_u = \frac{dP}{dt}\frac{dx(p)}{dP}\frac{R_{vessel}}{3}\left[1-\left(\frac{P_i}{P}\right)^{\frac{1}{\gamma_u}}(1-x(P))\right]^{-\frac{2}{3}}\left(\frac{P_i}{P}\right)^{\frac{1}{\gamma_u}} \quad 3.1$$

Several models were available in the literature, and the main difference among them was in estimating burned mass fraction from the *P-t* data. Widely used and recently developed models were considered for processing the data, as presented below.

Thermodynamic model by Lewis and von Elbe [104]

$$x(P) = \frac{P-P_i}{P_e-P_i} \quad 3.2$$

$$\frac{dx(P)}{dP} = \frac{1}{P_e-P_i} \quad 3.3$$

Thermodynamic model by Luitjen et al. [104]

$$x(P) = \frac{P-P_i f(P)}{P_e-P_i f(P)} \quad 3.4$$

$$f(P) = \left(\frac{\gamma_b-1}{\gamma_u-1}\right) + \left(\frac{\gamma_u-\gamma_b}{\gamma_u-1}\right)\left(\frac{P_i}{P}\right)^{\frac{\gamma_u-1}{\gamma_u}} \quad 3.5$$

$$\frac{dx}{dP} = \frac{1-P_i f'(P)}{P_e - P_i f(P)} + \frac{P_i f'(P)[P - P_i f(P)]}{[P_e - P_i f(P)]^2} \quad 3.6$$

$$P_i f'(P) = \left(\frac{\gamma_u - \gamma_b}{\gamma_u}\right)\left(\frac{P}{P_i}\right)^{-\frac{1}{\gamma_u}} \quad 3.7$$

Thermodynamic model by Omari et al. [50]

$$\gamma_{br} = \frac{1+\gamma_b}{2} \quad 3.8$$

$$P_r = \frac{P - P_i}{P_e - P_i} \quad 3.9$$

$$x(P) = \frac{P - P_i f(P)}{P_e - P_i f(P)} \quad 3.10$$

$$f(P) = \left(\frac{\gamma_{br} - 1}{\gamma_u - 1}\right) + \left(\frac{\gamma_u - \gamma_{br}}{\gamma_u - 1}\right)\left(\frac{P_i}{P}\right)^{\frac{\gamma_u - 1}{\gamma_u}} \quad 3.11$$

$$\frac{dx}{dP} = \frac{1-P_i f'(P)}{P_e - P_i f(P)} + \frac{P_i f'(P)[P - P_i f(P)]}{[P_e - P_i f(P)]^2} \quad 3.12$$

$$P_i f'(P) = \left(\frac{\gamma_u - \gamma_{br}}{\gamma_u}\right)\left(\frac{P}{P_i}\right)^{-\frac{1}{\gamma_u}} \quad 3.13$$

The flame front radius was estimated from the pressure and burned mass fraction using the following correlation:

$$\frac{R_f}{R_{vessel}} = \left[1 - \left(\frac{P_i}{P}\right)^{\frac{1}{\gamma_u}}(1 - x(P))\right]^{\frac{1}{3}} \quad 3.14$$

The following correlation was used to calculate the unburned mixture temperature at any intermediate stage of flame propagation.

$$T_u = T_i\left(\frac{P_i}{P}\right)^{\frac{\gamma_u - 1}{\gamma_u}} \quad 3.15$$

As presented in Eq. 3.16, a power-law correlation was used to fit the available *LBV* data at higher temperatures and pressures (corresponding to the flame front at the intermediate stage) and then extrapolated back to the initial condition.

$$\frac{S_u}{S_u^0} = \left(\frac{P}{P_i}\right)^{\alpha} \quad 3.16$$

The pressure-time data were processed using Eq. 3.1 iteratively to estimate *LBV* (S_u^0). Burned gas mass fraction and its variation with pressure were estimated using Eq. 3.2-3.13. The pressure data corresponding to an interval 0.25 to 0.5 times that of reduced pressure, P_r (Eq. 3.9) was chosen. Power law (Eq. 3.16) was employed in the selected data range, and laminar burning velocity at initial thermodynamic conditions was estimated through extrapolation. The above formulations were implemented in the data range with negligible stretch. For further analysis, the flame stretch was calculated with two different formulations K_1[3] and K_2[4].

$$K_1 = \frac{dP}{dt}\frac{\frac{dx}{dP}+\frac{1}{P\gamma_u}(1-x)}{\frac{3}{2}\left(\left(\frac{P}{P_i}\right)^{\frac{1}{\gamma_u}}-(1-x)\right)} \quad 3.17$$

$$K_2 = \frac{2}{3}\left(\frac{R_v}{R_f}\right)^3\left(1+\left(\frac{P_e-P}{\gamma_u P}\right)\right)\left(\frac{1}{P_e-P_i}\right)\left(\frac{P_i}{P}\right)^{\frac{1}{\gamma_u}}\frac{dP}{dt} \quad 3.18$$

3.4.2 Unconfined Flame Method (Radius-time data-driven)

Images recorded during the flame propagation inside the chamber corresponding to the constant pressure period were the essential input data needed for the post-processing in this method. The radius of the spherical flame (smooth and free from instabilities) was obtained using image processing. From the radius-time data, the unstretched *LBV* was estimated as explained below.

3.4.2.1 Image Processing algorithm

An in-house developed edge detection algorithm in MATLAB was used to measure the flame diameter from the images. This was developed to reduce the dependency on any single parameter and avoid the interpolation of pixels. Initially, a background image without any flame front was chosen. The image with the flame front was subtracted with the default background picture to obtain only the flame front-related data referred to as the working image. The working image was split into eight sectors: East, West, North, South, Northeast, Northwest, Southeast, and Southwest. A representative division is shown in Figure 3-4. The flame front was normal to axes in cardinal sectors. Either row

or column-wise marching/movement was used to identify the changes in the pixel intensity level. The distribution of pixel intensity levels from the Eastern sector is presented in Figure 3-5. The rate of change in the intensity was coupled with the moving average to identify the edge and nullify discreet points. The post averaged rate of change in intensity is presented in Figure 3-6. The outer edges were identified by specifying the stringent constraints, excluding all other edges in the image.

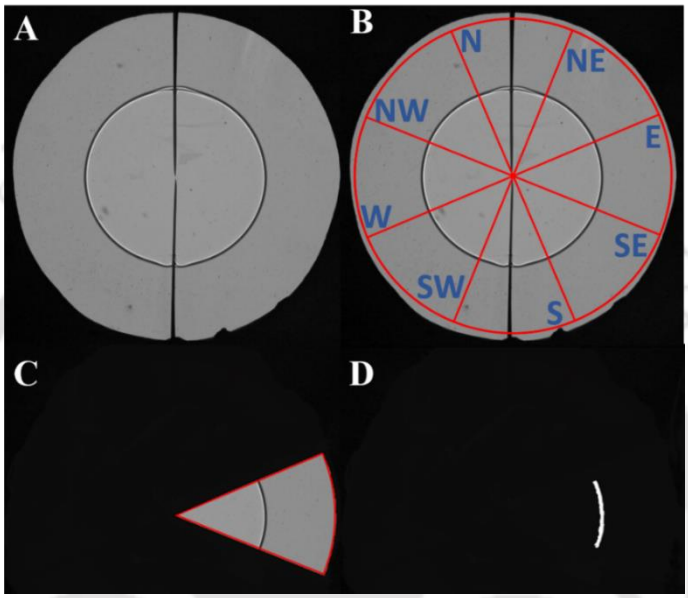

Figure 3-4 Various stages of a working image

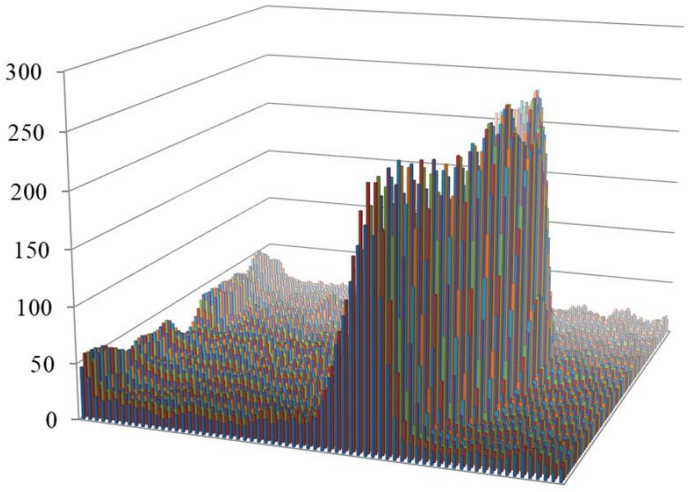

Figure 3-5 Pixel intensity distribution in the Eastern sector of the working image

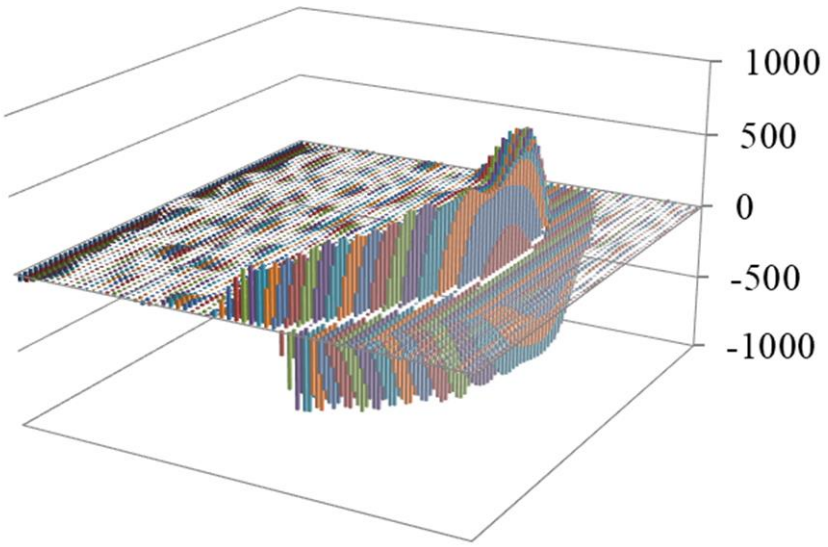

Figure 3-6 Rate of change in intensity in the Eastern sector of working image

The main challenge was identifying the edges in the ordinal directions as the flame front was at 45° to two cardinal directions. The marching, either row or column-wise, was not possible. Typically image was rotated by 45° to align with cardinal directions. This operation incorporated the interpolation of pixels, leading to distortion of original pixel data. This interpolation-based rotation was avoided by using the matrix-interlacing method.

3.4.2.1.1 Matrix-interlacing method

The pixel intensity distribution of the image was stored in a square matrix. The alternate pixels were separated, similar to the interlacing operation, and reassigned into a new matrix, as shown in Figure 3-7. The two new matrices were referred to as child matrices. The null points were dropped in the child matrix, as shown in Figure 3-8. New null points were added, and a new matrix was reconstructed, as presented in Figure 3-9. Figure 3-10 is the consolidated figure with all crucial steps of image rotation. The 45° rotated images were obtained without interpolating original pixel intensity data. The image rotation operation is executed on an image and presented in Figure 3-11.

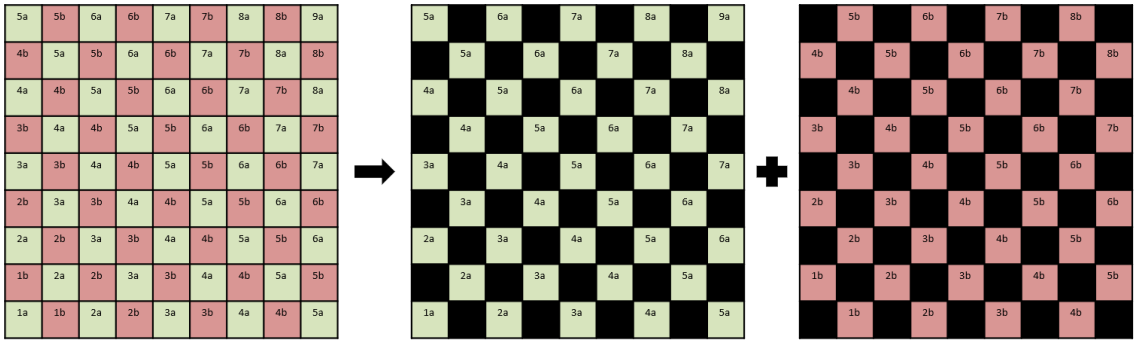

Figure 3-7 Parent matrix split into two child matrices

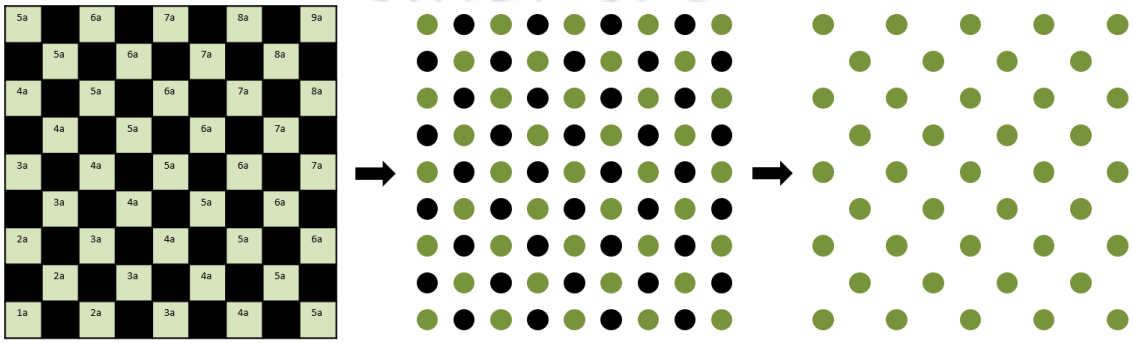

Figure 3-8 The removal of null values from the child matrix

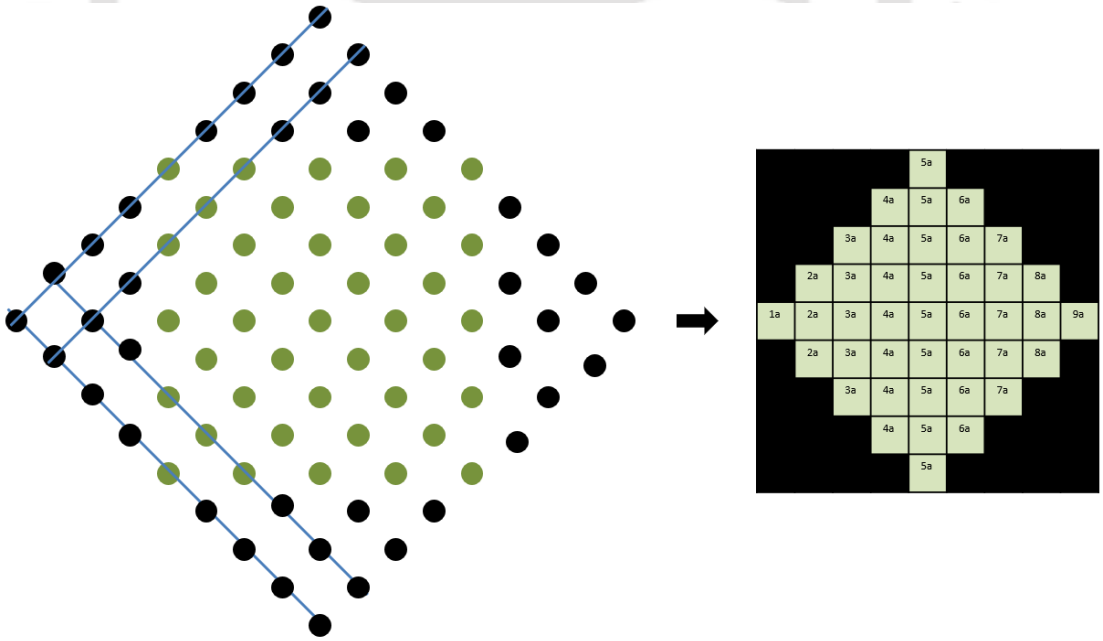

Figure 3-9 Reconstructing the child matrix with new null points

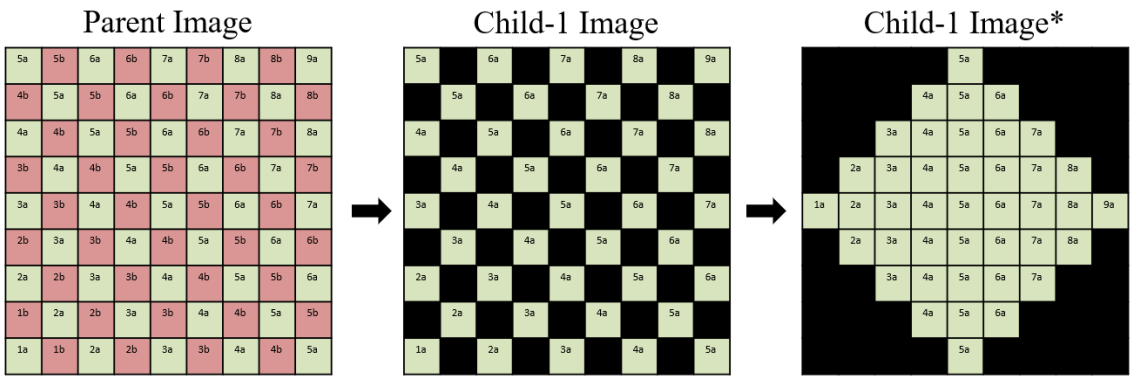

Figure 3-10 A consolidated image capturing the steps of image roatation

Figure 3-11 A test image split into two child images

The rotated images were processed similarly to cardinal sectors. The obtained edge data coordinates were reassigned back to the original configuration. The resultant data was corresponding to the ordinal sectors. All the coordinates were sorted, and duplicates were removed. The final edge list was fitted with a circle equation to compute the radius and its center. The procedure was repeated for all the images to obtain radius-time data. The main advantages of the developed algorithm were 1. The set of operations suitable enough to be implemented on any platform, 2. Minimized dependency on any single parameter, 3. The original pixel intensity distribution remained undisturbed, 4. Unwanted edges except the boundaries were ignored by default in the initial stages. As a result, the developed algorithm can be used for any non-smooth, turbulent, and unstable flame fronts, as shown in Figure 3-12. A word of caution was that edge detection of non-smooth images shown in Figure 3-12 was only for an illustration, and such non-smooth flames were never considered in the estimation of *LBV*.

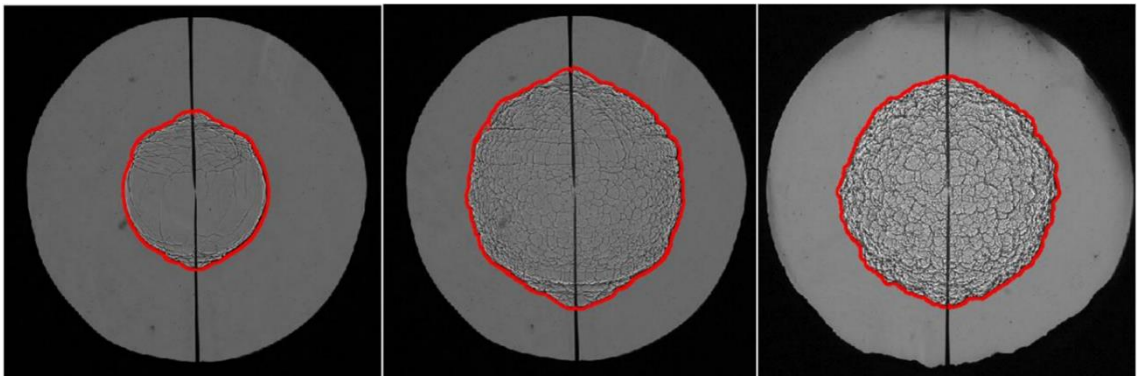

Figure 3-12 Edge detection of non-smooth spherical flames. This illustration is only for demonstrating the ability of the new edge detection algorithm. Non-smooth images were never considered for the estimation of *LBV*

3.4.2.2 Procedure for the estimation of Unstretched LBV

The measured/simulated radius-time data was processed as shown in the flowchart (Figure 3-13) to obtain unstretched *LBV* and burned gas Markstein length. Detailed description of each process mentioned in Figure 3-13 is discussed in the following section. Initially, stretched flame speed (S_b) was calculated using Eq. 3.19.

$$S_b = \frac{dr_f}{dt} \tag{3.19}$$

where r_f was the instantaneous flame radius. Eq. 3.19 was applicable only for thin flames where $(r_f/\delta_f) \ll 1$ (δ_f is the flame thickness) without ignition and buoyancy effects. As the spherical flames change curvature during the flame propagation, the stretch rate (K) was estimated using Eq. 3.20.

$$K = \frac{2}{r_f}\frac{dr_f}{dt} \tag{3.20}$$

Then, unstretched flame speed (S_b^0) at K = 0 was extrapolated using a linear model (Eq. 3.21[54]) and a non-linear model (Eq. 3.22[105]).

$$S_b = S_b^0 - L_b K \tag{3.21}$$

$$\frac{S_b}{S_b^0}\left(1 + \frac{2L_b}{r_f} + \frac{4L_b^2}{r_f^2} + \frac{16L_b^3}{3r_f^3} + O^4\left(\frac{L_b}{r_f}\right)\right) = 1 \tag{3.22}$$

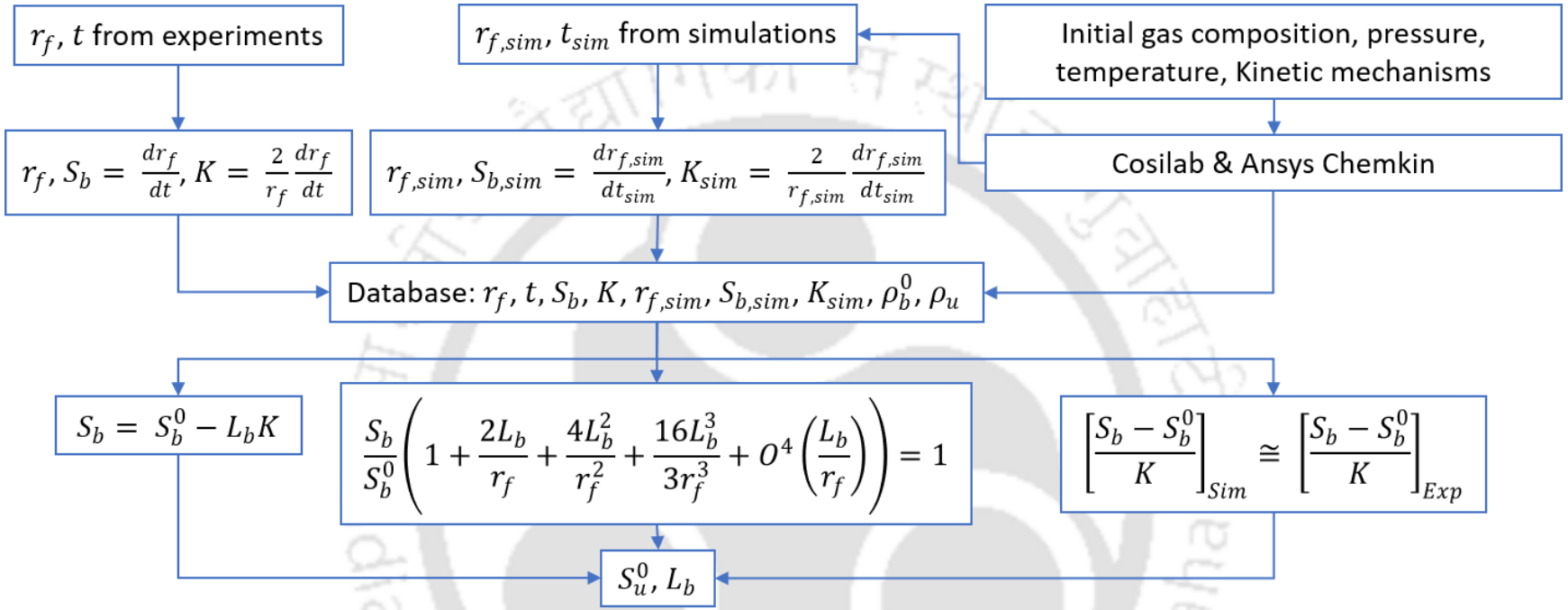

Figure 3-13 Flow chart of data processing in unconfined flame method

Also, the non-extrapolation model proposed by Xiouris et al. [51] for the estimation of S_b^0 as shown in the Eq. 3.23 was also used.

$$\left[\frac{S_b - S_b^0}{K}\right]_{Sim} \cong \left[\frac{S_b - S_b^0}{K}\right]_{Exp} \quad 3.23$$

The $S_{b,sim}^0$ was calculated from the freely propagating planar flame model in Ansys Chemkin [106] and instantaneous $S_{b,sim}$ and K_{sim} were estimated using one dimensional, expanding spherical flame model available in Cosilab [107]. For both the simulations, GRI Mech 3.0 [108] was used. From the known information of $S_{b,Exp}$ and $S_{b,Sim}$ at each K_{Exp}, $S_{b,Exp}^0$ was estimated by following Eq. 3.23. Then, the obtained $S_{b,Exp}^0$ at each K_{Exp} was averaged to find the final value of $S_{b,Exp}^0$ meant for that operating condition. Xiouris et al. [51] mentioned that the choice of chemical kinetic mechanism did not affect the accuracy of Eq. 3.23. Finally, laminar burning velocity (S_u^0) defined as the relative velocity of the reactants propagating normal to an adiabatic and stretch free planar flame was estimated using Eq. 3.24. Burned gas density (ρ_b^0) assumed to be in chemical equilibrium was estimated using equilibrium model in Ansys Chemkin.

$$S_u^0 = S_b^0 \left(\frac{\rho_b^0}{\rho_u}\right) \quad 3.24$$

3.4.3 Thermo-diffusive instability

From the linear (Eq. 3.21) and non-linear extrapolation (Eq. 3.22) models, the burned gas Markstein length (L_b) is also obtained. It quantifies the response of the flame to the stretch effects. A combustible mixture is stable/unstable to preferential diffusion effects in the cases (1) L_b is positive/negative, and (2) Lewis number of the mixture is greater/lesser than unity or critical Lewis number (Le^*). Lewis number (Le) is a ratio of mixture thermal diffusivity ($\propto_T$) to binary mass diffusivity (D_{ij}) where *i/j* represents the deficient/excess species. It indicates the stability of the flame towards an imbalance in thermal and mass diffusional effects. If $Le < Le^*$ (critical Lewis number) for a given combustible mixture, it indicates that the mixture will lead to an unstable flame due to the preferential diffusion effects.

Identifying the deficient reactant to estimate the binary mass diffusion coefficient was quite challenging if the combustible mixture: (a) was close to the stoichiometric

composition and (b) had more than three species. Recent studies [10] adopted a more sophisticated parameter called effective Lewis number (Le_{eff}) for multicomponent mixtures with several reactants eligible as deficient or excess species. Most of the models to estimate Le_{eff} were formulated using a weighted average of *Le* of different species available in the mixture, and the procedure for arriving at these weights differed from the selected model, such as arithmetic/harmonic mean [109], volume/mass fraction [110], and effective diffusion [110]. The heat release-based model by Law et al. [111] used a weighting factor of the normalized heating values of each fuel species, *i.e.*, the ratio of the heating value of a species to the heating value of the mixture. The mixture strength model by Matalon et al. [112] used Zeldovich number (*Ze*, Eq. 3.30) and *Le* of excess and deficient species to estimate the Le_{eff}. Recently, it was reported that the volume/effective diffusion-based models were well suited for PG mixtures [110,113]. Hence, the Le_{eff} in the present was calculated using both the volume-based (Eq. 3.25) and the effective diffusion-based (Eq. 3.26) models.

$$Le_{eff} = \sum_{i=1}^{4} X_i Le_i \qquad 3.25$$

$$\frac{1}{Le_{eff}} = \sum_{i=1}^{4} \frac{X_i}{Le_i} \qquad 3.26$$

where X_i referred to mole fraction, i representing CH_4, H_2, CO, O_2 and $Le_i = \propto_T / D_{im}$ was the Lewis number of the species i. α_T was the thermal diffusivity of the mixture (m^2/s) and D_{im} (m^2/s) was the effective diffusivity.

$$D_{im} = \left[(1 - X_i) / \left(\sum_{j=1, j\neq i}^{6} \left(\frac{X_j}{D_{ij}}\right)\right)\right] \qquad 3.27$$

where j represented CH_4, H_2, CO, O_2, N_2, and CO_2, and D_{ij} was the binary diffusivity. Needed transport properties were obtained using a Transport calculator by Colorado state university [114], Ansys Chemkin, and Cosilab. Critical Lewis numbers (Eq. 3.28 and 3.29) were calculated using Zeldovich number-based formulations [115].

$$Le_1^* = 1 - \frac{1}{\beta} \quad 3.28$$

$$Le_2^* = 1 - \frac{2}{\beta} \quad 3.29$$

$$\beta \text{ or } Ze = (E_a(T_{ad} - T_U))/(R_u T_{ad}^2) \quad 3.30$$

where β or Ze was the Zeldovich number or non-dimensional global activation energy, T_{ad} was equilibrium flame temperature, T_u -unburnt mixture temperature, and E_a/R_u - activation temperature. The activation temperature was calculated using Eq. 3.31 as proposed by Bradley et al. [116].

$$2ln(\rho_u S_u^0) = -\left(\frac{E_a}{R_u}\right)\left(\frac{1}{T_{ad}}\right) + C \quad 3.31$$

3.4.4 Hydrodynamic instability

The critical radius was the radius of the spherical flame where the flame started developing uniform cells on the surface in a significant amount. Quantification by earlier researchers was based on visual inspection. The present work estimated the radius using a MATLAB program based on cell identification criteria rather than visual inspection. For calculating the critical radius, the intensity of the pixels in a rectangular inspection area of 69920 pixels (two rectangles of size 190 × 184 to omit electrodes) within the diameter of the optical access window was monitored, as shown in Figure 3-14.

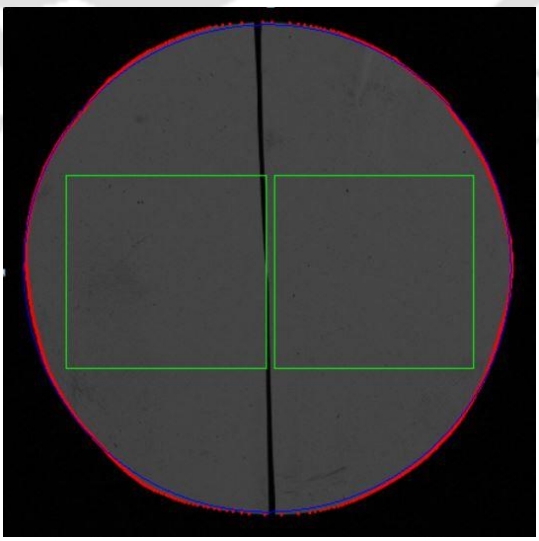

Figure 3-14 Inspection area of the spherical flame for cells

The developed criteria: 1) Image corresponding to the maximum change in the average intensity to the base image without the flame, 2) The maximum value of the second-order time derivative of intensity should occur within 0.1% of the frame rate after attaining a peak value of first-order time intensity and 3) The instant corresponding to a drop below 85% of the average intensity of at least 0.14% of the total number of pixels (equal to ~50 pixels, this value can be adjusted with intensity and tailored as per the requirement). All the criteria were verified and sequenced based on robustness and accuracy.

The resilience of a flame to hydrodynamic instability was directly proportional to its thickness (δ_f). Here, the necessary data of flame thickness, δ_f, was computed using Ansys Chemkin with GRI Mech 3.0 and calculated as, $\delta_f = (T_{ad} - T_U)/(dT/dx)_{max}$, Where T was equilibrium temperature at a location x in the considered computational spacial domain. The critical radius (R_{cr}) was normalized with flame thickness to calculate the critical Peclet number (Pe_{cr}) to categorize the instabilities. Thermal expansion ratio (σ) was obtained from burned, and unburned gas mixture densities, and this parameter provided information about the density jump across the flame. The coefficient of self-acceleration (α) was obtained by fitting the radius-time data in the equation, $R = R_0 + Ct^{\alpha}$, Where R_0 (referred to as virtual origin), C (constant), and α were the fitting parameters.

3.4.5 Numerical study

One-dimensional freely propagating simulations were performed for analysis in conjunction with experimental data. A freely propagating planar flame model in Ansys Chemkin [106] was used to estimate unstretched *LBV*. The 1D spherically expanding flame model in Cosilab [9] was used to estimate radius-time, stretched flame speed-time, stretch rate-time data, and later, unstretched flame speed and *LBV*. Apart from the above simulations, several transport parameters were obtained from the Transport property calculator by Colorado state university [114]. All simulations were performed using GRI Mech 3.0 (53 species and 325 elementary reactions) [108], FFCM-1 (38 species and 291 elementary reactions)[117] and USC Mech 2.0. model (111 species and 784 elementary reactions)[118].

3.4.5.1 Freely propagating planar flame model in Ansys Chemkin

Planar flame considered in this model was a quasi-steady and adiabatic flame with uniform inlet flow conditions, specified pressure, and temperature. As a result governing equations were reduced to the following forms [119].

$$\dot{m} = \rho u A \tag{3.32}$$

$$\dot{m}\frac{dT}{dx} - \frac{1}{c_p}\frac{d}{dx}\left(\lambda A \frac{dT}{dx}\right) + \frac{A}{c_p}\sum_{k=1}^{K}\rho Y_k V_k c_{pk}\frac{dT}{dx} + \frac{A}{c_p}\sum_{k=1}^{K}\dot{\omega}_k h_k W_k + \frac{A}{c_p}\dot{Q}_{rad} = 0 \tag{3.33}$$

$$\dot{m}\frac{dY_k}{dx} + \frac{d}{dx}(\rho A Y_k V_k) - A\dot{\omega}_k W_k = 0 \tag{3.34}$$

$$\rho = \frac{P\bar{W}}{RT} \tag{3.35}$$

Where P was the pressure, x - the spatial coordinate, A - cross-sectional area of the stream tube, $\dot{m}$ - mass flow rate (independent of x), $\dot{Q}_{rad}$ - heat loss due to gas and particle radiation, T - temperature, V_k - diffusion velocity of the k^{th} species, Y_k - mass fraction of the k^{th} species, h_k - specific enthalpy of the k^{th} species, u - velocity of the fluid mixture, $\dot{\omega}_k$ - molar rate of production by chemical reaction of k^{th} species per unit volume, ρ - mass density, c_{pk} - constant pressure heat capacity of the k^{th} species, W_k - molecular weight of the k^{th} species, c_p - constant pressure heat capacity of the mixture, $\bar{W}$ - mean molecular weight of the mixture, λ - thermal conductivity of the mixture, and R - universal gas constant. The mentioned continuity (Eq. 3.32), energy (Eq. 3.33), species (Eq. 3.34), and closure equation of state (Eq. 3.35) equations were solved by discretizing using implicit finite difference methods on a non-uniform grid. The molar rate of production by all species from all chemical reactions (represented by $\dot{\omega}_k$ for k^{th} species) as specified in the selected chemical kinetic mechanism was taken into account. In the present work, GRI Mech 3.0 and FFCM-1 were used. A mixture averaged transport model was used. The mass flow rate needed was determined as an eigenvalue in the current problem. This was achieved by fixing the flame in the computational domain at one location. The flame was tracked with a temperature of 500 K above the unburned gas temperature. Inlet boundary conditions were known mole fractions of reactants, initial temperature, and pressure. Boundary conditions on the burned gas side were defined as the zero gradients of all the parameters. The grid adaptation technique was used to resolve the strong gradients as the

conservation equations were stiff due to the inclusion of chemical kinetics. GRAD and CURV parameters were set to 0.02 and 0.2 and obtained grid-independent solutions. TWOPNT steady-state solver was primarily used for solving the governing equations[119,120]. The simulation was initiated with a few grid points, and the final solution was achieved through different continuation. The accuracy of the obtained result was crosschecked with equilibrium flame temperature and mole fractions of product species obtained from equilibrium calculations using the equilibrium (EQUIL) model.

3.4.5.2 Freely propagating flame simulation in Cosilab

In this case, the flame front was considered propagating in the defined spatial domain (the beginning and end of the domain corresponding to the center and end boundary wall of the spherical chamber). The flame propagation and tracking were achieved by fixing the frame of reference to the flame front and adopting a Lagrangian formulation. This simulation assisted in generating essential data such as flame front radius, flame speed, and flame stretch with respect to time analogous to propagation of flame in experiments. The flame simulations were performed under both constant volume and pressure configurations. The original governing equations were considered in a polar coordinate system to achieve a symmetrical domain to explore spherical flames. The transformation of governing equations into lagrangian form: The independent mass-weighted lagrangian variable (ψ) was used instead of the physical distance variable (r - the spatial coordinate).

$$\psi(r,t) = \int_{r_0}^{r} \rho(r,t) r^{\alpha} dr \qquad 3.36$$

Where r_0 was a reference value of r, t was time, ρ - mixture mass density, and α - geometrical parameter.

$$\frac{\partial \psi}{\partial r} = \rho r^{\alpha} \qquad 3.37$$

$$\frac{\partial \psi}{\partial t} = \int_{r_0}^{r} \frac{\partial \rho r^{\alpha}}{\partial t} dr = -\rho r^{\alpha} v + m_0(t) \qquad 3.38$$

Where m_0 was the value of $\rho r^{\alpha} v$ at reference coordinate r_0 and v was the flow velocity. The chain rule was implemented for the above differential operators and transformed into the new coordinate system$[(r,t) \rightarrow (\psi,\tau)]$.

3.4.5.2.1 Resultant differential operators in Lagrangian coordinates

$$\frac{\partial(\,)}{\partial r} = \rho r^{\alpha}\frac{\partial(\,)}{\partial \psi} \quad (3.39)$$

$$\frac{\partial(\,)}{\partial t} = \mathcal{L}(\,) - \rho r^{\alpha} v\frac{\partial(\,)}{\partial \psi} \quad (3.40)$$

$$\mathcal{L}(\,) = \frac{\partial(\,)}{\partial \tau} + m_0\frac{\partial(\,)}{\partial \psi} \quad (3.41)$$

3.4.5.2.2 Resultant governing equations in Lagrangian coordinates

$$0 = \frac{\partial r}{\partial \psi} - \frac{1}{\rho r^{\alpha}} \quad (3.42)$$

$$\mathcal{L}(\rho) = -\rho^2\frac{\partial r^{\alpha} v}{\partial \psi} \quad (3.43)$$

$$\mathcal{L}(Y_i) = -\frac{\partial(r^{\alpha} j_i)}{\partial \psi} + \frac{\omega_i}{\rho}, \quad i = 1, \ldots, I \quad (3.44)$$

$$\mathcal{L}(v) = -r^{\alpha}\frac{\partial p}{\partial \psi} + \frac{4r^{\alpha}}{3}\frac{\partial}{\partial \psi}\left(\rho\mu\frac{\partial r^{\alpha} v}{\partial \psi}\right) - 2\alpha r^{\alpha}\frac{v}{r}\frac{\partial \mu}{\partial \psi} \quad (3.45)$$

$$\mathcal{L}(T) - \frac{\mathcal{L}(p)}{\rho c_p} = \frac{1}{c_p}\frac{\partial}{\partial \psi}\left(\rho r^{2\alpha}\lambda\frac{\partial T}{\partial \psi}\right) - \frac{\sum_{i=1}^{I} h_i\omega_i}{\rho c_p} - r^{\alpha}\frac{\partial T}{\partial \psi}\sum_{i=1}^{I}\frac{c_{pi}}{c_p} j_i + \frac{\Phi}{\rho c_p} - \frac{1}{c_p}\frac{\partial(r^{\alpha} q_R)}{\partial \psi} + \frac{Q_e}{\rho c_p} \quad (3.46)$$

Where Φ, τ_{rr}, $\tau_{\theta\theta}$ and D_v were defined as presented below.

$$\Phi = \tau_{rr}\frac{\partial v}{\partial r} + \alpha\tau_{\theta\theta}\frac{v}{r} \quad 3.47$$

$$\tau_{rr} = D_v\left(\frac{\partial v}{\partial r} - \frac{\alpha v}{2r}\right) \quad 3.48$$

$$\tau_{\theta\theta} = -\frac{D_v}{2}\left(\frac{\partial v}{\partial r} - \frac{2v}{mr}\right) \quad for\ \alpha > 0; = 0 \quad for\ \alpha = 0 \quad 3.49$$

$$D_v = 4\mu/3 \quad 3.50$$

Where $j_i = \rho Y_i V_i$ was the diffusion of ith species, Y_i - mass fraction of ith species, V_i - diffusion velocity of ith species, ω_i - mass rate of production of ith species, I - total number of species in the system, p - pressure, μ - dynamic viscosity of the mixture, c_p- mass-based frozen specific heat at constant pressure, λ - thermal conductivity of the mixture, h_i - mass-based enthalpy of the ith species, T - temperature of the mixture, c_{pi} - specific heat at a constant pressure of the ith species, Q_e - the source of energy per unit volume and unit time and q_R - radiative heat flux. The above governing equations were solved with finite difference method discretization on a non-uniform-adaptive grid and associated boundary conditions, as discussed in the Cosilab theory manual[107]. Soret effect was included. GRAD and CURV, the grid adaptation parameters were set at 0.02 and 0.3, respectively, ensuring grid-independent solutions in Cosilab and Ansys Chemkin.

3.4.6 Uncertainty analysis

Table 3-3 Uncertainty in the parameters

Sl.No.	Parameter	Uncertainty (%)
1	Radius	± 1.47
2	Time	± 0.00
3	Flame speed	± 2.93
4	Flame stretch rate	± 3.28
5	Unstretched flame speed (Linear form)	± 4.50
6	Burned gas Markstein length (Linear form)	± 46.16
7	Unstretched flame speed (Non-Linear form)	± 4.11
8	Burned gas Markstein length (Non-Linear form)	± 55.46
9	Unstretched flame speed (Xiouris model)	± 4.39

The uncertainty in each parameter was calculated by following the procedure discussed in the literature on uncertainty calculation [121]. The detailed procedure is reported in Appendix. The corresponding uncertainty values are summarized in Table 3-3.

3.4.7 Summary

The constant pressure period was identified from the recorded pressure-time data. Then, the images with smooth spherical flames were only processed within the pre-pressure period. An in-house developed image processing code in MATLAB was used to obtain the flame radius from images. Flames having a radius less than 0.75cm were not considered to avoid transient ignition effects. The fuel mixtures used in this study had higher values of *LBV*, and hence, the buoyancy effects were not observed. The flame radius, stretched flame speed, flame thickness, flame stretch rate, unstretched laminar burning velocity, burned gas Markstein length, effective Lewis number, Zeldovich number, critical Lewis number, critical radius, normalized critical burning velocity, critical Peclet numbers, etc. were calculated.

Chapter 4 Results and Discussion

Detailed discussion on identifying the representative composition of producer gas is presented in chapter-2. The design of the experimental rig, post-processing procedure of experimental data, numerical models used in the present work, and procedure were reported in chapter-3. Important results obtained from different experiments/simulations are presented in this chapter.

4.1 Validation of the experimental rig and procedure

Experimental and simulated *LBV* of three binary fuel mixtures *viz.*, H_2:CO:CH_4 = 1:1:0, 0:1:1, and 1:0:1 and three ternary fuel mixtures *viz.*, H_2:CO:CH_4 = 1:1:2, 1:2:1 and 2:1:1 reacting in the air are presented in Figure 4-1 along with the corresponding literature data. The operating conditions were ϕ = 0.8 to 1.2, T = 300 K, and P = 1 bar. Measured values of *LBV* from the present study of an equimolar H_2:CO-Air mixture showed an excellent agreement with the literature data within an average deviation of ±3.96% (Min: 0.06% and Max:7.36%).

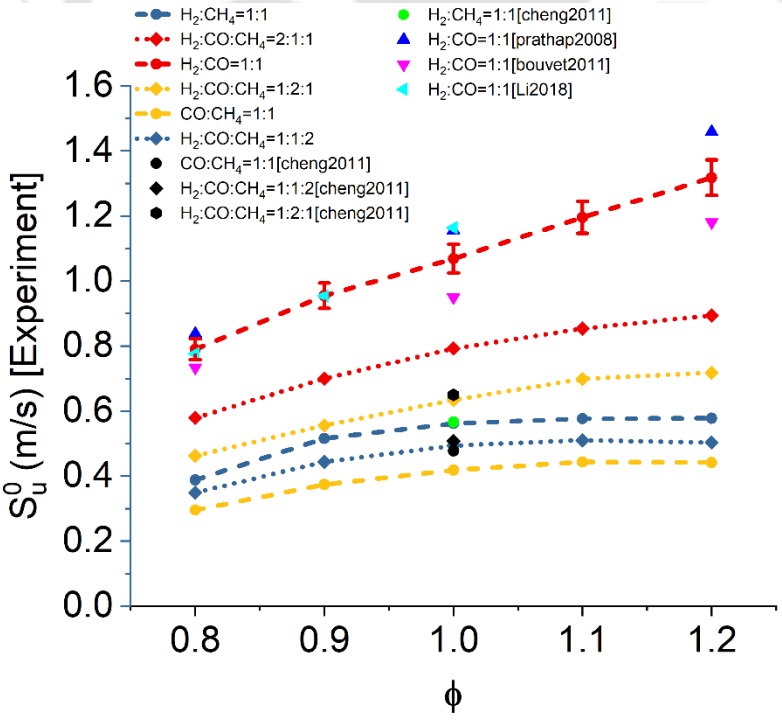

Figure 4-1 *LBV* of selected refined producer gas mixtures at 300 K and 1 bar

Data from Prathap et al. [122] were higher, and Bouvet et al. [59] were lower than the present measurements due to the application of a linear stretch extrapolation scheme in their work, respectively. *LBV* data of binary and ternary compositions such as H_2:CO:CH_4 = 0:1:1, 1:1:0, 1:0:1, 1:1:2, and 1:2:1 measured through the opposed jet method at 300 K, 1 bar, and stoichiometric condition were also presented, and they agreed well with the present measurements. Uncertainty in all cases is not included in Figure 4-1 for data legibility and is shown in the rest of the figures. The *LBV* of pure unary fuels such as H_2 and CO burning in air occupied the higher and lower extremes in Figure 4-1. Among the binary compositions H_2:CO:CH_4 = 1:1:0 and 0:1:1 placed at higher and lower extremes respectively while H_2:CO:CH_4 = 2:1:1 and 1:1:2 in ternary mixtures.

4.2 Chamber geometry, thermodynamic model, and processing data range selection

During the flame propagation in the constant-volume mode, the unburned mixture gets compressed, and the associated temperature and pressure will increase. As a result, the burning velocities at conditions other than the initial thermodynamic conditions are also encountered and can be considered an advantage. On the other side, the unsteady pressure-time data measured is extremely sensitive to the geometry of the chamber. Hence, an initial analysis was conducted in the constant volume mode for designing a chamber for the present work.

The results from this section played a crucial role while designing the chamber geometry and choosing the appropriate post-processing method. Three thermodynamic models were discussed for processing pressure-time data in chapter-3. All these models differed majorly in dividing the domain into multiple zones and the selection of reduced burned gas heat capacity ratio (γ_{br}) as summarized in Table 4.1. The reduced values were considered instead of the original to induce the radiation effect, which was proven to achieve accurate results[50,123].

These models were used to analyze the pressure-time data from different chambers: purely spherical, spherical with intrusions, and non-spherical chambers. The obtained *LBV* values from these different chambers and reduced burned gas heat capacity ratio are shown in Figure 4-2. Details of the associated chambers are presented in Table 4-1.

Table 4-1 Different correlations of reduced burned gas heat capacity ratio

Sl. No	Correlation		References
1	Omari et al.	$\gamma_{br} = \frac{1+\gamma_b}{2}$	[50]
2	Luijten et al.	$\gamma_{br} = \gamma_b$	[104]
3	Faghih et al.	$\gamma_{br} = \frac{8+\gamma_b}{8}$	[124]
4	Van Den Bulck	1.17	[123]

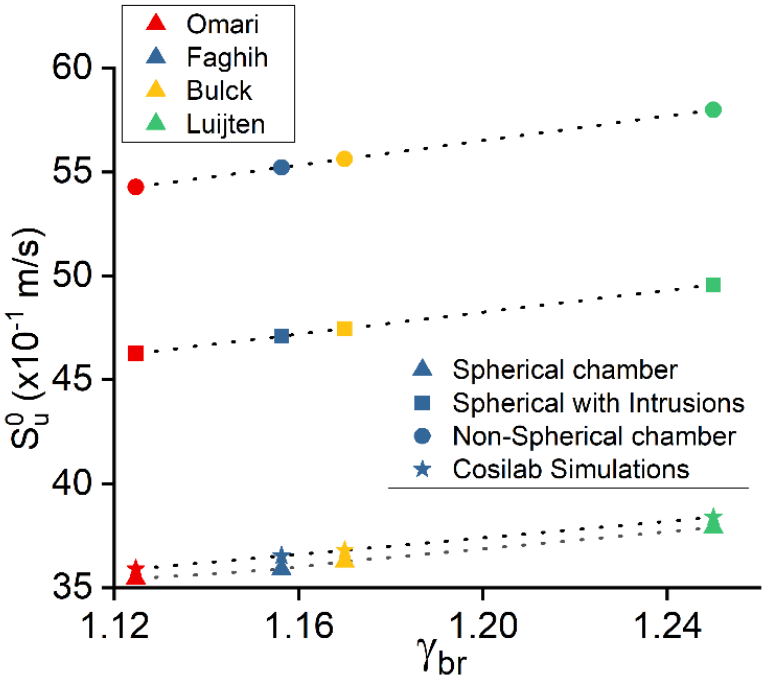

Figure 4-2 Laminar burning velocity variation with reduced burnt gas heat capacity ratio for different chamber confinements and simulations

Table 4-2 Design specifications of considered chambers

Sl.No.	Volume(L)	Geometry	Remarks	References
1	0.5	Spherical	-	[48]
2	1	Spherical	-	[49]
3	1	Spherical	-	[50]
4	4.4	Spherical	-	[51]
5	28.7	Spherical	Presence of fans inside chamber	[52]
6	43.7	Cylindrical with unity aspect ratio	Presence of Protruding structures inside chamber	[53]

The entire range of pressure-time data was not considered for the post-processing, as portions of data were affected by ignition effects, heat losses to the wall, hydrodynamic instability, etc. As a result, only a trimmed range of data that was free from the above-mentioned effects was selected for the estimation of *LBV* accurately. Different trimmed ranges in terms of reduced pressure were considered and presented in Figure 4-3. The following results show that a pure spherical chamber without intrusions, along with Omari et al. and Faghih et al. thermodynamic models and the data range corresponding to P_r = 0.2-0.5 is the best for obtaining accurate results.

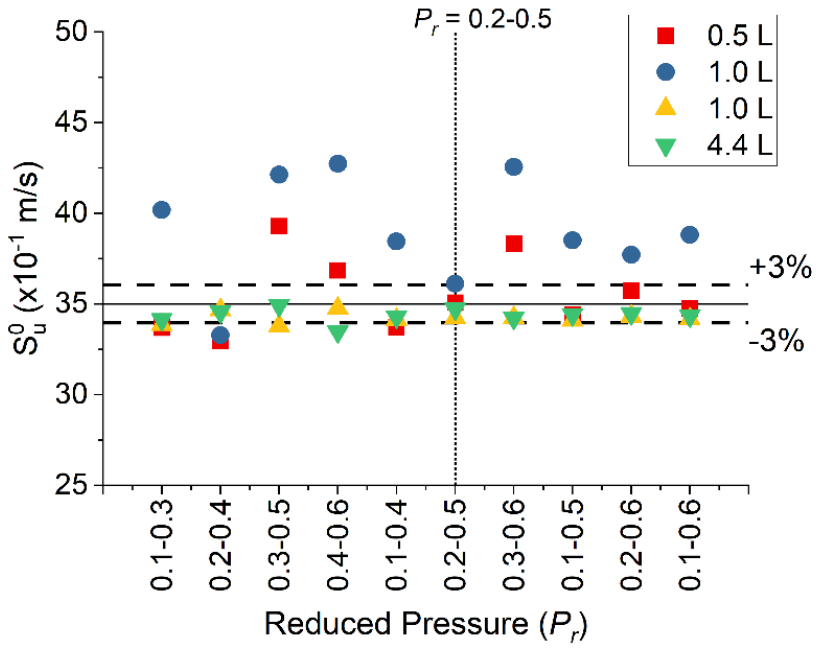

Figure 4-3 LBV values of the stoichiometric methane-air mixture at 1 bar, 300 K and corresponding to different reduced pressure data ranges

4.3 Effect of chamber volume and geometry on laminar burning velocity

A choice of the spherical chamber was made from the above results. Further analysis was conducted to arrive at an optimum chamber inner volume suitable for the present work to measure *LBV* in both constant pressure and volume modes. Figure 4-4 shows the stretched *LBV* data at different pressures (±0.01 bar) and temperatures (±5 K) obtained from 0.5 L [48], 1 L [50], 4.4 L [125], 20 L [126] spherical chambers at an initial pressure of 1 bar, and an initial temperature of 300±2 K. Symbols correspond to present measurements;

simulated stretched data correspond to Cosilab simulations, unstretched experimental data at 1 bar, 300 K corresponds to Hu et al. [127]. The deviation in values of stretched *LBV* between chambers of different volumes was observed at higher pressures and temperatures. Stretched *LBV* decreased with increased volume till 4.4 L and considerably increased for 20 L.

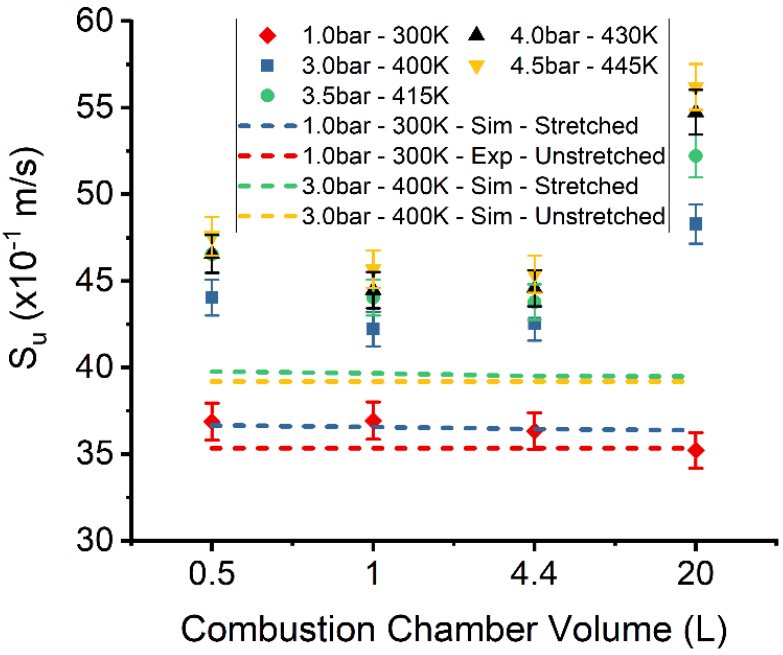

Figure 4-4 Laminar burning velocity of the stoichiometric methane-air mixture at different conditions.

To understand the deviation, the flame stretch rates were calculated using Eq. 3.17 and 3.18 for all the obtained data, and both the formulations provided nearly the same values under all conditions. Hence, stretch rate data obtained from Eq. 3.18 was only considered and shown in Figure 4-5. For relative comparison, all stretch rates were normalized using stretch rate data obtained from 20L at 4.5 bar and 445 K. The maximum difference in stretch rate for a given initial condition between chambers of different volumes was almost four times in magnitude, as shown in Figure 4-5. Flame stretch rates decreased with an increase in chamber volume due to a decrease in the ratio of the flame thickness (δ_f) to the flame radius (r_f) in the considered data range.

Estimated flame stretch rates could not explain the sudden increase in the value of *LBV* at 20 L. Then, the time derivative of pressure was calculated for all chambers and shown in Figure 4-6. For 0.5 L and 1 L, there was no remarkable change in the slope of *dp/dt* in the considered data range (2.8-5 bar). In 4.4 L, it was observed at P = 5.46 bar (as pointed by an arrow mark in Figure 4-6), but it happened outside the considered data range. The remarkable change in the slope of *dp/dt* indicated the onset of flow instabilities resulted in flame acceleration [50,128].

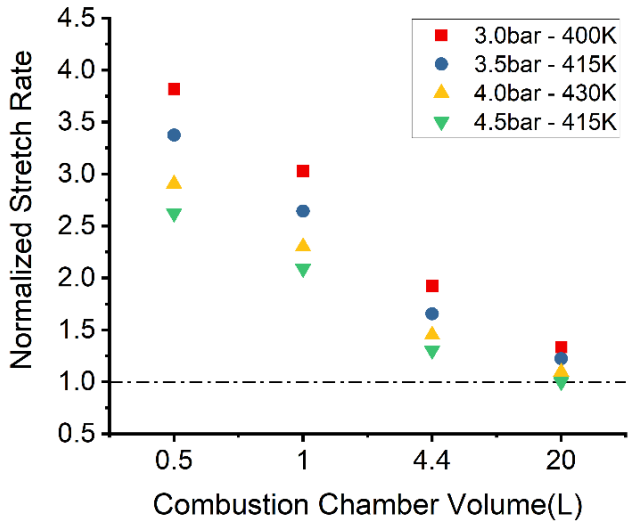

Figure 4-5 Normalized stretch rate comparison at different conditions

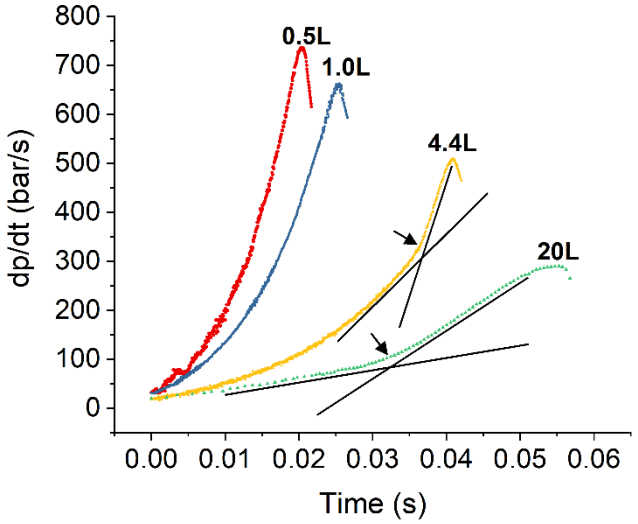

Figure 4-6 Variation of pressure gradient with time for all chambers.

In 20 L, it was observed at P = 2.89 bar, which was within the considered data. As the chamber volume increased, δ_f/r_f decreased in the chosen data range and hence, the propagating spherical flame was affected by flow instabilities. Before the onset of instability in 20 L, the data could not be used as it was very close to the considered lower pressure limit. Hence, it is advised to observe a remarkable change in the slope of *dp/dt* before choosing and processing pressure-time data in the constant volume spherical flame method in bigger chambers. Flame stretch rate estimation did not include flow instability. Hence, it could not estimate deviations in the 20 L chamber.

One dimensional, constant volume, spherical flame model in Cosilab was used to simulate pressure-time data for all studied spherical chambers. GRI Mech 3.0 was used for this study. Convergence of solutions in simulations was ensured. The simulated pressure-time data were processed identically to that of the experiments. Stretched *LBV* data at 3 bar and 400 K for all chambers are shown in Figure 4-4. Also, in Figure 4-4, unstretched *LBV* data at 3 bar and 400 K simulated using 1D freely propagating planar flame from Cosilab is also shown.

Stretch rates and the stretched *LBV* predicted by simulations did not change with an increase in chamber volume compared to experiments, and the possible reason could be δ_f/r_f became smaller even in the considered data range of the smallest chamber itself. The difference in *LBV* between measurement at 4.4 L and unstretched data could be further reduced by appropriate stretch correction. Another observation from Figure 4-4 was that as the chamber volume increased till 4.4 L, the measured stretched *LBV* approached that of predicted unstretched *LBV* at 3 bar and 400 K. From the above discussion, it is clear that the usage of a spherical chamber having a volume of 4.4 L to have lesser stretch effects will result in *LBV* with minimal stretch effects at elevated pressures and temperatures.

The stretched *LBV* data from both measurements and simulations as a function of pressure and temperature for a given chamber was fitted with a power-law (Eq. 3.16) to estimate it at 1 bar and 300 K. The extrapolated value of measured stretched *LBV* at 1 bar and 300 K obtained from different chambers including 20 L, showed good agreement with each other. One crucial observation with power-law was that the parameter, S_u^0 (36.9-35.2 cm/s) was least affected by a change in volume. But, the exponent (α) changed

considerably (0.15-0.31). Agreement in *LBV* at 1 bar and 300 K was good between simulations and measurements. A spherical chamber with 4.5 L was designed considering the outcomes from these sections and fabricated, and the same was used for further analysis.

4.4 Effect of Non-Combustible Components (N_2 and CO_2) on LBV and instability of PG-O_2 mixtures

As explained in the previous section, a combustion chamber having inner geometry as sphere was designed and fabricated. The same was used for the measurement of *LBV* of producer gas. In this section, the composition of PG was considered as *Z*% CC+(100-*Z*)% NCC, where *Z* was varied at 25, 35, and 45, as discussed and presented in chapter-2. It was referred to as the Inter-CC-NCC study. CC was considered (25CH_4:25CO:25H_2:25*Y*), where *Y* represented rich combustible species CH_4/CO/H_2 and referred to as an intra-CC study. Hence, a fuel with more CH_4/CO/H_2 was called CH_4/CO/H_2-rich PG fuel. In the Intra-CC study, each fuel species varied between 25 and 50%. A similar approach was followed for NCC as *P*%CO_2+(100-*P*)%N_2, where *P* was varied from 0-100 (by volume) and referred to as Intra-NCC study. The design of the compositions corresponding to CH_4-rich set presented in Figure *4-7*. Pure oxygen was chosen as the oxidizer than air to avoid N_2 present in air. This will provide valuable information on the combustion characteristics of producer gas reacting with oxygen.

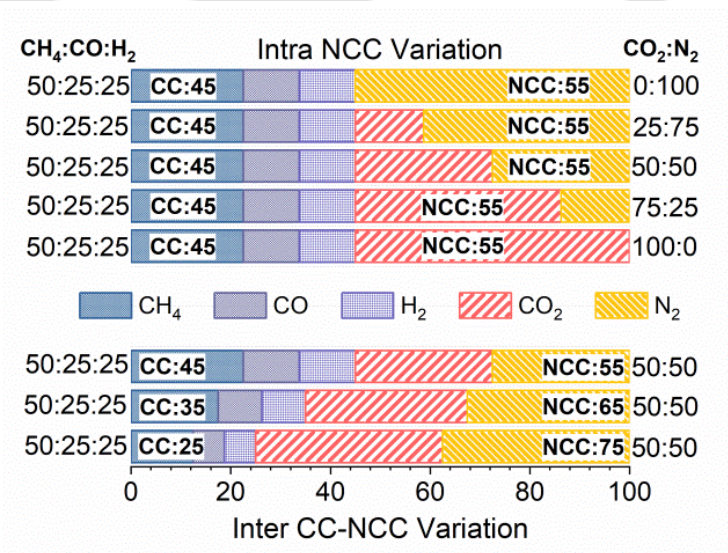

Figure 4-7 Producer gas compositions studied in the present work (CH_4-rich set)

In this method, a total of 45 different compositions was investigated. Each experiment was repeated twice to ensure repeatability. The obtained flame images were processed using in-house developed code reported in section 3.4.2.1. After obtained the radius-time data, the *LBV* was calculated as per the procedure reported in section 3.4.2.2. All the experimental operating conditions were simulated in Ansys Chemkin and Cosilab using contemporary reaction mechanisms. Important results obtained from this study along with the inferences are reported in this section.

4.4.1 Flame stretch rate and preferential diffusion instability

The stretched flame speed variation with radius corresponding to CH_4-rich, H_2-rich, and CO-rich mixtures are shown in Figure 4-8, Figure 4-9, and Figure 4-10. Figure 4-11 shows the stretched flame speed variation with the flame stretch rate for CO-rich PG-oxygen mixtures at $\phi = 0.8$, 1 bar, 300 K, and all inter-CC-NCC and intra-NCC variations. Stretched flame speed, S_b, varied smoothly for 100% N_2 mixtures. The magnitude of S_b was consistently higher for mixtures having a higher mole fraction of N_2 than CO_2 in NCC. It was due to the higher flame temperature (low values of mixture specific heat capacity) of those mixtures with high N_2. Minor disturbances were observed for 75 and 100% CO_2 mixtures, mainly due to minor cracks on the flames in the pre-pressure period. Similar trends were observed in the CH_4 and H_2-rich PG, as shown in Figure 4-12 and Figure 4-13. The stretched flame speed variations with both stretch rate and radius were used for extrapolating to zero stretch conditions for obtaining *LBV*.

Figure 4-14 shows stretched flame speed extrapolating to zero stretch rate using a linear stretch model and a sufficiently large flame radius through a non-linear model. Only three chosen cases representing positive, zero (almost), and negative values of burned gas Markstein length are shown to reduce the redundancy. Unstretched flame speed estimated from both linear and non-linear models agreed well for most studied mixtures.

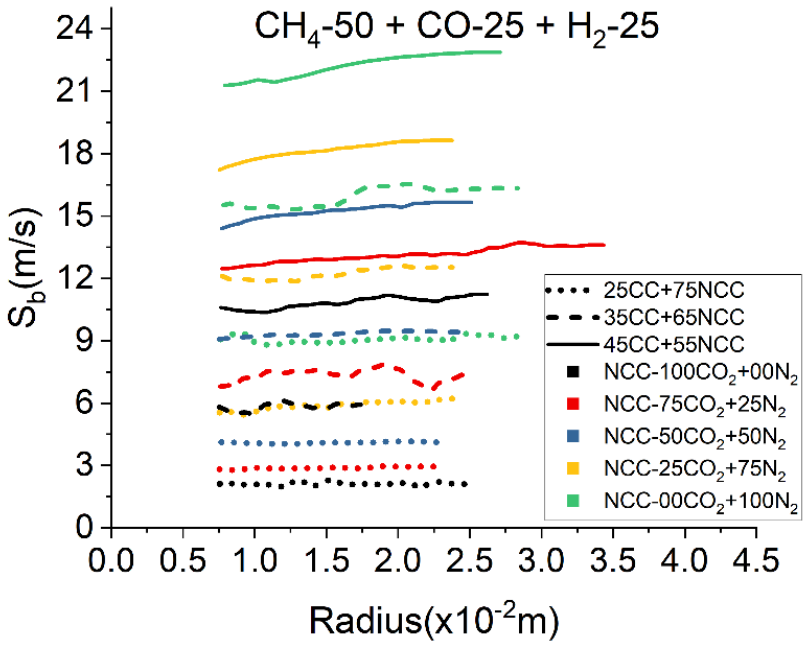

Figure 4-8 S_b variation with radius for CH_4-rich mixtures

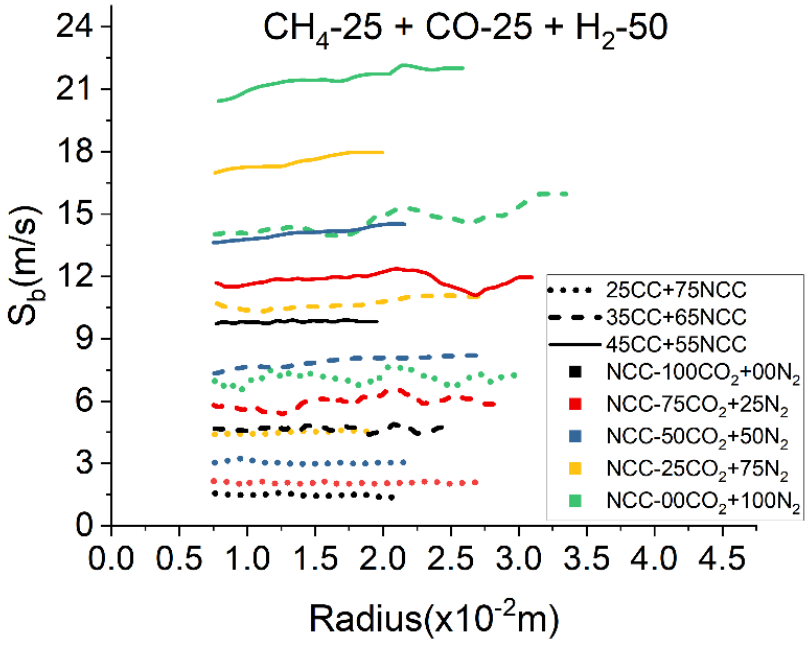

Figure 4-9 S_b variation with radius for H_2-rich mixtures

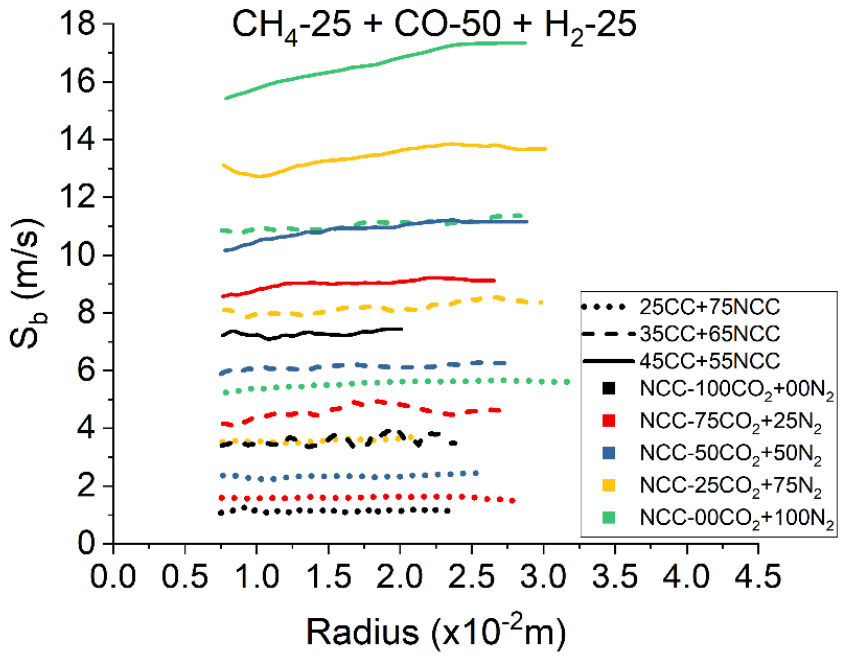

Figure 4-10 S_b variation with radius for CO-rich mixtures

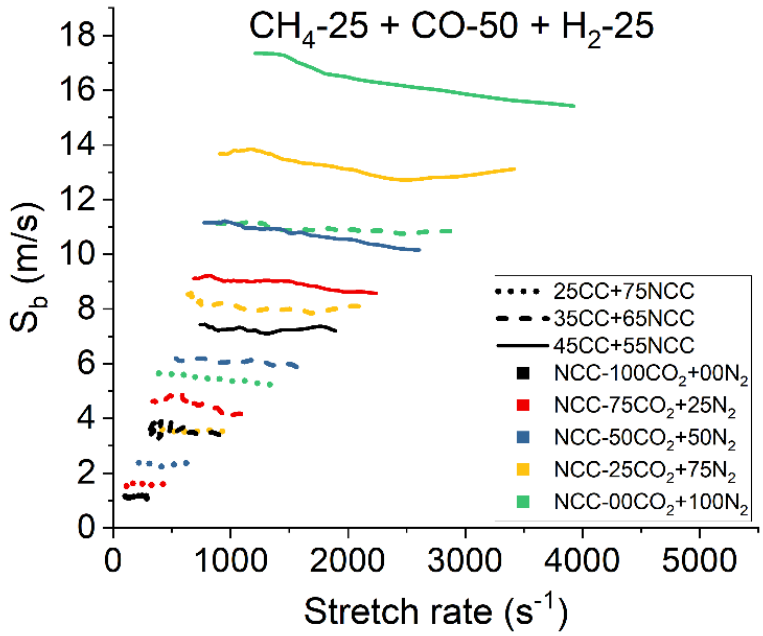

Figure 4-11 S_b variation with stretch rate for CO-rich mixtures.

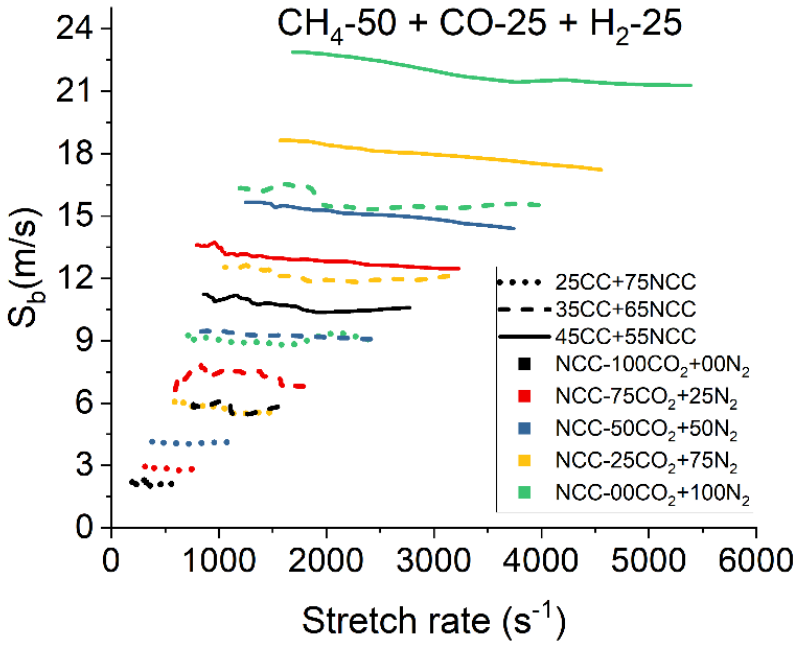

Figure 4-12 S_b variation with stretch rate for CH_4-rich mixtures.

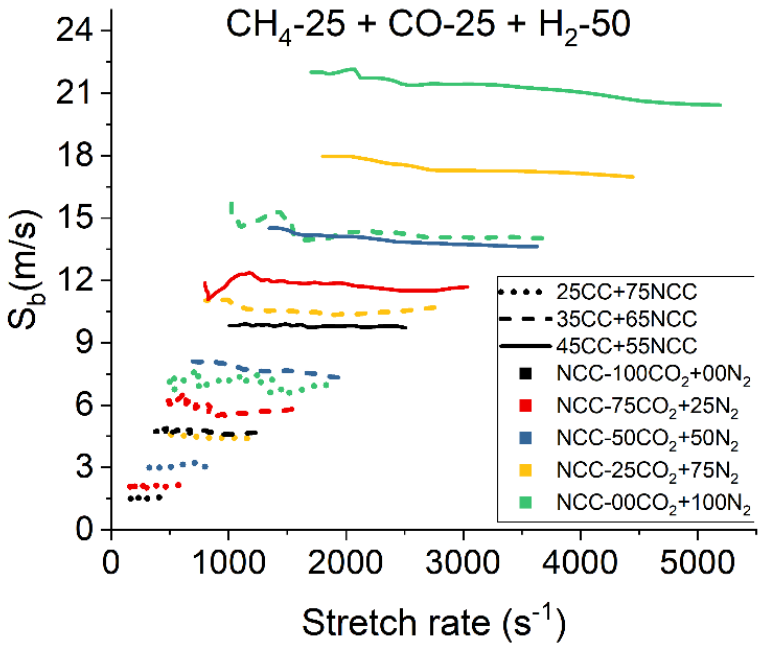

Figure 4-13 S_b variation with stretch rate for H_2-rich mixtures.

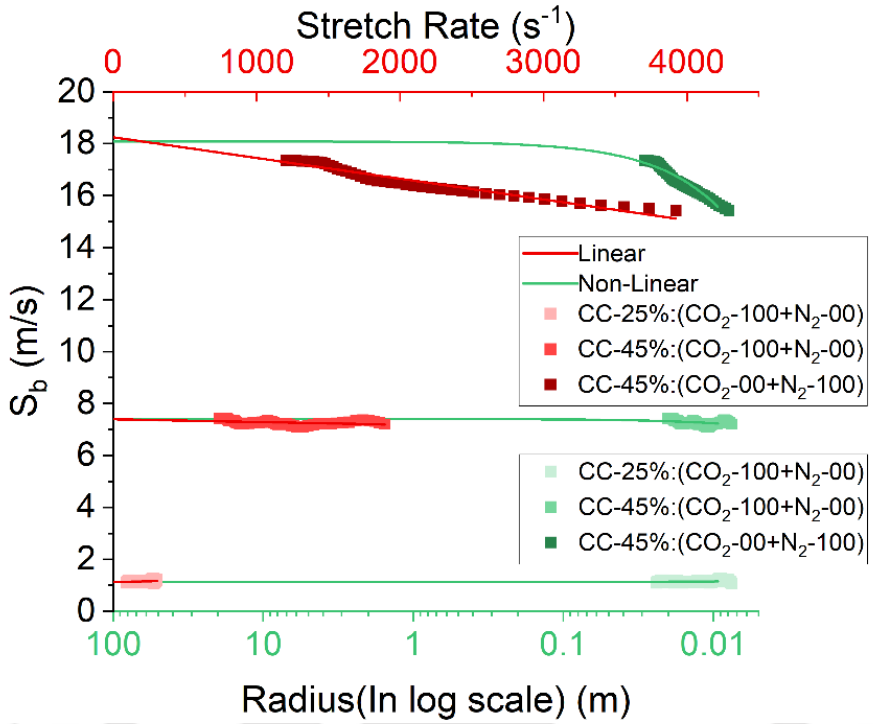

Figure 4-14 Extrapolation of unstretched flame speed through linear and non-linear models of three possible cases (L_b<0, L_b≈0, L_b>0). The symbols and lines represent the measured and fitted values.

4.4.2 Burned Gas Markstein Length

Burned gas Markstein length (L_b) was determined using non-linear models (Eq. 3.21 and 3.22) and presented in Figure 4-15. The solid symbols represent the averaged values from experiments, and open symbols represent the averaged values from simulations. The dashed and dotted lines represent the linear trend line of the experimental and simulation values, respectively. Figure 4-15A indicated that the values of burned gas Markstein length increased with an increase in the X_{CC} (Mole fraction of CH_4+H_2+CO in the total mixture) in the premixed producer gas-oxygen mixture. CO_2 and N_2 varied individually but the fraction of CO_2+N_2 remained constant. As discussed before, the composition of PG was considered as *Z*% CC+(100-*Z*)% NCC, where *Z* was varied at 25, 35, and 45. CC was considered (25CH_4:25CO:25H_2:25*Y*), where *Y* represented rich combustible species CH_4/CO/H_2. As a result, five variations of the non-combustible components (CO_2:N_2 = 100:00, 75:25, 50:50, 25:75 and 00:100) possessed the same mole fraction at any given set of Z and Y. Connecting lines were avoided to reduce the clutter as the intended objective was being served by scattered points. L_b becomes negative as X_{CC} fell below

20% for the analyzed hydrogen and carbon monoxide-rich PG at $\phi = 0.8$. This change was due to the increase in the significant presence of deficit species with high mass diffusivity. Further discussion on this change is presented in the next section.

Mean values of measured burned gas Markstein length of all the $CH_4/CO/H_2$ rich PG mixtures at a given inter-CC-NCC at each variant of intra-NCC ($P\%CO_2 + (100\text{-}P)\%N_2$) was estimated, and the same is presented in Figure 4-15B. It also includes the L_b estimated from simulations in Cosilab with GRI Mech 3.0 reaction mechanism. The linear trend lines were fitted to the measured as well as simulated values. The slopes decreased with an increase volume fraction of CC from 25-45%, indicating that mixtures with lower X_{CC} were more susceptible to preferential diffusional instability. This becomes significant as most PGs are expected to have a low fraction of CC.

In the case of the simulated values of L_b (estimated using the non-linear model), the slope of the trend lines was consistently smaller than the slope measured from experimental measurements. Predicted L_b reported that the flame remained unstable for all 25%CC cases if CO_2 was present in the mixture, which did not match well with experiments. This was primarily due to the limitation of GRI Mech 3.0 used for the considered species in this study. For all $CH_4/H_2/CO$-rich PG fuels, an increase in mole fraction of CO_2 resulted in smaller L_b values due to the occurrence of slow (example Figure 4-11 for CO-rich PG fuel) and thick flames. Prathap et al. [58,122] reported that the response of such flames to preferential diffusional effects was higher, resulting in a reduction in L_b values at lean mixture conditions. It was quite interesting to notice only positive values of L_b for methane-rich mixtures under all studied conditions.

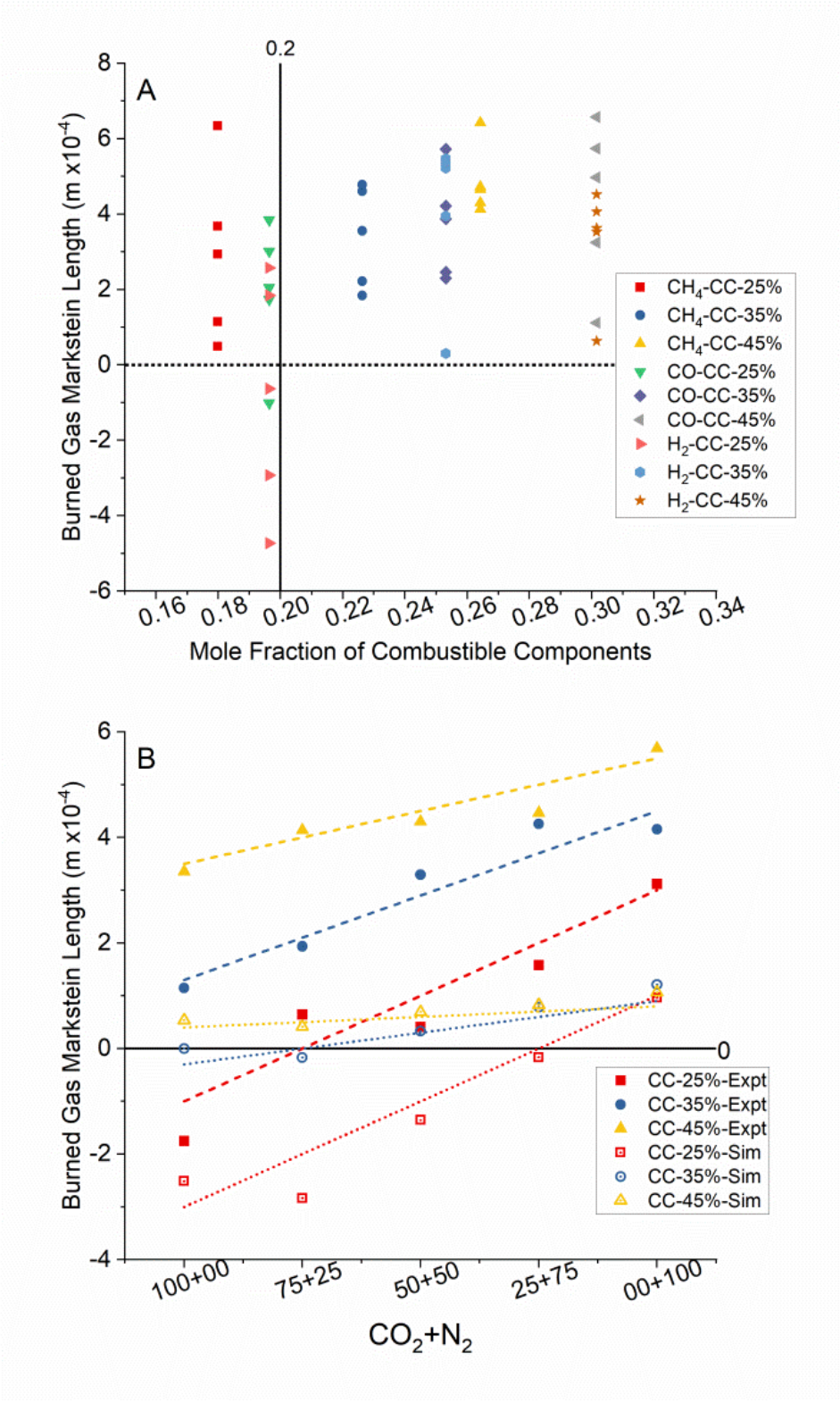

Figure 4-15 A) Variation of measured burned gas Markstein length with X_{CC} in the premixed combustible mixture at all studied compositions, 1 bar, 300 K and ϕ = 0.8. B). The trend of burned gas Markstein Length with variation in CO_2:N_2 composition.

Hence, methane-rich PG mixtures were stable towards preferential diffusion instability, typically a characteristic of pure methane-air/O_2 mixtures [129]. The above information strengthened the view that combustion characteristics of PG mixtures were strongly dependent on their rich fuel component. Hence, methane-rich PG displayed stability identical to methane towards preferential diffusion effects under all studied conditions.

4.4.3 Flame stability - Effective and critical Lewis Numbers

Figure 4-16 shows the effective Lewis numbers estimated from the volume and diffusion-based models along with the critical Lewis numbers (Le_1^* (Eq. 3.28) and Le_2^* (Eq. 3.29)). Of them, the Le_{eff} ((Eq. 3.25) volume-based) of three PG mixtures were less than the Le_1^* indicating that they were unstable due to the preferential diffusion effects. The values of the experimental burned gas Markstein length (L_b) of these three mixtures were also negative, as reported in Table 4-3. Unstable mixtures identified by Le_{eff} (diffusion-based model) and the respective Le_1^* or Le_2^* did not corroborate with measured L_b and hence, it was not used further.

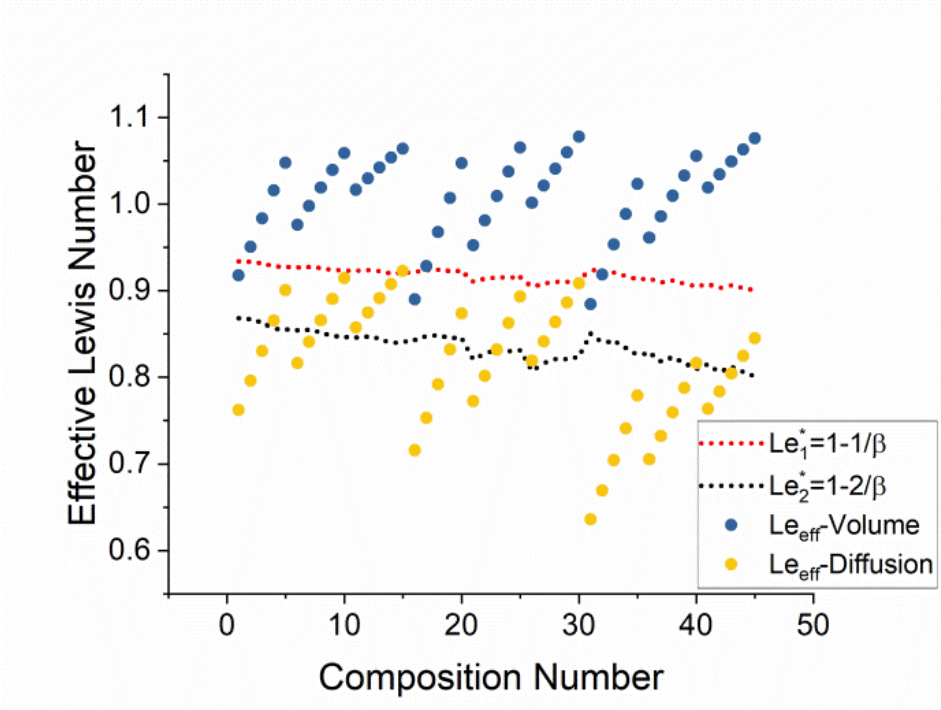

Figure 4-16 Effective Lewis Numbers based on volume and diffusion-based models with corresponding Critical Lewis Numbers of all the considered compositions

Table 4-3: Stability parameters of PG mixtures in unstable regime

Fuel composition	X_{CC}	Le_{eff}	Le^*	L_b (mm) (NL)
25% ($25CH_4$+$25CO$+$50H_2$) + 75%CO_2	0.196	0.88	0.93	-0.473
25% ($25CH_4$+$25CO$+$50H_2$) + 75% ($75CO_2$+$25N_2$)	0.196	0.91	0.92	-0.264
25% ($25CH_4$+$50CO$+$25H_2$) + 75%CO_2	0.196	0.89	0.92	-0.102

Based on the above corroboration, the Le_{eff} of all compositions were estimated using the volume-based model along with Le_1^* and plotted in Figure 4-17. The magnitudes of Le_{eff} were higher for PG mixtures that had higher values of mole fractions of combustible components due to an increase in the thermal diffusivity of the mixture. Hydrogen-rich PG displayed the lowest/highest Le_{eff} for 25/45% CC mixtures due to the respective change in the thermal diffusivities. Figure 4-17 shows that the PG mixtures with 25%CC and higher volume fractions of H_2 or CO in CC and CO_2 in NCC were more susceptible to preferential diffusion instability. Hence, removing CO_2 from PG mixtures is essential to avoid diffusional instabilities.

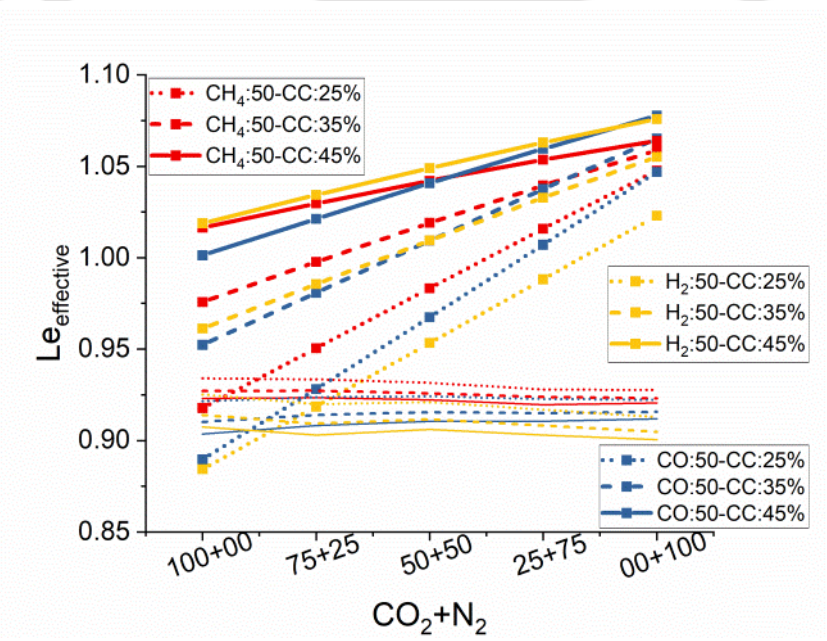

Figure 4-17 Effective Lewis Numbers of all PG mixtures along with the critical *Le* number. Lines with symbols represent effective *Le*, and Lines without symbols represent the corresponding Le_1^*.

4.4.4 Unstretched Laminar Burning Velocity

Figure 4-18A-C shows the unstretched *LBV* of CH_4/CO/H_2-rich-PG reacting in oxygen at all studied operating conditions obtained from experiments. Unstretched *LBV* obtained from linear (Eq. 3.21) and non-linear (Eq. 3.22) formulations agreed well within ± 1%. The results obtained through the Xiouris et al. model [51] also were in good agreement (± 4.92%) with the experimental results despite the underprediction of *LBV* and L_b by simulations.

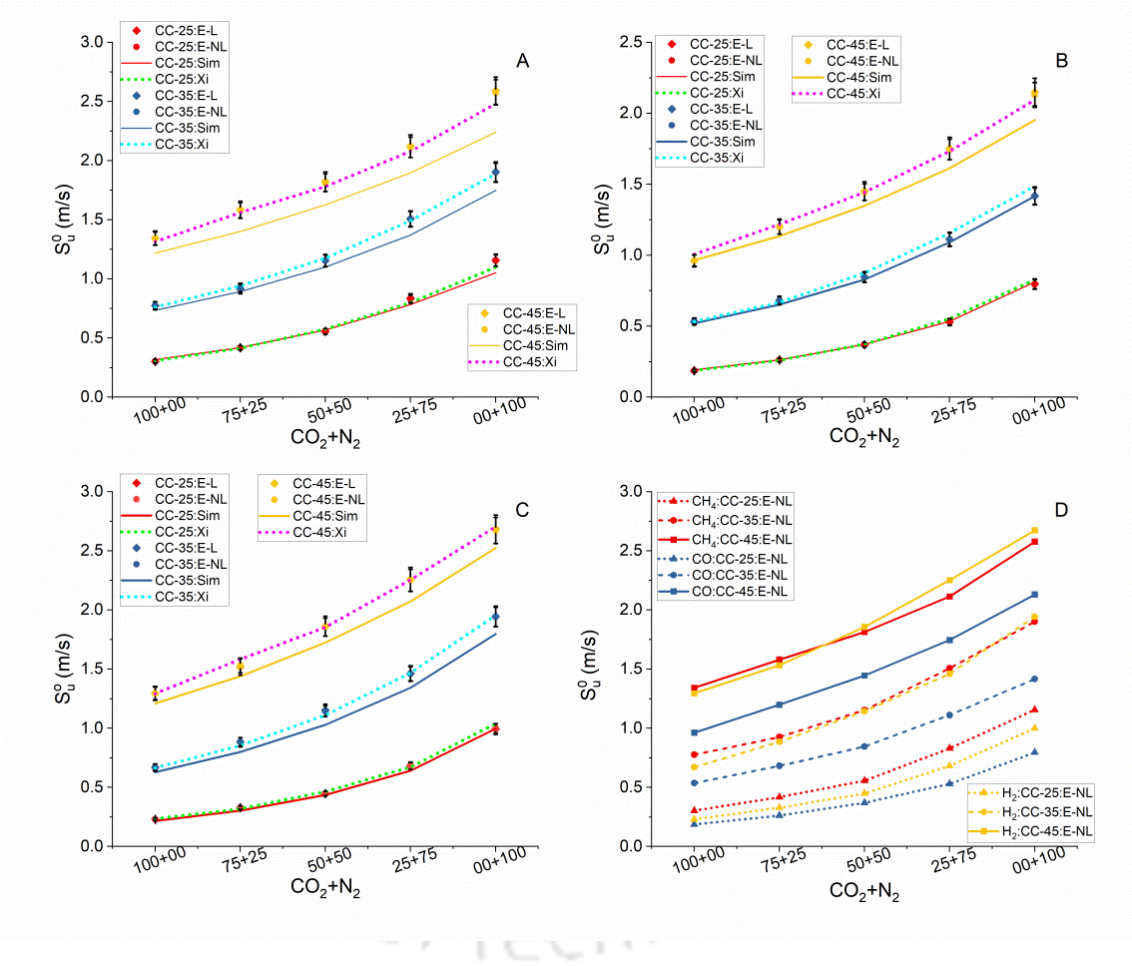

Figure 4-18 A) Unstretched Laminar Burning Velocities *LBV* of CH_4 rich producer gas mixtures as a function of CO_2+N_2 in NCC at ϕ = 0.8, 1 bar, and 300 K. B) Laminar Burning Velocities of CO rich producer gas mixtures. C) *LBV* of H_2-rich producer gas mixtures. D) Unstretched laminar burning velocities (NL-extrapolation) of CH_4/CO/H_2-rich PG fuel at different inter-CC-NCC as a function of intra-NCC reacting with 100%O_2 at ϕ = 0.8, 1 bar, and 300 K.

Figure 4-18A-C indicated that *LBV* enhanced with an increase in X_{CC} in the combustible mixture due to an increase in chemical energy and a decrease in the specific heat capacity of the mixture, resulting in higher flame temperature. Variation of *LBV* with an increase in X_{CO2} and simultaneous reduction in X_{N2} was non-monotonic for all reported measurements. The results from Cosilab simulations with GRI Mech 3.0 deviated (max 13.2%) from measurements at a higher volume fraction of CC in PG. Varghese and Kumar [81] had formulated a correlation to estimate the *LBV* of PG mixtures. Present mixtures did not fit into their range, so they could not be calculated. The operating conditions of Zhou et al. [82] were also well away from the present work. Hence, comparing current measurements with literature data could not be accomplished. Figure 4-18D shows the consolidated plot of all measured *LBV*s shown in Figure 4-18A-C. In Figure 4-18D, the values of unstretched *LBV* from experiments estimated using a non-linear formulation were only reported to attain better readability. *LBV* decreased with an increase in X_{N2+CO2} at all compositions of producer gas.

For a given mole fraction of X_{CO2} or X_{N2}, the magnitude of reduction in *LBV* was higher for CO_2 than N_2. The possible reasons were (a) the specific heat capacity of the mixture with CO_2 was higher, leading to lower flame temperature, and (b) participation of CO_2 in a chemical reaction [130]. It was interesting to note higher values of *LBV* for CH_4-rich mixture at 25%CC+75%NCC case for all combinations of NCC than H_2-rich mixtures. At 35–45%CC, CH_4-rich mixtures showed equal or higher values of *LBV* than H_2-rich or CO-rich mixtures for all NCC combinations having higher X_{CO2}. To understand the above-mentioned variation, the equilibrium flame temperature and mixture thermal diffusivity were estimated for all operating conditions and presented in Figure 4-19. The flame temperature of CH_4-rich PG at all %CC was higher than other mixtures, which corroborated with the obtained higher values of *LBV* at most operating conditions reported in Figure 4-18D. A similar observation was reported by Kolekar et al. [80]. But, at 45%CC, thermal diffusivity of H_2-rich PG increased significantly, resulting in higher *LBV* than other mixtures. From the foregoing discussion, it is clear that CH_4-rich PG mixtures resulted in higher flame temperature and larger magnitudes of *LBV* as compared to other H_2-rich or CO-rich mixtures.

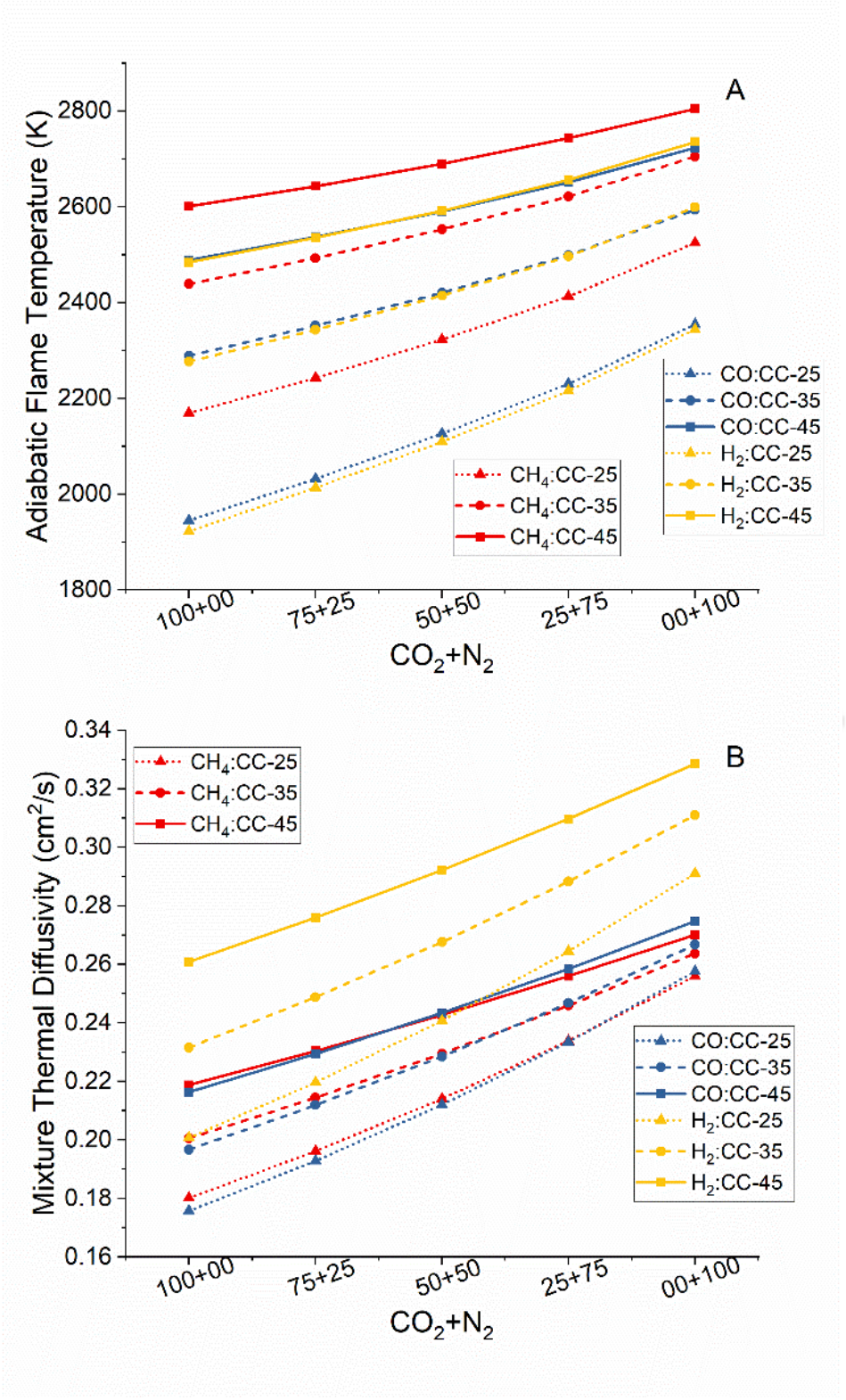

Figure 4-19 A) Adiabatic flame temperature and B)Mixture thermal diffusivity of all mixtures with the variation of CO_2/N_2 ratio

To better understand the change in *LBV* between CH_4/H_2-rich PG fuel, a sensitivity analysis was conducted with Ansys Chemkin using GRI Mech 3.0 for four fuel

compositions, as shown in Figure 4-20, to identify the important elementary reactions that affect *LBV*. Only contributions from the top ten elementary reactions were reported in Figure 4-20. Comparison of normalized sensitivity coefficients of CH_4-rich PG and H_2-rich PG at 25%CC showed that: (a) R166 ($HCO+H_2O \leftrightarrow H+CO+H_2O$), which was one of the important pathways in CH_4 combustion chemistry (obtained from reaction pathway analysis not presented here), was present only in CH_4-rich PG (b) the cumulative effect of R166 presence and only two negative sensitivity coefficient reactions R52 ($H+CH_3+M \leftrightarrow CH_4+M$) and R35 ($H+O_2+H_2O \leftrightarrow O_2+H_2$) were the reasons for higher *LBV* in CH_4-rich PG. (c) Reaction R46 ($H+HO_2 \leftrightarrow 2OH$) which was one of the important chain branching reactions was opposed by chain termination reaction R45 ($H+HO_2 \leftrightarrow O_2+H_2$) for H_2-rich PG and the same combination of opposing reactions were not present in CH_4-rich PG and hence, *LBV* of CH_4-rich PG fuel was higher. The above analysis indicated that CH_4-rich PG was dominated by hydrocarbon oxidation chemistry.

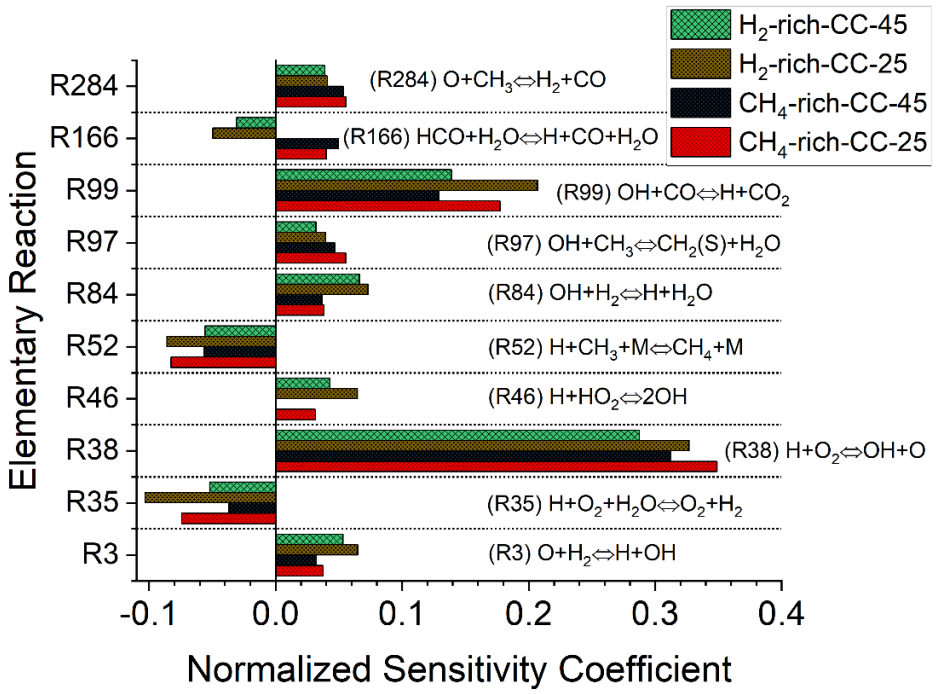

Figure 4-20 Sensitivity analysis for four variants of producer gas (i) CH_4-rich-CC45-45% ($50CH_4$:25CO:$25H_2$)+55%N_2, (ii) CH_4-rich-CC25-25%($25CH_4$:25CO:$50H_2$)+75%N_2 (iii) H_2-rich-CC45-45%($25CH_4$:25CO:$50H_2$)+55%N_2 (iv) H_2-rich-CC25-25%($25CH_4$:25CO:$50H_2$) +75%N_2

At 45%CC case, the important chain branching reactions, (a) higher positive values of sensitivity coefficients of R46 ($H+HO_2 \leftrightarrow 2OH$) and R3 ($O+H_2 \leftrightarrow H+OH$) indicated the dominance of the H_2-oxidation pathway for H_2-rich PG [131] and subsequent increase in reaction rates of R99 ($OH+CO \leftrightarrow H+CO_2$) and R84 ($OH+H_2 \leftrightarrow H+H_2O$) resulted in higher values of *LBV* for H_2-rich PG (b) R284 ($O+CH_3 \leftrightarrow H+H_2+CO$) was an important chain propagation reaction for CH_4-rich PG which helped to decompose CH_3 radical. But, R10 ($O+CH_3 \leftrightarrow H+CH_2O$) with negative sensitivity competed with R284. The reaction pathway analysis showed that the relative rate of consumption of CH_3 through R10 was 6.5%, while that of R284 was 4.3%. The reaction pathway analysis showed the dominance of reaction R10 over R284, and this was the additional reason for the slightly lower value of *LBV* for CH_4-rich PG fuel.

4.4.4.1 Intra-NCC-Variation

In this section, for a given volume fraction of NCC in a mixture, the variation in the composition of N_2 and CO_2 within NCC and its effect on *LBV* was discussed. *LBV* from the non-linear model was only considered as it was similar to the Xiouris model with lesser uncertainty. Figure 4-18A-C showed the impact of selective refinement of CO_2/N_2 represented by $P\%CO_2+(100-P)\%N_2$ in which *P* varied from 0 to 100 and its effect on the *LBV* of PG. Figures clearly showed that at a given $CH_4/CO/H_2$ rich PG and volume fraction of CC, the *LBV* varied nonlinearly with change in the proportion of CO_2 and N_2. Hence, 2nd order polynomial trend line was fitted to the data. The curvature of each trend line at each combination of CO_2/N_2 was estimated as per Eq. 4.1.

$$Curvature = \frac{|f''(x)|}{(1+(f'(x))^2)^{3/2}} \qquad 4.1$$

For CH_4-rich producer gas, absolute curvature of 25-45% CC at a given intra-NCC was averaged and reported in Figure 4-21 as black-filled square symbols. The blue shaded region represents the range of the change in normalized curvature with a decrease in CO_2 (and increase in N_2).

The dashed lines correspond to the averaged normalized curvature of the corresponding dilution level. Similar estimation was done for CO/H_2-rich producer gases and reported with green diamond and red circle symbols. Absolute curvature (averaged) of CH_4-rich mixture was the highest, and it was followed by CO and H_2-rich mixtures. This indicated

a higher degree of non-linearity in CH_4-rich mixtures with a change in CO_2/N_2. The response of CH_4-rich PG to increase in X_{CO2} was higher due to higher flame temperature. Absolute curvature of CO-rich PG was the lowest, as these mixtures had low values of flame temperature, and hence, the effects of an increase in X_{CO2} were not pronounced.

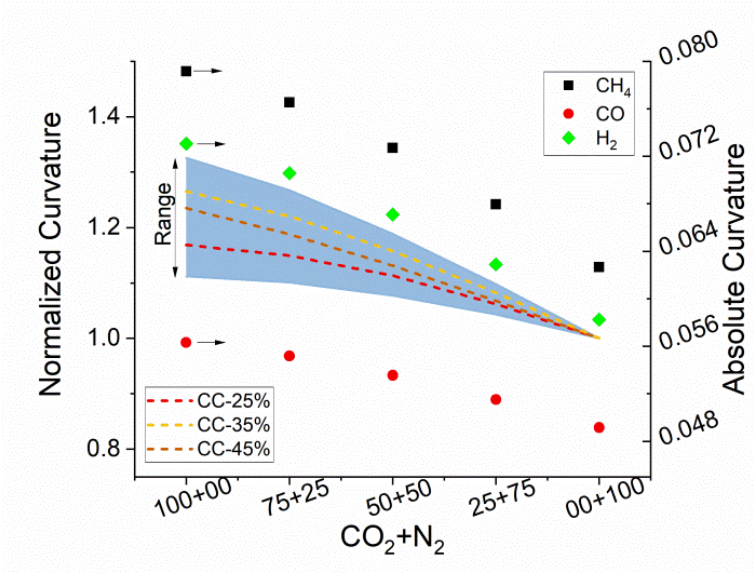

Figure 4-21 Non-Linearity variation in LBV of all compositions. Solid symbols represent the averaged values of absolute curvature of corresponding rich cases (CC-25%, 35% & 45%)

Then, the absolute curvature of each $CH_4/CO/H_2$ rich gas at each volume fraction of CC was normalized with the respective curvature value at N_2-100% at the same volume fraction of CC. The same was presented as area distribution with blue color in Figure 4-21. This was done to identify the variation of volume fraction of CC on normalized curvature. Magnitudes of normalized curvature showed a broader range at 100% CO_2, as shown in Figure 4-21. Normalized curvature values decreased with a reduction in X_{CO2} coupled with an increase in X_{N2}. Normalized curvature initially increased for an increase in volume fraction of CC from 25% to 35%, and then it decreased. It was interesting to observe that normalized curvature values of 35% CC and 45% CC were closer to each other even though the magnitude of *LBV* values were quite different. It seemed that a critical value of mole fraction of CO_2 exists above which CO_2 controls the combustion of producer gas. The involvement of CO_2 in the kinetics rather than inert can be explicitly interpreted from the above data as presented in Figure 4-21 and in agreement with a similar observation presented by Varghese et al.[132].

4.4.4.2 Inter-CC-NCC-Variation

As the earlier section discussed the effect of selective refinement of N_2/CO_2 and its effect on the variation of *LBV*, in this section, refinement of PG to remove NCC and its effects on *LBV* is discussed. Figure 4-22A shows the unstretched *LBV* estimated using the nonlinear stretch formulation for CH_4-rich PG at different volume fractions of CC. Symbols in the figure represent current experimental data. Dotted lines correspond to linear trend lines. The CO and H_2-rich PG cases were not presented here to avoid redundancy. Observations from the figures showed that *LBV* increased linearly with an increase in the volume fraction of CC at a given volume fraction of NCC for all studied cases due to the rise in the heating value and flame temperature. The slopes of linear regression fits were analyzed to understand the extent of linearity of fitted trendlines with respect to intra-NCC variation and the possibility of interpolation to obtain intermediate values.

For $CH_4/CO/H_2$-rich producer gas, the slopes corresponding to 25-45% CC at a given intra-NCC were obtained and plotted in Figure 4-22B. A linear variation in the slope values was observed for H_2 and CO-rich cases with a decrease in X_{CO2} (and simultaneous increase in X_{N2}) in diluents. Such a trend was non-existent in methane-rich cases. The combustible components fraction variation showed a linear variation in slopes for only hydrogen & carbon monoxide-rich cases, and any intermediate value can be interpolated within the studied conditions. It was also attempted to estimate the values of *LBV* of 35% CC by interpolating the measured value of *LBV* at 25 & 45% CC for all CH_4-rich, CO-rich, and H_2-rich PG mixtures.

The deviation in measured and interpolated *LBV* data was estimated for all studied conditions and presented in Figure 4-22B. At a given NCC, errors obtained with different %CC and different fuel-rich cases were averaged to ease overall comparison in their values with change in P%CO_2+(100-P)% N_2. The deviations were less than 4% for mixtures with 0CO_2:100N_2 and 50CO_2:50N_2 with the current choice of a linear fit. For higher mole fractions of CO_2, linear fit resulted in a more significant deviation, which could be observed in Figure 4-22B.

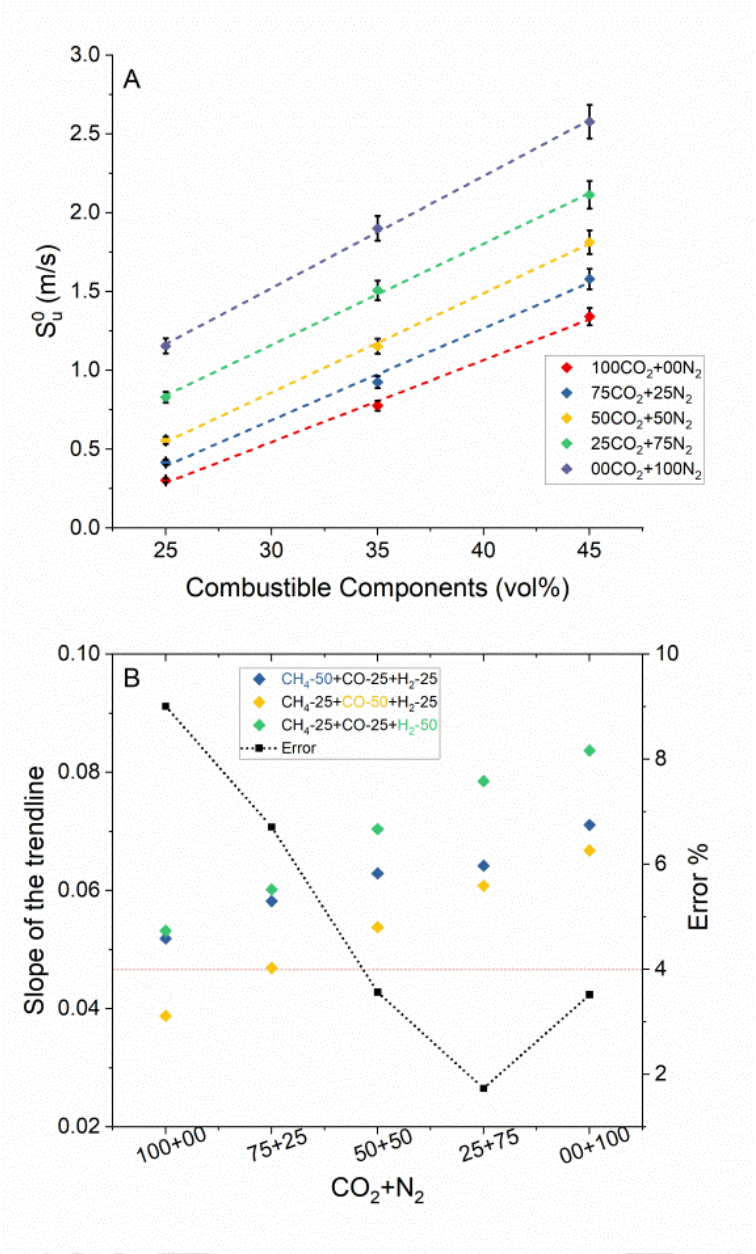

Figure 4-22 A) Inter-CC-NCC variation in CH_4 rich mixtures. B) The distribution of slopes of linear variation and error in interpolation at 35%CC+65%NCC

As earlier mentioned, flame characteristics were strongly dependent on the rich component in the fuel mixture, and the same observation held good for NCC mixtures. As the NCC mixture contained N_2 and CO_2, *LBV* values respond to the dominant dilution effect of either CO_2 (nonlinear variation due to the reduction of the flame temperature and also due to its participation in chemical kinetics to enhance chain termination reactions) or N_2 (linear variation due to the reduction of flame temperature only) whose mole fraction was greater than 50% in NCC.

4.5 Effect of Combustible Components (H_2, CO, and CH_4) on LBV and instability of RPG-air mixtures

Earlier section 4.4 discussed in length the effects of the independent variation of the combustible/ non-combustible components in the producer gas while reacting with pure oxygen. In this section, the combustion characteristics of Refined Producer Gas (producer gas without any inerts obtained through the refining process) reacting with air at 300±3 K and 1, 2, and 4 bar are discussed. The composition of RPG was considered as 50%*A*+*X*%*B*+(50-*X*)%*C* where *A*: CH_4/H_2/CO, *B*: H_2/CO/CH_4, *C*: CO/CH_4/H_2 and *X*: 00:50 in steps of 12.5% to understand the impact of change in the proportion of H_2:CO:CH_4 on *LBV* and flame stability. Table 4-4 shows the list of compositions investigated along with the associated lower calorific values (LCV). All the experiments were performed at 300±3 K and 1, 2, and 4 bar. At 1 bar, ϕ = 0.8, 0.9, 1.0, 1.1, & 1.2 was considered, whereas at 2 & 4 bars, ϕ = 0.8, 1.0, & 1.2 were studied. Total number of experiments performed were 132 without accounting for repeatability. As mentioned in the earlier section, here too, all experiments were repeated twice, and some of the high pressure experiments were repeated thrice to obtain accurate *LBV*. Post processing procedure remained identical to that of section 4.4. In this chapter, finer details on the variation of flame speed with stretch rate was not reported. Only unstretched *LBV* and burned gas Markstein length was discussed in detail in the following section.

Table 4-4 Refined producer gas composition variation

Case	H_2 (vol%)	CO (vol%)	CH_4 (vol%)	H_2:CO:CH_4	LCV(MJ/m^3)
1	50	0	50	4:0:4	23.3
2	50	12.5	37.5	4:1:3	20.4
3	50	25	25	4:2:2	17.5
4	50	37.5	12.5	4:3:1	14.6
5	50	50	0	4:4:0	11.7
6	37.5	50	12.5	3:4:1	14.8
7	25	50	25	2:4:2	18
8	12.5	50	37.5	1:4:3	21.1
9	0	50	50	0:4:4	24.2
10	12.5	37.5	50	1:3:4	24
11	25	25	50	2:2:4	23.8
12	37.5	12.5	50	3:1:4	23.5
1*	50	0	50	4:0:4	23.3

4.5.1 Unstretched Laminar Burning Velocity

LBV of twelve different RPG compositions (Table 4-4) were measured at ϕ = 0.8-1.2, 300 K, 1 bar and depicted in Figure 4-23. Here, the non-linear extrapolation model (Eq. 3.22) was used. Xiouris model was not used as (a) *LBV* estimated using it matched close to that of Eq. 3.22, (b) it was quite involved, as it needed radius-time simulation from the unsteady one-dimensional spherical flame model in Cosilab. Unstretched *LBV* data corresponding to all the experimental conditions was simulated using GRI Mech 3.0 and FFCM-1 mechanisms.

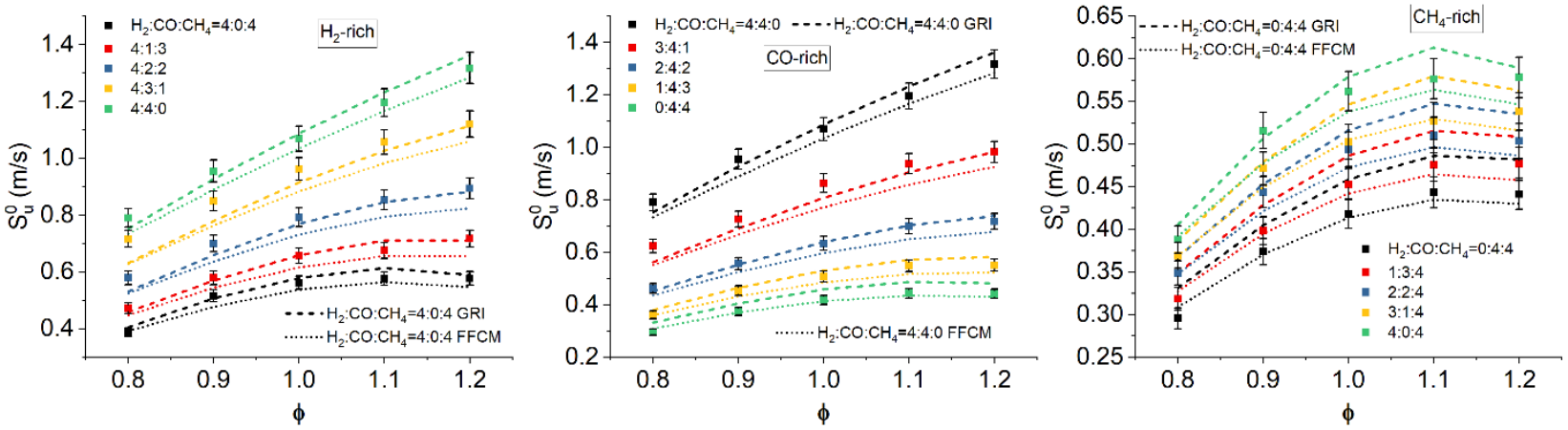

Figure 4-23 Laminar burning velocity of refined producer gas mixtures varying with equivalence ratio from 0.8 to 1.2 at 300 K and 1 bar

In the H_2-rich case, the magnitude of the *LBV* increased with an increase in CO and reduction in CH_4 at all equivalence ratios. The peak *LBV* shifted towards the richer side, *i.e.*, ϕ = 1.2, and the magnitude of the peak values increased continuously with an increase in CO and subsequent reduction in CH_4, which was typical behavior of H_2-CO mixtures [58,122]. This was essentially due to increased flame temperature and mixture diffusivities.

The *LBV* variation with an increase in the equivalence ratio in each fuel composition became non-linear with a simultaneous increase/reduction in CH_4/CO content, respectively, as the peak shifted towards ϕ = 1.1. In the CO-rich case, the magnitude of the *LBV* increased with an increase in H_2 (and reduction in CH_4) at any given equivalence ratio, and a similar trend was reported by Xie et al. [133]. An increase in H_2 increased the heating value and transport properties of the mixture and resulted in higher *LBV*. The peak shifted towards ϕ = 1.1 from ϕ = 1.2, and the magnitude of the peak values reduced with the increase in CH_4 (and reduction in H_2), and it showed the dominant behavior of methane.

In the CH_4-rich case, the magnitude of the *LBV* increased with an increase in H_2 (and reduction in CO) at any given equivalence ratio. Unlike as reported in H_2:CO:CH_4-Air mixture-related work by Xie et al. [133], an increment in CH_4 did not lead to an increment in *LBV*, but rather in the presence of H_2 and CO, and it led to the decrement of *LBV* in the present work. The peak *LBV* was obtained at ϕ = 1.1 in all the CH_4-rich cases, while the magnitude marginally reduced with an increase in H_2 (and reduction in CO) due to a decrease in flame temperature. In all CH_4-rich cases and a hike in CH_4 in all other compositions, the peak always occurred at ϕ = 1.1, resulting in a non-linear behavior. A similar trend in the peak *LBV* was reported by Lapalme et al. [79]. Generally, the simulated values obtained using GRI Mech 3.0 were consistently higher (Average deviation: +6.37%) in magnitude than those obtained using FFCM-1 under all conditions.

In CH_4-rich mixtures, the simulated *LBV* using FFCM-1 matched well with the experiments than GRI Mech 3.0, and the agreement slightly tended to shift towards the GRI Mech 3.0 with an increase in H_2 (and reduction in CO). In the considered ternary fuel variation, GRI Mech 3.0 performed better with CO-rich and H_2-rich mixtures, while FFCM performed better with CH_4-rich mixtures. The increment in CO had different effects based on the rich component of the mixture. Increment in H_2 always enhanced the *LBV* under most conditions. To further understand the reason for the impact of RPG composition on the *LBV*, equilibrium flame temperature (EFT) and thermal diffusivity of H_2:CO:CH_4 = 4:4:0, 2:2:4, 0:4:4, 4:2:2, 4:0:4 and 2:4:2 compositions were estimated and presented in Figure 4-24. The range of EFT variation was within 100 K for all compositions except for an equimolar mixture of H_2-CO. As the temperature of the products always peaked at ϕ = 1.1 independent of compositions, a similar trend was not

reflected in the peak value of *LBV* due to the simultaneous change in the thermal diffusivity and kinetic effect [79,89].

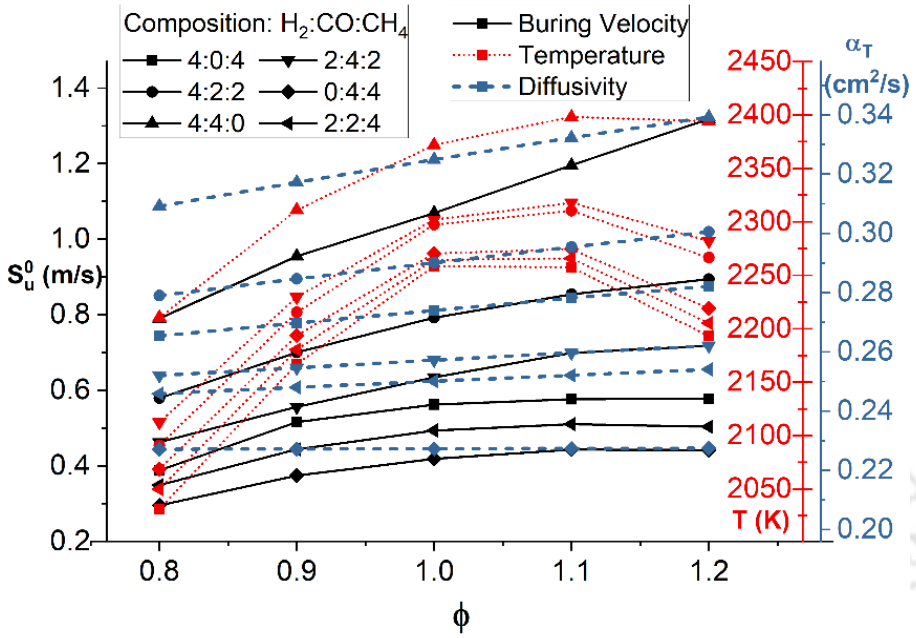

Figure 4-24 Adiabatic flame temperature and Thermal diffusivity of selected compositions of RPG at 300K and 1bar obtained using equilibrium calculations using Ansys Chemkin along with the laminar burning velocity values obtained from the experiment

4.6 Effect of Initial pressure on the LBV and flame stability of RPG-air mixtures

The effect of initial pressure on *LBV* of all compositions is presented in Figure 4-25 and Figure 4-26. The *LBV* of all the studied compositions decreased with an increase in pressure as the reactant mixtures were denser. In the H_2-rich mixtures, the *LBV* values were underestimated by the reaction mechanisms at elevated pressures and with a concurrent rise in CO and lowering in CH_4 mole fractions. The divergence in *LBV* between measurements and simulations was lesser till the absolute mole fraction of CH_4 (X_{CH4}) attained 25% and was significantly higher for cases that had X_{CH4} greater than 50%. As the initial pressure stepped up, CO-rich-air mixtures with X_{H2} exceeding 25% displayed a similar under prediction trend by GRI Mech 3.0 and FFCM-1.

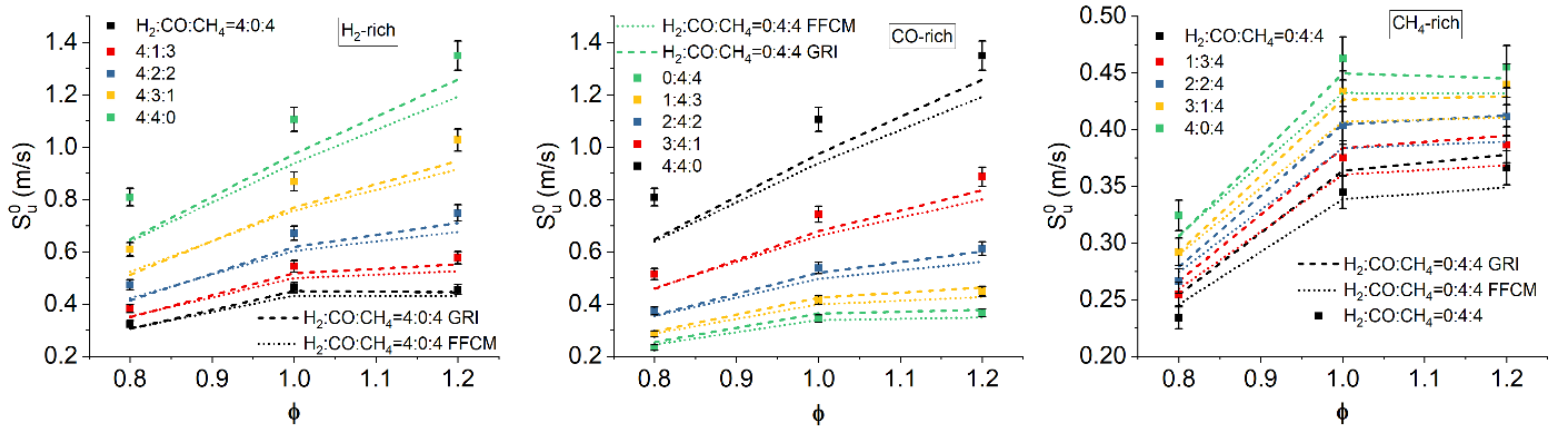

Figure 4-25 Laminar burning velocity of refined producer gas mixtures varying with equivalence ratio from 0.8-1.2 at 300 K and 2 bar

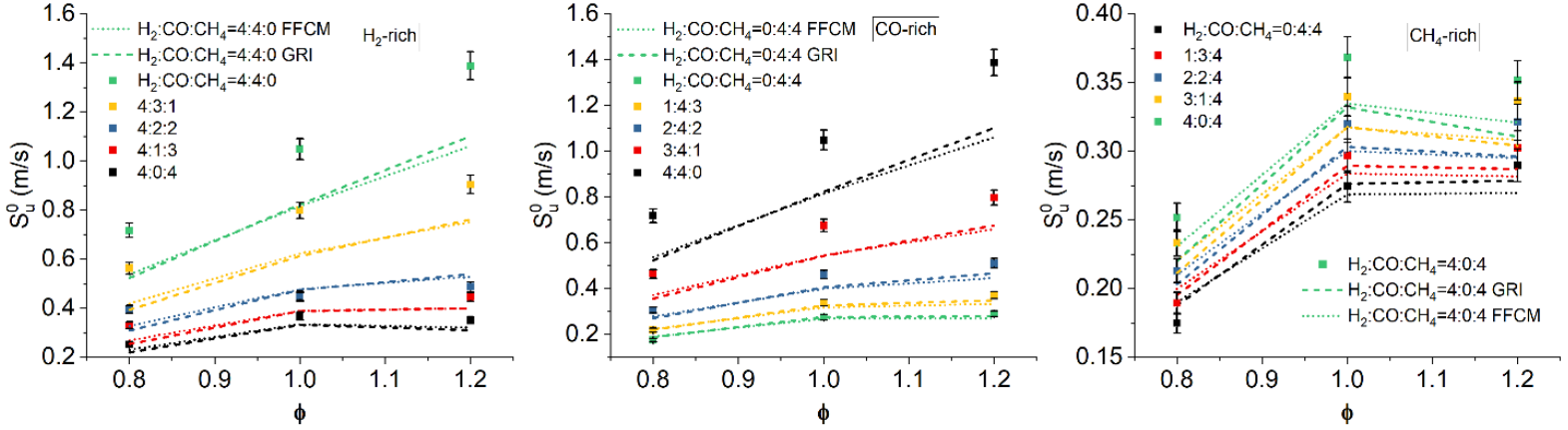

Figure 4-26 Laminar burning velocity of refined producer gas mixtures varying with equivalence ratio from 0.8-1.2 at 300 K and 4 bar

In CH_4-rich-air mixtures, at 2 bar, GRI Mech 3.0 over predicted the *LBV* of CO dominant mixtures but under-predicted the *LBV* of H_2 dominant mixtures, whereas results based on FFCM-1 showed that it was underestimated in all cases. At 4 bar, *LBV* obtained with GRI Mech 3.0 agreed well with experiments for mixtures with lower X_{H2} in the mixtures where FFCM-1 underperformed. The studied kinetic mechanisms needed further optimization to improve their accuracy.

4.6.1 Intrinsic instabilities

4.6.1.1 Thermo-diffusive instabilities

Burned gas Markstein lengths were presented against compositions and fuel mole fraction (X_{H2}+X_{CO}+X_{CH4}) in Figure 4-27a and Figure *4-27*b. Interestingly from Figure 4-27a, the L_b was either close to zero or negative for all the investigated combustible mixtures that had: (a) lower values of fuel mole fraction and (b) the mole fraction of methane in the mixture was the lowest. The stability of such mixtures was dominated by the presence of light and highly diffusive H_2 species. In contrast, some combustible mixtures remained stable to thermo-diffusive effects even at the lowest fuel mole fraction due to a higher methane mole fraction than H_2 or CO. The larger amount of CH_4 than H_2 or CO in these mixtures swindled them to be relatively stable to thermo-diffusive effects due to an increase in *Le*. The magnitude of the presented burned gas Markstein length values consolidated in Table 4-5.

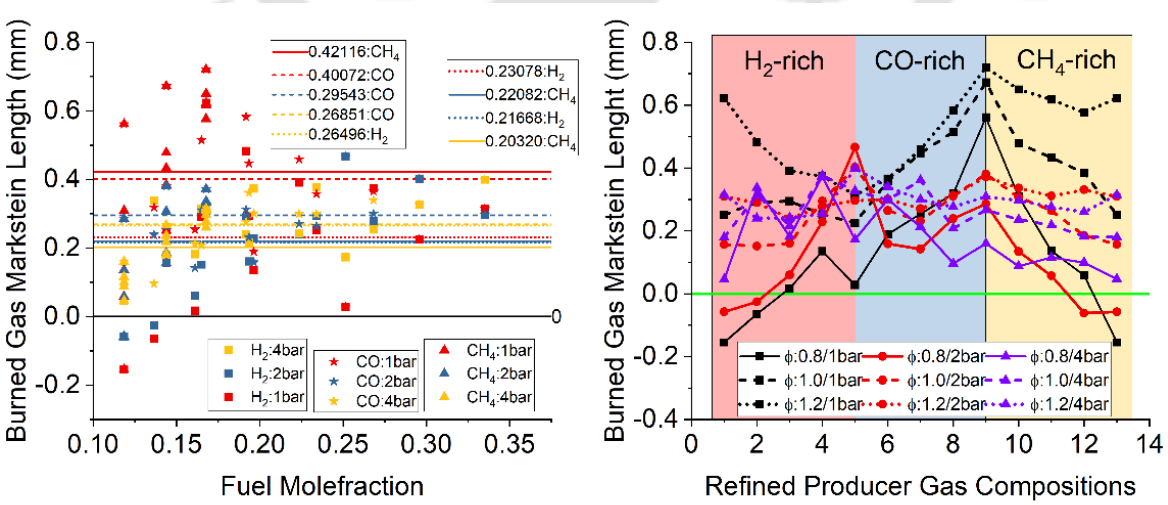

Figure 4-27 Burned Gas Markstein length variation with compositions and fuel mole fractions at different equivalence ratios and compositions

Table 4-5 Burned Gas Markstein length variation with compositions (in mm)

Case	Composition (vol%)			Equivalence ratio – Initial pressure (in bar)								
	H_2	CO	CH_4	0.8-1	1.0-1	1.2-1	0.8-2	1.0-2	1.2-2	0.8-4	1.0-4	1.2-4
1	50	0	50	-0.15446	0.25095	0.6229	-0.05733	0.15695	0.3093	0.04654	0.1801	0.3144
2	50	12.5	37.5	-0.06478	0.2916	0.48295	-0.02546	0.1515	0.2895	0.3374	0.31395	0.24
3	50	25	25	0.0175	0.29465	0.3909	0.06006	0.16075	0.2392	0.18193	0.21645	0.2419
4	50	37.5	12.5	0.1356	0.2525	0.3739	0.2286	0.29455	0.27865	0.3729	0.3764	0.2535
5	50	50	0	0.02799	0.225	0.3145	0.46595	0.40195	0.29595	0.1727	0.3269	0.3993
6	37.5	50	12.5	0.19005	0.3579	0.36575	0.1586	0.26455	0.3005	0.301	0.2988	0.33997
7	25	50	25	0.2544	0.44705	0.459	0.1423	0.2313	0.2707	0.2122	0.3612	0.2994
8	12.5	50	37.5	0.3184	0.5149	0.5826	0.2391	0.3104	0.3126	0.09614	0.20825	0.2763
9	0	50	50	0.56125	0.672	0.72	0.2854	0.38065	0.37155	0.1599	0.2666	0.30907
10	12.5	37.5	50	0.3091	0.4786	0.64985	0.1345	0.30703	0.3361	0.08768	0.2361	0.2966
11	25	25	50	0.1368	0.43325	0.61755	0.05728	0.2649	0.311	0.1156	0.218	0.27655
12	37.5	12.5	50	0.05857	0.3848	0.5763	-0.06147	0.18525	0.3312	0.09902	0.1821	0.2597
13	50	0	50	-0.15446	0.25095	0.6229	-0.05733	0.15695	0.3093	0.04654	0.1801	0.3144

Additionally, in Figure 4-27a, the magnitude of the L_b across the equivalence ratios was estimated for each H_2/CO/CH_4-rich mixture at each pressure and plotted as color lines. The L_b of the CH_4-rich mixture showed the largest variation due to its stronger/weaker response to H_2/CO. The mean L_b values of H_2-rich mixtures varied differently than the trend observed in the CH_4 and CO-rich mixtures. The average value initially decreased with pressure and then increased, making H_2-rich mixtures more resilient to thermo-diffusive instabilities, which were unexpected. Multiple repetitive experiments were performed, but no improvement.

At higher pressures, the flame became cellular for H_2-rich mixtures, resulting in higher uncertainty. Mean L_b of CO-rich mixtures irrespective of initial pressure varied within a small range resulting in almost consistent exposure/vulnerability to the thermo-diffusive instabilities due to its slow reactivity and low diffusivity. The rise in pressure decreased the flame thickness and the magnitude of L_b under all conditions, and also, the magnitude of L_b varied within a small range. All the investigated richer (ϕ = 1.2) mixtures had positive L_b as the deficient reactant O_2 was less diffusive than the fuel species. Conversely, few of the lean (ϕ = 0.8) mixtures of certain compositions were unstable to thermo-diffusive effects due to the active presence of H_2. Further analysis into the thermo-diffusive instabilities was conducted with the effective Lewis number analysis. As discussed in the previous section, effective *Le* estimation using volume and diffusion-based models suited well for RPG type of multicomponent fuel. The present work also used the same models to find effective *Le* as shown in Figure 4-28.

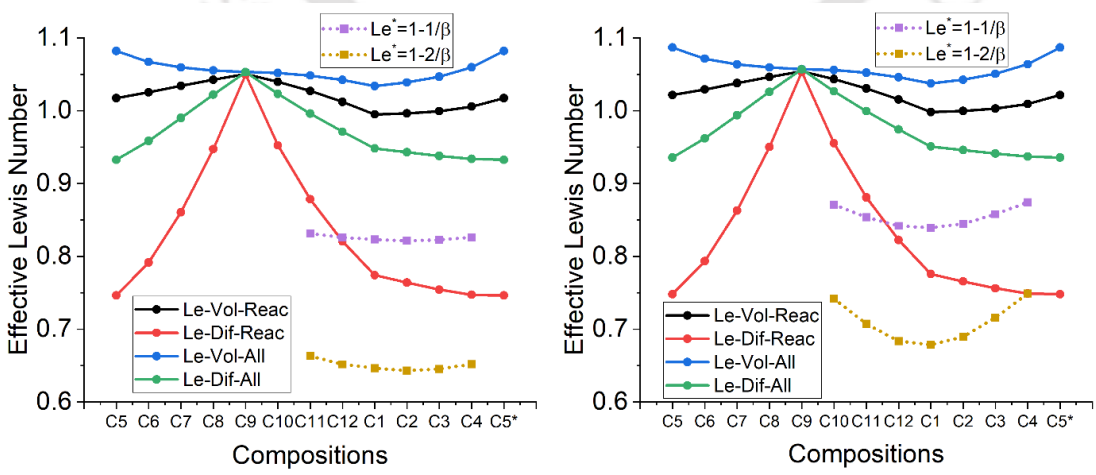

Figure 4-28 Effective Lewis number of RPG by Volume and Diffusion based models along with corresponding critical values

For RPG-air mixtures, $Le_{eff,\,diff}$ showed good agreement with the measured L_b, and hence, it was estimated for all the studied mixtures and presented in Figure 4-29 along with the corresponding critical values. Except for the compositions ranging from 7-11, the Le_{eff} of other compositions was below the Le^*, pronouncing the potential vulnerability of these mixtures towards the thermo-diffusive instabilities. H_2:CO:CH_4 = 1:2:1-1:1:2 (2:4:2-2:2:4) were the mixtures had an effective *Le* value above the critical *Le* values. The mole fraction of H_2 in those compositions never exceeded 25%, concluding the crucial role of H_2 in inducing the thermo-diffusive instability in the RPG-air mixtures. From the L_b and effective Lewis number analysis, the addition of CO increased the resilience of the mixtures against thermo-diffusive instabilities while supported by CH_4 and opposed by H_2.

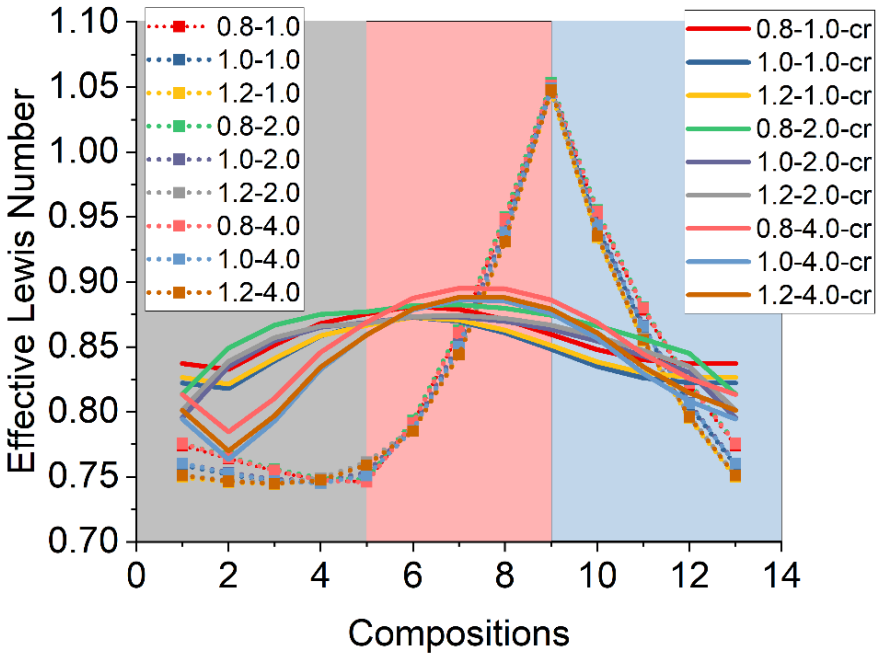

Figure 4-29 Effective Lewis Number and corresponding critical Lewis numbers at all the initial pressure conditions

4.6.1.2 Hydrodynamic instabilities

The six parameters such as critical radius (R_{cr}), flame thickness (δ_f), density ratio (σ) of reactants (ρ_u) to products (ρ_b^o), normalized critical *LBV* $\left(S_{u,cr}/S_u^o\right)$ where $S_{u,cr}$ was the stretched *LBV* at the critical radius, and S_u^o was the unstretched *LBV*, coefficient of self-

acceleration (α), and critical Peclet number (Pe_{cr}) were essential in addressing the tendency of a mixture towards the occurrence of hydrodynamic instability. The critical radius corresponding to the onset of hydrodynamic instability obtained by an in-house code of all the analyzed RPG-air mixtures at 1-4 bar, 300 K, and ϕ = 1 were displayed in Figure 4-30. Results corresponding to different equivalence ratios at 4 bar were presented in Figure 4-31. The data was split into three categories, H_2, CO, and CH_4 rich mixtures, respectively, where the volume fraction of the rich component was 50% in the fuel. The critical radius decreased with an increase in the hydrogen volume fraction irrespective of variation in the mole fraction of other constituents and vice versa in the case of CH_4. CO variation did not significantly affect the critical radius as it depended on the other components. There was a significant increase in the critical radius when H_2/CH_4 was decreased/increased.

The flame thickness was estimated from the predicted temperature profile of 1D planar flames. At 1 bar, H_2:CO:CH_4 = 4:4:0 has the thickest flame owing to higher mass diffusivity and lower expansion ratio due to lighter reactants, but still it has the lowest critical radius and Peclet number due to higher *LBV*. Next thicker flame was observed for H_2:CO:CH_4 = 0:4:4 due to lower mass diffusivity. Also, the expansion ratio of the mixture was higher due to heavy reactants, which eventually resulted in a larger critical radius due to lower *LBV*. All mixtures yielded thinner flames at elevated pressures due to a hike in the reaction rate. At elevated pressures, the critical radius decreased due to thin flames irrespective of lower values of *LBV*. It can be concluded that flame thickness was an important factor in commanding the earlier or delayed occurrence of hydrodynamic instability. The expansion ratio varied over a smaller range, and its variation on the instability was unclear. The coefficient of self-acceleration [84,93] and normalized critical *LBV* [84] were estimated to identify self-acceleration flames due to thermo-diffusive effects.

At 4 bar, normalized critical *LBV* was greater than unity for H_2-rich cases, and mixtures with lower methane content due to smaller critical radius resulted in stronger curvature effects and higher stretched *LBV* than the unstretched *LBV*. These mixtures had higher values of acceleration coefficient too. At lower pressures, the critical radius was larger, the flame curvature effects were smaller, local pressure and temperature were different

from the initial pressure and temperature, and all these effects made the normalized *LBV* less than unity and also with lower values of acceleration coefficient.

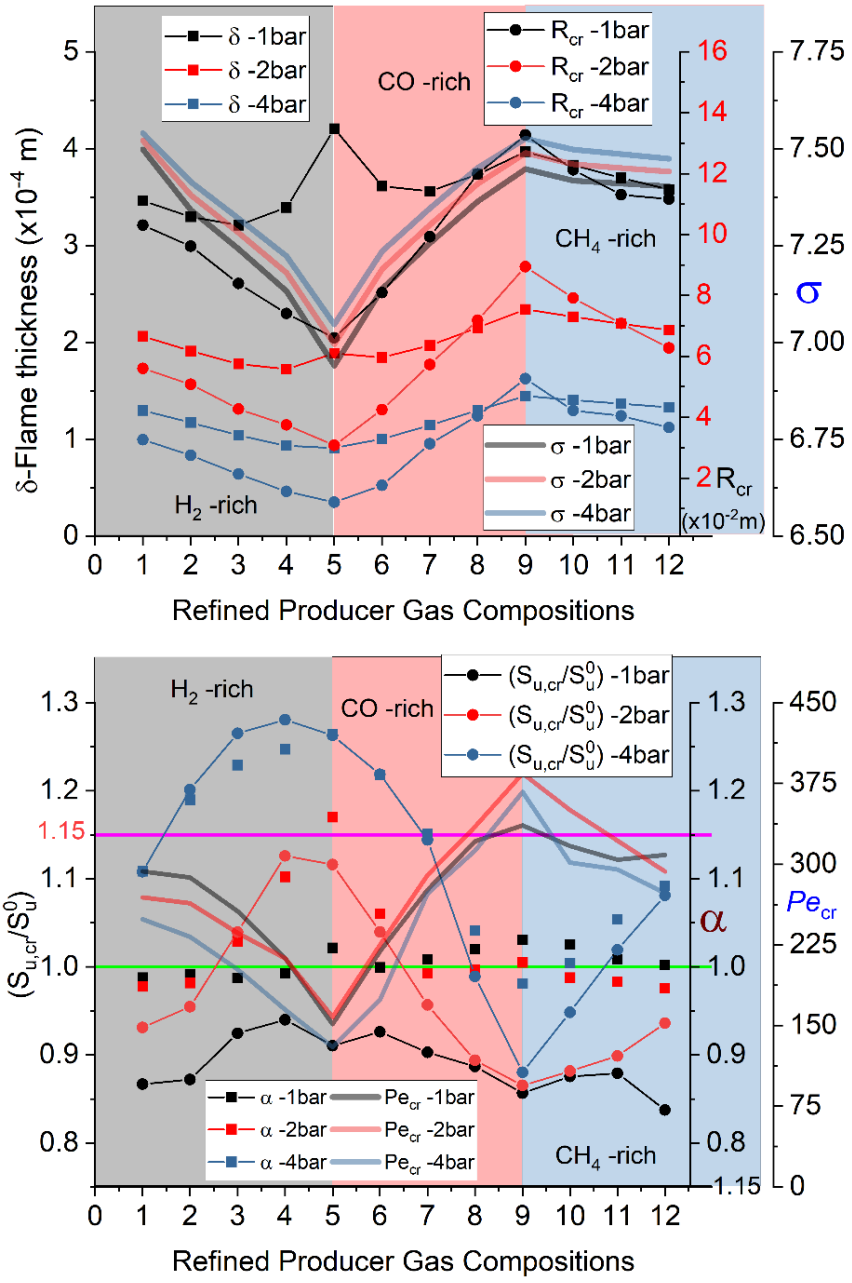

Figure 4-30 Hydrodynamic instability characterization parameters of all compositions at stoichiometric and different initial pressure conditions.

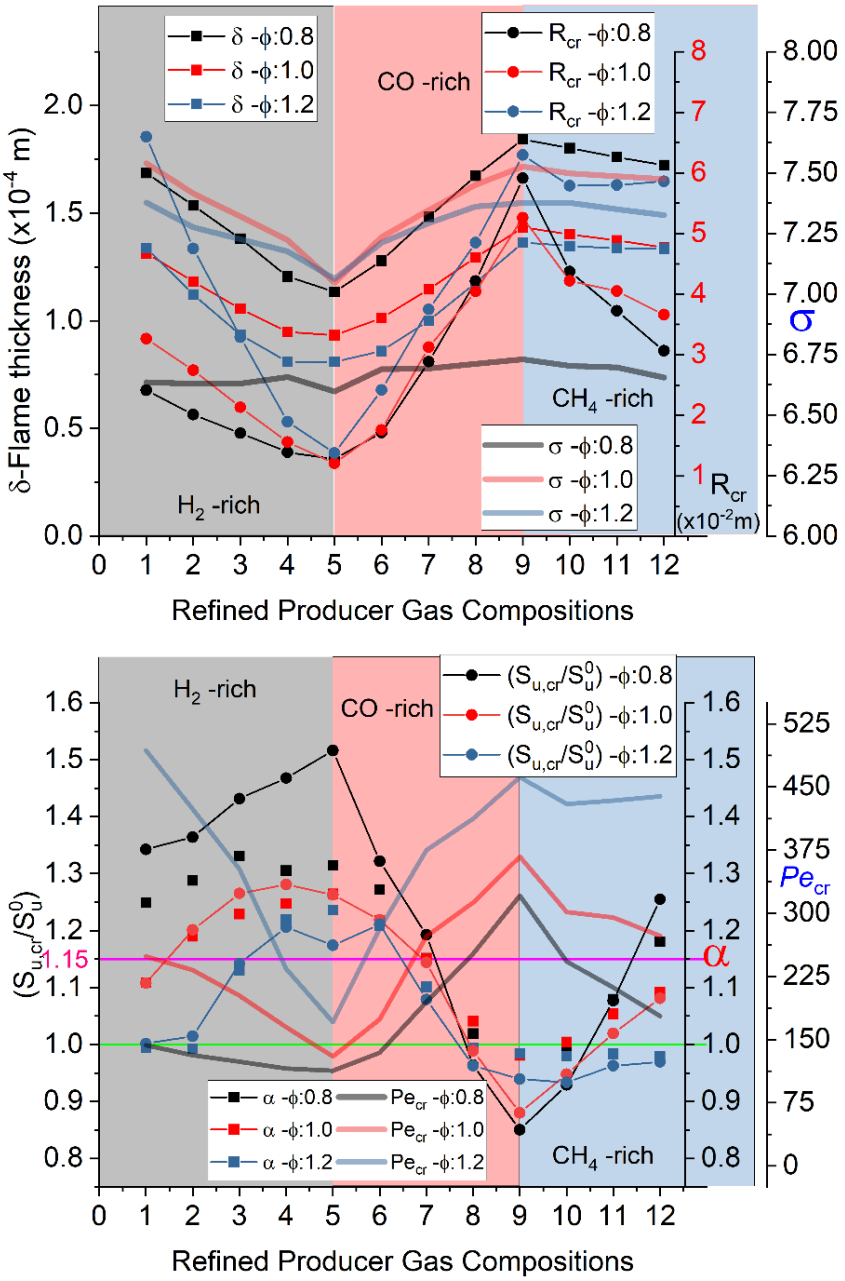

Figure 4-31 Hydrodynamic instability characterization parameters of all compositions corresponding to 4 bar at different equivalence ratios.

The values of α corresponding to 1-1.15 referred to hydrodynamic instability in a thermo-diffusive stable mixture, and beyond 1.15 indicated the existence of both the thermo-diffusive and hydrodynamic instabilities and first one being dominant. Depending on the

scenario, one of the parameters play crucial role in triggering the instability and it cannot be singled out.

4.6.1.3 Comprehensive LBV-Instability profile/analysis

The preceding discussion brought out the contradictions, such as the high-density ratio favored while the thickness disfavored the earliest occurrence of hydrodynamic instability. These two parameters were independently found to be highest at composition no. 9 (H_2:CO:CH_4=0:4:4), leading to contradicting conclusion. A similar conflict was observed with other considered parameters due to the diversity of three fuel species present in the fuel mixture. Hence, a ranking system was proposed to understand the susceptibility to instability. The ranking was done in the following manner: the most favorable and unfavorable parameters to the instability of a given mixture received the lowest and highest rank on a scale of 1-12 (as the total number of compositions considered was 12 and hence the maximum attainable rank was 12). Flame thickness, expansion ratio, critical radius, normalized critical *LBV*, and coefficient of self-acceleration were chosen for the ranking. The mixtures were independently arranged based on the: (1) flame thickness, (2) critical radius, values from largest to smallest and were ranked from 1 to 12.

Similarly, the mixtures were based on: (1) coefficient of self-acceleration, (2) normalized critical *LBV*, and (3) expansion ratio, values from smallest to largest were ranked from 1 to 12. Then, the ranks from all parameters were averaged to calculate the combined representative susceptibility rank to address the occurrence of hydrodynamic instability. The calculated susceptibility score (average) of all mixtures is displayed in Figure 4-32. Some of the mixtures had common ranks, and therefore a maximum susceptibility score of 10 was obtained. The susceptibility score was estimated for all the 12 compositions at each operating condition of pressure and equivalence ratio independently. All the susceptibility score plots were identical to Figure 4-32 with minor variations. So, the susceptibility score of composition was estimated by averaging the susceptibility scores obtained at all the studied operating conditions and rounded off to the nearest integer. The final trend obtained from all above averaging is displayed in Figure 4-32.

An identical ranking system was followed with burned gas Markstein length and effective Lewis number (higher to lower values will be allotted with ranks 1 to 12) to calculate the

mixture's susceptibility (average) to the thermo-diffusive instability and plotted in Figure 4-32. The susceptibility scores of thermo-diffusive and hydrodynamic instabilities were averaged, and their rounded-off values were plotted as an intrinsic instability curve. After that, the measured *LBV* at all operating conditions of compositions were averaged to find the average *LBV* of that composition. Then, the average *LBV* of the C9 mixture with the lowest susceptibility score was chosen to normalize the average *LBV* of all the mixtures. The normalized values were plotted in Figure 4-32. It was included in the figure to have a comprehensive perspective on the instabilities and their relation with *LBV*. As the susceptibility of compositions varied cyclically, as shown in Figure 4-32, the compositions were arranged from C3-C12-C3 for better explanation. The C9 (H_2:CO:CH_4 = 0:4:4) had the highest resilience to both instabilities. The susceptibility to combined intrinsic instabilities increased on either side of C9. The compositions on the CH_4-rich side (along with an increase in H_2 and decrease in CO) were more susceptible to the thermo-diffusive instabilities.

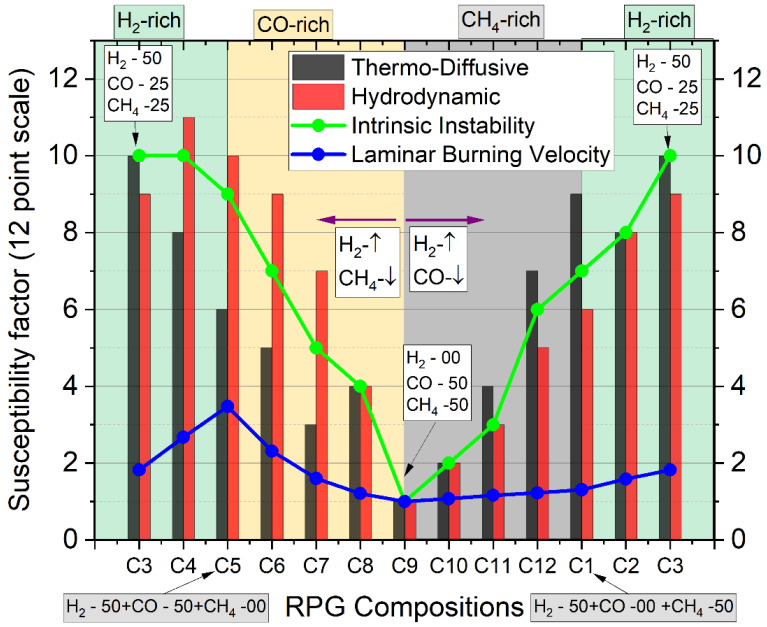

Figure 4-32 The susceptibility of the mixtures to intrinsic, thermo-diffusive, and hydrodynamic instabilities along with the representative laminar burning velocity variation

Similarly, compositions on the CO-rich side (along with an increase in H_2 and a decrease in CH_4) were more susceptible to hydrodynamic instability. The susceptibility inflection

between thermo-diffusive and hydrodynamic instability occurred in the H_2-rich mixtures depending on the content of the CH_4 and CO. The susceptibility to intrinsic instabilities grew tremendously as the H_2 content shot up. Higher mole fractions of H_2 in the presence of CO favored an earlier onset of hydrodynamic instability, while accompanied with CH_4 preferred the onset of thermo-diffusive instability. Larger mole fractions of CH_4 in the mixture reduced the susceptibility to hydrodynamic instability, while CO increment suppressed the thermo-diffusive instability. The equimolar CO-CH_4 mixture displayed the highest resilience to both kinds of instabilities. The H_2:CO:CH_4 = 4:2:2 mixture had the highest susceptibility to both instabilities. It was clear that the H_2 content variation in a mixture affected its overall susceptibility to instabilities. In contrast, a change of CH_4 or CO in a mixture was oriented towards either thermo-diffusive or hydrodynamic instability. The laminar burning velocity was directly proportional to the susceptibility to the instabilities, while the degree of proportionality was different for CO and CH_4-rich cases.

Chapter 5 Conclusions

The objective of the present research work was to investigate the combustion characteristics of a multicomponent producer gas comprehensively. An exhaustive literature review was undertaken to find a representative composition of producer gas comprising of H_2, CO, CH_4, CO_2, and N_2. To understand the combustion characteristics of PG comprehensively, two different strategies were implemented. To measure the unstretched LBV and burned gas Markstein length, freely expanding spherical flames were generated in a new spherical combustion chamber (4.5 L), and were imaged using a high-speed shadowgraph. A versatile non-linear extrapolation model was used to estimate the unstretched *LBV*. Around 450+ experiments (inclusive of repeatable experiments) comprising of various compositions at different initial pressures were performed. Significant findings from this research are summarized below.

5.1 Effect of chamber volume on laminar burning velocity

To arrive at a proper design of the geometry and volume of the combustion chamber to cater for both constant-volume (pressure-time data-based) and constant pressure (radius-time data-based) experiments, the unsteady pressure-time history of stoichiometric methane-air mixtures measured in four different spherical chambers having volumes as 0.5 L, 1 L, 4.4 L, and 20 L was obtained from the literature. Power law was used to obtain extrapolated values of *LBV* at 1 bar and 300 K1D Constant Volume Spherical Flame model in Cosilab was used to simulate all the experimental conditions.

- A pure spherical chamber without intrusions, along with Omari et al. and/or Faghih et al. thermodynamic models and the data range corresponding to P_r = 0.2-0.5 is the best for obtaining accurate results.
- The deviation in values of stretched *LBV* between chambers of different volumes was observed at higher pressures and temperatures.
- Stretched *LBV* decreased with increased volume till 4.4 L and considerably increased for 20 L. Flame stretch rates decreased with an increase in chamber volume due to a decrease in the ratio of the flame thickness (δ_f) to the flame radius (r_f) in the considered data range.

- Estimated flame stretch rates alone could not explain the sudden increase in the value of *LBV* at 20 L. A significant change in the slope of *dp/dt* indicated the onset of flow instabilities resulted in flame acceleration
- Stretch rates and the stretched *LBV* predicted by simulations did not change with an increase in chamber volume compared to experiments, and the possible reason could be δ_f / r_f became smaller even in the considered data range of the smallest chamber itself.
- It is recommended to use a spherical chamber having a volume in the range of 4.4 L to have lesser stretch effects will resulting in *LBV* with minimal stretch effects at elevated pressures and temperatures.

5.2 Effect of Non-Combustible Components (N_2 and CO_2) in PG on LBV and flame stability of PG-O_2 mixtures

In this first strategy, the composition of PG was considered as *Z*% CC+(100-*Z*)% NCC and it reacted with O_2, where *Z* was varied at 25, 35, and 45. It was referred to as the Inter-CC-NCC study. CC was considered (25CH_4:25CO:25H_2:25*Y*), where *Y* represented rich combustible species such as CH_4 or CO or H_2 and referred to as an intra-CC study. Hence, a fuel with more CH_4/CO/H_2 was called CH_4/CO/H_2-rich PG fuel. In the Intra-CC study, each fuel species varied between 25-and 50%. A similar approach was followed for NCC as *P*%CO_2+(100-*P*)%N_2, where *P* was varied from 0-100 (by volume) and referred to as Intra-NCC study. All experiments and simulations were performed at 1 bar, 300 K, and ϕ = 0.8. Notable findings are:

- From the analysis of 800 PG compositions, the combustible components, *i.e.*, CH_4+CO+H_2, varied around 20-50 vol%.
- Within the combustible components, CH_4, CO, and H_2 varied about 0-20%, 25-65%, and 25-65%, respectively.
- Within the non-combustible components, CO_2 and N_2 were narrowly dispersed around 25% and 75%, respectively.
- *LBV* estimated using the linear/non-linear extrapolation schemes and non-extrapolation mapping methods were close in magnitude for the studied PG-oxygen mixtures.

- *LBV* obtained from simulations based on GRI Mech 3.0 deviated from experimental values with an increase in X_{CC} and X_{N2}.
- L_b increased with an increase in X_{CC} for all reported PG mixtures. The values became negative when X_{CC} fell below 20% for hydrogen and carbon monoxide-rich mixtures.
- Methane-rich mixtures were stable ($L_b > 0$) under all studied conditions. In the present study, simulated values of L_b were lower than measured values.
- Volume-based model was strongly recommended to estimate effective Lewis numbers for the oxy-producer gas and similar mixtures.
- Producer gas mixtures having 25%CC and having higher mole fractions of CO/H_2 in CC and CO_2 in NCC were more susceptible to the preferential diffusion instability. An increase in either X_{CH4} or X_{N2} resulted in stable flames.
- Unstretched laminar burning velocity decreased with increased X_{CO2} (and reduction in X_{N2}) for all studied producer gas compositions. It was due to a reduction in the heating value of fuel, flame temperature, and participation of CO_2 in chemical reactions.
- At 25%CC+75%NCC, the *LBV* of CH_4-rich mixtures was higher for all combinations of NCC than H_2/CO-rich mixtures because of higher flame temperature. CO-rich mixtures had the lowest values of *LBV* at all mixture conditions owing to low flame temperature and thermal diffusivity.
- From the intra-NCC study, the non-linearity of the trend line increased either with an increase in X_{CO2} (reduction in X_{N2}) in all considered cases pointing out the involvement of CO_2 in the kinetics rather than being inert.
- From the inter-CC-NCC study, the changes in *LBV* values with variation in X_{CC} were linear in the cases where NCC had CO_2 less than 50%.

As a whole, a higher volume fraction of fuel/inert species in combustible/non-combustible components commands the combustion characteristics of PG. PG with high hydrogen, carbon monoxide, and nitrogen content with relatively lesser amounts of methane and carbon dioxide can lead to stable flames of better resilience with systematic deviation to fluctuations in composition. Combustion properties of intermediate compositions can be well estimated in mixtures with Non-combustible components variation, *i.e.*, CO_2:N_2 proportion ranging from 50:50 to 00:100. Nitrogen adds stability to the combustion for preferential diffusion effects.

5.3 Effect of Combustible Components (H_2, CO, and CH_4) and Initial pressure on LBV and instability of RPG-air mixtures

In this second strategy, Refined Producer Gas (producer gas without any inerts) reacting with air at 300±3 K, ϕ = 0.8-1.2, and 1, 2, and 4 bar was studied. The composition of RPG was considered as 50%*A*+*X*%*B*+(50-*X*)%*C* where *A*: $CH_4/H_2/CO$, *B*: $H_2/CO/CH_4$, *C*: $CO/CH_4/H_2$ and *X*: 00:50 in steps of 12.5% to understand the impact of change in the proportion of H_2:CO:CH_4 on *LBV* and flame stability. Important inferences are:

- The *LBV* of RPG-air mixtures followed a decreasing order with respect to the rich/higher mole fractions (50% vol) of H_2, followed by CO and CH_4 in the mixture due to the respective variation in the flame temperature and thermal & mass diffusivities
- The non-linear variation of *LBV* with equivalence ratio at any given RPG-air composition increased with an increase in the mole fraction of CH_4 in the mixture due to a shift in the peak *LBV* towards the stoichiometric condition. The simulated values obtained using GRI Mech 3.0 were consistently higher in magnitude than those obtained using FFCM-1 at all the conditions.
- From the burned gas Markstein length and effective Lewis number analysis, CO added resilience to the mixtures against thermo-diffusive instabilities while supported by CH_4 and opposed by H_2.
- The onset of hydrodynamic instability was strongly dependent on critical radius and flame thickness.
- From the exclusive susceptibility score/ranking system related to the onset of hydrodynamic instability, composition no.9 H_2:CO:CH_4 = 0:1:1 (0:4:4) has the highest resilience. The increase in the content of H_2 in the presence of CO favoured the onset of hydrodynamic instability, while in the presence of CH_4 favoured the onset of thermo-diffusive instability. CH_4 increment suppressed the susceptibility to hydrodynamic instability, while CO increment suppressed the thermo-diffusive instability.
- Lower values of *LBV* promoted thermo-diffusive effects, and the higher values resulted in earlier onset of hydrodynamic instability.

5.4 The overall contribution of the present work

- Development of a multi-functional test facility and robust post-processing algorithms.
- A detailed study on the variation in the composition of producer gas.
- Effect of absolute refinement, non-combustible components, combustible components, and initial pressure on laminar burning velocity & intrinsic instabilities.
- Comprehensive analysis of the burning velocity-instability susceptibility profile.

5.5 The application potential of the present work

- High fidelity data useful for optimizing chemical kinetic mechanisms & simulations.
- Development of refinement and mixing criteria for processing non-condensable gases from multiple sources to achieve a fuel composition Pareto-front. (Example:[134])
- It can be used to develop exclusive data-driven controllers for achieving consistent operation in applications such as burners, IC engines, Gas turbines/engines. etc.

5.6 Future scope of the present work

- Upgradation of test facility into a full-fledged double chamber test facility to achieve higher initial pressure conditions suitable for gaseous and liquid fuel mixtures.
- Study on the impact of chamber cavities & geometry on combustion characteristics.
- Estimation of intrinsic instabilities from the pressure/deflagration characteristics.
- Development of gas refinement system for reducing the inerts in producer gas.
- Development of porous radiant burner for burning producer gas in atmospheric air.

References

[1] Abe N, Furuhata T, Kitagawa K, Katagiri H. Measurement of Burning Velocity of Diluted and Preheated CH4/CO/H2 Mixture. 1st Int. Energy Convers. Eng. Conf., 2003. https://doi.org/10.2514/6.2003-5924.

[2] Park J, Lee MC. Combustion instability characteristics of H2/CO/CH4 syngases and synthetic natural gases in a partially-premixed gas turbine combustor: Part 1 - Frequency and mode analysis. Int J Hydrogen Energy 2016;41:7484–93. https://doi.org/10.1016/j.ijhydene.2016.02.047.

[3] Lee IB, Woo IS, Lee MC. Effects of nitrogen dilution on the NOx and CO emission of H2/CO/CH4 syngases in a partially-premixed gas turbine model combustor. Int J Hydrogen Energy 2016;41:15841–51. https://doi.org/10.1016/j.ijhydene.2016.04.131.

[4] Lee MC, Yoon J, Joo S, Kim J, Hwang J, Yoon Y. Investigation into the cause of high multi-mode combustion instability of H2/CO/CH4 syngas in a partially premixed gas turbine model combustor. Proc Combust Inst 2015;35:3263–71. https://doi.org/10.1016/j.proci.2014.07.013.

[5] Joo S, Yoon J, Kim J, Lee M, Yoon Y. NOx emissions characteristics of the partially premixed combustion of H2/CO/CH4 syngas using artificial neural networks. Appl Therm Eng 2015;80:436–44. https://doi.org/10.1016/j.applthermaleng.2015.01.057.

[6] Choi M, Park Y, Li X, Sung Y, Park S, Moon K, et al. Study on flame structures and emission characteristics according to various swirl combinations and fuel compositions in a CH4/H2/CO syngas swirl-stabilized combustor. Fuel 2019;253:887–903. https://doi.org/10.1016/j.fuel.2019.05.049.

[7] Barbato PS, Landi G, Russo G. Catalytic combustion of CH4-H2-CO mixtures at pressure up to 10 bar. Fuel Process Technol 2013;107:147–54. https://doi.org/10.1016/j.fuproc.2012.08.024.

[8] Liu C, Song H, Zhang P, Wang Z, Wooldridge MS, He X, et al. A rapid

compression machine study of autoignition, spark-ignition and flame propagation characteristics of H2/CH4/CO/air mixtures. Combust Flame 2018;188:150–61. https://doi.org/10.1016/j.combustflame.2017.09.031.

[9] Morovatiyan M, Shahsavan M, Baghirzade M, Mack JH. Impact of Syngas Addition to Methane On Laminar Burning Velocity. J Eng Gas Turbines Power 2021;143:051004. https://doi.org/10.1115/1.4049012.

[10] Meng F, Ma Q, Wang H, Liu Y, Wang D. Effect of gasifying agents on sawdust gasification in a novel pilot scale bubbling fluidized bed system 2019;249:112–8. https://doi.org/10.1016/j.fuel.2019.03.107.

[11] Raveendran K, Ganesh A. Heating value of biomass and biomass pyrolysis products. Fuel 1996;75:1715–20. https://doi.org/10.1016/S0016-2361(96)00158-5.

[12] Jie X, Chau J, Obuskovic G, Sirkar KK. Preliminary studies of CO2 removal from precombustion syngas through pressure swing membrane absorption process with ionic liquid as absorbent. Ind Eng Chem Res 2013;52:8783–99. https://doi.org/10.1021/ie302122s.

[13] Rufford TE, Smart S, Watson GCY, Graham BF, Boxall J, Diniz da Costa JC, et al. The removal of CO2 and N2 from natural gas: A review of conventional and emerging process technologies. J Pet Sci Eng 2012;94–95:123–54. https://doi.org/10.1016/j.petrol.2012.06.016.

[14] Yan B, Wu Y, Liu C, Yu JF, Li B, Li ZS, et al. Experimental and modeling study of laminar burning velocity of biomass derived gases/air mixtures. Int J Hydrogen Energy 2011;36:3769–77. https://doi.org/10.1016/j.ijhydene.2010.12.015.

[15] Vu TM, Park J, Kwon OB, Kim JS. Effects of hydrocarbon addition on cellular instabilities in expanding syngas-air spherical premixed flames. Int J Hydrogen Energy 2009;34:6961–9. https://doi.org/10.1016/j.ijhydene.2009.06.067.

[16] Yaliwal VS, Banapurmath NR, Hosmath RS, Khandal S V., Budzianowski WM. Utilization of hydrogen in low calorific value producer gas derived from municipal

solid waste and biodiesel for diesel engine power generation application. Renew Energy 2016;99:1253–61. https://doi.org/10.1016/j.renene.2016.08.002.

[17] Przybyla G, Szlek A, Haggith D, Sobiesiak A. Fuelling of spark ignition and homogenous charge compression ignition engines with low calorific value producer gas. Energy 2016;116:1464–78. https://doi.org/10.1016/j.energy.2016.06.036.

[18] Augustine MA, Sekhar SJ. Improvement in the Calorific Value of Producer Gas from Rice Husk with Addition of Spent Tea Waste as Secondary Fuel. Energy & Fuels 2019;33:12492–8. https://doi.org/10.1021/acs.energyfuels.9b03052.

[19] Sridhar G. Experimental and modeling aspects of producer gas engine. 2008 IEEE Int. Conf. Sustain. Energy Technol., 2008, p. 995–1000. https://doi.org/10.1109/ICSET.2008.4747152.

[20] Sridhar G, Paul PJ, Mukunda HS. Zero-dimensional modelling of a producer gas-based reciprocating engine. Proc Inst Mech Eng Part A J Power Energy 2006;220:923–31. https://doi.org/10.1243/09576509JPE265.

[21] Sridhar G, Paul PJ, Mukunda HS. Computational studies of the laminar burning velocity of a producer gas and air mixture under typical engine conditions. Proc Inst Mech Eng Part A J Power Energy 2005;219:195–201. https://doi.org/10.1243/095765005X6917.

[22] Sridhar G, Paul PJ, Mukunda HS. Biomass derived producer gas as a reciprocating engine fuel—an experimental analysis. Biomass and Bioenergy 2001;21:61–72. https://doi.org/https://doi.org/10.1016/S0961-9534(01)00014-9.

[23] Sridhar G, Paul PJ, Mukunda HS. Experiments and Modelling of Producer Gas Based Reciprocating Engines. ASME 2002 Intern Combust Engine Div Fall Tech Conf 2002:377–87. https://doi.org/10.1115/ICEF2002-520.

[24] Sridhar G, Sridhar H V, Dasappa S, Paul PJ, Rajan NKS, Mukunda HS. Development of producer gas engines. Proc Inst Mech Eng Part D J Automob Eng 2005;219:423–38. https://doi.org/10.1243/095440705X6596.

[25] Carpentieri M, Corti A, Lombardi L. Life cycle assessment (LCA) of an integrated biomass gasification combined cycle (IBGCC) with CO2 removal. Energy Convers Manag 2005;46:1790–808. https://doi.org/10.1016/j.enconman.2004.08.010.

[26] Hassanzadeh A, Abbasian J. Regenerable MgO-based sorbents for high-temperature CO2 removal from syngas: 1. Sorbent development, evaluation, and reaction modeling. Fuel 2010;89:1287–97. https://doi.org/10.1016/j.fuel.2009.11.017.

[27] Krishnan G, Steele D, O'Brien K, Callahan R, Berchtold K, Figueroa J. Simulation of a Process to Capture CO2 From IGCC Syngas Using a High Temperature PBI Membrane. Energy Procedia 2009;1:4079–88. https://doi.org/10.1016/j.egypro.2009.02.215.

[28] Lin H, He Z, Sun Z, Vu J, Ng A, Mohammed M, et al. CO2-selective membranes for hydrogen production and CO2 capture - Part I: Membrane development. J Memb Sci 2014;457:149–61. https://doi.org/10.1016/j.memsci.2014.01.020.

[29] Liu SL, Shao L, Chua ML, Lau CH, Wang H, Quan S. Recent progress in the design of advanced PEO-containing membranes for CO2 removal. Prog Polym Sci 2013;38:1089–120. https://doi.org/10.1016/j.progpolymsci.2013.02.002.

[30] Pröll T, Hofbauer H. H2 rich syngas by selective CO2 removal from biomass gasification in a dual fluidized bed system - Process modelling approach. Fuel Process Technol 2008;89:1207–17. https://doi.org/10.1016/j.fuproc.2008.05.020.

[31] Allegue LB, Hinge J. Biogas and bio-syngas upgrading. Danish Technol Inst 2012.

[32] Prathap C, Ray A, Ravi MR. Effects of dilution with carbon dioxide on the laminar burning velocity and flame stability of H2-CO mixtures at atmospheric condition. Combust Flame 2012;159:482–92. https://doi.org/10.1016/j.combustflame.2011.08.006.

[33] Egolfopoulos FN, Hansen N, Ju Y, Kohse-Höinghaus K, Law CK, Qi F. Advances and challenges in laminar flame experiments and implications for combustion

chemistry. Prog Energy Combust Sci 2014;43:36–67. https://doi.org/10.1016/j.pecs.2014.04.004.

[34] Goswami M, Griensven JGH Van, Bastiaans RJM. Experimental and modeling study of the effect of elevated pressure on lean high-hydrogen syngas flames. Proc Combust Inst 2015;35:655–62. https://doi.org/10.1016/j.proci.2014.05.057.

[35] Natarajan J, Kochar Y, Lieuwen T, Seitzman J. Pressure and preheat dependence of laminar flame speeds of H2/CO/CO2/O2/He mixtures. Proc Combust Inst 2009;32:1261–8. https://doi.org/10.1016/j.proci.2008.06.110.

[36] Kuznetsov M, Redlinger R, Breitung W, Grune J, Friedrich A, Ichikawa N. Laminar burning velocities of hydrogen-oxygen-steam mixtures at elevated temperatures and pressures. Proc Combust Inst 2011;33:895–903. https://doi.org/10.1016/j.proci.2010.06.050.

[37] Tse SD, Zhu D, Law CK. Optically accessible high-pressure combustion apparatus. Rev Sci Instrum 2004;233. https://doi.org/10.1063/1.1634358.

[38] Tse SD, Zhu DL, Law CK. Morphology and burning rates of expanding spherical flames in H 2/O2/inert mixtures up to 60 Atmospheres. Proc Combust Inst 2000;28:1793–800. https://doi.org/10.1016/S0082-0784(00)80581-0.

[39] Qin X, Ju Y. Measurements of burning velocities of dimethyl ether and air premixed flames at elevated pressures. Proc Combust Inst 2005;30:233–40. https://doi.org/10.1016/j.proci.2004.08.251.

[40] Kelley AP, Smallbone AJ, Zhu DL, Law CK. Experimental measurement of n-pentane flame speeds at elevated pressures and temperatures. Proc. 6th US Natl. Combust. Meet., 2009.

[41] Liu CC, Shy SS, Chen HC, Peng MW. On interaction of centrally-ignited , outwardly-propagating premixed flames with fully- developed isotropic turbulence at elevated pressure. Proc Combust Inst 2011;33:1293–9. https://doi.org/10.1016/j.proci.2010.06.083.

[42] Chaudhuri S, Wu F, Zhu D, Law CK. Flame Speed and Self-Similar Propagation

of Expanding Turbulent Premixed Flames. Phys Rev Lett 2012;108:044503(5). https://doi.org/10.1103/PhysRevLett.108.044503.

[43] Santner J, Dryer FL, Ju Y. The effects of water dilution on hydrogen , syngas , and ethylene flames at elevated pressure. Proc Combust Inst 2013;34:719–26. https://doi.org/10.1016/j.proci.2012.06.065.

[44] Nassouri M, Chauveau C, Halter F, Gökalp I. Flame structure of ethanol-air premixed mixtures at high pressures in microgravity 2013:1–6.

[45] Ai Y, Zhou Z, Chen Z, Kong W. Supplementary Material Laminar flame speed and Markstein length of syngas at normal and elevated pressures and temperatures n.d.:1–9.

[46] Of C, Instabilities C, Flame OFA, In P, Aerosol AN. GT2015-44022 2017:1–11.

[47] Jiang LJ, Shy SS, Li WY, Huang HM, Nguyen MT. High-temperature , high-pressure burning velocities of expanding turbulent premixed flames and their comparison with Bunsen-type flames 2016;172:173–82. https://doi.org/10.1016/j.combustflame.2016.07.021.

[48] Razus D, Brinzea V, Mitu M, Movileanu C, Oancea D. Burning velocity of propane-air mixtures from pressure-time records during explosions in a closed spherical vessel. Energy and Fuels 2012;26:901–9. https://doi.org/10.1021/ef201561r.

[49] Keshava Murthy T.V. Combustion Characteristics of Multicomponent Fuel-Air Mixtures 2005:347.

[50] Omari A, Tartakovsky L. Measurement of the laminar burning velocityusing the confined and unconfined spherical flame methods - A comparative analysis. Combust Flame 2016;168:127–37. https://doi.org/10.1016/j.combustflame.2016.03.012.

[51] Xiouris C, Ye T, Jayachandran J, Egolfopoulos FN. Laminar flame speeds under engine-relevant conditions: Uncertainty quantification and minimization in spherically expanding flame experiments. Combust Flame 2016;163:270–83.

https://doi.org/10.1016/j.combustflame.2015.10.003.

[52] Bradley D, Haq MZ, Hicks RA, Kitagawa T, Lawes M, Sheppard CGW, et al. Turbulent burning velocity, burned gas distribution, and associated flame surface definition. Combust Flame 2003;133:415–30. https://doi.org/10.1016/S0010-2180(03)00039-7.

[53] Prathap C, Ray A, Ravi MR. Effects of dilution with carbon dioxide on the laminar burning velocity and flame stability of H2-CO mixtures at atmospheric condition. Combust Flame 2012;159:482–92. https://doi.org/10.1016/j.combustflame.2011.08.006.

[54] Konnov AA, Mohammad A, Kishore VR, Kim N Il, Prathap C, Kumar S. A comprehensive review of measurements and data analysis of laminar burning velocities for various fuel+air mixtures. Prog Energy Combust Sci 2018;68:197–267. https://doi.org/10.1016/j.pecs.2018.05.003.

[55] Natarajan J, Lieuwen T, Seitzman J. Laminar flame speeds of H2/CO mixtures: Effect of CO2 dilution, preheat temperature, and pressure. Combust Flame 2007;151:104–19. https://doi.org/10.1016/j.combustflame.2007.05.003.

[56] Burbano HJ, Pareja J, Amell AA. Laminar burning velocities and flame stability analysis of H2/CO/air mixtures with dilution of N2 and CO2. Int J Hydrogen Energy 2011;36:3232–42. https://doi.org/10.1016/j.ijhydene.2010.11.089.

[57] Brown MJ, McLean IC, Smith DB, Taylor SC. Markstein lengths of CO/H2/air flames, using expanding spherical flames. Symp Combust 1996;26:875–81. https://doi.org/10.1016/S0082-0784(96)80297-9.

[58] Prathap C, Ray A, Ravi MR. Effects of dilution with carbon dioxide on the laminar burning velocity and flame stability of H2-CO mixtures at atmospheric condition. Combust Flame 2012;159:482–92. https://doi.org/10.1016/j.combustflame.2011.08.006.

[59] Bouvet N, Chauveau C, Gökalp I, Halter F. Experimental studies of the fundamental flame speeds of syngas (H2/CO)/air mixtures. Proc Combust Inst

2011;33:913–20. https://doi.org/10.1016/j.proci.2010.05.088.

[60] Hassan MI, Aung KT, Faeth GM. Properties of Laminar Premixed CO/H2/Air Flames at Various Pressures 1997;13:239–45.

[61] Zainal ZA, Ali R, Lean CH, Seetharamu KN. Prediction of performance of a downdraft gasifier using equilibrium modeling for different biomass materials. Energy Convers Manag 2001;42:1499–515. https://doi.org/10.1016/S0196-8904(00)00078-9.

[62] Uma R, Kandpal TC, Kishore VVN. Emission characteristics of an electricity generation system in diesel alone and dual fuel modes. Biomass and Bioenergy 2004;27:195–203. https://doi.org/10.1016/j.biombioe.2004.01.003.

[63] Zhang R, Cummer K, Suby A, Brown RC. Biomass-derived hydrogen from an air-blown gasifier. Fuel Process Technol 2005;86:861–74. https://doi.org/10.1016/j.fuproc.2004.09.001.

[64] Singh RN, Jena U, Patel JB, Sharma AM. Feasibility study of cashew nut shells as an open core gasifier feedstock. Renew Energy 2006;31:481–7. https://doi.org/10.1016/j.renene.2005.04.010.

[65] Vyas DK, Singh RN. Feasibility study of Jatropha seed husk as an open core gasifier feedstock. Renew Energy 2007;32:512–7. https://doi.org/10.1016/j.renene.2006.06.006.

[66] Skoulou V, Koufodimos G, Samaras Z, Zabaniotou A. Low temperature gasification of olive kernels in a 5-kW fluidized bed reactor for H2-rich producer gas. Int J Hydrogen Energy 2008;33:6515–24. https://doi.org/10.1016/j.ijhydene.2008.07.074.

[67] Mohon Roy M, Tomita E, Kawahara N, Harada Y, Sakane A. Performance and emission comparison of a supercharged dual-fuel engine fueled by producer gases with varying hydrogen content. Int J Hydrogen Energy 2009;34:7811–22. https://doi.org/10.1016/j.ijhydene.2009.07.056.

[68] Alauddin ZABZ, Lahijani P, Mohammadi M, Mohamed AR. Gasification of

lignocellulosic biomass in fluidized beds for renewable energy development: A review. Renew Sustain Energy Rev 2010;14:2852–62. https://doi.org/10.1016/j.rser.2010.07.026.

[69] Tippayawong N, Chaichana C, Promwangkwa A, Rerkkriangkrai P. Gasification of cashew nut shells for thermal application in local food processing factory. Energy Sustain Dev 2011;15:69–72. https://doi.org/10.1016/j.esd.2010.10.001.

[70] Street J, Yu F, Wooten J, Columbus E, White MG, Warnock J. Gasoline-range hydrocarbon production using biomass derived synthesis gas over Mo/H +ZSM-5. Fuel 2012;96:239–49. https://doi.org/10.1016/j.fuel.2011.12.036.

[71] Szwaja S, Kovacs VB, Bereczky A, Penninger A. Sewage sludge producer gas enriched with methane as a fuel to a spark ignited engine. Fuel Process Technol 2013;110:160–6. https://doi.org/10.1016/j.fuproc.2012.12.008.

[72] Vera D, Jurado F, Margaritis NK, Grammelis P. Experimental and economic study of a gasification plant fuelled with olive industry wastes. Energy Sustain Dev 2014;23:247–57. https://doi.org/10.1016/j.esd.2014.09.011.

[73] Simanjuntak JP, Zainal ZA. Experimental study and characterization of a two-compartment cylindrical internally circulating fluidized bed gasifier. Biomass and Bioenergy 2015;77:147–54. https://doi.org/10.1016/j.biombioe.2015.03.023.

[74] Warsita A, Al-attab KA, Zainal ZA. Effect of water addition in a microwave assisted thermal cracking of biomass tar models. Appl Therm Eng 2017;113:722–30. https://doi.org/10.1016/j.applthermaleng.2016.11.076.

[75] Wang Y, Pang S. Investigation of hydrogen sulphide removal from simulated producer gas of biomass gasification by titanomagnetite. Biomass and Bioenergy 2018;109:61–70. https://doi.org/10.1016/j.biombioe.2017.12.021.

[76] Piemsinlapakunchon T, Paul MC. Effects of fuel compositions on the heat generation and emission of syngas/producer gas laminar diffusion flame. Int J Hydrogen Energy 2019;44:18505–16. https://doi.org/10.1016/j.ijhydene.2019.05.178.

[77] Vu TM, Park J, Kwon OB, Kim JS. Effects of hydrocarbon addition on cellular instabilities in expanding syngas-air spherical premixed flames. Int J Hydrogen Energy 2009;34:6961–9. https://doi.org/10.1016/j.ijhydene.2009.06.067.

[78] He Y, Wang Z, Weng W, Zhu Y, Zhou J, Cen K. Effects of CO content on laminar burning velocity of typical syngas by heat flux method and kinetic modeling. Int J Hydrogen Energy 2014;39:9534–44. https://doi.org/10.1016/j.ijhydene.2014.03.216.

[79] Lapalme D, Seers P. Influence of CO2, CH4, and initial temperature on H2/CO laminar flame speed. Int J Hydrogen Energy 2014;39:3477–86. https://doi.org/10.1016/j.ijhydene.2013.12.109.

[80] Kolekar HD, Varghese RJ, Kumar S. Laminar Burning Velocities of Typical Syngas-air Mixtures at Elevated Temperatures. Proc 44th Natl Conf Fluid Mech Fluid Power 2017;2.

[81] Varghese RJ, Kumar S. Machine learning model to predict the laminar burning velocities of H2/CO/CH4/CO2/N2/air mixtures at high pressure and temperature conditions. Int J Hydrogen Energy 2020;45:3216–32. https://doi.org/10.1016/j.ijhydene.2019.11.134.

[82] Zhou Q, Cheung CS, Leung CW, Li X, Huang Z. Effects of diluents on laminar burning characteristics of bio-syngas at elevated pressure. Fuel 2019;248:8–15. https://doi.org/10.1016/j.fuel.2019.03.062.

[83] Li J, Zhao Z, Kazakov A, Chaos M, Dryer FL, Scire JJ. A comprehensive kinetic mechanism for CO, CH2O, and CH3OH combustion. Int J Chem Kinet 2007;39:109–36. https://doi.org/10.1002/kin.20218.

[84] Lapalme D, Halter F, Mounaïm-Rousselle C, Seers P. Characterization of thermodiffusive and hydrodynamic mechanisms on the cellular instability of syngas fuel blended with CH4 or CO2. Combust Flame 2018;193:481–90. https://doi.org/10.1016/j.combustflame.2018.03.028.

[85] Oliveira GP, Sbampato ME, Martins CA, Santos LR, Barreta LG, Boschi

Gonçalves RF. Experimental laminar burning velocity of syngas from fixed-bed downdraft biomass gasifiers. Renew Energy 2020;153:1251–60. https://doi.org/10.1016/j.renene.2020.02.083.

[86] Cheng TS, Chang Y-C, Chao Y-C, Chen G-B, Li Y-H, Wu C-Y. An experimental and numerical study on characteristics of laminar premixed H2/CO/CH4/air flames. Int J Hydrogen Energy 2011;36:13207–17. https://doi.org/10.1016/j.ijhydene.2011.07.077.

[87] Cheng TS, Chang YC, Chao YC, Chen GB, Li YH, Wu CY. Characteristics of Laminar Premixed H2/CO/CH4/Air Opposed-jet Flames. 23rd Int. Colloq. Dyn. Explos. React. Syst., Irvine, USA: 2011.

[88] Xie Y, Wang X, Bi H, Yuan Y, Wang J, Huang Z, et al. A comprehensive review on laminar spherically premixed flame propagation of syngas. Fuel Process Technol 2018;181:97–114. https://doi.org/10.1016/j.fuproc.2018.09.016.

[89] Zhou Q, Cheung CS, Leung CW, Li X, Li X, Huang Z. Effects of fuel composition and initial pressure on laminar flame speed of H2/CO/CH4 bio-syngas. Fuel 2019;238:149–58. https://doi.org/10.1016/j.fuel.2018.10.106.

[90] Jomaas G, Law CK, Bechtold JK. On transition to cellularity in expanding spherical flames. J Fluid Mech 2007;583:1–26. https://doi.org/10.1017/S0022112007005885.

[91] Yang S, Saha A, Wu F, Law CK. Morphology and self-acceleration of expanding laminar flames with flame-front cellular instabilities. Combust Flame 2016;171:112–8. https://doi.org/10.1016/j.combustflame.2016.05.017.

[92] Li Y, Bi M, Zhang S, Jiang H, Gan B, Gao W. Dynamic couplings of hydrogen / air flame morphology and explosion pressure evolution in the spherical chamber. Int J Hydrogen Energy 2018;43:2503–13. https://doi.org/10.1016/j.ijhydene.2017.12.044.

[93] Kwon OC, Rozenchan G, Law CK. CELLULAR INSTABILITIES AND SELF-ACCELERATION OF OUTWARDLY PROPAGATING SPHERICAL

FLAMES 2002;29:1775–83.

[94] Kim HJ, Van K, Lee DK, Yoo CS, Park J, Chung SH. Laminar flame speed , Markstein length , and cellular instability for spherically propagating methane / ethylene – air premixed flames. Combust Flame 2020;214:464–74. https://doi.org/10.1016/j.combustflame.2020.01.011.

[95] Kim W, Endo T, Mogi T, Kuwana K, Dobashi R. Wrinkling of Large-Scale Flame in Lean Propane – Air Mixture Due to Cellular Instabilities. Combust Sci Technol 2019;191:491–503. https://doi.org/10.1080/00102202.2018.1502757.

[96] Kim W, Sato Y, Johzaki T, Endo T, Shimokuri D, Miyoshi A. Experimental study on self-acceleration in expanding spherical hydrogen-air flames. Int J Hydrogen Energy 2018;43:12556–64. https://doi.org/10.1016/j.ijhydene.2018.04.153.

[97] Kim W, Imamura T, Mogi T, Dobashi R. Experimental investigation on the onset of cellular instabilities and acceleration of expanding spherical flames. Int J Hydrogen Energy 2017;42:14821–8. https://doi.org/10.1016/j.ijhydene.2017.04.068.

[98] Hu Z, Wang Y, Zhang J, Hou X. Experimental study on self-acceleration characteristics of unstable flame of low calorific value gas blended with hydrogen. Int J Hydrogen Energy 2019;44:25248–56. https://doi.org/10.1016/j.ijhydene.2019.03.141.

[99] Cai X, Wang J, Bian Z, Zhao H, Dai H, Huang Z. On transition to self-similar acceleration of spherically expanding flames with cellular instabilities. Combust Flame 2020;215:364–75. https://doi.org/10.1016/j.combustflame.2020.02.001.

[100] Cai X, Wang J, Zhao H, Zhang M, Huang Z. Flame morphology and self-acceleration of syngas spherically expanding flames. Int J Hydrogen Energy 2018;43:17531–41. https://doi.org/10.1016/j.ijhydene.2018.07.140.

[101] Law CK, Jomaas G, Bechtold JK. Cellular instabilities of expanding hydrogen / propane spherical flames at elevated pressures : theory and experiment. Proc Combust Inst 2005;30:159–67. https://doi.org/10.1016/j.proci.2004.08.266.

[102] Chandrasekaran A, Ramachandran S, Subbiah S. Modeling, experimental validation and optimization of Prosopis juliflora fuelwood pyrolysis in fixed-bed tubular reactor. Bioresour Technol 2018;264:66–77. https://doi.org/10.1016/j.biortech.2018.05.013.

[103] Tippa M, Subbiah S, Prathap C. Impact of chamber volume on the measurement of laminar burning velocity using constant volume spherical fl ame method. Fuel 2019;256:115936. https://doi.org/10.1016/j.fuel.2019.115936.

[104] Luijten CCM, Doosje E, de Goey LPH. Accurate analytical models for fractional pressure rise in constant volume combustion. Int J Therm Sci 2009;48:1213–22. https://doi.org/10.1016/j.ijthermalsci.2008.12.020.

[105] Kelley AP, Bechtold JK, Law CK. Premixed flame propagation in a confining vessel with weak pressure rise. J Fluid Mech 2012;691:26–51. https://doi.org/10.1017/jfm.2011.439.

[106] Ansys Chemkin n.d. https://www.ansys.com/en-in/products/fluids/ansys-chemkin-pro.

[107] Cosilab 2011. https://www.rotexo.com/index.php/en/.

[108] Smith GP, Golden DM, Frenklach M, Moriarty NW, Eiteneer B, Goldenberg M, et al. GRI-Mech 3.0 n.d. http://www.me.berkeley.edu/gri_mech/.

[109] Aldushin AP, Matkowsky BJ, Volpert VA. Stoichiometric flames and their stability. Combust Flame 1995;101:15–25. https://doi.org/10.1016/0010-2180(94)00197-Z.

[110] Dinkelacker F, Manickam B, Muppala SPR. Modelling and simulation of lean premixed turbulent methane/hydrogen/air flames with an effective Lewis number approach. Combust Flame 2011;158:1742–9. https://doi.org/10.1016/j.combustflame.2010.12.003.

[111] Law CK, Jomaas G, Bechtold JK. Cellular instabilities of expanding hydrogen/propane spherical flames at elevated pressures: Theory and experiment. Proc Combust Inst 2005;30:159–67. https://doi.org/10.1016/j.proci.2004.08.266.

[112] Addabbo R, Bechtold JK, Matalon M. Wrinkling of spherically expanding flames. Proc Combust Inst 2002;29:1527–35. https://doi.org/10.1016/s1540-7489(02)80187-0.

[113] Lapalme D, Lemaire R, Seers P. Assessment of the method for calculating the Lewis number of H2/CO/CH4 mixtures and comparison with experimental results. Int J Hydrogen Energy 2017;42:8314–28. https://doi.org/10.1016/j.ijhydene.2017.01.099.

[114] Dandy D. Transport Property Calculator, Bioanalytical Microfluidics Program, Department of Chemical and Biological Engineering, Colorado State University n.d. http://navier.engr.colostate.edu/code/code-2/index.html.

[115] Clarke A. Calculation and consideration of the Lewis number for explosion studies. Process Saf Environ Prot Trans Inst Chem Eng Part B 2002;80:135–40. https://doi.org/10.1205/095758202317576238.

[116] Bradley D, Hicks RA, Lawes M, Sheppard CGW, Woolley R. The measurement of laminar burning velocities and Markstein numbers for iso-octane-air and iso-octane-n-heptane-air mixtures at elevated temperatures and pressures in an explosion bomb. Combust Flame 1998;115:126–44. https://doi.org/10.1016/S0010-2180(97)00349-0.

[117] Smith GP, Tao Y, Wang H. Foundational Fuel Chemistry Model Version 1.0 (FFCM-1) 2016.

[118] Hai W, Xiaoqing Y, Ameya VJ, Scott GD, Alexander L, Fokion E, et al. USC Mech Version II. High-Temperature Combustion Reaction Model of H2/CO/C1-C4 Compounds. n.d. http://ignis.usc.edu/USC_Mech_II.htm, May 2007.

[119] ANSYS Chemkin Theory Manual 17.0 (15151). 2015.

[120] Grcar JF. The twopnt program for boundary value problems: Version 3.10 of March 1992. United States: 1992.

[121] Taylor JR. An Introduction to Error Analysis : The study of uncertainties in physical measurements. 2nd ed. University Science Books, Sausalito, California;

1982.

[122] Prathap C, Ray A, Ravi MR. Investigation of nitrogen dilution effects on the laminar burning velocity and flame stability of syngas fuel at atmospheric condition. Combust Flame 2008;155:145–60. https://doi.org/10.1016/j.combustflame.2008.04.005.

[123] Van Den Bulck E. Closed algebraic expressions for the adiabatic limit value of the explosion constant in closed volume combustion. J Loss Prev Process Ind 2005;18:35–42. https://doi.org/10.1016/j.jlp.2004.10.004.

[124] Faghih M, Chen Z. The constant-volume propagating spherical flame method for laminar flame speed measurement. Sci Bull 2016;61:1296–310. https://doi.org/10.1007/s11434-016-1143-6.

[125] Xiouris C, Ye T, Jayachandran J, Egolfopoulos FN. Laminar flame speeds under engine-relevant conditions: Uncertainty quantification and minimization in spherically expanding flame experiments. Combust Flame 2016;163:270–83. https://doi.org/10.1016/j.combustflame.2015.10.003.

[126] Dahoe AE, Skjold T, Roekaerts DJEM, Pasman HJ, Eckhoff RK, Hanjalic K, et al. On the Application of the Levenberg – Marquardt Method in Conjunction with an Explicit Runge – Kutta and an Implicit Rosenbrock Method to Assess Burning Velocities from Confined Deflagrations. Flow, Turbul Combust 2013;91:281–317. https://doi.org/10.1007/s10494-013-9462-z.

[127] Hu E, Li X, Meng X, Chen Y, Cheng Y, Xie Y, et al. Laminar flame speeds and ignition delay times of methane-air mixtures at elevated temperatures and pressures. Fuel 2015;158:1–10. https://doi.org/10.1016/j.fuel.2015.05.010.

[128] Reyes M, Tinaut F V., Horrillo A, Lafuente A. Experimental characterization of burning velocities of premixed methane-air and hydrogen-air mixtures in a constant volume combustion bomb at moderate pressure and temperature. Appl Therm Eng 2018;130:684–97. https://doi.org/10.1016/j.applthermaleng.2017.10.165.

[129] Khan AR, Anbusaravanan S, Kalathi L, Velamati R, Prathap C. Investigation of dilution effect with N2/CO2 on laminar burning velocity of premixed methane/oxygen mixtures using freely expanding spherical flames. Fuel 2017;196:225–32. https://doi.org/10.1016/j.fuel.2017.01.086.

[130] Liu F, Guo H, Smallwood GJ. The chemical effect of CO2 replacement of N2 in air on the burning velocity of CH4 and H2 premixed flames. Combust Flame 2003;133:495–7. https://doi.org/10.1016/S0010-2180(03)00019-1.

[131] Khan AR, Ravi MR, Ray A. Experimental and chemical kinetic studies of the effect of H2 enrichment on the laminar burning velocity and flame stability of various multicomponent natural gas blends. Int J Hydrogen Energy 2019;44:1192–212. https://doi.org/10.1016/j.ijhydene.2018.10.207.

[132] Varghese RJ, Kolekar H, Kumar S. Demarcation of reaction effects on laminar burning velocities of diluted syngas–air mixtures at elevated temperatures. Int J Chem Kinet 2019;51:95–104. https://doi.org/https://doi.org/10.1002/kin.21232.

[133] Xie Y, Li Q. A review on mixing laws of laminar flame speed and their applications on H2/CH4/CO/air mixtures. Int J Hydrogen Energy 2020;45:20482–90. https://doi.org/10.1016/j.ijhydene.2019.10.136.

[134] vom Lehn F, Cai L, Copa Cáceres B, Pitsch H. Exploring the fuel structure dependence of laminar burning velocity: A machine learning based group contribution approach. Combust Flame 2021;232:111525. https://doi.org/10.1016/j.combustflame.2021.111525.

Appendix-1: Data on the composition of producer gas obtained from the literature

In the following table, all quantitative data on producer gas composition, feedstock, and data extraction methods were presented.

Sl.No	CO_2	N_2	CH_4	H_2	CO	Source	Data Extraction	Reference
1	14.44	na	4.19	5.84	15.77	Seed Corn	Absolute	[1]
2	19.85	na	3.06	17.83	6.73	Seed Corn	Absolute	[1]
3	26.8	na	3.27	28.13	2.13	Seed Corn	Absolute	[1]
4	26.4	na	3.27	26.6	2.66	Seed Corn	Absolute	[1]
5	25.8	na	3.27	25.13	2.7	Seed Corn	Absolute	[1]
6	16.69	na	3.89	7.74	13.27	Seed Corn	Absolute	[1]
7	20.71	na	3.19	19.85	8.38	Seed Corn	Absolute	[1]
8	27.4	na	2.97	27.78	2.58	Seed Corn	Absolute	[1]
9	27.8	na	2.94	28.48	1.14	Seed Corn	Absolute	[1]
10	27.82	na	2.95	28.3	1.21	Seed Corn	Absolute	[1]
11	27.72	na	2.94	28.14	1.38	Seed Corn	Absolute	[1]
12	16.69	na	3.89	7.74	13.27	Seed Corn	Absolute	[1]
13	23.14	na	3.05	21.61	5.42	Seed Corn	Absolute	[1]
14	21.6	na	3.17	20.47	7.22	Seed Corn	Absolute	[1]
15	20.7	na	3.19	19.85	8.38	Seed Corn	Absolute	[1]
16	19.3	na	3.24	18.52	10.21	Seed Corn	Absolute	[1]
17	27.63	na	2.94	29.97	1.02	Seed Corn	Absolute	[1]
18	27.54	na	2.95	28.78	1.22	Seed Corn	Absolute	[1]
19	27.56	na	2.94	28.48	1.39	Seed Corn	Absolute	[1]
20	27.58	na	2.95	27.65	2.03	Seed Corn	Absolute	[1]

21	16.3	na	4.04	6.53	14.18	Seed Corn	Absolute	[1]
22	20.9	na	3.17	20.5	8.04	Seed Corn	Absolute	[1]
23	28.83	na	2.97	36.11	0.4	Seed Corn	Absolute	[1]
24	28.63	na	2.97	29.68	0.43	Seed Corn	Absolute	[1]
25	28.72	na	2.97	29.13	0.49	Seed Corn	Absolute	[1]
26	16.3	na	4.04	6.53	14.18	Seed Corn	Absolute	[1]
27	20.9	na	3.17	20.5	8.04	Seed Corn	Absolute	[1]
28	28.5	na	2.97	29.68	0.2	Seed Corn	Absolute	[1]
29	28.45	na	2.97	29.6	0.31	Seed Corn	Absolute	[1]
30	28.51	na	2.98	29.56	0.37	Seed Corn	Absolute	[1]
31	28.3	na	2.98	29.44	0.46	Seed Corn	Absolute	[1]
32	17.01	na	3.81	8.81	13.23	Seed Corn	Absolute	[1]
33	20.85	na	3.13	23.86	7.99	Seed Corn	Absolute	[1]
34	20.41	na	3.34	23.53	9.01	Seed Corn	Absolute	[1]
35	19.38	na	3.51	22.8	10.33	Seed Corn	Absolute	[1]
36	17.37	na	3.44	21.07	12.63	Seed Corn	Absolute	[1]
37	27.2	na	3.05	27.83	0.19	Seed Corn	Absolute	[1]
38	27.04	na	3.05	28.1	0.16	Seed Corn	Absolute	[1]
39	26.9	na	3.05	27.75	0.2	Seed Corn	Absolute	[1]
40	26.7	na	3.05	27.51	0.4	Seed Corn	Absolute	[1]
41	6.2666	43.2408	0.9145	20.7936	28.8706	Unspecified Wood Chips	Digitized	[2]
42	8.9367	42.3037	1.0949	22.4834	25.2673	Unspecified Wood Chips	Digitized	[2]
43	11.5872	41.543	1.3144	24.1145	21.5855	Unspecified Wood Chips	Digitized	[2]
44	14.1789	41.1352	1.4947	25.3731	17.9234	Unspecified Wood Chips	Digitized	[2]
45	16.653	41.2567	1.675	26.2788	14.32	Unspecified Wood Chips	Digitized	[2]
46	na	na	0.79033	18.6904	23.9824	Municipal Waste	Digitized	[2]
47	na	na	0.92046	19.9905	21.3093	Municipal Waste	Digitized	[2]

48	na	na	1.05139	21.2015	18.5223	Municipal Waste	Digitized	[2]
49	na	na	1.18256	22.2244	15.6594	Municipal Waste	Digitized	[2]
50	na	na	0.74003	17.381	18.1409	Paddy Husk	Digitized	[2]
51	na	na	0.84125	18.3664	15.8264	Paddy Husk	Digitized	[2]
52	na	na	0.93114	19.1966	13.532	Paddy Husk	Digitized	[2]
53	na	na	1.01226	19.8087	11.2527	Paddy Husk	Digitized	[2]
54	na	na	1.05655	22.4283	27.7158	Paper	Digitized	[2]
55	na	na	1.24996	24.0655	24.156	Paper	Digitized	[2]
56	na	na	1.44044	25.5094	20.4766	Paper	Digitized	[2]
57	na	na	1.61143	26.6227	16.8271	Paper	Digitized	[2]
58	na	na	0.91102	20.73	28.8177	Unspecified Wood Chips	Digitized	[2]
59	na	na	1.09128	22.4607	25.2111	Unspecified Wood Chips	Digitized	[2]
60	na	na	1.28215	24.0232	21.582	Unspecified Wood Chips	Digitized	[2]
61	na	na	1.46295	25.3283	17.8794	Unspecified Wood Chips	Digitized	[2]
62	16.42	42.31	1.58	15.23	23.04	Unspecified Wood Chips	Digitized	[2]
63	9	50	3	17	20	Babul wood	Averaged	[3]
64	11	50	3	14	19	Unspecified Wood Chips	Averaged	[4]
65	23	57.5	2.5	11.5	23	Mixed Biomass	Averaged	[4]
66	15	45	5	15	20	Simulated Gas	Absolute	[5]
67	20.5	0	15.5	42.8	21.2	Simulated Gas	Absolute	[6]
68	19.1	0	14.4	47.6	18.9	Simulated Gas	Absolute	[7]
69	20	25	5	30	20	Simulated Gas	Absolute	[7]
70	10.3	36.8	4.6	16.7	16.5	Simulated Gas	Absolute	[7]
71	19.3	0	19.5	42.8	18.4	Simulated Gas	Absolute	[7]
72	9.8	0	13.3	45.4	31.5	Simulated Gas	Absolute	[7]
73	6.3	0	8.9	49.7	35.1	Simulated Gas	Absolute	[7]
74	na	51.471	1.864	14.083	14.049	Jatropha Seed Husk	Absolute	[8]

75	na	48.634	1.709	10.619	19.259	Jatropha Seed Husk	Absolute	[8]
76	10	47.5	3	18	19	Olive Wood Chips	Averaged	[9]
77	11.2	48	2.7	16.9	19.9	Olive Wood Chips	Absolute	[9]
78	10.7	47.9	2.5	16.1	21.6	Olive Wood Chips	Absolute	[9]
79	9	47.5	2	18	19	Unspecified Wood Chips	Averaged	[9]
80	10.1	48.4	3.1	14.9	21.5	Hazelnut Shells	Absolute	[9]
81	16.4	42.3	1.6	15.2	23	Unspecified Wood Chips	Absolute	[9]
82	12.8	45.9	2.5	16.3	21.3	pellets	Absolute	[9]
83	9.3	41.5	2.2	14.8	19.5	Olive Wood Chips	Absolute	[10]
84	12.6	46	2.5	17.2	21.2	Unspecified Sawdust Pellets	Absolute	[9]
85	9.5	47.5	2	18.5	19.5	Unspecified Wood Chips	Averaged	[11]
86	11.18	47.95	2.73	16.96	19.9	Olive Wood Chips	Absolute	[11]
87	5.11	51.27	3.43	16	22.83	Olive Pits	Absolute	[11]
88	10	55.1	1.9	14	19	Keekar Wood Chips	Absolute	[12]
89	11.81	na	2.02	8.47	22.78	Oil Palm Fronds	Absolute	[13]
90	12.8	na	2.03	10.53	24.94	Oil Palm Fronds	Absolute	[13]
91	13.51	na	2.6	13.5	23.8	Unspecified Wood Chips	Absolute	[13]
92	11	na	4	13	23	Hazelnut Shells	Absolute	[13]
93	9.9	na	2.6	11.9	25.7	Unspecified Wood Pellets	Absolute	[13]
94	6.5	na	2	10	18.5	Unspecified Wood Waste	Averaged	[13]
95	27.5	na	9	40	23.5	Cedar Wood	Averaged	[13]
96	10.5	na	1.65	3	23	Juniper Wood	Averaged	[13]
97	16.5	na	4	8	14	Rice Straw	Averaged	[13]
98	14.8	na	11.8	25.1	33.1	Unspecified Wood Pellets	Absolute	[13]
99	19.3	na	10.4	33.1	25.1	Almond Shells	Absolute	[13]
100	19.42	na	3.75	23.98	14.26	Olive Kernel	Absolute	[13]
101	28	na	15	40	25	Olive Kernel	Absolute	[13]

102	17.5	na	9.5	34	31	Pine Woodchips	Averaged	[13]
103	2.8	51	2	27	11	Simulated Gas	Absolute	[13]
104	16	46.5	1.5	16	20	Simulated Gas	Absolute	[14]
105	10	48	2	15	20	na	Absolute	[14]
106	13.3	6.3	6.3	20.8	13.3	na	Absolute	[14]
107	13	na	4	48	5	na	Absolute	[14]
108	2.8	51	2	27	11	Simulated Gas	Absolute	[14]
109	19	0	0	34	31	Simulated Gas	Absolute	[14]
110	12	3.2	0	29.1	28.6	Simulated Gas	Absolute	[14]
111	4.66	52.29	3.41	16.58	23.06	Olive Kernel	Absolute	[15]
112	5.27	51.91	10.72	12.14	19.96	Peach Kernel	Absolute	[15]
113	6.02	56.39	2.02	18.63	16.94	Grape Kernel	Absolute	[15]
114	19.72	55.02	3.15	5.04	17.07	Cashew Nut Shells	Absolute	[16]
115	9.4	46.5	1.8	18	24.3	Simulated Gas	Absolute	[17]
116	13	45.8	2.5	19.2	19.5	Simulated Gas	Absolute	[17]
117	17	45.4	3.6	19.9	14.2	Simulated Gas	Absolute	[17]
118	11.2	41.7	6.4	15.8	24.9	Simulated Gas	Absolute	[17]
119	16.2	40.9	7.4	17.4	18	Simulated Gas	Absolute	[17]
120	21.2	40.6	8.8	18.1	11.3	Simulated Gas	Absolute	[17]
121	15	53	3	13	16	Modified-Municipal Sewage Sludge	Absolute	[18]
122	9.3	59.51	1.49	12.1	17.6	Woody Biomass	Absolute	[19]
123	14.22	48.14	1.3	17.14	19.2	Eucalyptus Chips	Absolute	[20]
124	na	na	0.89	16.78	19.04	Eucalyptus Chips	Absolute	[20]
125	17.46	na	7.9	3.29	20.4	Unspecified Wood Powder	Absolute	[21]
126	18.3	na	3.49	4.9	14.7	Unspecified Wood Powder	Absolute	[21]
127	18.3325	na	7.1324	3.6465	19.1489	Unspecified Wood Powder	Digitized	[21]
128	18.2514	na	5.3274	4.5073	17.7526	Unspecified Wood Powder	Digitized	[21]

129	16.01	na	3.84	5.03	18.6	Unspecified Wood Powder	Absolute	[21]
130	18.01	na	3.22	7.1	22	Unspecified Wood Powder	Absolute	[21]
131	15.81	na	4.47	6	20.5	Unspecified Wood Powder	Absolute	[21]
132	13.56	41.32	6.85	11.33	16.91	Unspecified Wood	Absolute	[22]
133	14.88	40.16	7.42	10.46	16.26	Modified-Wood	Absolute	[22]
134	12.87	41.04	7.66	7.01	12.55	Modified-Wood	Absolute	[22]
135	10.3	48.8	2.37	14.62	22.2	Sludge+Softwood	Absolute	[23]
136	8.72	52.75	1.17	13.19	23.42	Sludge+Softwood	Absolute	[23]
137	9	48	2	15	20	Average of Unspecified Biomass	Absolute	[24]
138	10.8	43.6	9	17.1	19.2	Spruce+Pine Wood Pellets	Absolute	[24]
139	21	39.6	6.5	15.8	16.2	Spruce+Pine Wood Pellets	Absolute	[24]
140	12	26	2	40	20	Simulated Gas	Absolute	[25]
141	12	47	2	19	20	Simulated Gas	Absolute	[25]
142	12	46	2	19	20	Simulated Gas	Absolute	[25]
143	20	na	12	45	30	Unspecified Wood Chips	Absolute	[26]
144	12	46	2	19	19	Causurina Wood Chips	Absolute	[27]
145	na	59.5	0	3.7	29.65	Charcoal	Averaged	[28]
146	19.42	na	3.75	23.98	14.26	Olive Kernels	Absolute	[29]
147	42.48	na	6.73	26.68	22.79	Olive Kernels	Absolute	[29]
148	48	na	8.5	30	15	Olive Kernels	Absolute	[29]
149	19.7	na	1.8	7.6	7.5	Olive Kernels	Absolute	[29]
150	21.7	na	3	5.4	8.6	Olive Kernels	Absolute	[29]
151	19	na	1.9	9.3	8.4	Olive Kernels	Absolute	[29]
152	55.12	na	7.97	19.55	15.25	Olive Tree Cuttings	Absolute	[29]
153	5	na	17	12.5	9	Olive Kernels	Absolute	[29]
154	15.1486	54.3452	1.3082	12.578	16.62	Prosopis Juliflora Wood pieces	Absolute	[30]
155	15.4075	53.4592	0.8368	12.1035	18.193	Prosopis Juliflora Wood pieces	Absolute	[30]

156	13.3439	56.5952	1.0593	12.0239	18.037	Prosopis Juliflora Wood pieces	Absolute	[30]
157	18.93	55.63	1.51	12.03	11.9	Cashew Nut Shells	Absolute	[31]
158	16.53	54.75	2.25	11.27	15.2	Cashew Nut Shells	Absolute	[31]
159	18.41	50.71	1.7	12.67	16.51	Cashew Nut Shells	Absolute	[31]
160	18.13	52.61	4.96	2.45	20.64	Rubber Wood Sawdust	Absolute	[32]
161	19.28	47.43	5.8	2.68	23.41	Rubber Wood Sawdust	Absolute	[32]
162	22.48	38.11	8.2	3.13	25.8	Rubber Wood Sawdust	Absolute	[32]
163	21.49	43.6	5.82	3.11	23.98	Rubber Wood Sawdust	Absolute	[32]
164	30	na	na	16	10	na	Absolute	[32]
165	7.5	na	3.5	7.5	27	na	Absolute	[32]
166	12	na	2.45	14.6	25.71	na	Absolute	[32]
167	13.5	na	4.5	9.5	18	na	Absolute	[32]
168	13.75	na	2.5	19.5	17.5	na	Absolute	[32]
169	13.28	na	4.21	9.27	9.25	na	Absolute	[32]
170	18	na	3	7	16	na	Absolute	[32]
171	14.45	56.57	2.9	4	19.9	na	Absolute	[32]
172	19.42	na	3.75	23.98	14.26	na	Absolute	[32]
173	15.5	na	5	6.5	18.5	na	Averaged	[32]
174	18.5	na	6	11	15	na	Averaged	[32]
175	12.59	58.99	1.24	10	17.18	Garden Waste Pellets	Absolute	[33]
176	10.39	58.68	1.4	11.39	18.14	Unspecified Wood Blocks	Absolute	[33]
177	11.49	58.18	1.36	10.28	18.69	Garden Waste Pellets	Absolute	[33]
178	11.72	58.96	0.96	11.13	17.23	Garden Waste Pellets	Absolute	[33]
179	12.18	59.22	1.29	11.77	15.55	Garden Waste Pellets	Absolute	[33]
180	12.36	59.34	1.33	12.25	14.72	Garden Waste Pellets	Absolute	[33]
181	13.77	58.56	1.46	12.58	13.64	Garden Waste Pellets	Absolute	[33]
182	12	49.2	1.8	18	19	na	Absolute	[34]

183	na	na	2	20	19.5	na	Absolute	[34]
184	na	na	2	20	19.5	na	Absolute	[34]
185	na	na	0	21	24	na	Absolute	[34]
186	na	na	5.8	12	19	na	Absolute	[34]
187	na	na	2	20	24	na	Absolute	[34]
188	16.42	42.31	1.58	15.23	23.04	Unspecified Wood	Absolute	[35]
189	10.6	52.7	1.03	17	18.4	Municipal Waste	Absolute	[35]
190	12.06	50.79	2.31	14	20.14	Unspecified Sawdust Pellet	Absolute	[35]
191	15	3	2	32	48	na	Absolute	[35]
192	15	48	2	15	20	na	Absolute	[36]
193	20	0	0	40	40	na	Absolute	[36]
194	25	2	8	40	25	na	Absolute	[36]
195	20	2	8	32	38	na	Absolute	[36]
196	12	na	1.5	19	19	Multisource Averaged	Absolute	[36]
197	10	48	2	20	20	Simulated Gas	Absolute	[36]
198	12.8	49.7	2.03	10.53	24.94	Simulated Gas	Absolute	[37]
199	19.69	22.49	3.72	21.62	32.48	Simulated Gas	Absolute	[37]
200	36.6	6	3.1	30.4	23.9	na	Absolute	[38]
201	23.2	24.2	2.7	22.3	27.6	na	Absolute	[38]
202	16.8	45.3	1.9	13.7	22.3	na	Absolute	[38]
203	16	21.1	28.9	14.6	19.4	na	Absolute	[38]
204	16.8	45.3	1.9	13.7	22.3	Simulated Gas	Absolute	[38]
205	16.8	39	1.9	20	22.3	Simulated Gas	Absolute	[38]
206	2.2	5.6	29.5	56.8	5.9	Simulated Gas(Coke Oven Gas)	Absolute	[38]
207	5	na	4	17	17	Olive Oil Processing Waste	Absolute	[39]
208	5	na	10	13	20	Grape Processing Waste	Absolute	[39]
209	6	na	2	18	16	Peach Processing Waste	Absolute	[39]

210	16.8	51.2	7.5	5.2	19.3	Simulated Gas	Absolute	[40]
211	9	46.1	0.9	23	21	Fuel Wood Pieces	Absolute	[41]
212	na	50	3	17	20	Multisource Averaged	Averaged	[42]
213	4.08	40.12	0	18.67	35.23	Charcoal	Absolute	[43]
214	3.94	57.44	0	8.5	30.12	Charcoal	Absolute	[43]
215	6.13	52.41	0	12.46	27.55	Charcoal	Absolute	[43]
216	4.17	49.34	0	9.42	36.48	Charcoal	Absolute	[43]
217	4.01	51.12	0	11.64	31.75	Charcoal	Absolute	[43]
218	3.04	53.79	0	8.56	34.04	Charcoal	Absolute	[43]
219	5.52	52.65	0	10.27	31.56	Charcoal	Absolute	[43]
220	4.55	52.07	0	11.41	29.76	Charcoal	Absolute	[43]
221	1.79	57.97	0	7.2	31.79	Charcoal	Absolute	[43]
222	10.27	62.58	3.36	9.62	11.55	Unspecified Wood Chips	Absolute	[44]
223	na	na	3.5	22.5	27.5	Multisource Averaged	Averaged	[45]
224	5.4	57.5	2.1	10.3	24.7	Simulated Gas	Absolute	[45]
225	5.2	57.8	2	10.1	24.9	Simulated Gas	Absolute	[45]
226	20	30	3	30	17	na	Absolute	[45]
227	15	53	3	13	16	Sewage Sludge	Absolute	[45]
228	4.6	55.1	4.2	24.1	10.7	Olive Tree Seeds	Absolute	[45]
229	15	34	1	30	20	Simulated Gas	Absolute	[45]
230	5.98	59.55	0.98	14.03	19.46	Pongamia Shell Pellets-Small	Absolute	[46]
231	13.53	58.68	1.61	13.42	12.76	Pongamia Shell Pellets-Big	Absolute	[45]
232	11.46	55.55	1.04	14.95	17.03	Unspecified Wood Chips	Absolute	[45]
233	15.5	57.5	3	9.5	13.5	na	Averaged	[47]
234	27	0	5	32	33.5	na	Averaged	[47]
235	14.5	0	8.5	37	37.5	na	Averaged	[47]
236	17.5	0	2.5	48	19	na	Averaged	[47]

237	14.2	57.8	1.8	13	13.2	Casuarina Wood Chips+Coconut Shells	Absolute	[47]
238	12.05	na	1.95	5.75	12.3	Eucalyptus Chips+Wood Char Particles	Averaged	[48]
239	9.2	na	3.05	12.1	25.9	Eucalyptus Chips+Wood Char Particles	Averaged	[48]
240	14.45	na	3.45	12.85	16.15	na	Averaged	[48]
241	5.1	na	0	13.8	35.9	na	Averaged	[48]
242	14.1	na	2.65	12	16.35	Unspecified Wood Pellets Chars	Averaged	[48]
243	11.9	45.9	1.5	19.7	21	Bamboo	Absolute	[49]
244	10.8	49.8	1.4	17.6	20.4	Rubber Wood Sawdust	Absolute	[49]
245	12.6	42.7	2.2	21.7	20.8	Unspecified Wood Pellets	Absolute	[49]
246	13.1	42.5	2	19.8	22.6	Rice Husk	Absolute	[49]
247	12	57.7	0.4	12.5	16.5	Marabou	Absolute	[50]
248	19	na	4.32	7.07	26.97	Japanese Poplar Woodchips	Absolute	[51]
249	15.84	na	3.43	4.64	18.9	Japanese Poplar Woodchips	Absolute	[51]
250	23.39	na	4.66	6.76	28.9	Japanese Poplar Woodchips	Absolute	[51]
251	21.22	na	4.63	5.96	26.53	Japanese Poplar Woodchips	Absolute	[51]
252	22.34	na	4.69	6.62	28.62	Japanese Poplar Woodchips	Absolute	[51]
253	13	55	2	15	15	Simulated Gas	Absolute	[52]
254	12.41	50.9	5	15.74	15.95	na	Absolute	[52]
255	11	45.75	1.75	17.5	20.5	Multisource Averaged	Averaged	[53]
256	11.1	42.6	1.9	18.5	18.5	Simulated Gas	Absolute	[53]
257	14.66	43.62	2.02	14.05	24.04	Unspecified Wood Chips	Absolute	[54]
258	10.7	61.9	2.3	9.2	12.4	Olive pits	Absolute	[54]
259	10.6	52.7	1.3	17	18.4	Rubber Wood	Absolute	[54]
260	9.52	53.33	2.18	13.13	20.66	Hazelnut Shells	Absolute	[54]
261	13.3	44.2	3.1	17.5	21.3	Unspecified Sawdust Pellets	Absolute	[54]
262	14.7	52.3	5.4	10.75	16.85	Unspecified Wood Pellets	Absolute	[54]
263	16.7	48.7	4.8	15.85	13.95	Unspecified Wood Pellets	Absolute	[54]

264	14.66	43.62	2.02	14.05	24.04	na	Absolute	[54]
265	10.7	61.9	2.3	9.2	12.4	na	Absolute	[54]
266	10.6	52.7	1.3	17	18.4	na	Absolute	[54]
267	9.52	53.33	2.18	13.13	20.66	na	Absolute	[54]
268	13.3	44.2	3.1	17.5	21.3	na	Absolute	[54]
269	14.7	52.3	5.4	10.75	16.85	na	Absolute	[54]
270	16.7	48.7	4.8	15.85	13.95	na	Absolute	[54]
271	7.94	46.12	0.21	21.81	23.91	Olive pits	Absolute	[54]
272	8.35	45.45	0.19	21.03	24.98	Wood bark (Averaged)	Absolute	[54]
273	8.28	45.47	0.18	20.29	25.79	Hazelnut Shells	Absolute	[54]
274	8.41	45.31	0.2	21.3	24.79	Spruce Wood	Absolute	[54]
275	8.59	43.6	0.21	21.97	25.64	Fir mill	Absolute	[54]
276	8.75	45.27	0.19	21.16	24.63	Softwood (Averaged)	Absolute	[54]
277	9.17	43.52	0.2	21.53	25.59	Coconut Shells	Absolute	[54]
278	8.88	45.04	0.21	21.94	23.93	Pist. Shells	Absolute	[54]
279	9.18	46.44	0.19	20.76	23.44	Hybrid Poplar	Absolute	[54]
280	9.28	45.24	0.17	20.06	25.25	Hazelnut Seedcoat	Absolute	[54]
281	9.22	45.06	0.2	21.19	24.33	Willow Wood	Absolute	[54]
282	9.35	44.19	0.19	21.14	25.12	Akhrot Shells	Absolute	[54]
283	9.58	46.92	0.18	20.4	22.92	Almond Shells	Absolute	[54]
284	9.79	43.49	0.19	21.04	25.49	Corn Cobs	Absolute	[54]
285	9.6	45.15	0.21	21.91	23.14	Bamboo Wood	Absolute	[54]
286	9.92	45.44	0.19	20.95	23.5	Sugarcane Bagasse	Absolute	[54]
287	9.75	46.01	0.19	21.26	22.78	Hardwood (Averaged)	Absolute	[54]
288	10.31	49.26	0.15	18.64	21.65	Groudnut Shells	Absolute	[54]
289	9.7	44.92	0.21	21.91	23.26	Casurina Wood	Absolute	[54]
290	9.83	44.86	0.21	21.97	23.14	Neem Wood	Absolute	[54]

291	9.88	47.34	0.18	20.33	22.28	Olive Husk	Absolute	[54]
292	10.02	43.64	0.21	21.87	24.26	Dry Subabul Wood	Absolute	[54]
293	9.83	45.44	0.19	21.12	23.42	Ply Wood	Absolute	[54]
294	10.39	52.37	0.15	18.54	18.56	Mixed Paper	Absolute	[54]
295	10.2	45.16	0.2	21.59	22.86	Jujuba Wood	Absolute	[54]
296	10.47	49.91	0.15	18.95	20.51	Almond Hulls	Absolute	[54]
297	10.2	49.49	0.16	19.38	20.76	Alfalfa Stems	Absolute	[54]
298	10.33	44.98	0.2	21.71	22.78	Block Wood	Absolute	[54]
299	11.16	52.53	0.13	17.33	18.85	Switchgrass	Absolute	[54]
300	11.88	56.22	0.09	14.77	17.04	Demo. Wood	Absolute	[54]
301	10.88	43.02	0.21	22.15	23.75	Fresh Subabul Wood	Absolute	[54]
302	10.82	45.62	0.19	21.34	22.03	Mango Tree Wood	Absolute	[54]
303	11.3	47.15	0.16	19.42	21.97	Unspecified Waste Material	Absolute	[54]
304	11.09	45.82	0.18	20.76	22.15	Eucalyptus Wood	Absolute	[54]
305	12.11	56.71	0.08	14.23	16.87	Wheat Straw	Absolute	[54]
306	11.27	45.53	0.19	21.17	21.84	Sugarcane Bagasse	Absolute	[54]
307	12	49.63	0.14	18.21	20.02	Wheat Straw	Absolute	[54]
308	12.25	47.41	0.17	20.03	20.15	Millet Straw	Absolute	[54]
309	12.73	47.18	0.15	18.66	21.28	Coconut Coir Pith	Absolute	[54]
310	13.05	48.67	0.14	18.47	19.67	Wheat Straw	Absolute	[54]
311	12.44	42.66	0.22	22.9	21.78	Cottongin Waste	Absolute	[54]
312	13.22	50.93	0.13	17.81	17.9	Jawar Straw	Absolute	[54]
313	14.09	61.49	0.05	11.37	12.99	Yard Waste	Absolute	[54]
314	14.18	49.77	0.13	17.77	18.16	Millet Grain Waste	Absolute	[54]
315	13.91	66.56	0.04	10.07	9.42	RDF	Absolute	[54]
316	14.74	59.74	0.07	12.67	12.5	Rice Husk Bran	Absolute	[54]
317	15.13	60.78	0.06	11.6	12.44	Rice Husk	Absolute	[54]

318	14.09	60.59	0.07	13.5	11.75	Rice Straw	Absolute	[54]
319	14.79	61.98	0.06	11.67	11.51	Rice Husk	Absolute	[54]
320	16.59	60.03	0.05	11.64	11.7	Rice Straw	Absolute	[54]
321	12.5	50.23	1.82	17.33	15.81	Prosopis Juliflora Wood pieces	Absolute	[55]
322	12.88	51.21	1.85	16.84	17.3	Prosopis Juliflora Wood pieces	Absolute	[55]
323	12.14	50.88	1.92	15.56	16.85	Prosopis Juliflora Wood pieces	Absolute	[55]
324	12.71	42.49	5.21	16.24	23.34	Paper Mill Rejects+Wood Chips	Absolute	[56]
325	12	45	2.4	16.2	24.4	Paper Mill Rejects+Wood Chips	Absolute	[56]
326	11.94	45.04	2.42	16.16	24.43	Paper Mill Rejects+Wood Chips	Absolute	[56]
327	11.8	47.27	2.16	14.41	24.35	Paper Mill Rejects+Wood Chips	Absolute	[56]
328	11.87	47.46	0.94	15	24.73	Paper Mill Rejects+Wood Chips	Absolute	[56]
329	15.43	49.67	1.59	11.5	21.79	Paper Mill Rejects+Wood Chips	Absolute	[56]
330	16.11	51.49	2.31	11	19.09	Paper Mill Rejects+Wood Chips	Absolute	[56]
331	6.99	38.08	2.17	17.74	35.02	Paper Mill Rejects+Wood Chips	Absolute	[56]
332	6.88	50.44	1.51	16.64	24.53	Paper Mill Rejects+Wood Chips	Absolute	[56]
333	4.5	na	10.9	11.5	22	na	Absolute	[57]
334	9	50	5	18	18	Babul wood	Absolute	[58]
335	9.2	59.22	1.05	14	16.4	Pine+Spruce Wood Pellets	Absolute	[59]
336	8	40.1	1.7	13	22	Simulated Gas	Absolute	[60]
337	14.62	51.37	6.96	10.48	12.94	Sewage Sludge	Absolute	[61]
338	9.46	58.29	6.78	10.62	11.03	Sewage Sludge	Absolute	[61]
339	7.78	64.42	5.77	9.6	9.17	Sewage Sludge	Absolute	[61]
340	8.62	48.93	5.17	22.31	12.31	Sewage Sludge	Absolute	[61]
341	6.49	47.16	3.36	29.8	13.17	Sewage Sludge	Absolute	[61]
342	12.48	44.18	3.13	24.34	15.86	Sewage Sludge	Absolute	[61]
343	14.48	42.38	2.71	23.22	17.22	Sewage Sludge	Absolute	[61]
344	15.24	38.39	3.61	30.92	11.84	Sewage Sludge	Absolute	[61]

345	11.78	41.28	3.65	34.1	9.18	Sewage Sludge	Absolute	[61]
346	11.39	41.83	3.56	27.73	15.48	Sewage Sludge	Absolute	[61]
347	8.38	41.85	8.11	20.42	15.8	Sewage Sludge	Absolute	[62]
348	9.59	43.43	6.03	20.48	16.94	Sewage Sludge	Absolute	[62]
349	10.1	41.83	6.29	21.29	16.79	Sewage Sludge	Absolute	[62]
350	8.98	41.52	5.73	22	18.56	Sewage Sludge	Absolute	[62]
351	8.84	39.37	5.35	21.11	22.64	Sewage Sludge	Absolute	[62]
352	7.53	40.07	5.72	27.37	18.77	Sewage Sludge	Absolute	[62]
353	9.77	36.24	5.68	29.4	18.56	Sewage Sludge	Absolute	[62]
354	11.57	34.77	6.17	31.23	15.62	Sewage Sludge	Absolute	[62]
355	12.41	34.49	6.2	32.11	14.19	Sewage Sludge	Absolute	[62]
356	10.89	35.89	6.33	29.21	17.02	Sewage Sludge	Absolute	[62]
357	9.1	32.38	10.47	18.36	27.09	Railroad Wood Ties	Absolute	[63]
358	8.91	35.58	4.83	22.77	26.23	Railroad Wood Ties	Absolute	[63]
359	2.65	52.83	7.28	28.86	7.46	Railroad Wood Ties	Absolute	[63]
360	8.42	38.67	5.38	28.54	18.69	Railroad Wood Ties	Absolute	[63]
361	7.25	33.03	3.56	28.85	27.25	Railroad Wood Ties	Absolute	[63]
362	7.6	38.66	3.08	25.37	25.2	Railroad Wood Ties	Absolute	[63]
363	7.21	44.31	2.18	20.94	25.34	Railroad Wood Ties	Absolute	[63]
364	8.88	53.12	1.22	15.5	21.27	Railroad Wood Ties	Absolute	[63]
365	8.13	35.84	3.87	25.33	26.14	Railroad Wood Ties	Absolute	[63]
366	7.04	34.88	3.99	25.07	28.13	Railroad Wood Ties	Absolute	[63]
367	9.1	37.3	8.8	17.6	24.8	Construction Woody Wastes	Absolute	[64]
368	9.4	49	6.9	13.4	19.6	Construction Woody Wastes	Absolute	[64]
369	9.2	50.4	6.4	13.2	19.2	Construction Woody Wastes	Absolute	[64]
370	8.2	38.3	8.3	18.3	24.9	Construction Woody Wastes	Absolute	[64]
371	7.6	46	7.5	12.7	23.1	Construction Woody Wastes	Absolute	[64]

372	7.9	44.6	7.8	12.2	24.1	Construction Woody Wastes	Absolute	[64]
373	7.3	46.2	7.8	11.3	24	Construction Woody Wastes	Absolute	[64]
374	5.2	63	4.8	10	15.3	Construction Woody Wastes	Absolute	[64]
375	8.5	39.9	8	15.3	25.8	Construction Woody Wastes	Absolute	[64]
376	9.2	30.4	9.8	20.9	28.4	Construction Woody Wastes	Absolute	[64]
377	9	38.5	7	22.6	22.1	Construction Woody Wastes	Absolute	[64]
378	10.4	37.4	5.2	24.7	22.1	Construction Woody Wastes	Absolute	[64]
379	10.4	37.5	4.9	25.3	21.6	Construction Woody Wastes	Absolute	[64]
380	10.6	41.7	6.1	14.6	24.4	Construction Woody Wastes	Absolute	[64]
381	24.66	24.81	5.6	12.22	31.58	Unspecified Wood Waste	Absolute	[65]
382	22.58	28	5.9	11.88	30.46	Unspecified Wood Waste	Absolute	[65]
383	23.01	28.94	5	11.36	30.61	Unspecified Wood Waste	Absolute	[65]
384	23.16	28.08	6.2	9.73	31.11	Unspecified Wood Waste	Absolute	[65]
385	21.13	26.55	7.1	11.24	32.01	Unspecified Wood Waste	Absolute	[65]
386	18.97	18.43	8.11	13.23	38.53	Unspecified Wood Waste	Absolute	[65]
387	20.44	22.12	7.37	12.44	35.09	Unspecified Wood Waste	Absolute	[65]
388	28.91	31.68	4.09	9.81	25.02	Unspecified Wood Waste	Absolute	[65]
389	31.58	38.06	2.55	7.95	19.58	Unspecified Wood Waste	Absolute	[65]
390	22.15	28.08	6.35	6.35	33.93	Unspecified Wood Waste	Absolute	[65]
391	20.9	25.39	6.89	10.67	33.88	Unspecified Wood Waste	Absolute	[65]
392	9.53	52.6	0.98	12.3	18.9	Unspecified Wood Chips	Absolute	[66]
393	36.6	6	3.1	30.4	23.9	na	Absolute	[67]
394	23.2	24.2	2.7	22.3	27.6	na	Absolute	[67]
395	16.8	45.3	1.9	13.7	22.3	na	Absolute	[67]
396	16	21.1	28.9	14.6	19.4	na	Absolute	[67]
397	16.8	45.3	1.9	13.7	22.3	Simulated Gas	Absolute	[67]
398	16.8	39	1.9	20	22.3	Simulated Gas	Absolute	[67]

399	19.1	30.9	5.7	35.4	8.9	German Brown Coal+Pine Wood Chips	Absolute	[68]
400	18.9	43.7	4.7	22.6	10.1	German Brown Coal+Pine Wood Chips	Absolute	[68]
401	17.1	34.3	4.4	32.5	11.7	German Brown Coal+Pine Wood Chips	Absolute	[68]
402	18.3	44.1	3.7	22.9	11	German Brown Coal+Pine Wood Chips	Absolute	[68]
403	18	43.8	3.4	23.3	11.5	German Brown Coal+Pine Wood Chips	Absolute	[68]
404	18.4	46.4	3.4	21.2	10.6	German Brown Coal+Pine Wood Chips	Absolute	[68]
405	17.6	50	3.1	18.6	10.7	German Brown Coal+Pine Wood Chips	Absolute	[68]
406	16.6	52.9	3.3	15.3	11.9	German Brown Coal+Pine Wood Chips	Absolute	[68]
407	14.5	61.8	2.4	9.2	12.1	German Brown Coal+Pine Wood Chips	Absolute	[68]
408	15.7	63.6	2.3	7.8	10.6	German Brown Coal+Pine Wood Chips	Absolute	[68]
409	16.5	42	3.1	25.2	13.2	German Brown Coal+Pine Wood Chips	Absolute	[68]
410	16.6	46.7	2.8	22.2	11.7	German Brown Coal+Pine Wood Chips	Absolute	[68]
411	15	63	2.1	9.1	10.8	German Brown Coal+Pine Wood Chips	Absolute	[68]
412	19.1	50.1	1.8	21.9	7.1	German Brown Coal+Pine Wood Chips	Absolute	[68]
413	18.8	28.3	5	33.7	14.2	German Brown Coal+Pine Wood Chips	Absolute	[68]
414	11.7	53.7	2.4	14.2	18	German Brown Coal+Pine Wood Chips	Absolute	[68]
415	17.8	42.4	3.1	25.7	11	German Brown Coal+Pine Wood Chips	Absolute	[68]
416	16.2	43.8	2.9	24.1	13	German Brown Coal+Pine Wood Chips	Absolute	[68]
417	14	50.2	2.7	18	15.1	German Brown Coal+Pine Wood Chips	Absolute	[68]
418	12.7	59.2	2.3	10.8	15	German Brown Coal+Pine Wood Chips	Absolute	[68]
419	20.4	42.2	2.2	27.9	7.3	German Brown Coal+Pine Wood Chips	Absolute	[68]
420	14.9	41.5	2.7	26.1	14.8	German Brown Coal+Pine Wood Chips	Absolute	[68]
421	13.9	51.5	2.2	18.4	14	German Brown Coal+Pine Wood Chips	Absolute	[68]
422	13.5	59.2	1.9	11.9	13.5	German Brown Coal+Pine Wood Chips	Absolute	[68]
423	12.8	58.6	2.2	11.4	15	German Brown Coal+Pine Wood Chips	Absolute	[68]
424	12.61	62.91	2.04	8.79	13.65	Maize Cobs	Absolute	[69]
425	21.8	6	10.34	9.4	49.8	Unspecified Sawdust	Absolute	[70]

426	21.92	7.8	10.2	9.6	46.9	Unspecified Sawdust	Absolute	[70]
427	23.5	7.69	10.01	8.7	47.3	Unspecified Sawdust	Absolute	[70]
428	23.5	12.75	9.65	8.1	43.4	Unspecified Sawdust	Absolute	[70]
429	23.6	15.69	8.31	7.8	41.1	Unspecified Sawdust	Absolute	[70]
430	23.11	21.85	7.86	7.5	37.08	Unspecified Sawdust	Absolute	[70]
431	22.54	24.98	7.35	7.34	33.65	Unspecified Sawdust	Absolute	[70]
432	22.27	36.91	7.01	6.98	23.45	Unspecified Sawdust	Absolute	[70]
433	18.22	52.45	6.75	5.25	14.16	Unspecified Sawdust	Absolute	[70]
434	9.0844	39.3347	4.9614	16.1186	27.448	Unspecified Sawdust	Digitized	[70]
435	9.78	39.5042	4.8885	16.8586	26.194	Unspecified Sawdust	Digitized	[70]
436	10.3426	39.2965	4.7714	18.3965	24.7524	Unspecified Sawdust	Digitized	[70]
437	10.7279	39.7722	4.669	18.8853	23.6157	Unspecified Sawdust	Digitized	[70]
438	11.0393	39.6474	4.5961	19.6178	22.8895	Unspecified Sawdust	Digitized	[70]
439	11.3654	39.694	4.4494	20.3551	22.0461	Unspecified Sawdust	Digitized	[70]
440	11.7211	39.4968	4.4061	21.2034	21.2026	Unspecified Sawdust	Digitized	[70]
441	11.9439	39.4362	4.3628	21.8468	20.4765	Unspecified Sawdust	Digitized	[70]
442	22.0323	12.1415	7.929	20.5342	35.0303	Unspecified Sawdust	Digitized	[70]
443	25.1225	8.926	8.0011	23.0398	32.3971	Unspecified Sawdust	Digitized	[70]
444	21.9333	9.9403	8.3307	24.7343	31.6824	Unspecified Sawdust	Digitized	[70]
445	22.3344	10.0853	8.3885	26.1586	29.7076	Unspecified Sawdust	Digitized	[70]
446	23.6223	7.3841	8.4462	29.6553	27.7101	Unspecified Sawdust	Digitized	[70]
447	25.8256	5.833	8.6185	30.0704	26.6322	Unspecified Sawdust	Digitized	[70]
448	26.6701	3.7163	8.5618	32.3056	25.8154	Unspecified Sawdust	Digitized	[70]
449	28.0295	2.553	8.8056	32.7928	24.9418	Unspecified Sawdust	Digitized	[70]
450	11.4	52.9	1.1	15.5	19.1	na	Absolute	[71]
451	na	na	2	7	26.5	Unspecified Wood Chips	Absolute	[72]
452	na	na	2.9	13.4	22.1	Unspecified Wood Chips	Absolute	[72]

453	na	na	1.7	14.12	16.8	Hazelnut Shells	Absolute	[72]
454	na	na	1.1	18.3	20.2	Rubber Wood	Absolute	[72]
455	na	na	3.96	18.89	19.48	Unspecified Sawdust	Absolute	[72]
456	na	na	6.82	28.93	25.53	Pine Wood Blocks	Absolute	[72]
457	na	na	1.2	14.8	9.4	Unspecified Wood Chips	Absolute	[72]
458	na	na	3.96	18.89	19.48	Unspecified Wood Chips	Absolute	[72]
459	na	na	0.1	14	22	Unspecified Wood Waste	Absolute	[72]
460	12	46	2	19	19	Simulated Gas	Absolute	[72]
461	6.2	42.5	1.7	3.9	26.1	Softwood Pellets	Absolute	[73]
462	4.7	41.4	1.6	5	24.4	Softwood Pellets	Absolute	[73]
463	5	40.4	1.7	6.3	26.6	Softwood Pellets	Absolute	[73]
464	8.6	48.8	1.6	3.4	20	Softwood Pellets	Absolute	[73]
465	9.7	48.3	1.8	5.2	18.9	Softwood Pellets	Absolute	[73]
466	8.6	48.3	1.7	4.5	18.8	Softwood Pellets	Absolute	[73]
467	4.5	na	2	11	21	Olive+Mixed Biomass	Absolute	[74]
468	6	na	2	9	18	Olive+Mixed Biomass	Absolute	[74]
469	9	na	2	9	13	Olive+Mixed Biomass	Absolute	[74]
470	7.5	na	2.5	9	15	Olive+Mixed Biomass	Absolute	[74]
471	7.5	na	3	10	18	Olive+Mixed Biomass	Absolute	[74]
472	9	na	2	8	11	Olive+Mixed Biomass	Absolute	[74]
473	9	na	2.5	8	13	Olive+Mixed Biomass	Absolute	[74]
474	10.5	na	3.5	9.5	14.5	Olive+Mixed Biomass	Absolute	[74]
475	10	2	9	16	20	Simulated Gas	Absolute	[75]
476	na	na	0.25	6.5	22.995	Corn Cobs	Averaged	[76]
477	11.78	76.2	0.03	0.97	5.72	Corn Cobs	Absolute	[76]
478	6.07	67.05	0.31	3.63	18.6	Corn Cobs	Absolute	[76]
479	6.95	60.48	0.33	9.37	22.35	Corn Cobs	Absolute	[76]

480	3.61	60.81	0.17	6.39	27.79	Corn Cobs	Absolute	[76]
481	12.51	56.21	1.38	11.17	17.79	Unspecified Wood Chips+Charcoal	Absolute	[77]
482	13.17	55.15	1.34	12.01	17.9	Unspecified Wood Chips+Charcoal	Absolute	[77]
483	13.51	54.91	2.46	10.98	17.01	Unspecified Wood Chips+Charcoal	Absolute	[77]
484	13.46	53.75	2.68	11.45	18.28	Unspecified Wood Chips+Charcoal	Absolute	[77]
485	11.1	57.01	1.67	11.6	17.31	Unspecified Wood Chips+Charcoal	Absolute	[77]
486	13.72	55.87	1.71	11.1	17.28	Unspecified Wood Chips+Charcoal	Absolute	[77]
487	14	56.6	3.1	8.2	18.1	Unspecified Sawdust+Cotton Stalks	Averaged	[78]
488	11.2	59.7	4.4	10.6	11.2	Fresh Soyabean Oil	Absolute	[79]
489	12.7	62.1	3.2	9.6	10.6	Fresh Soyabean Oil	Absolute	[79]
490	13.3	65.5	2.9	7.8	8.9	Fresh Soyabean Oil	Absolute	[79]
491	7.8	51.7	4.2	15.5	19.1	Waste Soyabean Oil	Absolute	[79]
492	9.8	55.4	3.4	13.9	15.9	Waste Soyabean Oil	Absolute	[79]
493	10	58	2.8	12.7	15.1	Waste Soyabean Oil	Absolute	[79]
494	7	50.7	3.8	16.9	20.2	Waste Soyabean Oil	Absolute	[79]
495	6.2	51	4	16.8	20.9	Waste Soyabean Oil	Absolute	[79]
496	3.96	50.99	15.7	14.18	6.56	Mixed Plastic Waste	Absolute	[80]
497	5.02	56.91	12.63	13.34	5.61	Mixed Plastic Waste	Absolute	[80]
498	5.17	64.02	8.71	12.67	5.37	Mixed Plastic Waste	Absolute	[80]
499	6.74	71.54	3.64	12.56	5.01	Mixed Plastic Waste	Absolute	[80]
500	4.52	53.67	14.07	13.52	5.49	Mixed Plastic Waste	Absolute	[80]
501	3.69	49.8	15.03	18.15	7.18	Mixed Plastic Waste	Absolute	[80]
502	4.28	48.54	15.1	17.47	6.87	Mixed Plastic Waste	Absolute	[80]
503	4.22	46.75	15.49	21.33	5.97	Mixed Plastic Waste	Absolute	[80]
504	5.48	51.91	17.09	10.98	5.04	Mixed Plastic Waste	Absolute	[80]
505	7.03	46.14	16.61	13.21	7.72	Mixed Plastic Waste	Absolute	[80]
506	7.24	46.16	16.01	13.16	8.29	Mixed Plastic Waste	Absolute	[80]

507	4.46	50.68	14.76	15.26	6.67	Mixed Plastic Waste	Absolute	[80]
508	15.92	49.63	2.18	8.63	6.93	Grass Pellets	Absolute	[81]
509	16.42	48.66	2.9	9.18	7.55	Grass Pellets	Absolute	[81]
510	16.28	47.62	3.08	10.11	8.25	Grass Pellets	Absolute	[81]
511	13.22	49.72	2.85	12.39	11.22	Unspecified Wood Pellets	Absolute	[81]
512	13.59	47.14	3.32	12.58	11.88	Unspecified Wood Pellets	Absolute	[81]
513	13.96	42.26	4.17	13.21	12.74	Unspecified Wood Pellets	Absolute	[81]
514	na	na	35.5	43.9	28.2	Eucalyptus Chips	Absolute	[82]
515	na	na	2.9	11.1	14.3	Eucalyptus Chips	Absolute	[82]
516	na	na	2.7	15.7	17.1	Eucalyptus Chips	Absolute	[82]
517	na	na	2.8	20.9	20.2	Eucalyptus Chips	Absolute	[82]
518	11.78	49.54	2.35	9.44	22.15	Unspecified Wood Residue	Averaged	[83]
519	9	55	1.75	11	25	Mixed Biomass	Averaged	[84]
520	4.8	49.55	0.35	8.5	30.5	Charcoal	Absolute	[85]
521	22	0	12	34	26	Simulated Gas	Absolute	[86]
522	15	50	4	14	15	na	Averaged	[87]
523	19.5	1.5	14.5	40.5	33.5	na	Averaged	[87]
524	13.82	na	1.54	7.01	16.33	Oil Palm Fronds	Absolute	[88]
525	15.51	na	1.52	7.11	17.41	Oil Palm Fronds	Absolute	[88]
526	14.93	na	2.34	10.68	21.66	Oil Palm Fronds	Absolute	[88]
527	14.61	na	2.48	10.84	21.11	Oil Palm Fronds	Absolute	[88]
528	14.48	na	2.66	10.77	22.43	Oil Palm Fronds	Absolute	[88]
529	15.61	na	2.68	10.54	21.02	Oil Palm Fronds	Absolute	[88]
530	15.99	na	2.43	7.89	14.35	Oil Palm Fronds	Absolute	[88]
531	15.03	na	2.5	8.23	16.5	Oil Palm Fronds	Absolute	[88]
532	11.24	na	1.98	9.67	22.49	Oil Palm Fronds	Absolute	[88]
533	12.88	na	2.49	13.58	24.98	Oil Palm Fronds	Absolute	[88]

534	14.22	na	1.44	5.45	12.01	Oil Palm Fronds	Absolute	[88]
535	15.65	na	2.45	8.87	17.02	Oil Palm Fronds	Absolute	[88]
536	13.22	na	2.3	10.69	22.23	Oil Palm Fronds	Absolute	[88]
537	12.01	na	2.22	11.49	22.85	Oil Palm Fronds	Absolute	[88]
538	12.74	na	2.41	10.99	21.99	Oil Palm Fronds	Absolute	[88]
539	12.63	na	2.12	11.22	21.56	Oil Palm Fronds	Absolute	[88]
540	13.47	na	2.01	11.7	21.1	Oil Palm Fronds	Absolute	[88]
541	12	49	1	18	20	na	Absolute	[89]
542	7.1	na	3.97	8.74	9.84	Coffee Husk	Absolute	[90]
543	7.2	na	3.88	7.68	9.49	Coffee Husk	Absolute	[90]
544	9.8	na	8.1	6.9	9.1	Unspecified Wood Sawdust	Absolute	[90]
545	8.9	na	5.4	5.9	7.6	Unspecified Wood Sawdust	Absolute	[90]
546	9.2	na	5.6	7.46	10.7	Coffee Husk+Sawdust	Absolute	[90]
547	9.05	na	4.6	6.6	9.84	Coffee Husk+Sawdust	Absolute	[90]
548	14.04	53.77	2.8	7.48	15.91	Cane Trash	Absolute	[91]
549	16.69	54.3	2.47	8.48	14.36	Cane Trash	Absolute	[91]
550	10.3	51.5	1.2	17.5	19.2	Neem Wood	Absolute	[92]
551	10.5	51.3	1.25	17.6	19	Neem Wood	Absolute	[92]
552	10.8	51	1.25	17.8	18.7	Neem Wood	Absolute	[92]
553	11	50.5	1.35	18.2	18.5	Neem Wood	Absolute	[92]
554	10.5	48.5	1.15	17.8	20.5	Bamboo	Absolute	[92]
555	10.8	48	1.15	18	20.2	Bamboo	Absolute	[92]
556	11	47.5	1.25	18.5	20	Bamboo	Absolute	[92]
557	11.2	46	1.25	18.8	19.5	Bamboo	Absolute	[92]
558	11	49.1	1.2	18	20.2	Shisham	Absolute	[92]
559	10.9	48.8	1.2	18.5	20	Shisham	Absolute	[92]
560	11.5	48.6	1.25	18.5	19.5	Shisham	Absolute	[92]

561	11.4	48.9	1.3	19	19	Shisham	Absolute	[92]
562	10.7	52.4	1.2	17	18.5	Gulmohar	Absolute	[92]
563	10.8	52.3	1.25	17	18.5	Gulmohar	Absolute	[92]
564	11	51.8	1.25	17.5	18.2	Gulmohar	Absolute	[92]
565	11.5	51.5	1.35	17.5	18	Gulmohar	Absolute	[92]
566	11.5	53	0.85	16.5	17.5	Dimaru	Absolute	[92]
567	11.5	52.3	0.88	16.5	17.5	Dimaru	Absolute	[92]
568	12	52.5	0.88	17	17	Dimaru	Absolute	[92]
569	12	52.5	0.95	17	17	Dimaru	Absolute	[92]
570	10.2	43.1	2.1	21.6	23	Rice Husk	Averaged	[93]
571	9.08	na	8.6	10.74	20.24	Eucalyptus Chips	Absolute	[94]
572	12.14	na	14.77	6.64	13.81	Coffee Husk	Absolute	[94]
573	10.39	na	6.51	12.42	14.03	Coffee Wood	Absolute	[94]
574	11	47.6	1.65	15.5	20.5	na	Averaged	[95]
575	14.45	51.76	6.46	13.42	10.06	Dried Sewage Sludge	Absolute	[96]
576	11.28	47.81	4.91	25.02	10.92	Dried Sewage Sludge	Absolute	[96]
577	11.5	46.86	4.87	25.21	11.21	Dried Sewage Sludge	Absolute	[96]
578	9.36	44.12	4.93	28.13	13.38	Dried Sewage Sludge	Absolute	[96]
579	10.72	47.85	4.23	26.33	10.78	Dried Sewage Sludge	Absolute	[96]
580	11.43	48.13	4.41	23.65	12.16	Dried Sewage Sludge	Absolute	[96]
581	11.9	50.37	4.01	20.94	12.39	Dried Sewage Sludge	Absolute	[96]
582	14.5	51.6	6.4	14.1	10.3	Dried Sewage Sludge	Absolute	[97]
583	10.4	43.4	5.11	28.4	12.8	Dried Sewage Sludge	Absolute	[97]
584	12.3	50.4	6.3	21.3	9.2	Dried Sewage Sludge	Absolute	[97]
585	12.4	48.2	4.7	24.4	10.3	Dried Sewage Sludge	Absolute	[97]
586	10.5	48.8	4	26.3	10.3	Dried Sewage Sludge	Absolute	[97]
587	9.1	46.3	3.8	28.5	12.3	Dried Sewage Sludge	Absolute	[97]

588	9.1	45.8	3.8	29	12.2	Dried Sewage Sludge	Absolute	[97]
589	10.7	48.5	2.6	27.3	11	Dried Sewage Sludge	Absolute	[97]
590	11.3	46.6	3.3	24.9	13.8	Dried Sewage Sludge	Absolute	[97]
591	14.71	54.41	5.8	11.78	9.1	Dried Sewage Sludge	Absolute	[98]
592	7.92	51.56	3.48	26.09	10.94	Dried Sewage Sludge	Absolute	[98]
593	11.19	46.69	4.07	26.69	13.86	Dried Sewage Sludge	Absolute	[98]
594	11.21	46.35	3.77	26.14	12.53	Dried Sewage Sludge	Absolute	[98]
595	8.98	42.97	3.18	29.15	15.9	Dried Sewage Sludge	Absolute	[98]
596	7.95	39.49	3.43	31.3	17.8	Dried Sewage Sludge	Absolute	[98]
597	9.64	45.79	4.86	28.17	11.54	Dried Sewage Sludge	Absolute	[98]
598	7.62	40.87	3.67	30.36	18.41	Dried Sewage Sludge	Absolute	[98]
599	13.66	54.4	6.18	12.23	10.37	Dried Sewage Sludge	Absolute	[99]
600	11.39	53.81	4.96	19.94	9.2	Dried Sewage Sludge	Absolute	[99]
601	14.46	52.35	6.42	13.66	10.09	Dried Sewage Sludge	Absolute	[99]
602	9.36	44.62	5.77	28.63	11.43	Dried Sewage Sludge	Absolute	[99]
603	10.47	46.1	4.95	28.85	9.49	Dried Sewage Sludge	Absolute	[99]
604	7.5	46.39	5.68	28.77	11.61	Dried Sewage Sludge	Absolute	[99]
605	11.99	51.14	6.34	21.19	8.79	Dried Sewage Sludge	Absolute	[99]
606	13.06	55.02	5.9	16.62	8.44	Dried Sewage Sludge	Absolute	[99]
607	10.17	52.62	5.49	22.42	8.91	Dried Sewage Sludge	Absolute	[99]
608	11.39	55.91	5.34	19.63	7.36	Dried Sewage Sludge	Absolute	[99]
609	9.3	58.9	11.3	11.2	3.1	Plastic Pellets	Absolute	[100]
610	7.1	53.6	11.4	13.4	8.5	Plastic Pellets	Absolute	[100]
611	7.4	55.3	10.5	11.6	8.6	Plastic Pellets	Absolute	[100]
612	6.2	54.2	9.1	14.2	11.7	Plastic Pellets	Absolute	[100]
613	6.3	50.5	7.3	29.8	6	Plastic Pellets	Absolute	[100]
614	3.7	48	6.8	29.7	11.7	Plastic Pellets	Absolute	[100]

615	0.7	46	7.7	29.8	15.5	Plastic Pellets	Absolute	[100]
616	7	53.2	10.7	17.9	6.3	Plastic Pellets	Absolute	[100]
617	3.18	54.08	8.77	17.03	13.59	Plastic Pellets	Absolute	[101]
618	2.5	52.38	8.72	23.43	12.04	Plastic Pellets	Absolute	[101]
619	5.56	48.24	7.7	25.14	13.32	Plastic Pellets	Absolute	[101]
620	8.82	50.75	7.11	26.88	6.39	Plastic Pellets	Absolute	[101]
621	8.72	50.9	6.39	26.69	7.27	Plastic Pellets	Absolute	[101]
622	8.44	51.24	7.33	27.02	5.73	Plastic Pellets	Absolute	[101]
623	8.08	50.82	6.58	27.25	7.15	Plastic Pellets	Absolute	[101]
624	1.89	52.03	7.4	26.93	11.71	Plastic Pellets	Absolute	[101]
625	8.56	51.14	6.39	27.09	6.7	Plastic Pellets	Absolute	[101]
626	4.24	63.35	12.57	10.49	2.84	Plastic Pellets	Absolute	[102]
627	0.99	57.58	11.1	14.89	9.35	Plastic Pellets	Absolute	[102]
628	3.06	45.34	12.68	17.73	13.65	Plastic Pellets	Absolute	[102]
629	4.53	49.81	10.56	17.7	12.4	Plastic Pellets	Absolute	[102]
630	8.05	59.59	7.66	12.92	7.88	Plastic Pellets	Absolute	[102]
631	7.96	51.33	8.76	18.13	11.38	Plastic Pellets	Absolute	[102]
632	5.18	45.61	10.26	24.79	13.82	Plastic Pellets	Absolute	[102]
633	4.23	45.3	7.5	26.11	16.82	Plastic Pellets	Absolute	[102]
634	2.7	47.1	3.8	27.96	18.42	Plastic Pellets	Absolute	[102]
635	1.93	53.4	11.1	27.63	5.82	Plastic Pellets	Absolute	[102]
636	13.04	60.23	9.1	9.34	3.19	Plastic Pellets	Absolute	[103]
637	8.56	51.14	6.39	27.09	6.7	Plastic Pellets	Absolute	[103]
638	7.76	48.47	5.88	30.25	7.62	Plastic Pellets	Absolute	[103]
639	8.46	46.31	5.57	31.05	8.6	Plastic Pellets	Absolute	[103]
640	4.61	52.51	4.59	30.63	7.66	Plastic Pellets	Absolute	[103]
641	9.88	58.17	2.24	19.61	10.11	Plastic Pellets	Absolute	[103]

642	8.65	45.2	6.35	31.78	8.01	Plastic Pellets	Absolute	[103]
643	9.58	50.17	4.78	25.48	9.99	Plastic Pellets	Absolute	[103]
644	13.92	50.83	5.12	22.16	7.48	Plastic Pellets	Absolute	[103]
645	5.15	53.09	13.74	14.65	6.32	Mixed Plastic Waste	Absolute	[104]
646	18.1	54	2.7	10.7	16.2	Corn Straw	Absolute	[104]
647	19.42	na	3.75	23.98	14.26	Olive Kernels	Absolute	[104]
648	8.65	53.95	3.55	14.75	17.58	Waste Cooking Oil	Absolute	[104]
649	12.38	56.87	1.95	13.51	14.62	Hazelnut Shells	Absolute	[104]
650	23.24	4.72	7.85	35.52	26.82	Oil Palm Trunk	Absolute	[104]
651	18.36	43.3	3.5	19.53	13.99	Oil Palm Trunk	Absolute	[104]
652	21	2.3	2.8	36	38	Cotton Stalk Pellets	Absolute	[104]
653	11.7	na	11.5	43.6	33.2	Crushed Almond Shells	Absolute	[104]
654	27	5	11	33	32	Almond Shells	Absolute	[104]
655	32.35	6.66	8.5	28.02	19.3	Sewage Sludge	Absolute	[104]
656	4.02	na	1.52	10.19	21.61	Refuse-Derived Fuel Pellets	Averaged	[105]
657	4.25	na	0.97	10.46	17.69	Refuse-Derived Fuel Pellets	Averaged	[105]
658	3.09	na	1.14	9.44	19.35	Refuse-Derived Fuel Pellets	Averaged	[105]
659	8.48	na	2.97	7.04	15.85	leucaena Wood Chips	Absolute	[106]
660	13.53	na	3.2	6.75	16.33	leucaena Wood Chips	Absolute	[106]
661	5.73	na	3.64	8.47	13.86	leucaena Wood Chips	Absolute	[106]
662	7.6	na	3.25	6.76	14.05	leucaena Wood Chips	Absolute	[106]
663	8.44	na	2.42	5.39	12.94	Eucalyptus Wood Chips	Absolute	[106]
664	10.02	na	2.95	4.67	13.85	Eucalyptus Wood Chips	Absolute	[106]
665	12.04	na	18.58	6.85	19.05	Eucalyptus Wood Chips	Absolute	[106]
666	13.34	na	3.58	5.05	16.29	Eucalyptus Wood Chips	Absolute	[106]
667	11.62	58.87	2.11	15.23	16.15	Prosopis Juliflora Wood pieces	Absolute	[107]
668	12.58	50.12	1.87	16.82	17.31	Prosopis Juliflora Wood pieces	Absolute	[107]

669	12.28	49.79	1.94	17.25	15.86	Prosopis Juliflora Wood pieces	Absolute	[107]
670	12.29	50.8	1.87	17.34	15.8	Prosopis Juliflora Wood pieces	Absolute	[107]
671	10	50	3	18	19	na	Absolute	[108]
672	23	3	10	40	24	na	Absolute	[109]
673	15.4	33.3	1.6	30.5	19.6	na	Absolute	[109]
674	12	48.5	1.5	19	19	na	Absolute	[109]
675	11.9	40.7	5.3	19.3	22.8	na	Absolute	[109]
676	1.4	56.7	2.2	18.8	21	na	Absolute	[109]
677	12.89	52.55	1.77	12.96	16.67	Rubber Wood	Absolute	[110]
678	14	52	4	10.5	16	na	Absolute	[111]
679	15	0	9.5	47	24.5	na	Absolute	[111]
680	25	0	7	23	47.5	na	Absolute	[111]
681	9.2	na	8.1	25.7	28.5	Unspecified Wood Pellets	Absolute	[112]
682	14.45	56.57	2.9	4	19.9	Rice Husk	Absolute	[112]
683	27.62	na	7.02	38.38	24.89	Pine Sawdust	Absolute	[112]
684	29.23	na	5.72	55.97	7.71	Larch Wood	Absolute	[112]
685	19.43	28.2	2.54	20.71	29.13	Coal+Pine Sawdust+Rice Straw	Absolute	[112]
686	19.42	na	3.75	23.98	14.26	Olive Kernel	Absolute	[112]
687	15.5	na	5	6.5	18.5	Rice Husk	Averaged	[112]
688	18.5	na	6	11	15	Pine Sawdust+Coal+Plastic Waste	Averaged	[112]
689	29.9	na	4.5	38.74	35.72	Coconut Shells	Absolute	[112]
690	15.9	50.8	4.3	10.8	16	Unspecified Bagasse	Absolute	[112]
691	13.28	62.47	4.21	9.27	9.25	Unspecified Wood Sawdust	Absolute	[112]
692	16.9	na	7.9	52.2	23	Almond Shells	Absolute	[112]
693	8	na	na	14	8.2	Coffee Ground+Coal	Absolute	[112]
694	16.9	na	7.9	52.2	23	Almond Shells	Absolute	[112]
695	14.1	na	6.4	55.5	24	Almond Shells	Absolute	[112]

696	11.7	na	11.5	43.6	33.2	Almond Shells	Absolute	[112]
697	17.5	na	11.4	39.1	29.1	Unspecified Wood Pellets	Absolute	[112]
698	6	na	11.4	73.9	6.1	Unspecified Wood Pellets	Absolute	[112]
699	16.3	55.4	3.2	7.3	17.9	Unspecified Wood Sawdust	Absolute	[112]
700	15.6	43.25	6.9	16.32	16.7	Unspecified Wood Powder	Absolute	[112]
701	19.2	44.3	3.46	10.88	20.46	na	Absolute	[113]
702	15.5	56	4.5	5	16.5	Switchgrass	Absolute	[114]
703	8.9	na	0.2	31.1	59.8	na	Absolute	[115]
704	9	na	4.3	31	59.8	na	Absolute	[115]
705	7.3	na	0	30.4	62.4	na	Absolute	[115]
706	7.3	na	5.9	30.3	62.4	na	Absolute	[115]
707	6.2	na	0	29.6	64.2	na	Absolute	[115]
708	6.3	na	7.1	29.4	64.3	na	Absolute	[115]
709	9.8	na	0	30.7	60	na	Absolute	[116]
710	9.01	na	4.3	30.98	59.78	na	Absolute	[116]
711	8.1	na	0	29	62.5	na	Absolute	[116]
712	7.33	na	5.87	30.25	62.41	na	Absolute	[116]
713	6.7	na	0	29	65	na	Absolute	[116]
714	6.28	na	7.1	29.43	64.29	na	Absolute	[116]
715	13.8	46.2	3	11.2	17.7	Macadamia Shells	Absolute	[117]
716	13.8	39.7	2.9	14.9	22.5	Coffee Bean Pulp	Absolute	[117]
717	29.8	na	11.1	22.7	28.1	Corn Stover	Absolute	[118]
718	23.9	na	12	22.4	36.8	Rice Husk	Absolute	[118]
719	22.3	na	12.8	25	35.2	Pine Wood	Absolute	[118]
720	26.3	na	10.1	25.9	28.9	Corn Stover	Absolute	[118]
721	18.3	na	11.3	28.1	37.1	Rice Husk	Absolute	[118]
722	16.2	na	12.1	30.7	36.3	Pine Wood	Absolute	[118]

723	12.4	54.9	0.8	13.2	17.4	Olive Wood	Absolute	[119]
724	13.5	51.7	1.2	15	17.7	Peach Wood	Absolute	[119]
725	11.4	59.4	0.2	12.1	16	Pine Wood	Absolute	[119]
726	11	44.8	1.2	20.9	22	Simulated Gas	Absolute	[120]
727	11.1	44.4	1.2	21	22.1	Simulated Gas	Absolute	[120]
728	11	44.1	1.2	20.8	21.9	Simulated Gas	Absolute	[120]
729	10.9	43.6	1.2	20.6	21.7	Simulated Gas	Absolute	[120]
730	12	na	16	39	33	Simulated Gas	Absolute	[121]
731	20	na	15	45	20	Simulated Gas	Absolute	[121]
732	10.05	na	3	14.45	20.75	Olive Leaves	Averaged	[122]
733	13	na	1.35	2.3	17	Mesquite	Averaged	[122]
734	10	na	1.6	2.95	23	Juniper	Averaged	[122]
735	9.9	na	4.5	12	32	Black Pellets	Absolute	[122]
736	14.5	na	2.5	16	19	Grey Pellets	Absolute	[122]
737	13.4	na	4.9	8.8	19	Pine Wood Sawdust	Averaged	[122]
738	9.1	na	1.9	6	29	Unspecified Wood Pellets	Absolute	[122]
739	14.3	na	1.49	30.3	17.6	Spruce Wood Pellets	Absolute	[112]
740	8.39	59.13	1.63	13.05	16.81	Pine Wood Chips+Coal	Absolute	[112]
741	17.3	na	13.6	31.2	28.2	Coffee Ground	Absolute	[112]
742	9.5	na	17.5	19.3	38.2	Coffee Ground	Absolute	[112]
743	9.1	38.1	3.1	17.6	23.6	Aspen Chips	Absolute	[123]
744	9.7	38.2	2.9	18.3	23	Aspen Chips	Absolute	[123]
745	9.2	38.8	2.8	18.3	23.8	Aspen Chips	Absolute	[123]
746	9.7	39.8	2.6	17.5	23.1	Aspen Chips	Absolute	[123]
747	10.8	40.7	2.8	16.2	19.8	Aspen Chips	Absolute	[123]
748	10.8	41.5	2.6	16.8	20	Aspen Chips	Absolute	[123]
749	10.7	41.7	2.5	16.3	19.9	Aspen Chips	Absolute	[123]

750	12.2	44.8	2.1	14.6	16.2	Aspen Chips	Absolute	[123]
751	16.5	52.7	3	10.9	16.7	Corn Straw	Absolute	[123]
752	13.1	53.5	4	12.8	19	Corn Straw	Absolute	[123]
753	11.6	55.7	3.7	13.5	19.8	Corn Straw	Absolute	[123]
754	13.8	56.9	3.7	12.3	18	Corn Straw	Absolute	[123]
755	18.4	59.7	1.6	10.6	15.2	Corn Straw	Absolute	[123]
756	10.65	na	2.31	13.45	23.06	Unspecified Wood Chips	Absolute	[123]
757	10.89	na	2.43	13.51	23.55	Unspecified Wood Chips	Absolute	[123]
758	10.89	na	2.62	13.69	24.03	Unspecified Wood Chips	Absolute	[123]
759	11.5	na	2.68	13.39	22.64	Unspecified Wood Chips	Absolute	[123]
760	11.58	45.2	2.41	19.19	21.62	Hardwood Chips	Absolute	[123]
761	10.6	52.7	1.3	17	18.4	Unspecified Wood Chips	Absolute	[123]
762	8.7	na	4.95	15.57	16.71	Red Wood Pellets	Absolute	[123]
763	9.86	na	3.77	14.85	17.23	Red Wood Pellets	Absolute	[123]
764	9.93	na	2.43	14.13	18.44	Red Wood Pellets	Absolute	[123]
765	10.29	na	2.22	12.83	19.54	Red Wood Pellets	Absolute	[123]
766	na	na	1.2	13	19.1	Rubber Wood	Absolute	[123]
767	na	na	1.3	12.7	22.1	Rubber Wood	Absolute	[123]
768	na	na	1.2	12.5	18.9	Rubber Wood	Absolute	[123]
769	na	na	1.1	17.2	19.4	Rubber Wood	Absolute	[123]
770	na	na	1.3	13.2	19.4	Rubber Wood	Absolute	[123]
771	na	na	1.1	18.3	19.7	Rubber Wood	Absolute	[123]
772	na	na	1.4	17.2	9.6	Rubber Wood	Absolute	[123]
773	13.87	na	3.69	15.84	18.98	Unspecified Biomass	Absolute	[123]
774	13.01	na	3.29	16.75	19.69	Unspecified Biomass Pellets	Absolute	[123]
775	na	na	1.61	12.78	15.78	Corn Cobs	Absolute	[123]
776	na	na	1.53	13.05	17	Corn Cobs	Absolute	[123]

777	na	na	1.07	12.2	15.28	Corn Cobs	Absolute	[123]
778	na	na	1.03	10.93	15.08	Corn Cobs	Absolute	[123]
779	11.05	44.9	4.8	16.4	22.6	Mixed Wood Chips	Absolute	[123]
780	11.8	47.07	4.12	14.04	24.27	Softwood Pellets	Absolute	[123]
781	8.7	na	4.95	15.57	16.71	Oil Palm Fronds	Absolute	[123]
782	9.86	na	3.77	14.85	17.23	Oil Palm Fronds	Absolute	[123]
783	9.93	na	2.43	14.13	18.44	Oil Palm Fronds	Absolute	[123]
784	10.29	na	2.22	12.83	19.54	Oil Palm Fronds	Absolute	[123]
785	12.33	46.46	2.25	15.83	22.46	Corn Cobs	Absolute	[123]
786	12.12	46.13	4.3	15.3	22.11	Corn Cobs	Absolute	[123]
787	11.78	46.59	1.91	16.6	22.55	Corn Cobs	Absolute	[123]
788	12.39	46.59	2.28	16.35	21.29	Unspecified Wood Pellets	Absolute	[123]
789	10.58	60.5	0.69	7.97	20.04	Rice Husk	Absolute	[123]
790	13.02	45.07	2.55	17.06	21.74	Vine Pruning	Absolute	[123]
791	13.73	47.64	1.92	17.19	19.52	Eucalyptus	Absolute	[123]
792	13.35	48.18	1.89	16.56	20.02	Eucalyptus	Absolute	[123]
793	15.3	50.2	2.3	16.5	15.9	Unspecified Wood Chips	Absolute	[123]
794	12.06	50.79	2.31	14	20.14	Unspecified Wood Sawdust	Absolute	[123]
795	16.42	42.31	1.58	15.23	23.04	Unspecified Wood	Absolute	[123]
796	13.3	44.2	3.1	17.5	21.3	Unspecified Wood Sawdust Pellets	Absolute	[123]
797	11.76	na	2.05	16.75	21.3	Corn Cobs	Absolute	[123]
798	11.92	na	2.36	16.02	22.43	Unspecified Wood Chips	Absolute	[123]
799	12.18	na	2.78	15.86	22.27	Pinus Elliotis Sawdust	Absolute	[123]
800	12.03	na	2.31	16.86	22.58	Unspecified Wood	Absolute	[123]

[1] R. Zhang, K. Cummer, A. Suby, R.C. Brown, Biomass-derived hydrogen from an air-blown gasifier, Fuel Process. Technol. 86 (8) (2005) 861–874.

[2] Z.A. Zainal, R. Ali, C.H. Lean, K.N. Seetharamu, Prediction of performance of a downdraft gasifier using equilibrium modeling for different biomass materials, Energy Convers. Manag. 42 (12) (2001) 1499–1515.

[3] V.S. Yaliwal, N.R. Banapurmath, N.M. Gireesh, R.S. Hosmath, T. Donateo, P.G. Tewari, Effect of nozzle and combustion chamber geometry on the performance of a diesel engine operated on dual fuel mode using renewable fuels, Renew. Energy 93 (2016) 483–501.

[4] V.S. Yaliwal, N.R. Banapurmath, R.S. Hosmath, S. V. Khandal, W.M. Budzianowski, Utilization of hydrogen in low calorific value producer gas derived from municipal solid waste and biodiesel for diesel engine power generation application, Renew. Energy 99 (2016) 1253–1261.

[5] A. Warsita, K.A. Al-attab, Z.A. Zainal, Effect of water addition in a microwave assisted thermal cracking of biomass tar models, Appl. Therm. Eng. 113 (2017) 722–730.

[6] Y. Wang, S. Pang, Investigation of hydrogen sulphide removal from simulated producer gas of biomass gasification by titanomagnetite, Biomass and Bioenergy 109 (November 2016) (2018) 61–70.

[7] Y. Wang, S. Pang, Investigation of ammonia removal from the simulated producer gas of biomass gasification by H2-reduced titanomagnetite, Eur. Biomass Conf. Exhib. Proc. 2017 (25thEUBCE) (2017) 876–879.

[8] D.K. Vyas, R.N. Singh, Feasibility study of Jatropha seed husk as an open core gasifier feedstock, Renew. Energy 32 (3) (2007) 512–517.

[9] D. Vera, F. Jurado, J.P. Torreglosa, M. Ortega, Biomass Gasification for Power Generation Applications: A Modeling, Economic, and Experimental Study.

[10] D. Vera, F. Jurado, J. Carpio, S. Kamel, Biomass gasification coupled to an EFGT-ORC combined system to maximize the electrical energy generation: A case applied to the olive oil industry, Energy 144 (2018) 41–53.

[11] D. Vera, F. Jurado, N.K. Margaritis, P. Grammelis, Experimental and economic study of a gasification plant fuelled with olive industry wastes, Energy Sustain. Dev. 23 (2014) 247–257.

[12] R. Uma, T.C. Kandpal, V.V.N. Kishore, Emission characteristics of an electricity generation system in diesel alone and dual fuel modes, Biomass and Bioenergy 27 (2) (2004) 195–203.

[13] Z. Ud Din, Z.A. Zainal, Biomass integrated gasification-SOFC systems: Technology overview, Renew. Sustain. Energy Rev. 53 (2016) 1356–1376.

[14] Z. Ud Din, Z.A. Zainal, The fate of SOFC anodes under biomass producer gas contaminants, Renew. Sustain. Energy Rev. 72 (March) (2017) 1050–1066.

[15] S. Tsiakmakis, D. Mertzis, A. Dimaratos, Z. Toumasatos, Z. Samaras, Experimental study of combustion in a spark ignition engine operating with producer gas from various biomass feedstocks, Fuel 122 (2014) 126–139.

[16] N. Tippayawong, C. Chaichana, A. Promwangkwa, P. Rerkkriangkrai, Gasification of cashew nut shells for thermal application in local food processing factory, Energy Sustain. Dev. 15 (1) (2011) 69–72.

[17] F. V. Tinaut, A. Melgar, B. Giménez, M. Reyes, Characterization of the combustion of biomass producer gas in a constant volume combustion bomb, Fuel 89 (3) (2010) 724–731.

[18] S. Szwaja, V.B. Kovacs, A. Bereczky, A. Penninger, Sewage sludge producer gas enriched with methane as a fuel to a spark ignited engine, Fuel Process. Technol. 110 (2013) 160–166.

[19] K.B. Sutar, M.R. Ravi, S. Kohli, Design of a partially aerated naturally aspirated burner for producer gas, Energy 116 (2016) 773–785.

[20] A.A.P. Susastriawan, H. Saptoadi, Purnomo, Small-scale downdraft gasifiers for biomass gasification: A review, Renew. Sustain. Energy Rev. 76 (February) (2017) 989–1003.

[21] S. Sun, Y. Zhao, H. Tian, F. Ling, F. Su, Experimental study on cyclone air gasification of wood powder, Bioresour. Technol. 100 (17) (2009) 4047–4049.

[22] S. Sukumaran, S.C. Kong, Modeling fuel NOx formation from combustion of biomass-derived producer gas in a large-scale burner, Combust. Flame 160 (10) (2013) 2159–2168.

[23] N. Striūgas, V. Valinčius, N. Pedišius, R. Poškas, K. Zakarauskas, Investigation of sewage sludge treatment using air plasma assisted gasification, Waste Manag. 64 (2017) 149–160.

[24] N. Striugas, K. Zakarauskas, A. Džiugys, V. Grigaitiene, Experimental modelling of tar destruction with addition of CO2 for application in the biomass gasification system, Appl. Therm. Eng. 61 (2) (2013) 213–219.

[25] J. Street, F. Yu, J. Wooten, E. Columbus, M.G. White, J. Warnock, Gasoline-range hydrocarbon production using biomass derived synthesis gas over Mo/H +ZSM-5, Fuel 96 (2012) 239–249.

[26] D. Stanghelle, T. Slungaard, O.K. Sønju, Granular bed filtration of high temperature biomass gasification gas, J. Hazard. Mater. 144 (3) (2007) 668–672.

[27] G. Sridhar, P.J. Paul, H.S. Mukunda, Biomass derived producer gas as a reciprocating engine fuel - An experimental analysis, Biomass and Bioenergy 21

(1) (2001) 61–72.

[28] P. Sombatwong, P. Thaiyasuit, K. Pianthong, Effect of pilot fuel quantity on the performance and emission of a dual producer gas - Diesel engine, Energy Procedia 34 (2013) 218–227.

[29] V. Skoulou, G. Koufodimos, Z. Samaras, A. Zabaniotou, Low temperature gasification of olive kernels in a 5-kW fluidized bed reactor for H2-rich producer gas, Int. J. Hydrogen Energy 33 (22) (2008) 6515–6524.

[30] R.N. Singh, S.P. Singh, B.S. Pathak, Investigations on operation of CI engine using producer gas and rice bran oil in mixed fuel mode, Renew. Energy 32 (9) (2007) 1565–1580.

[31] R.N. Singh, U. Jena, J.B. Patel, A.M. Sharma, Feasibility study of cashew nut shells as an open core gasifier feedstock, Renew. Energy 31 (4) (2006) 481–487.

[32] J.P. Simanjuntak, Z.A. Zainal, Experimental study and characterization of a two-compartment cylindrical internally circulating fluidized bed gasifier, Biomass and Bioenergy 77 (2015) 147–154.

[33] H. Siddiqui, S.K. Thengane, S. Sharma, S.M. Mahajani, Revamping downdraft gasifier to minimize clinker formation for high-ash garden waste as feedstock, Bioresour. Technol. 266 (June) (2018) 220–231.

[34] A.M. Shivapuji, S. Dasappa, Analysis of thermodynamic scope engine simulation model empirical coefficients: Suitability assessment and tuning of conventional hydrocarbon fuel coefficients for bio syngas, Int. J. Hydrogen Energy 42 (26) (2017) 16834–16854.

[35] E. Shayan, V. Zare, I. Mirzaee, Hydrogen production from biomass gasification; a theoretical comparison of using different gasification agents, Energy Convers. Manag. 159 (December 2017) (2018) 30–41.

[36] M. Sharma, N. Rakesh, S. Dasappa, Solid oxide fuel cell operating with biomass derived producer gas: Status and challenges, Renew. Sustain. Energy Rev. 60 (2016) 450–463.

[37] H. Sadig, S.A. Sulaiman, M.A. Said, Effect of producer gas staged combustion on the performance and emissions of a single shaft micro-gas turbine running in a dual fuel mode, J. Energy Inst. 90 (1) (2017) 132–144.

[38] M.M. Roy, E. Tomita, N. Kawahara, Y. Harada, A. Sakane, Comparison of performance and emissions of a supercharged dual-fuel engine fueled by hydrogen and hydrogen-containing gaseous fuels, Int. J. Hydrogen Energy 36 (12) (2011) 7339–7352.

[39] D. Rovas, A. Zabaniotou, Exergy analysis of a small gasification-ICE integrated system for CHP production fueled with Mediterranean agro-food processing wastes: The SMARt-CHP, Renew. Energy 83 (2015) 510–517.

[40] G. Ravenni, Z. Sárossy, J. Ahrenfeldt, U.B. Henriksen, Activity of chars and activated carbons for removal and decomposition of tar model compounds – A review, Renew. Sustain. Energy Rev. 94 (October 2017) (2018) 1044–1056.

[41] P. Raman, N.K. Ram, Performance analysis of an internal combustion engine operated on producer gas, in comparison with the performance of the natural gas and diesel engines, Energy 63 (2013) 317–333.

[42] A.S. Ramadhas, S. Jayaraj, C. Muraleedharan, Dual fuel mode operation in diesel engines using renewable fuels: Rubber seed oil and coir-pith producer gas, Renew. Energy 33 (9) (2008) 2077–2083.

[43] P. Punnarapong, T. Sucharitakul, N. Tippayawong, Performance evaluation of premixed burner fueled with biomass derived producer gas, Case Stud. Therm. Eng. 9 (October 2016) (2017) 40–46.

[44] P. Punnarapong, A. Promwungkwa, N. Tippayawong, Development and Performance Evaluation of a Biomass Gasification System for Ceramic Firing Process, Energy Procedia 110 (December 2016) (2017) 53–58.

[45] G. Przybyla, A. Szlek, D. Haggith, A. Sobiesiak, Fuelling of spark ignition and homogenous charge compression ignition engines with low calorific value producer gas, Energy 116 (2016) 1464–1478.

[46] L. Prasad, P.M.V. Subbarao, J.P. Subrahmanyam, Experimental investigation on gasification characteristic of high lignin biomass (Pongamia shells), Renew. Energy 80 (2015) 415–423.

[47] D. Prando, S. Shivananda Ail, D. Chiaramonti, M. Baratieri, S. Dasappa, Characterisation of the producer gas from an open top gasifier: Assessment of different tar analysis approaches, Fuel 181 (2016) 566–572.

[48] D.T. Pio, L.A.C. Tarelho, R.G. Pinto, M.A.A. Matos, J.R. Frade, A. Yaremchenko, G.S. Mishra, P.C.R. Pinto, Low-cost catalysts for in-situ improvement of producer gas quality during direct gasification of biomass, Energy 165 (2018) 442–454.

[49] T. Piemsinlapakunchon, M.C. Paul, Effects of fuel compositions on the heat generation and emission of syngas/producer gas laminar diffusion flame, Int. J. Hydrogen Energy 44 (33) (2019) 18505–18516.

[50] N.P. Pérez, E.B. Machin, D.T. Pedroso, J.J. Roberts, J.S. Antunes, J.L. Silveira, Biomass gasification for combined heat and power generation in the Cuban context: Energetic and economic analysis, Appl. Therm. Eng. 90 (2015) 1–12.

[51] D.T. Pedroso, E.B. Machín, J.L. Silveira, Y. Nemoto, Experimental study of bottom feed updraft gasifier, Renew. Energy 57 (2013) 311–316.

[52] T.K. Patra, S. Mukherjee, P.N. Sheth, Process simulation of hydrogen rich gas production from producer gas using HTS catalysis, Energy (2019) 1130–1140.

[53] A.K.S. Parihar, T. Hammer, G. Sridhar, Development and testing of plate type wet ESP for removal of particulate matter and tar from producer gas, Renew. Energy 77 (2015) 473–481.

[54] P. Pradhan, A. Arora, S.M. Mahajani, A semi-empirical approach towards predicting producer gas composition in biomass gasification, Bioresour. Technol. (2019) 535–544.

[55] N.L. Panwar, B.L. Salvi, V.S. Reddy, Performance evaluation of producer gas burner for industrial application, Biomass and Bioenergy 35 (3) (2011) 1373–1377.

[56] M. Ouadi, J.G. Brammer, M. Kay, A. Hornung, Fixed bed downdraft gasification of paper industry wastes, Appl. Energy 103 (2013) 692–699.

[57] M.M. Omar, A. Munir, M. Ahmad, A. Tanveer, Downdraft gasifier structure and process improvement for high quality and quantity producer gas production, J. Energy Inst. 91 (6) (2018) 1034–1044.

[58] S.K. Nayak, P.C. Mishra, Achieving high performance and low emission in a dual fuel operated engine with varied injection parameters and combustion chamber shapes, Energy Convers. Manag. 180 (October 2018) (2019) 1–24.

[59] R. Navakas, A. Saliamonas, N. Striūgas, A. Džiugys, R. Paulauskas, K. Zakarauskas, Effect of producer gas addition and air excess ratio on natural gas flame luminescence, Fuel 217 (November 2017) (2018) 478–489.

[60] P.C. Murugan, S. Joseph Sekhar, Species – Transport CFD model for the gasification of rice husk (Oryza Sativa) using downdraft gasifier, Comput. Electron. Agric. 139 (2017) 33–40.

[61] T.Y. Mun, M.H. Cho, J.S. Kim, Air gasification of dried sewage sludge in a two-stage gasifier Part 3: Application of olivine as a bed material and nickel coated distributor for the production of a clean hydrogen-rich producer gas, Int. J. Hydrogen Energy 39 (11) (2014) 5634–5643.

[62] T.Y. Mun, J.S. Kim, Air gasification of dried sewage sludge in a two-stage gasifier Part 2: Calcined dolomite as a bed material and effect of moisture content of dried sewage sludge for the hydrogen production and tar removal, Int. J. Hydrogen Energy 38 (13) (2013) 5235–5242.

[63] T.Y. Mun, J.W. Kim, J.S. Kim, Air gasification of railroad wood ties treated with creosote: Effects of additives and their combination on the removal of tar in a two-stage gasifier, Fuel 102 (2012) 326–332.

[64] T.Y. Mun, J.O. Kim, J.W. Kim, J.S. Kim, Influence of operation conditions and additives on the development of producer gas and tar reduction in air gasification of construction woody wastes using a two-stage gasifier, Bioresour. Technol. 102 (14) (2011) 7196–7203.

[65] T.Y. Mun, P.G. Seon, J.S. Kim, Production of a producer gas from woody waste

via air gasification using activated carbon and a two-stage gasifier and characterization of tar, Fuel 89 (11) (2010) 3226–3234.

[66] N. Moriconi, P. Laranci, M. D'Amico, P. Bartocci, B. D'Alessandro, G. Cinti, A. Baldinelli, G. Discepoli, G. Bidini, U. Desideri, F. Cotana, F. Fantozzi, Design and preliminary operation of a gasification plant for micro-CHP with internal combustion engine and SOFC, Energy Procedia 81 (2015) 298–308.

[67] M. Mohon Roy, E. Tomita, N. Kawahara, Y. Harada, A. Sakane, Performance and emission comparison of a supercharged dual-fuel engine fueled by producer gases with varying hydrogen content, Int. J. Hydrogen Energy 34 (18) (2009) 7811–7822.

[68] F. Miccio, G. Ruoppolo, S. Kalisz, L. Andersen, T.J. Morgan, D. Baxter, Combined gasification of coal and biomass in internal circulating fluidized bed, Fuel Process. Technol. 95 (2012) 45–54.

[69] E. Menya, J. Olwa, P. Hagström, M. Okure, Assessment of pollution levels resulting from biomass gasification, J. Environ. Chem. Eng. 2 (3) (2014) 1228–1235.

[70] F. Meng, Q. Ma, H. Wang, Y. Liu, D. Wang, Effect of gasifying agents on sawdust gasification in a novel pilot scale bubbling fluidized bed system, Fuel 249 (February) (2019) 112–118.

[71] A. Melgar, J.F. Pérez, H. Laget, A. Horillo, Thermochemical equilibrium modelling of a gasifying process, Energy Convers. Manag. 48 (1) (2007) 59–67.

[72] J.D. Martínez, K. Mahkamov, R. V. Andrade, E.E. Silva Lora, Syngas production in downdraft biomass gasifiers and its application using internal combustion engines, Renew. Energy 38 (1) (2012) 1–9.

[73] C. Mandl, I. Obernberger, I.R. Scharler, Characterisation of fuel bound nitrogen in the gasification process and the staged combustion of producer gas from the updraft gasification of softwood pellets, Biomass and Bioenergy 35 (11) (2011) 4595–4604.

[74] S. Link, S. Arvelakis, A. Paist, A. Martin, T. Liliedahl, K. Sjöström, Atmospheric fluidized bed gasification of untreated and leached olive residue, and co-gasification of olive residue, reed, pine pellets and Douglas fir wood chips, Appl. Energy 94 (2012) 89–97.

[75] D. Laprune, D. Farrusseng, Y. Schuurman, F.C. Meunier, J.A.Z. Pieterse, A.M. Steele, S. Thorpe, Effects of H2S and phenanthrene on the activity of Ni and Rh-based catalysts for the reforming of a simulated biomass-derived producer gas, Appl. Catal. B Environ. 221 (2018) 206–214.

[76] K. Laohalidanond, N. Kongkaew, S. Kerdsuwan, Gasification Behavior Study of Torrefied Empty Corn Cobs, Energy Procedia 138 (2017) 175–180.

[77] L. Lang, W. Yang, J. Xie, X. Yin, C. Wu, J.Y.S. Lin, Oxidative filtration for flyash & tar removal from 10 MW th fixed-bed biomass air gasification, Biomass and Bioenergy 122 (January) (2019) 145–155.

[78] S. Lal, S.K. Mohapatra, The effect of compression ratio on the performance and emission characteristics of a dual fuel diesel engine using biomass derived producer gas, Appl. Therm. Eng. 119 (2017) 63–72.

[79] Y.D. Kim, S.H. Jung, J.Y. Jeong, W. Yang, U. Do Lee, Production of producer gas from waste cooking oil in a fluidized bed reactor: Influence of low-temperature oxidation of fuel, Fuel 146 (2015) 125–131.

[80] J.W. Kim, T.Y. Mun, J.O. Kim, J.S. Kim, Air gasification of mixed plastic wastes using a two-stage gasifier for the production of producer gas with low tar and a high caloric value, Fuel 90 (6) (2011) 2266–2272.

[81] M.D. Kaufman Rechulski, T.J. Schildhauer, S.M.A. Biollaz, C. Ludwig, Sulfur containing organic compounds in the raw producer gas of wood and grass gasification, Fuel 128 (March) (2014) 330–339.

[82] K. Jaojaruek, S. Jarungthammachote, M.K.B. Gratuito, H. Wongsuwan, S. Homhual, Experimental study of wood downdraft gasification for an improved producer gas quality through an innovative two-stage air and premixed air/gas supply approach, Bioresour. Technol. 102 (7) (2011) 4834–4840.

[83] W. Jangsawang, Utilization of Biomass Gasifier System for Drying Applications, Energy Procedia 138 (2017) 1041–1047.

[84] A. Tudge, Solution to grog on the cards, Aust. 90 (December 2015) (2015) 423–431.

[85] N. Homdoung, N. Tippayawong, N. Dussadee, Prediction of small spark ignited engine performance using producer gas as fuel, Case Stud. Therm. Eng. 5 (2015) 98–103.

[86] J.J. Hernández, M. Lapuerta, J. Barba, Flame stability and OH and CH radical emissions from mixtures of natural gas with biomass gasification gas, Appl. Therm. Eng. 55 (1–2) (2013) 133–139.

[87] S. Heidenreich, M. Müller, P.U. Foscolo, Fundamental Concepts in Biomass Gasification, Adv. Biomass Gasif. (2016) 4–10.

[88] F.M. Guangul, S.A. Sulaiman, A. Ramli, Study of the effects of operating factors on the resulting producer gas of oil palm fronds gasification with a single throat downdraft gasifier, Renew. Energy 72 (2014) 271–283.

[89] P. Gobbato, M. Masi, M. Benetti, Performance analysis of a producer gas-fuelled heavy-duty SI engine at full-load operation, Energy Procedia 82 (2015) 149–155.

[90] J. George, P. Arun, C. Muraleedharan, Experimental investigation on co-

gasification of coffee husk and sawdust in a bubbling fluidised bed gasifier, J. Energy Inst. (November) (2018) 1–10.

[91] M. Gabra, E. Pettersson, R. Backman, B. Kjellstrom, Evaluation of cyclone gasiÿer performance for gasiÿcation of sugar cane residue — Part 2 : gasiÿcation of cane trash, Biomass and Bioenergy 21 (2001) 371–380.

[92] P.P. Dutta, V. Pandey, A.R. Das, S. Sen, D.C. Baruah, Down draft gasification modelling and experimentation of some indigenous biomass for thermal applications, Energy Procedia 54 (03712) (2014) 21–34.

[93] A.E. Dhole, R.B. Yarasu, D.B. Lata, Effect of hydrogen and producer gas as secondary fuels on combustion parameters of a dual fuel diesel engine, Appl. Therm. Eng. 108 (2016) 764–773.

[94] J.L. de Oliveira, J.N. da Silva, M.A. Martins, E.G. Pereira, M. da Conceição Trindade Bezerra e Oliveira, Gasification of waste from coffee and eucalyptus production as an alternative source of bioenergy in Brazil, Sustain. Energy Technol. Assessments 27 (April) (2018) 159–166.

[95] S. Dattarajan, R. Kaluri, G. Sridhar, Development of a Combustor to burn raw producer gas, Fuel Process. Technol. 126 (2014) 76–87.

[96] Y.K. Choi, J.H. Ko, J.S. Kim, Gasification of dried sewage sludge using an innovative three-stage gasifier: Clean and H2-rich gas production using condensers as the only secondary tar removal apparatus, Fuel 216 (December 2017) (2018) 810–817.

[97] Y.K. Choi, J.H. Ko, J.S. Kim, A new type three-stage gasification of dried sewage sludge: Effects of equivalence ratio, weight ratio of activated carbon to feed, and feed rate on gas composition and tar, NH3, and H2S removal and results of approximately 5 h gasification, Energy 118 (2017) 139–146.

[98] Y.K. Choi, M.H. Cho, J.S. Kim, Air gasification of dried sewage sludge in a two-stage gasifier Part 4: Application of additives including Ni-impregnated activated carbon for the production of a tar-free and H 2 -rich producer gas with a low NH 3 content, Int. J. Hydrogen Energy 41 (3) (2016) 1460–1467.

[99] Y.K. Choi, T.Y. Mun, M.H. Cho, J.S. Kim, Gasification of dried sewage sludge in a newly developed three-stage gasifier: Effect of each reactor temperature on the producer gas composition and impurity removal, Energy 114 (2016) 121–128.

[100] M.H. Cho, Y.K. Choi, J.S. Kim, Air gasification of PVC (polyvinyl chloride)-containing plastic wasteina two-stage gasifier using Ca-based additives andNi-loadedactivated carbon for the production of clean andhydrogen-rich producer gas, Energy 87 (2015) 586–593.

[101] M.H. Cho, T.Y. Mun, Y.K. Choi, J.S. Kim, Two-stage air gasification of mixed plastic waste: Olivine as the bed material and effects of various additives and a nickel-plated distributor on the tar removal, Energy 70 (2014) 128–134.

[102] M.H. Cho, T.Y. Mun, J.S. Kim, Air gasification of mixed plastic wastes using calcined dolomite and activated carbon in a two-stage gasifier to reduce tar, Energy 53 (2013) 299–305.

[103] M.H. Cho, T.Y. Mun, J.S. Kim, Production of low-tar producer gas from air gasification of mixed plastic waste in a two-stage gasifier using olivine combined with activated carbon, Energy 58 (2013) 688–694.

[104] L. Chanphavong, Z.A. Zainal, Characterization and challenge of development of producer gas fuel combustor: A review, J. Energy Inst. (2018).

[105] S. Chalermcharoenrat, K. Laohalidanond, S. Kerdsuwan, Optimization of Combustion Behavior and Producer Gas Quality from Reclaimed Landfill Through Highly Densify RDF-Gasification.

[106] S. Bunchan, T. Poowadin, K. Trairatanasirichai, A Study of Throat Size Effect on Downdraft Biomass Gasifier Efficiency, Energy Procedia 138 (2017) 745–750.

[107] P.R. Bhoi, S.A. Channiwala, Emission characteristics and axial flame temperature distribution of producer gas fired premixed burner, Biomass and Bioenergy 33 (3) (2009) 469–477.

[108] N.R. Banapurmath, P.G. Tewari, Comparative performance studies of a 4-stroke CI engine operated on dual fuel mode with producer gas and Honge oil and its methyl ester (HOME) with and without carburetor, Renew. Energy 34 (4) (2009) 1009–1015.

[109] A. Arunachalam, D.B. Olsen, Experimental evaluation of knock characteristics of producer gas, Biomass and Bioenergy 37 (2012) 169–176.

[110] S. Anis, Z.A. Zainal, Upgrading producer gas quality from rubber wood gasification in a radio frequency tar thermocatalytic treatment reactor, Bioresour. Technol. 150 (2013) 328–337.

[111] S. Anis, Z.A. Zainal, Tar reduction in biomass producer gas via mechanical, catalytic and thermal methods: A review, Renew. Sustain. Energy Rev. 15 (5) (2011) 2355–2377.

[112] Z.A.B.Z. Alauddin, P. Lahijani, M. Mohammadi, A.R. Mohamed, Gasification of lignocellulosic biomass in fluidized beds for renewable energy development: A review, Renew. Sustain. Energy Rev. 14 (9) (2010) 2852–2862.

[113] K.A. Al-attab, J.C. Ho, Z.A. Zainal, Experimental investigation of submerged flame in packed bed porous media burner fueled by low heating value producer gas, Exp. Therm. Fluid Sci. 62 (2015) 1–8.

[114] A. Ahmed, B.G. Cateni, R.L. Huhnke, R.S. Lewis, Effects of biomass-generated producer gas constituents on cell growth, product distribution and hydrogenase activity of Clostridium carboxidivorans P7T, Biomass and Bioenergy 30 (7) (2006) 665–672.

[115] M.A. Adnan, M.M. Hossain, Gasification of various biomasses including microalgae using CO2 – A thermodynamic study, Renew. Energy 119 (2018) 598–607.

[116] M.A. Adnan, H. Susanto, H. Binous, O. Muraza, M.M. Hossain, Feed compositions and gasification potential of several biomasses including a microalgae: A thermodynamic modeling approach, Int. J. Hydrogen Energy 42 (27) (2017) 17009–17019.

[117] Y. Achawangkul, N. Maruyama, C. Chaichana, M. Hirota, Biomass gasification utilization for double-chambered crematory, Energy Procedia 52 (2014) 308–315.

[118] Z. Zhang, S. Pang, Experimental investigation of tar formation and producer gas composition in biomass steam gasification in a 100 kW dual fluidised bed gasifier, Renew. Energy 132 (2019) 416–424.

[119] P.C. Roy, A. Datta, N. Chakraborty, Assessment of cow dung as a supplementary fuel in a downdraft biomass gasifier, Renew. Energy 35 (2) (2010) 379–386.

[120] A.M. Valencia-López, F. Bustamante, A. Loukou, B. Stelzner, D. Trimis, M. Frenklach, N.A. Slavinskaya, Effect of benzene doping on soot precursors formation in non-premixed flames of producer gas (PG), Combust. Flame 207 (2019) 265–280.

[121] J. Hongrapipat, A.C.K. Yip, A.T. Marshall, W.L. Saw, S. Pang, Investigation of simultaneous removal of ammonia and hydrogen sulphide from producer gas in biomass gasification by titanomagnetite, Fuel 135 (2014) 235–242.

[122] B. de Mena, D. Vera, F. Jurado, M. Ortega, Updraft gasifier and ORC system for high ash content biomass: A modelling and simulation study, Fuel Process. Technol. 156 (2017) 394–406.

[123] D.S. Upadhyay, A.K. Sakhiya, K. Panchal, A.H. Patel, R.N. Patel, Effect of equivalence ratio on the performance of the downdraft gasifier – An experimental and modelling approach, Energy (2019) 833–846.

Appendix-2: Design development and commissioning of the test facility

Associated symbols, Acronyms, and Abbreviations

Core Chamber:

t_{cc}	Minimum shell thickness required (mm)
P_{cc}	Internal pressure (MPa)
R_{icc}	Inner radius (mm)
S_{cc}	Allowable stress (MPa)
E_{cc}	Joint efficiency
FS	Factor of Safety
Y_{cc}	Yield strength

Glass window:

t_{gw}	Thickness (mm)
R_{gw}	Unsupported radius (mm)
K_{gw}	Empirical constant; 0.75 if mounted with clamped edge(s)
P_{gw}	Pressure differential (MPa)
FS	Factor of safety
MOR	Modulus of rupture (MPa)

Fastener:

L_b	Minimum thread engagement length
A_{tb}	Tensile stress area
D_b	Diameter of the bolt
p_b	Threads per inch
P_b	Pressure Load
N_b	No. of fasteners required

Flange:

t_{fl}	flange thickness (mm)
M_{ofl}	total moment on the flange
Y_{fl}^{*}	shape factor value
S_{f_o}	allowable stress on the flange
B	flange Inner Diameter
M_D	moment due to H_D
M_T	moment due to H_T
M_G	moment due to H_G
H_D	hydrostatic end force on the inside of the flange
H_t	pressure force on the flange
H_G	gasket load
B	flange inner diameter

P_{fl} design pressure

H hydrostatic end force

G_{fl} diameter at gasket load reaction (mean dia)

C bolt circle diameter

The test facility design development was carried out in three stages per the regular engineering practice. The requirements, essential features, and different designs of core parts were discussed in the conceptual design phase. A particular design concept was selected based on the practical feasibility and extent of desired requirements. The major design parameters were defined, and other subsystems were identified with essential information during the preliminary design phase. The entire design parameters were calculated in detail and updated to achieve an optimized setup during the Detail design phase. After concluding this phase, the execution, redesign, and refinement were carried out.

Conceptual Design

The design parameters of the existing setups were collected and analyzed. The main complexities associated with double chamber setups from installation, operational, and maintenance points of view were found to be:

- Gas release mechanism connecting inner and outer chambers: The connection between the inner and outer chamber must be established immediately or just before the ignition. The gas release should be uniform; else, it will lead to flame front distortion. The gas diffusion between chambers should be considered to avoid mixture contamination. The gas release should be coupled with the successful ignition event.
- Inner and outer chambers: The inner chamber has to be placed at the center of the outer chamber. Gas release system installation, heating system, gas filling, instrument accommodation, and optical window alignment brings in several constraints on geometry and size.

- Gas filling and evacuation: Fresh gases must be fed into the inner chamber and outer chamber simultaneously while maintaining a specific differential pressure between them throughout the filling process. The burned gases should be purged and evacuated to achieve zero vacuum before refilling. Other complexities are gas mixing in the inner chamber and inert gas reutilization in the outer chamber.
- Heating system: Achieving a stable and uniform elevated temperature profile is necessary to obtain initial thermodynamic conditions and vaporize the liquid fuels. Isolating the instruments from heat and minimizing the heat loss and warm-up time are other challenges to be addressed.
- Other minor issues: Leak arresting techniques need to be implemented as high-pressure chambers are severely prone to leakages. It is almost impossible to achieve perfect flat surfaces in fabrication; misalignment and improper fittings must be dealt with as they lead to gas leaks. The more complex setup becomes with more number of parts, frequent and extended maintenance cycles will creep in.

A chamber with the following characteristics can address most of the above issues:

- Spherical inner chamber with optical access to monitor flame front evolution
- Flat surface for accommodating the instrumentation and pressure release systems
- Gas pressure release mechanism with the minimum number of moving parts, less complex, replaceable, reliable, and provision for synchronous operation.
- Non-exclusive, detachable, and spherical chambers with minimum required volume
- Simple heating mechanism with less warm-up time and with better active control
- Small maintenance cycle, provision for sample collection, and reuse of inert gases

Based on the above design requirements few design variants were developed:

Variant-1:

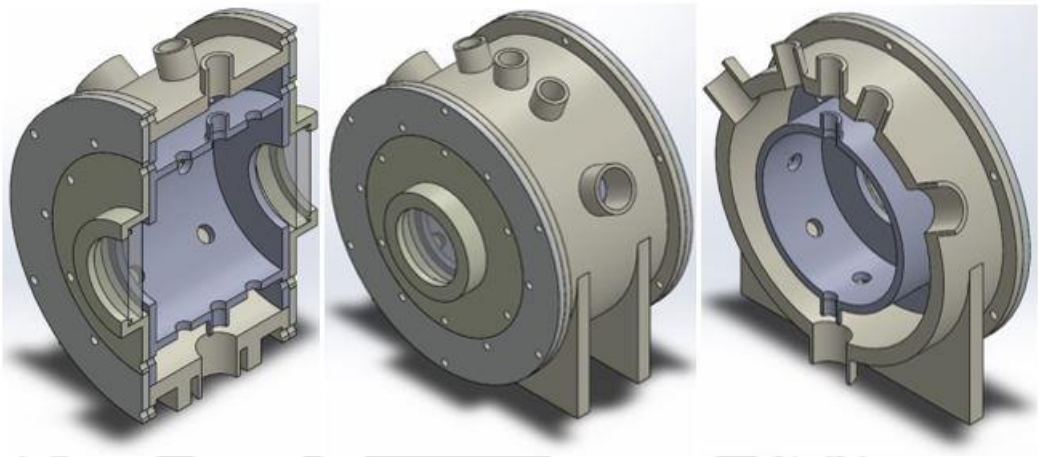

Figure A2-1 Sectional and projected view of variant-1

Two concentric cylindrical vessels were used as inner and outer chambers. The inner chamber was of unity aspect ratio. Two glass windows were used for optical access. Ports were made to accommodate instruments. The outer chamber was designed to be twice the inner chamber volume to cut downtime for heating and space occupancy. A small reservoir tank was necessary to compensate for the pressure rise. A smaller volume was chosen to achieve better control over the environment. Flanges were used to position the inner chamber, outer chamber, and glass windows.

Variant-2:

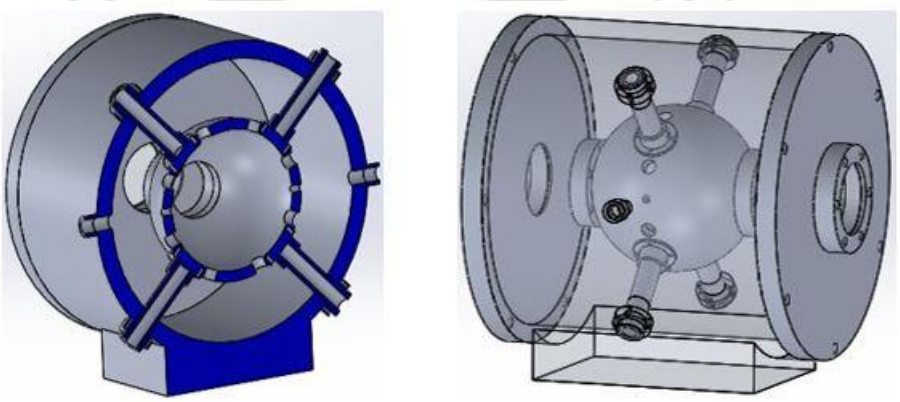

Figure A2-2 Sectional and projected view of variant-2

In this variant, the inner chamber was considered spherical in shape and ten times smaller in volume. A mounting tube was used to position the inner chamber. Four glass windows were used for optical access. This chamber offered the least flow distortion and symmetrical confinement due to the spherical inner chamber. Instruments were accommodated in spacious annular volume on the inner chamber surface. Unlike other designs, this integral chamber setup did not require an auxiliary tank.

Variant-3:

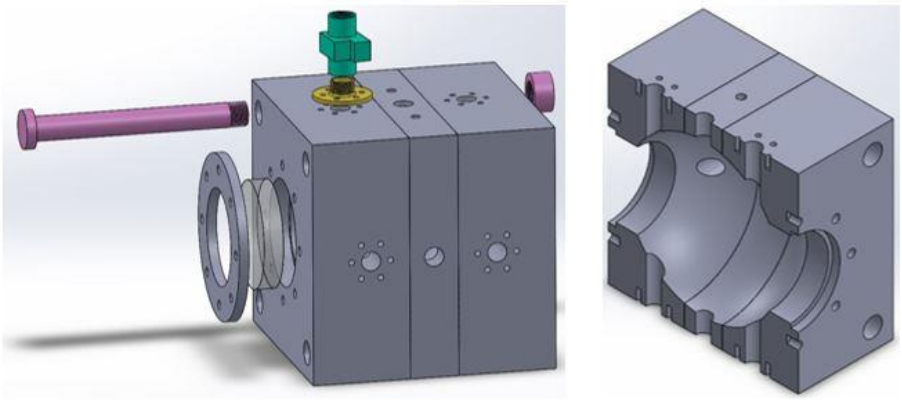

Figure A2-3 Sectional and projected view of variant-3

The inner chamber was mechanically separated from the outer chamber in this design. The primary combustion chamber was spherical from the inside and cubical on the outside. An additional reservoir was used to reduce the post-combustion pressure in the inner chamber. Two glass windows were used for optical access. Instruments were directly installed on the surface of the main chamber.

Preliminary Design

Iterative and incremental development with a concurrent design approach was adopted to develop the high-pressure combustion test facility. The core chamber was designed first, and other subsystems were developed incrementally due to the mechanical interactions, which depend on the parent structure dimensions.

Core Chamber

The three variants developed in the conceptual design phase have specific advantages and associated disadvantages. Small volume, fabrication, commercially available off-the-shelf parts, and ease of maintenance were the main advantages of variant-1. Flow distortion and instruments installation were the main drawbacks. The spherical inner chamber was the main advantage of variant-2. The main disadvantages were the fabrication, alignment issues, instruments placement, warm-up time, and maintenance. Moreover, the chambers were exclusive and could not be replaced by a chamber with different specifications. Variant-3 had the advantage of spherical geometry and plain surface for instrumentation installation. The main chamber and reservoir can be replaced with chambers of different specifications. Heating the main chamber was sufficient, unlike heating the entire setup in other variants. Provision for testing different gas release mechanisms was also possible in this variant. Due to all these reasons, variant-3 was considered for the present study.

The following were set as the constraints:

Table A2-1 Design constraints

Sl.No	Design parameter	Constraint
1	Volume of the sphere	≥20 cm diameter
2	Optical window visibility	≥10 cm diameter
3	Heating cartridges	Vertically aligned
4	Working Pressure	100 bar
5	Material	Non-Magnetic SS
6	Temperature	500 K
7	Ports	Standard 1/2” BSP
8	Sealing	Step and O-ring

The chamber has been modified iteratively by considering the above necessary constraints.

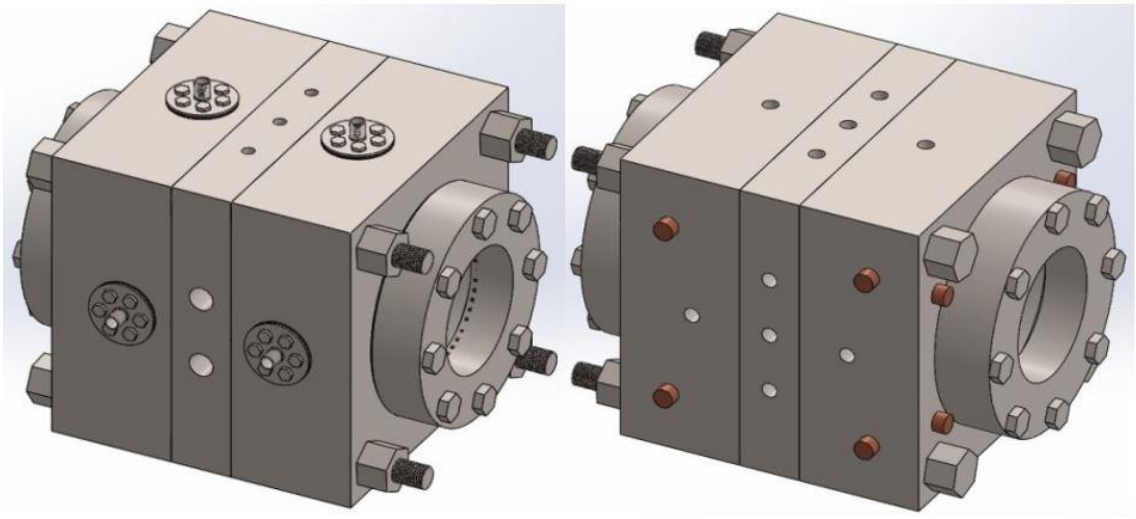

Figure A2-4 Designs at the end of 4th and 5th iterations

Subsystems with processes

Table A2-2 Subsystems with associated processes of the test facility

Sl.No	List of processes	Functionality
1	Purging	To purge the chamber with air after the combustion to replace the burned gases and bring down the chamber temperature.
2	Evacuating	To evacuate the leftover gases from the chamber after combustion & purging before creating a vacuum to refill with fresh gases.
3	Filling	To channel the high purity fresh gases from cylinders to the chamber to fill it with the desired combustible mixture.
4	2nd chamber	To collect the gases from the core chamber with active control during/at the end of the spherical flame propagation.
5	Heating	To achieve a stable and uniform set temperature in the core chamber with minimum warm-up time.

6	Ignition	To generate a spark of specific energy and duration at the center of the chamber upon triggering.
7	Imaging	To capture the propagating flame with an excellent resolution to facilitate edge and cracks detection.
8	Triggering	To send the trigger signals to the various devices/systems depending on the response times in synchronization with ignition.
9	Data Acquisition	To acquire, monitor, and store the data of important parameters.

Core Chamber Detail Design

The development details of the core chamber have been reported concisely in the following sections.

Core Chamber

Table A2-3 Design specifications of core chamber design parameters

Sl.No	Design Parameter	Specification
1	Material	SS321: High-temperature application SS304: Standard grade
2	Chamber Diameter	200 mm
3	Working Pressure	100 bar

Development:

The thickness of the Spherical chamber was calculated from the formula based on the Inner Diameter

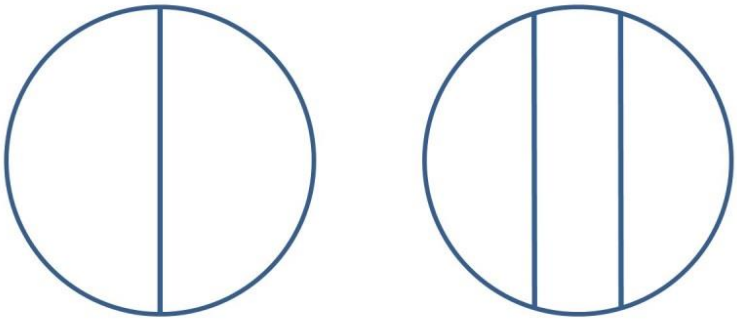

Figure A2-5 Schematic diagram of sphere assembly

$$t_{cc} = \frac{P_{cc}R_{icc}}{2S_{cc}E_{cc}\text{-}0.2P_{cc}} \quad (1)$$

$$S_{cc} = \frac{Y_{cc}}{FS} \quad (2)$$

Table A2-4 Shell thickness calculation for multiple combinations

Sl.No.	Case				Thickness (in mm)
1	P_{cc} = 10	E_{cc} = 0.8	FS = 4	Y_{cc} = 205	12.5
2				Y_{cc} = 240	10.6383
3			FS = 2	Y_{cc} = 205	6.17284
4				Y_{cc} = 240	5.263158
5		E_{cc} = 0.6	FS = 4	Y_{cc} = 205	16.80672
6				Y_{cc} = 240	14.28571
7			FS = 2	Y_{cc} = 205	8.264463
8				Y_{cc} = 240	7.042254

The original formula was for a spherical chamber formed by joining two parts. In the present case, three parts were considered with a trade-off in joint efficiency. It was evident from the above calculations that the thickness value varied from 5.26 mm to 16.8 mm depending on the various combinations of the mechanical and design properties.

Considered value: 25mm

Reverse calculation: Assuming the best combination Y_{cc}= 240 MPa, FS = 2, R_{icc} = 100 mm and E_{cc} = 0.8

Resulting withstand Pressure: 45.71 MPa

From the reverse calculation, the setup can easily go up to 450 bars with a safety factor of 2.

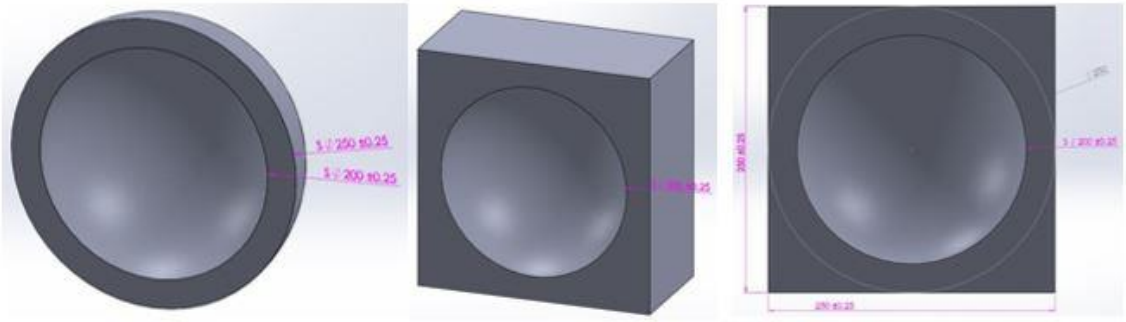

Figure A2-6 CAD models of the Spherical Shell

Instead of a spherical shell, a spherical inner and cubical outer was chosen for fabrication and facilitating the mounting of other parts and instruments on the outer surface.

Glass Window

Table A2-5 Design specifications of glass window

Sl.No	Design Parameter	Specification
1	Material	GE-124; Very pure fused quartz and made from crystalline silica. It has excellent thermal properties and high chemical resistance (stain-resistant). BK-7; Regular glass and typically used in visible light applications
2	Shape	Circular
3	Clear Aperture Diameter	100 mm
4	Working Pressure	25 & 40 bar

Development:

The thickness of the glass was calculated depending on the unsupported portion, pressure differential expected, and rupture modulus of the glass. Modulus of rupture was a measure of the specimen's strength before rupture since glass was more prone to break than bend.

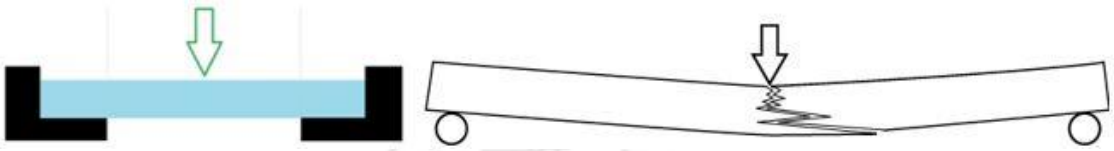

Figure A2-7 Failure of the glass at an unsupported portion on load application

$$t_{gw} = R_{gw} * \sqrt{\frac{P_{gw} K_{gw} FS}{MOR}} \qquad 3$$

Desired clear aperture has been 100 mm; to avoid the optical distortion effect at the boundary 106 mm diameter has been considered.

Table A2-6 Glass thickness calculation for multiple combinations

Sl. No.	**Case**			**Thickness(in mm)**
1	K_{gw} = 0.75 R_{gw} = 53 FS = 4	P_{gw} = 2.5 MPa	MOR = 80 MPa	16.84024
2			MOR = 16.55 MPa	37.02494
3			MOR = 63.5 MPa	18.90194
4		P_{gw} = 4 MPa	MOR = 80 MPa	21.30141
5			MOR = 16.55 MPa	46.83325
6			MOR = 63.5 MPa	23.90928

Considered value: 35mm

Reverse calculation: Assuming the best combination K_{gw} = 0.75, R_{gw} = 53 mm, MOR = 80 MPa and SF = 4.

Resultant withstand Pressure: 10.8 MPa

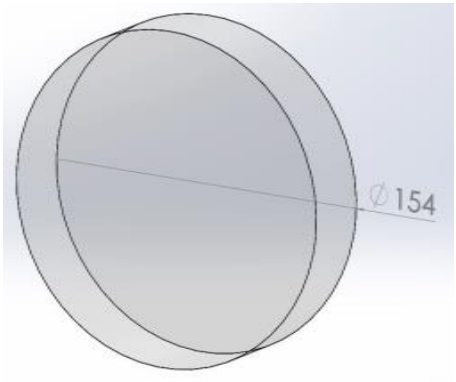

Figure A2-8 CAD model of the glass window

110 mm diameter potion would be unsupported and up to 154 mm diameter supported by flanges on 22 mm wide strip.

Optical Window Sealing

The glass was placed between rubber materials to avoid direct contact with metal for two reasons. The first was to prevent the leakage of the gases due to imperfect contact between surfaces. The second was to provide a facility for glass expansion and contraction due to temperature fluctuations.

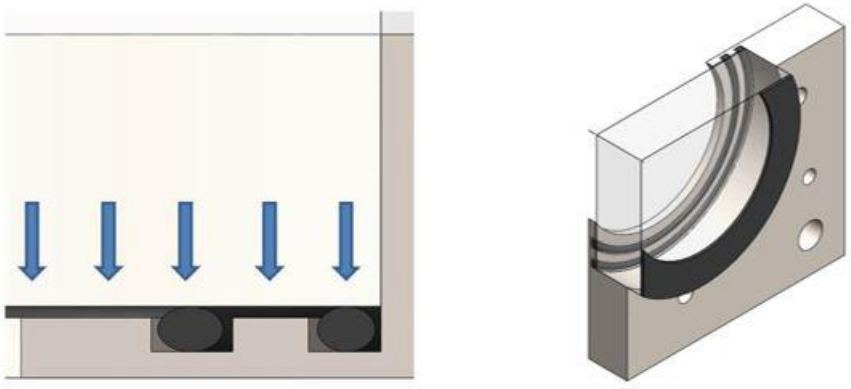

Figure A2-9 O-ring placements in the optical window slot

O-ring:

O-rings offer better leak arrest when compared to gaskets. Hence these were chosen with the prime goal to arrest the leakage. Two O-rings were placed between the cubical chamber and glass. The force exerted by the flange on the glass led to compression of O-rings. Two rings were used to distribute the load on the glass and for better leak protection. 4mm diameter O-rings were placed in 5 mm wide and 2 mm deep grooves, and glass was directly placed over them. 64.5 mm and 74.5 mm were the mean diameters of the grooves. Commercially available O-ring cords were cut and customized as per the requirement. The gasket was placed between the glass window and flange inner surface. These gaskets act as cushion layers for glass windows to counter the load of the internal pressure developed inside the chamber due to combustion and default exerted force by the fasteners.

Flanges and Fasteners

Table A2-7 Design specifications of Flanges and Fasteners

Sl.No	Design Parameter	Specification
1	Material	SS321: High-temperature application SS304: Standard grade
2	Inner Diameter	110 mm
3	Contact strip width	20 mm
4	Working Pressure	40 bar
5	Bolts	M12-16

Development:

The flange design was approximated to the ring flange design and developed for the given requirement.

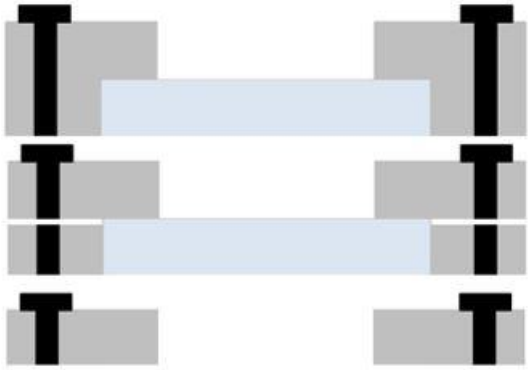

Figure A2-10 Ring flange approximation

Bolts:

Table A2-8 Details of the fastener properties

Bolt diameter(mm)	**Coarse Pitch(mm)**	**Stress Area(mm^2)**	**Fine pitch(mm)**	**Stress Area(mm^2)**
M12	1.75	84.27	1.5	88.13
M14	2.00	115.45	1.5	124.45
M16	2.00	156.68	1.5	167.26

Table A2-9 Details of the fastener classification

Class	**Proof load**
8.8	580 MPa
10.9	830 MPa

Development:

Force experienced by bolts = Force experienced by the glass window

In high-pressure conditions, the force exerted by the compressed gasket was neglected.

Force = Design Pressure × Area Exposed

Force balance equation:

No. of bolts × Stress Area of each bolt × Allowed proof load = Total force experienced

Allowed proof load = Proof load / Safety factor

Table A2-10 Minimum number of fasteners calculation for multiple combinations

Sl. No.	Case				N_b	Min No. of Bolts
1	P_b= 10 MPa	Class 10.9 (830 MPa)	M12	SF = 6	7.795153	8
2				SF = 4	5.196769	6
3				SF = 2	2.598384	3
4			M14	SF = 6	5.520184	6
5				SF = 4	3.680122	4
6				SF = 2	1.840061	2
7			M16	SF = 6	4.107299	5
8				SF = 4	2.738199	3
9				SF = 2	1.3691	2

Minimum thread length engagement:

$$L_b = \frac{2A_{tb}}{0.5\pi(D_b - 0.64952p_b)} \quad 4$$

Table A2-11 Minimum thread engagement length for different bolts

Sl. No.	Bolt	Pitch(mm)	Min. Thread engagement Length (mm)
1	M12	1.75	9.735312
2		1.50	10.0523
3	M14	2.00	11.42594
4		1.50	12.05992
5	M16	2.00	13.43508
6		1.50	14.0716

The general rule of thumb: The length of thread engagement should be equal to or greater than one full diameter of the bolt and be of comparable strength.

Table A2-12 Minimum thread engagement length based on rule of thumb for bolts

Bolt	Min. Thread engagement Length (mm)
M12	12
M14	14
M16	16

Considered values: Upon comparing the bolt diameter, number, and thread engagement length, the following combination looks more suitable for the setup.

Table A2-13 Considered bolt specification values

Bolt	M12
Class	10.9
Pitch	1.5
Threading	Fine
Number of bolts	8
Minimum thread engagement length	20mm

Reverse calculation:

Table A2-14 Combined withstand pressure of all fasteners from the reverse calculation

SF	**Withstand pressure**
6	10.263 MPa
4	15.394 MPa
2	30.788 MPa

Hence the above-considered bolts can withstand up to 300 bars safely.

Ring Flange:

Figure A2-11 Ring flange

Development:

$$t_{fl} = \sqrt{\frac{M_{ofl} Y^*_{fl}}{S_{f_o} B}} \quad (5)$$

$$M_o = M_D + M_T + M_G \quad (6)$$

$$M_D = H_D h_D \quad (7)$$

$$M_T = H_T h_T \quad (8)$$

$$M_G = H_G h_G \quad (9)$$

$$H_D = \frac{\pi B^2 P_{fl}}{4} \quad (10)$$

$$H_T = H - H_D \quad (11)$$

$$H = \frac{G_{fl}^2 \pi P_{fl}}{4} \quad (12)$$

$$h_D = \frac{1}{2}(C-B). \quad (13)$$

$$h_T = \frac{1}{2}(h_D + h_G) \quad (14)$$

$$h_G = \frac{1}{2}(C-G) \quad (15)$$

Determination of bolt circle diameter:

$$C = B + 2R_{fl} \quad (16)$$

R_{fl} = 20 mm

B = 110 mm

C = 150 mm

Determination of flange Outer diameter:

$$A = C + 2E \qquad (17)$$

$$E = 15.5 \text{ mm}$$

$$A = 181 \text{ mm}$$

Since the value obtained from the above calculation cannot be directly used as this was for a different flange and the geometrical parts in contact were quite different. The following dimensions were considered after considering the bolt diameter and fabrication ease.

Table A2-15 Intermediate design parameter calculation

Sl. No.	A (O.D.)	B(I.D.)	C (Bolt circle)	G (P_{fl} loading)
1	190	106	172	130
2	190	108	172	131
3	190	110	172	132
4	200	106	177	130
5	200	108	177	131
6	200	110	177	132

Table A2-16 Flange thickness for various combinations

Sl.No	Case							Thickness (mm)
	P	FS	Y	A	B	C	G	
1	10 MPa	4	205	190	106	172	130	51.48155
2				190	108	172	131	51.50384
3				190	110	172	132	51.51065
4				200	106	177	130	51.39175
5				200	108	177	131	51.4189
6				200	110	177	132	51.36207
7			240	190	106	172	130	47.57984
8				190	108	172	131	47.60043
9				190	110	172	132	47.60673
10				200	106	177	130	47.49684

11				200	108	177	131	47.52194
12				200	110	177	132	47.46941
13			215	190	106	172	130	50.27005
14				190	108	172	131	50.29181
15				190	110	172	132	50.29847
16				200	106	177	130	50.18236
17				200	108	177	131	50.20888
18				200	110	177	132	50.15338
19		2	205	190	106	172	130	36.40296
20				190	108	172	131	36.41871
21				190	110	172	132	36.42353
22				200	106	177	130	36.33945
23				200	108	177	131	36.35866
24				200	110	177	132	36.31847
25			240	190	106	172	130	33.64403
26				190	108	172	131	33.65859
27				190	110	172	132	33.66304
28				200	106	177	130	33.58533
29				200	108	177	131	33.60308
30				200	110	177	132	33.56594
31			215	190	106	172	130	35.5463
32				190	108	172	131	35.56168
33				190	110	172	132	35.56639
34				200	106	177	130	35.48429
35				200	108	177	131	35.50304
36				200	110	177	132	35.46379

From the above calculations, the following trends were observed: 1. Thickness reduced with increasing outer diameter. 2. Thickness reduced with reducing bolt circle

Table A2-17 Flange design parameters

Design Parameter	Length (mm)
Flange Inner diameter	110
Glass Outer diameter	154
Mean Force loading diameter	132
Bolt circle diameter	178
Flange Outer diameter	200
Flange Thickness (excluding glass accommodation)	35
Complete flange thickness	45(+1)

Reverse calculation:

Considering the above specifications, the least yield strength case and safety factor 2 the withstand pressure had come around 8.8109 MPa. But the yield strength was expected to be more than the considered value, and the outer thickness was around 45 mm. From these considerations, the flange can withstand 10 MPa safely.

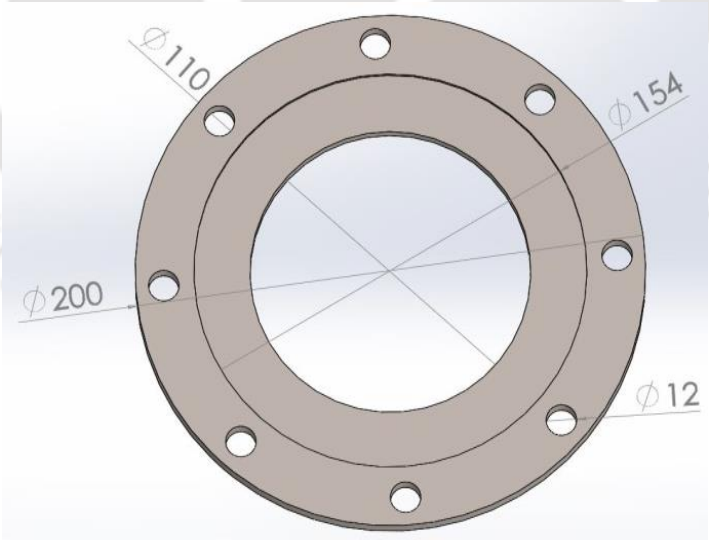

Figure A2-12 CAD model of the flange

Ports

Table A2-18 Instrument port details

Sl.No.	Purpose	Diameter	No.s	Location
1	Gas release	0.5 inch	8	2 on each face excluding front and back
2	Ignition port	0.5 inch	2	One on top and the other on the bottom face
3	Gas injection and evacuation	0.5 inch	2	On side face
4	Safety valves	0.5 inch	2	Bottom face
5	Static Pressure sensor port	0.5 inch	1	Top face
6	Unsteady Pressure sensor port	14 mm	1	On the left side face
7	Temperature sensor port	0.5 inch	1	On Side face
8	Emission analyser port	0.5 inch	1	On side face
Total			18	

All the ports were half-inch diameter with BSP threading except the unsteady pressure transducer port (instrument-specific). Extension and reducers will be used to accommodate all the other instruments.

With all the above considerations, the setup was designed to easily withstand up to 100 bar pressure**.**

Detail Design of Subsystems/Subprocesses

Filling System

Functionality: Tap the high purity fresh gases from sources and fill the chamber with the required amount.

Crucial components: Gas cylinders with regulators, ball valves, needle valves, steel pipes, connectors, adapters, and steel braided hoses.

Layout/Connection: The Gas cylinders were connected to the main flow control panel with braided hoses and ball valves. All the gas inlets were further connected to a single outlet that went down to the chamber. A needle valve was placed between the inlet and chamber.

Operation: The partial pressures of the gases in the mixture to be burnt will be calculated prior. The inlet line from the control panel will be vacuumed and flushed with new gas after filling up with previous gas. The gases will be filled with the lowest partial pressure first, and so on. The needle valve operated manually to control the flow and a static pressure transducer reading as feedback.

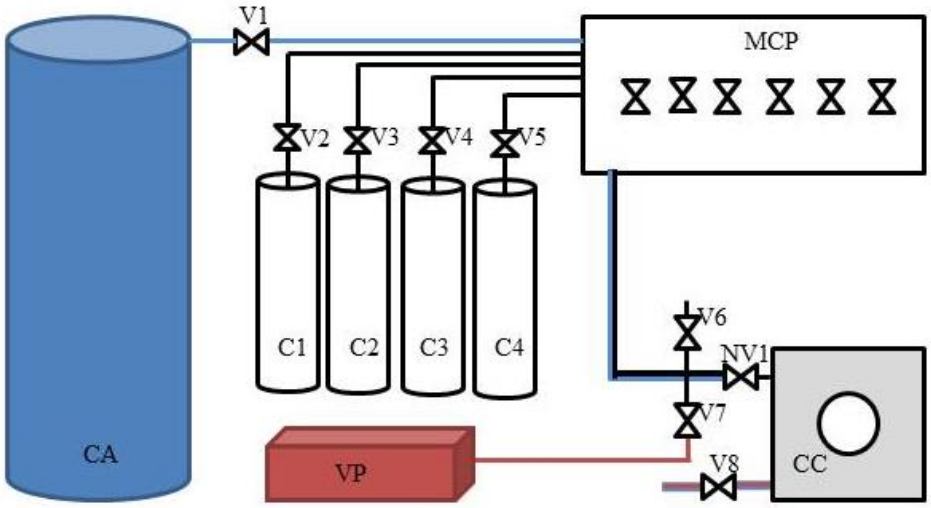

Figure A2-13 Schematic of the gas line system. Black, Blue, and Red connection lines correspond to filling, Purge, and Exhaust systems respectively.

Purging System

Functionality: To purge the chamber with air after the combustion to replace the burnt gases and bring down the chamber temperature.

Crucial Components: Compressed air, braided plastic hose, ball valves, and necessary connectors.

Layout/Connection: The ambient air was compressed and stored in a tank. A braided plastic hose was used to connect with the main control panel. The single inlet line used in the filling system was common. An outlet line with a ball valve was fitted to the chamber in a different port.

Operation: The compressed air will be supplied to the chamber, circulating inside the chamber and leaving through the outlet line. This operation continues for a few minutes until the temperature comes down to a stable set value.

Evacuation System

Functionality: To evacuate the burned gases from the chamber after combustion and create a vacuum before refilling with fresh gases.

Crucial Components: Vacuum pump, braided plastic hose, ball valves, and necessary connectors.

Layout/Connection: The vacuum pump was connected to the T-junction of the single inlet line with a braided plastic hose. An outlet line with a ball valve was fitted to the chamber in a different port.

Operation:

a) The outlet line will be opened after the combustion, and the burned gases will be vented out because of the pressure differential.

b) The vacuum pump will draw the trapped gases in the inlet line and chamber during the filling stage. The outlet line will remain closed while creating a vacuum in the chamber.

Reservoir System

Functionality: To draw the gases from the core chamber and feed them to the auxiliary chamber with active control over the flow.

Crucial Components: Auxiliary tank, manifold, steel braided hoses, solenoid valves, and necessary connectors.

Layout/Connection: The gas outlets from the chamber were connected to the manifold, and solenoid values were placed in between. The manifold was further connected to an auxiliary tank nearly ten times the combustion chamber volume.

Operation: The manifold and auxiliary tank will be filled with inert gases at the combustion chamber pressure. A trigger signal synchronized with the ignition will be sent to a relay system connected to the solenoid valves. The normally closed solenoid valves will open and allow the gases to rush into the manifold. The solenoid values de-energize after the specific set time duration, and valves will be closed.

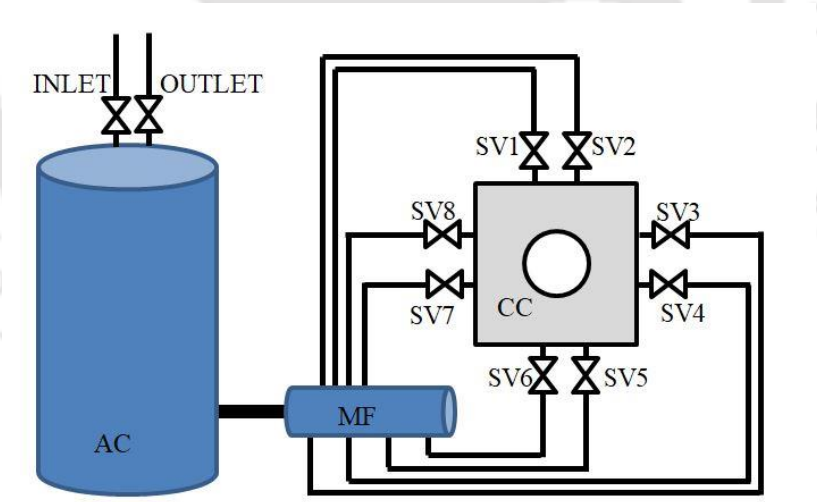

Figure A2-14 Schematic of the reservoir system

Ignition System

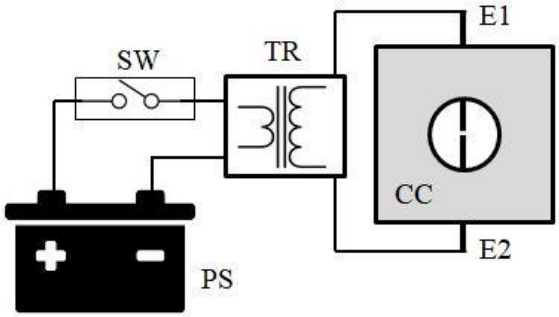

Figure A2-15 Schematic of the Ignition system

Functionality: Generate a spark of specific energy and duration at the center of the chamber after the trigger.

Crucial Components: DC power source, relay system, step-up voltage coil, electrodes, and insulation material.

Layout/Connection: The DC power source was connected to the step-up coil, which amplified the voltage to multiple folds. A relay switch was placed in between to avoid continuous supply. The output terminals of the coil were connected to the electrodes mounted on the chamber.

Operation: The relay allows the current to flow to the coil after receiving the trigger signal. The voltage will multiply, and the air between the electrodes breaks down to conduct the current. As a result, a spark will be generated at the breakdown location leading to ignition.

Heating System

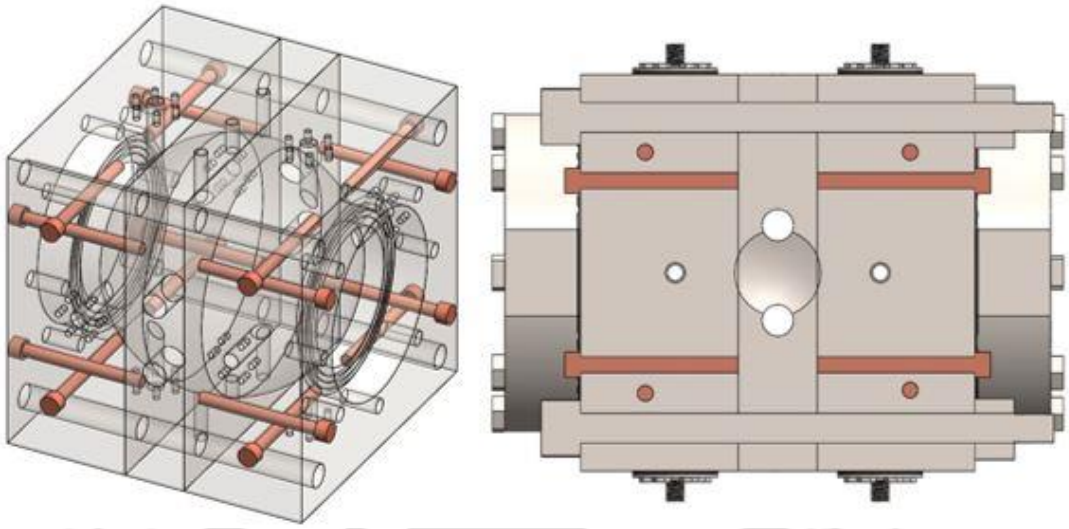

Figure A2-16 Schematic of heating system

Functionality: Achieve a stable and uniform set temperature in the core chamber with minimum warm-up time.

Crucial Components: AC power source, a temperature control box with multiple controllers, indicators, heating cartridges, and thermocouples.

Layout/Connection: The AC power source was connected to the temperature control box. The heating cartridges inserted into the chamber were connected to the control box. Thermocouples were inserted at various locations in the chamber to measure the local temperature.

Operation: The desired temperature will be set in the control box. The current supply to the cartridges will be regulated by the temperature controller from the thermocouple feedback. The desired temperature will be achieved and maintained by the PID controller throughout the run.

Imaging System

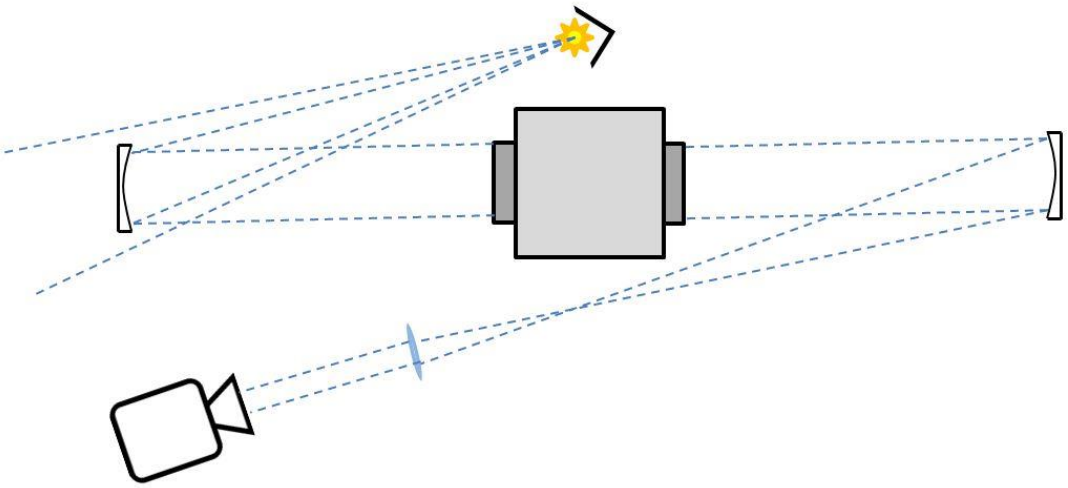

Figure A2-17 Schematic of the imaging system

Functionality: To capture the propagating flame with great detail, especially the cracks and edges of the flame. Both shadowgraph and Schlieren techniques captured the required edge details because of their density gradient dependence.

Crucial Components: Light source, High reflectivity concave mirrors, a double convex lens, and high-speed camera.

Arrangement: The light source was kept close to the central axis of the concave mirrors at a distance of focal length. Nearly double the focal length distance was maintained between concave mirrors. A double convex lens was placed on the reflected path of the beam from the secondary mirror after the focal point. A high-speed camera was placed after the lens to capture the light.

Operation: The diverging light rays become parallel rays after getting reflected by the concave mirror. The parallel rays then pass through the optical windows and fall on the second concave mirror on the other end. The mirror reflects the beam into converging and diverging rays. The rays converge at the focal point and then diverge. A double convex lens will be placed to make the diverging rays parallel. The camera will be positioned such that these parallel rays fall on the camera sensor. The recording will start after getting the trigger signal synchronized with the ignition event.

Triggering System

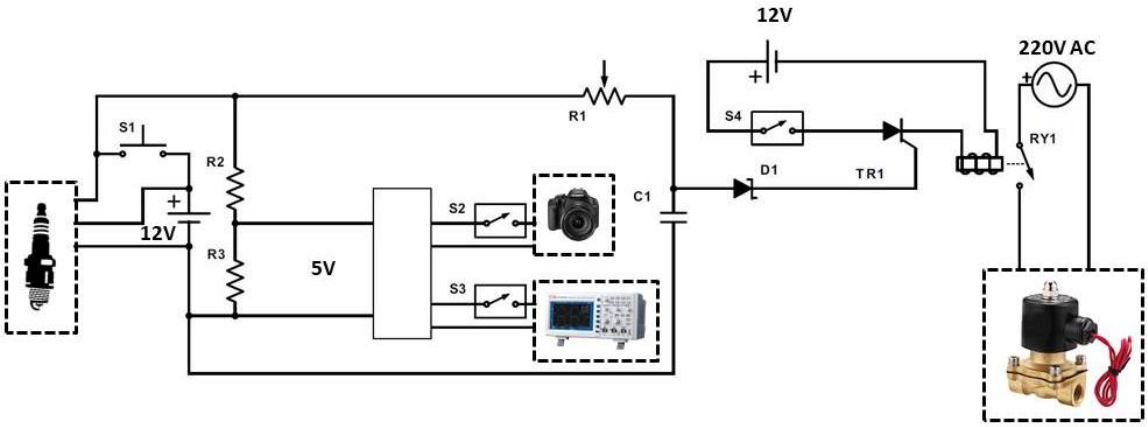

Figure A2-18 Schematic of triggering system

Functionality: To send the signals to the various devices/systems depending on their reaction time in synchronization with the ignition event.

Crucial Components: DC power source, resistors, Zener diode, variable resistor, relay, and necessary connectors.

Operation: The electrical and electronic components are arranged and connected as depicted in the above figure. The input signal from the user will generate four trigger signals to different systems. Three systems such as ignition, imaging, and data acquisition require a 5V gate signal and solenoid valves of the reservoir system require a continuous step signal.

Data Acquisition System

Functionality: To monitor the live parameters, record and store the measured data of the experiment.

Crucial Components: Static pressure transducers, unsteady pressure transducers, thermocouples, computer system, charge amplifier, indicators, and oscilloscope.

Arrangement & Operation:

- The temperature of the core chamber was measured continuously by using a thermocouple. The temperature will be monitored most of the time and recorded for specific instances.
- The absolute pressure of the chamber was monitored by using a static pressure transducer for leaks and internal pressure. The output will be recorded during the filling stage and monitored for the rest of the time.
- Unsteady pressure transducer transmits the change in the pressure. The current signal from the transducer will be converted and amplified by the charge amplifier into a voltage signal. These signals are then recorded using an oscilloscope.
- The flame propagation images captured by the high-speed camera will be stored in a computer system.

Mounting:

Functionality: To accommodate the core chamber, manifold, gas release valves, etc., systems/instruments in their respective position within a small space.

Crucial Components: Aluminium profiles, connectors, MS base plates, SS studs, nuts, and heavy-duty wheels.

Arrangement: The lightweight and high-strength aluminum profiles were fixed as per the above figure. The core chamber was placed over the base plat with access to the bottom part. The height of the chamber was adjusted with the help of studs. The heavy-duty wheels with a lock facility give mobility to the system.

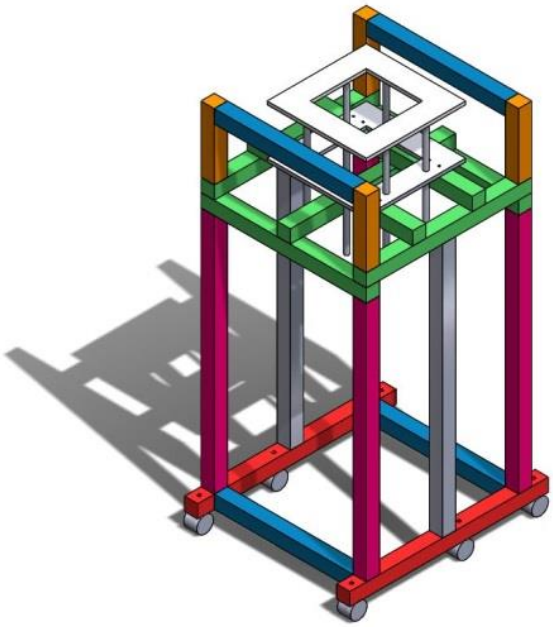

Figure A2-19 Schematic of mounting system

Execution and Refinement

Due to the adoption of the concurrent development approach, design, fabrication, and refinement were carried out simultaneously. The design modification in any system could be because of a constraint/challenge from the same or another system. The components and subsystems were developed to achieve an optimized assembly performance rather than individual optimized performance.

Core Chamber

Stainless steel 321 grade was forged into billets. SS321 has high corrosion resistance, enhanced creep resistance, and stress rupture than standard grades of stainless steel, even at high temperatures ranging up to 800°C. Regular applications include piston engine manifolds, chemical processing equipment, etc. It exhibits good toughness even in the lower temperature range. Because of these properties, the machining was challenging with the regular tools. The feed rate was kept at a very low value, and High-speed steel (HSS) tool bits were used. A customized T-shaped tool bit whose functionality was similar to the lollypop tool bit was fabricated and used to achieve a curved shape in the central part.

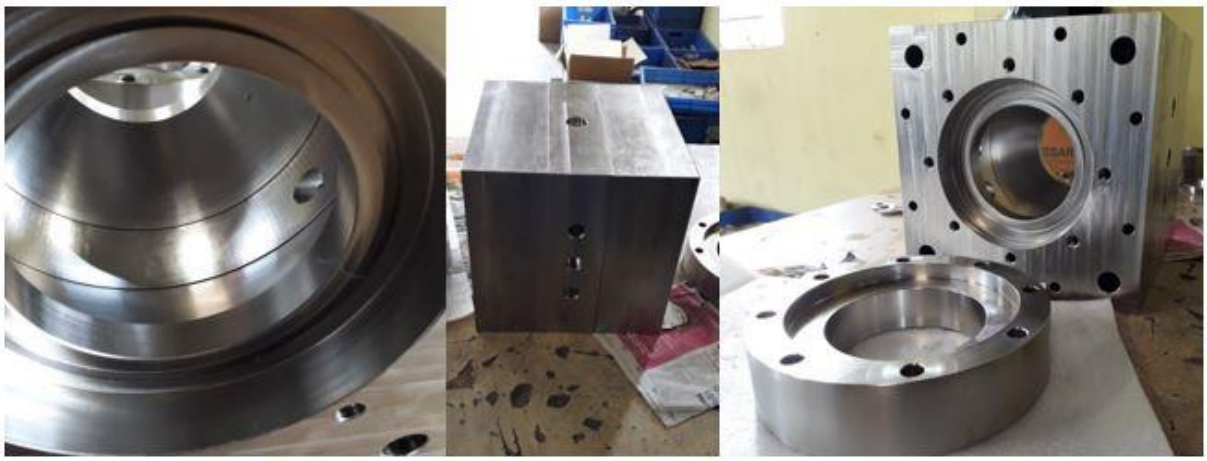

Figure A2-20 Chamber parts during fabrication

Due to the fabrication difficulty, the dual O-ring groves for leak arrest at optical window slots were reduced to a single O-ring groove of a bigger size. In the case of heating cartridge failure, removing the damaged part will become challenging in the case of side

entry cylindrical slots. Hence, the side entry slots were replaced by the front entry thru slots for ease of removal, further reducing the machining time.

Sub systems

Filling, purging, and evacuation system

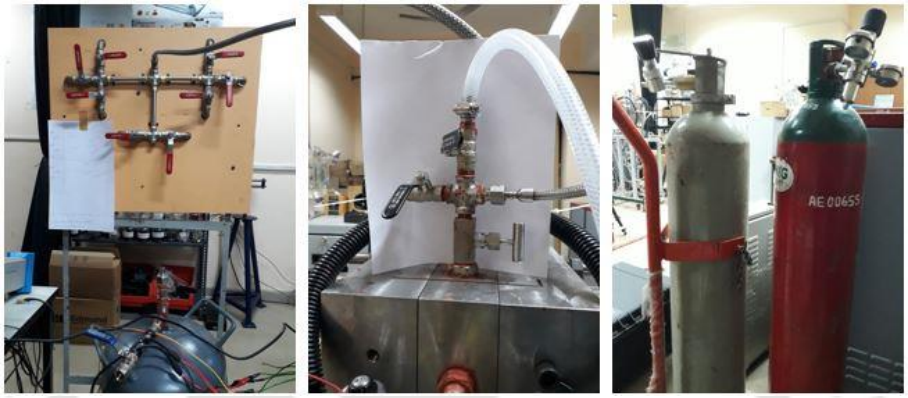

Figure A2-21 Filling system

The systems have not gone under any significant modifications. A dedicated cylinder cage and complete steel tubes connections were considered for upgradation.

Figure A2-22 Purge and Evacuation systems

Reservoir system

Figure A2-23 Reservoir system

A 50 L steel tank was used for the auxiliary tank. All the steel braided hoses have a pressure withstand capacity of 150 bar. Simultaneous operation of solenoid valves leads to maximum flow rate and highest pressure drop in the combustion chamber. Dedicated electromagnetic relays for each solenoid valve were tested. The reaction time was found to be long and varying among the relays. These were replaced with a solid-state relay which offered significantly lower reaction time. A single channel parallel connection addressed the variable delay. The relays were normally in OFF state, and they conduct upon supply of 5V DC.

Figure A2-24 8-channel electromagnetic relay and 4-channel solid state relay

Ignition system

Figure A2-25 12V Acid Battery and Adjustable Digital DC power supply

A 12V acid battery was used initially for power supply to the ignition coil, but it was found to be supplying excess ignition energy and absence of active control over the supply. It was replaced by an Adjustable DC power source in which both current and voltage were varied.

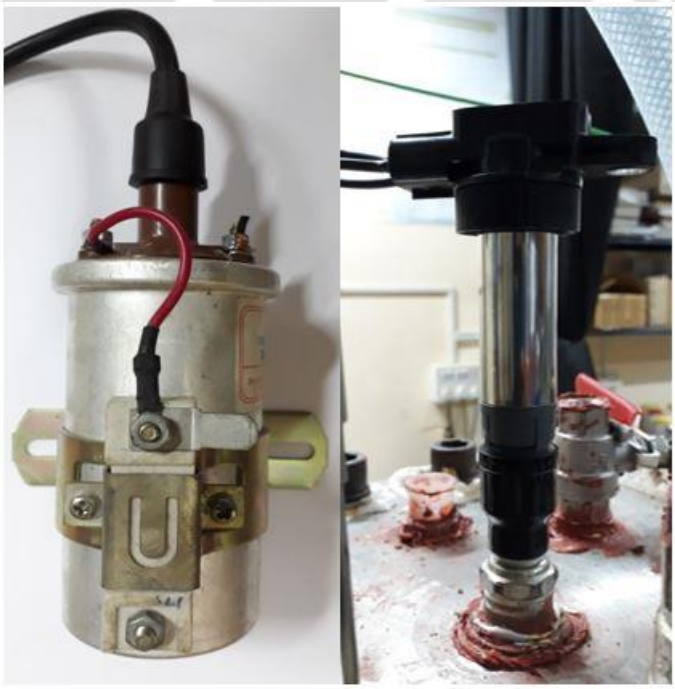

Figure A2-26 Standard voltage step-up coil and an ignition stick coil with a built-in trigger circuit

A standard voltage step-up coil required a separate triggering circuit for generating a high voltage signal; it occupied more space. It cannot be directly attached to the electrodes. Due to high potential difference, the terminal wires connecting the coil and electrodes were isolated to avoid current jump to other conducting parts. A compact ignition stick coil later replaced the unit with an inbuilt triggering circuit. The coil can be directly fixed to the electrodes, eliminating the current jump to the nearby instruments/parts. A 5V DC pulse signal was required to generate a spark.

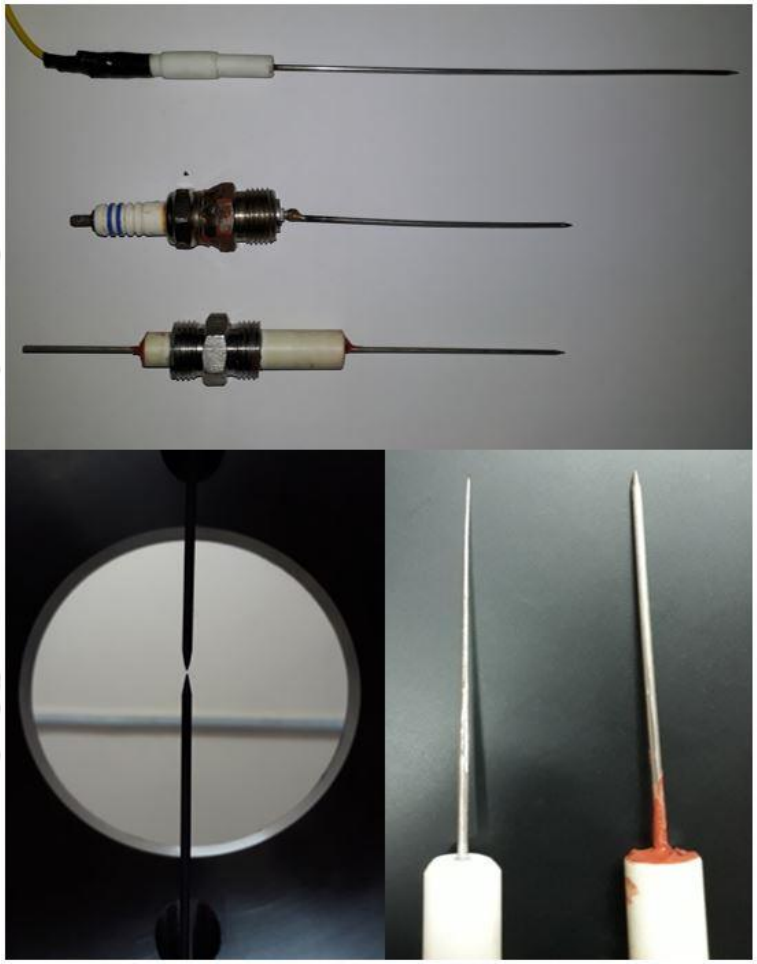

Figure A2-27 Teflon insulated electrode, modified electrode, and customized ceramic electrode. Thick electrodes at the center of the chamber and tapered electrode comparison with a standard electrode.

The electrodes were custom made with a Teflon holder as insulation material. The insulation was insufficient to avoid the spark jump with the metal body and multiple sparks at different locations. 2 to 3 mm diameter stainless steel rods were used as electrodes. Commercially available automotive sparkplugs were modified, and the tip was

extended to serve as spark electrodes. The insulation was found to be not sufficient. The electrodes were misaligned due to the brazing at the extension spot. A high-temperature custom-made ceramic cylinder was later fabricated with a straight rod passing through that offered the best insulation. The spark jumps were eliminated from the system. The spherical flame generated by the spark discharge was affected by early-stage wrinkles. The distortion in the flame front was due to heat loss to the electrodes and drag in the vertical direction. This was resolved by introducing a thin, non-linearly tapered electrode of a diameter ranging from 0.75 mm to 2 mm.

Heating system

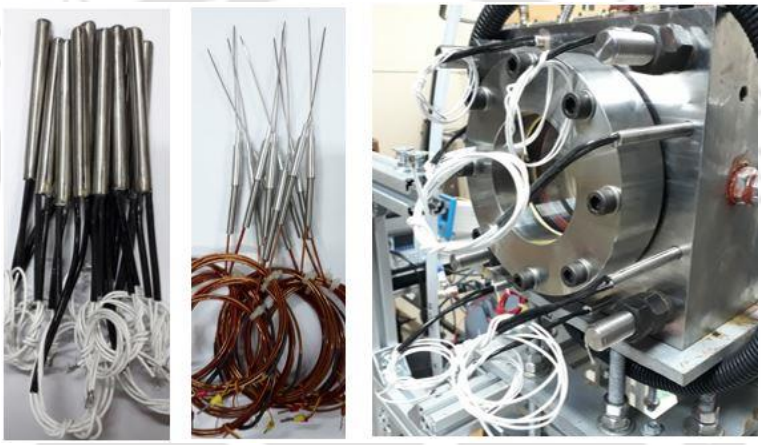

Figure A2-28 Heating cartridges, thermocouples, and cartridges in the chamber

D-type/split type high-density heating cartridges were inserted into the chamber. The heat transfer was solely due to the surface contact between the cartridge and chamber. D-type cartridges expand, resulting in good surface contact and heat transfer. They contract to their original size under normal temperatures leading to high ease of removal. The K-type thermocouples were inserted at the center of the cartridge to read the cartridge core temperature. The temperature output was used as the feedback for controlling the heating and health monitoring of the cartridges.

Figure A2-29 Temperature Control box

9 PID controllers, 9 Ammeters, MCBs, glass fuse, Isolation transformer, etc., were used in a custom-made temperature control box. All nine power supplies can be used independently.

Imaging system

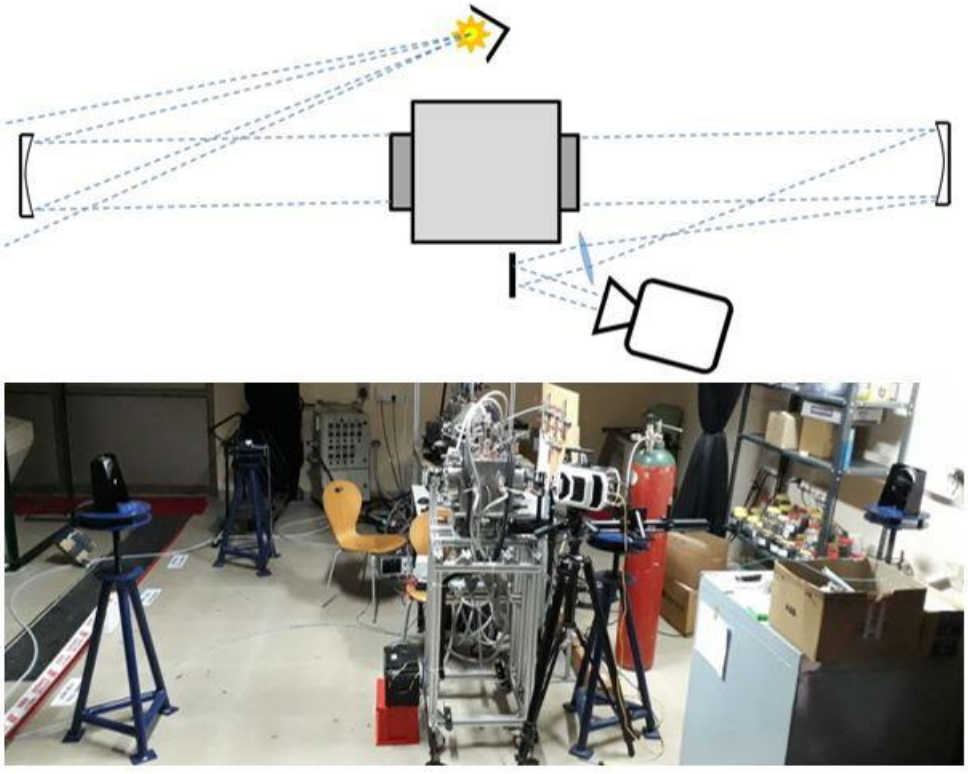

Figure A2-30 Schematic and Actual arrangement of shadowgraph system

A high-speed shadowgraph system consisted of a light source, circular concave mirrors, a biconvex lens, and a high-speed camera. An LED torch was used as a light source. Two 6-inch diameter and 60-inch focal length concave mirrors were used for reflecting. A 30 mm diameter and 250 mm focal length biconvex lens was used for converting divergent beams to parallel. A phantom v220 8-bit monochrome camera was used to capture the propagating flame. The camera was set to external trigger mode to start capturing the video only upon receiving the trigger signal. Due to the space constraint, the reflected parallel beam was reflected by a plain mirror away from the chamber, where the camera was isolated from heat and kept well away from the chamber.

Figure A2-31 High-speed camera and light source of the imaging system

Triggering system

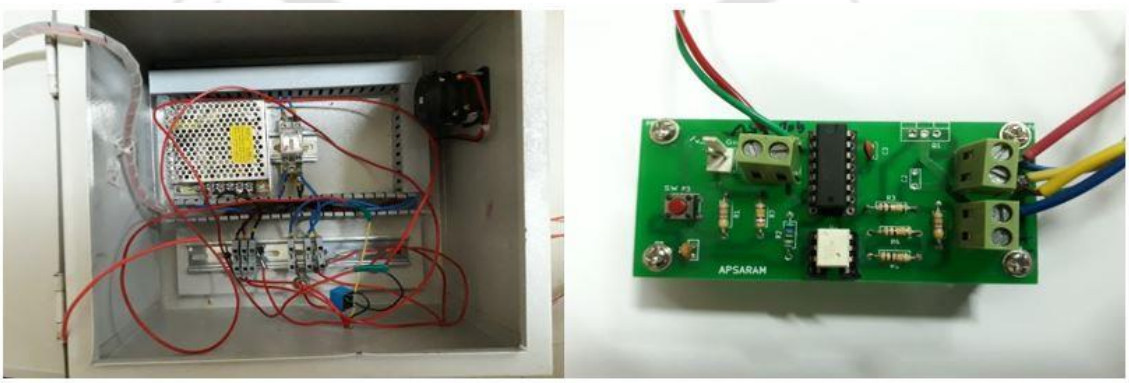

Figure A2-32 Customized triggering circuits made up of ICs

The triggering circuit generated four single-shot 5V DC pulse signals with predefined duration length. In the initial stage, custom-made printed circuit boards with ICs and other electronic components were used for the triggering. The consistency of the generated signals was found to be poor. A microcontroller-based commercially available Arduino board was used for generating pulse signals and found to be consistent. A dedicated 8-channel pulse generator further replaced these with complete control over the pulse width, amplitude, frequency, etc., of the generated pulses.

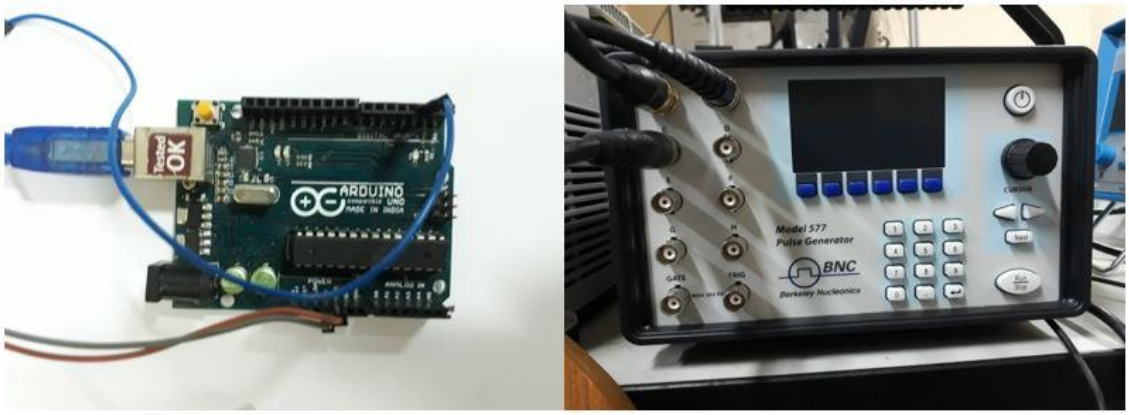

Figure A2-33 Arduino board and Pulse generator

Mounting:

The aluminum profiles were cut and assembled to make a stand. It was modified by removing unnecessary profiles, adjusting the height, and fitting with extra profiles for holding other instruments. The entire load of the system was transferred evenly to 4 heavy-duty wheels with a locking mechanism. The wheels did not completely arrest the movement despite the locking feature, and the rubber started peeling off. An angled frame was added to arrest the movement and to take over the load from the wheels. The custom-made height-adjustable metal bushes were found to be efficient.

Figure A2-34 Modification of the mounting system

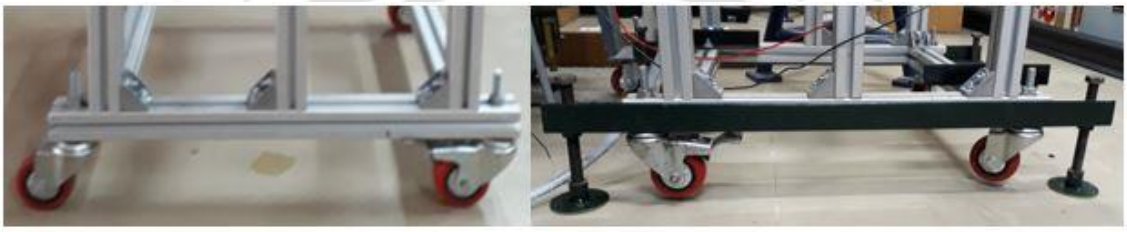

Figure A2-35 Upgraded base of the system for better locking

Data Acquisition system

Figure A2-36 Data Acquisition systems

Testing and leak arrest

Before commissioning, the chamber was tested for leaks in both directions, such as vacuum and high-pressure conditions. The testing was carried out in three stages, and the identified leaks were arrested in the corresponding stage.

General Leak Test

In this stage, the chamber was sealed completely and pressurized with air. The pressure drop in the chamber pressure was monitored. Soap solution was used to identify the locations of the leak and were fixed. This was repeated until other locations could not be identified despite the pressure drop. Teflon and gasket maker high-temperature red silicon paste was used to arrest the leak from joints.

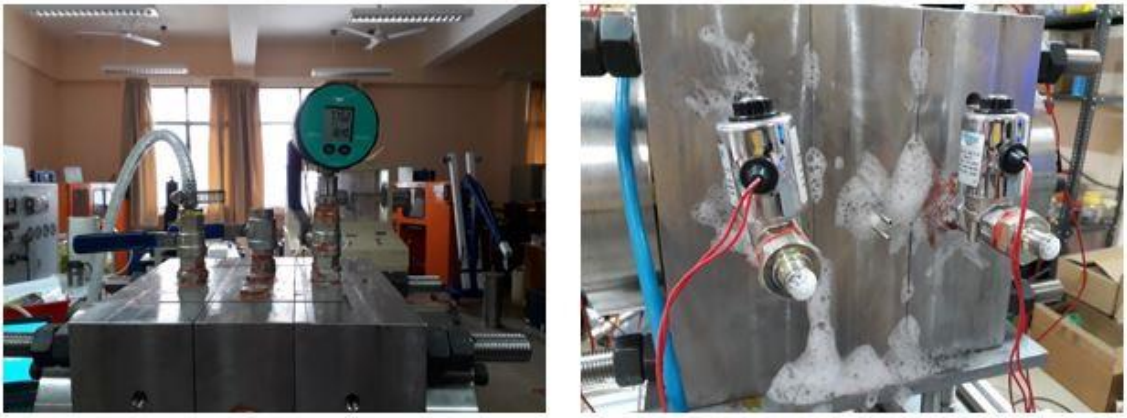

Figure A2-37 General leak test

Water Immersion Test

Minute leaks might not be a significant problem under ambient conditions but will lead to a substantial pressure drop at high pressures. Due to the minute leak and short lifetime of soap film, certain leak locations were not identified in the previous stage. The chamber was pressurized and immersed in a water tank. Then the origin location of the bubbles was determined and fixed.

Figure A2-38 Water immersion leak test

Figure A2-39 Reinforcing O-ring with gasket maker to arrest the minute leak

A minute leak at the optical window base was identified. A combination of gasket and O-ring was replaced by an O-ring and gasket maker paste to arrest the leak.

Hydraulic Pressure Test

After the complete leak arrest, the chamber was tested for the design pressure.

Figure A2-40 Hydraulic pressure test

The chamber was filled with deionized water, and pressure was supplied as per the requirement. The current setup was tested up to 75 bar with the optical windows for a duration of 15mins and found zero drop in the chamber pressure. Hence the chamber can be operated for up to 75bar with glass windows.

Subsystems

The subsystems were tested with appropriate tests before commissioning to avoid the failure and malfunction of the system.

Figure A2-41 General leak and water immersion test for the pressure manifold

Figure A2-42 Temperature controller and heating cartridge test using a load cell

Figure A2-43 Synchronous operation test of solenoid valves

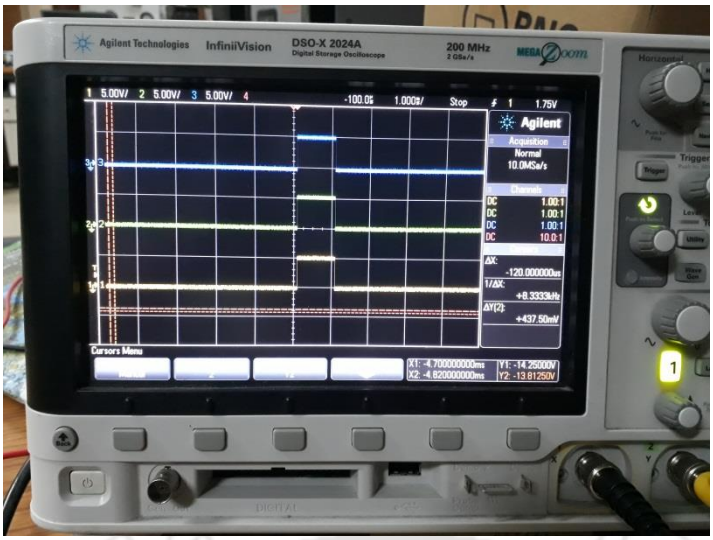

Figure A2-44 Triggering system test with an oscilloscope

Final Setup

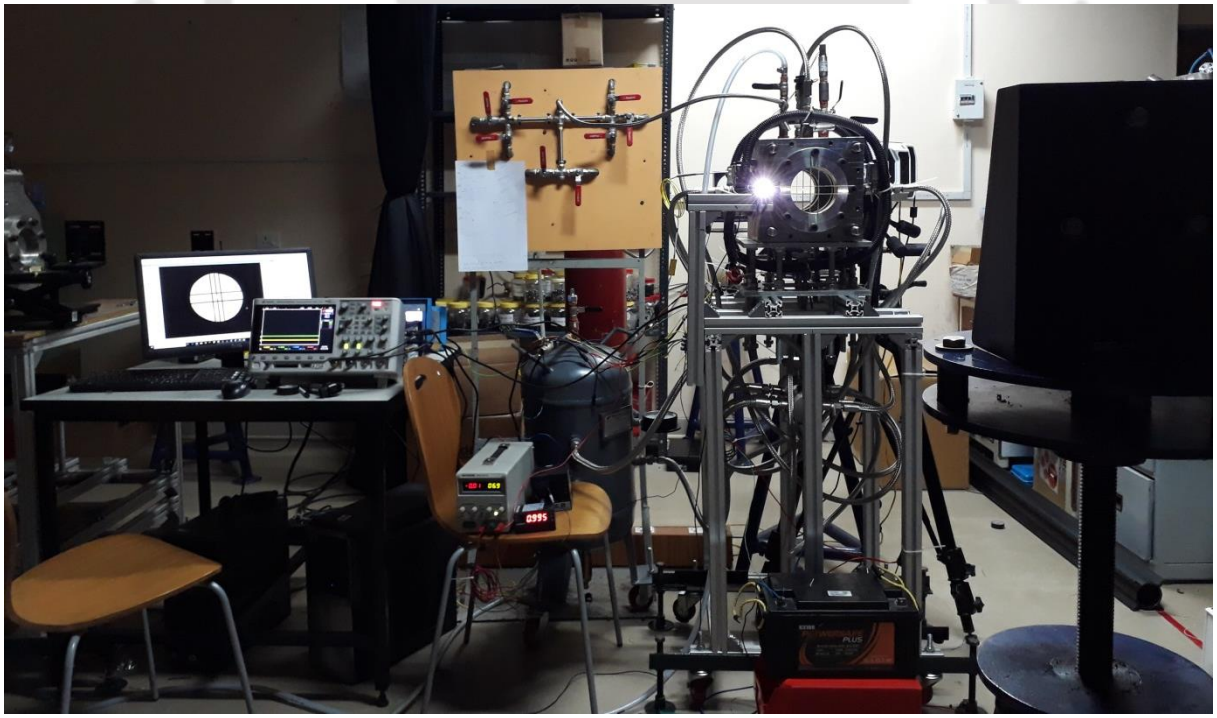

Figure A2-45 Elevated pressure combustion test facility under operation

Appendix-3: Uncertainty Analysis - freely expanding spherical flame method

This section reports the methodology followed to quantify uncertainties in all parameters estimated from freely expanding spherical flame method experiments. The present procedure was primarily adapted from literature [1]-[4]. The estimation of uncertainty in the result is calculated based on the uncertainties in the primary measurements. As shown below, the result R is a given function of the independent variables x_1, x_2, $x_3 \ldots x_n$.

$$R = f(x_1, x_2, \ldots . x_n)$$

Let δ_R be the uncertainty in the result and δ_{x1}, δ_{x2}, δ_{x3} be the uncertainties in the independent variables. If the uncertainties in the independent variables are all given with the same odds, then the uncertainty in the result having these odds is given as

$$\delta_R = \sqrt{\left(\frac{\partial R}{\partial x_1}\delta x_1\right)^2 + \left(\frac{\partial R}{\partial x_1}\delta x_2\right)^2 + \cdots + \left(\frac{\partial R}{\partial x_n}\delta x_n\right)^2}$$

Uncertainty in equivalence ratio

The equivalence ratio is the ratio of stoichiometric air-fuel ratio (AFR_{stoich}) to actual air-fuel ratio (AFR_{actual}). AFR_{stoich} is estimated from chemical balance, and hence, it does not involve any uncertainty. AFR_{actual} is achieved through the partial pressure method. In the present work, six species are involved. An absolute pressure transducer having a range of 0-4 bar with an accuracy of 0.1%FSL was used. Absolute error in pressure, δ_p is 0.004 bar.

$$\frac{\delta_f}{f} = \sqrt{\sum_{m=1}^{6}\left(\frac{dp}{p_m}\right)^2}$$

Where p_m represents partial pressure of each species. This is estimated for all producer gas compositions, and uncertainty in equivalence ratio (δ_ϕ) was in the range of ±8.1% to ±13.8%.

Uncertainty in radius:

In the present case, an image processing code written in MATLAB was employed to post-process the flame images to obtain flame radius. It utilizes a standard edge detection technique. In-house code estimates the diameter of the flame front as per the defined constraints in terms of pixels. Possible errors in the estimation of flame radius are identifying the correct edge and its dimension in pixels and converting pixels into the physical distance.

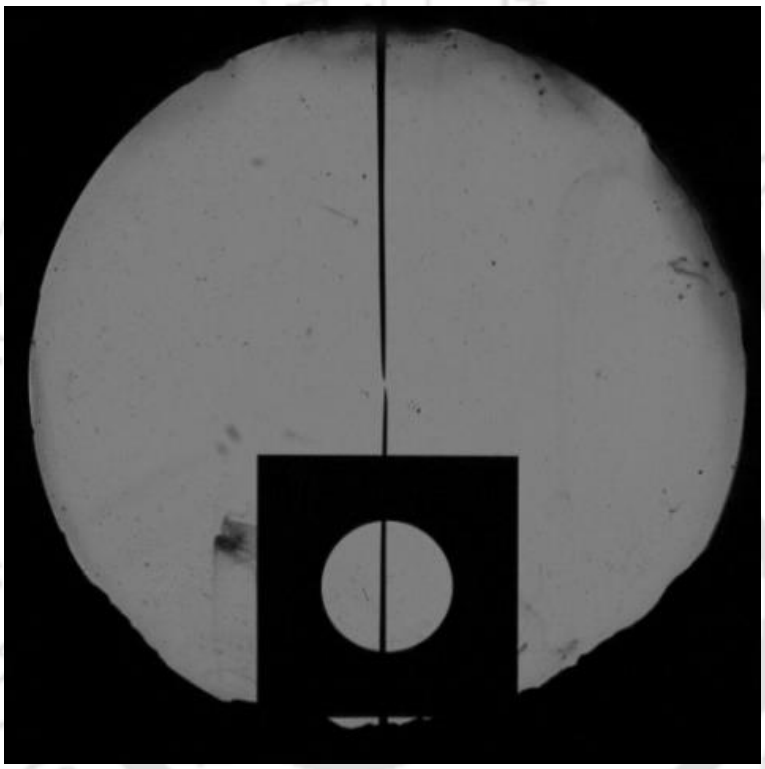

Figure A3-1 A shadowgraph image with a calibration plate

Figure A3-1 shows the image of the calibration plate kept on the window access. The calibration plate was square. The length of its sides was 40 mm. It had a circular hole with a radius of 10 mm at its center. It has precisely machined sides. The hole was drilled with a tolerance of H6. The pixel-to-physical length was calculated from the sides of the square and compared with the identified pixels corresponding to the radius of the hole and window access.

Table A3-1: Error in the estimation of radius from flame image

Item	Actual Radius (mm)	Estimated radius from MATLAB code	Absolute Error	Relative Error
Hole in the calibration plate	10	10. 147	0.147	1.47%
Window access	55	55.347	0.347	0.63%

Table 1 shows that the error became small with an increase in radius. Hence it is important to consider the error corresponding to the lower radius range considered for the calculations. In the present case, the lower range of the radius was in the range of 0.75-1 cm. Hence the above-estimated error corresponds to the maximum possible error in studied conditions. Therefore, the uncertainty in radius is ±1.47%.

Uncertainty in time:

The time stamp on the recorded frames is from a high-precision internal clock in the camera. Further, in the present case, the relative time difference (time interval) is used to calculate the required parameters rather than the absolute time. On the other side, the error originating from the camera is insignificant and fixed-systematic in nature. This type of error gets nullified while subtracting each other. Hence, the uncertainty corresponding to time is not considered.

Uncertainty in time = 0.00%

Uncertainty in flame speed:

As the uncertainty in time is zero, uncertainty in flame speed was estimated as shown below

$$S_b = \frac{dr_f}{dt} = \frac{r_{f2}\text{-}r_{f1}}{\Delta t}$$

Uncertainty in flame speed is ±2.93%

Uncertainty in flame stretch rate:

Flame stretch rate is defined as $K = \left(\frac{2}{r_f}\right)\frac{dr_f}{dt} = \frac{2S_b}{r_f}$. From the information of errors in flame radius and flame speed, uncertainty in flame stretch rate is estimated as

$$\frac{d_K}{K} = \sqrt{\left(\frac{d_{rf}}{r_f}\right)^2 + \left(\frac{d_{S_b}}{S_b}\right)^2}$$

Uncertainty in flame stretch rate is ±3.28%

Uncertainty in unstretched flame speed and burned gas Markstein length:

Unstretched flame speed and burned gas Markstein length are estimated using $S_b = S_b^0\text{-}L_bK$, which are functions of both stretched flame speed and stretch rate. The following approach is used when a parameter is a function of multiple variables with non-linear dependency. The sensitivity of the parameter $\left(\frac{\partial R}{\partial x_i}\right)$ to each variable is calculated and multiplied with the perturbed value of the variable to obtain the corresponding contribution, as shown below.

$$\frac{\partial R}{\partial x_1} = \frac{f(x_1 + \Delta x, x_2, \ldots x_n)\text{-}f(x_1, x_2, \ldots x_n)}{\delta x_1}$$

After estimating all sensitivities, following corelations were used to estimate the error in unstretched flame speed and burned gas Markstein length.

Linear form:

$$S_b = S_b^0\text{-}L_bK$$

Calculation of absolute deviation in estimated parameters: follows $\Delta L_b|^K = |L_b|^K\text{-}L_b|$, $\Delta L_b|^{Sb} = \left|L_b|^{Sb}\text{-}L_b\right|$, $\Delta S_b^0|^K = |S_b^0|^K\text{-}S_b|$ and $\Delta S_b^0|^{Sb} = |S_b^0|^{Sb}\text{-}S_b|$. Perturbation in

stretch rate was done to estimate $L_b|^K$ and $S_b^0|^K$. Maximum value of perturbation corresponds to absolute error in stretch rate, i.e., ±3.28%. Only stretch rate term was perturbed. Then, flame speed was perturbed to find $L_b|^{Sb}$ and $S_b^0|^{Sb}$. Then absolute error in S_b^0 and L_b was estimated as follows:

$$\delta S_b^0 = \sqrt[2]{\left(1 + K\frac{\Delta L_b|^S}{\Delta S_b} + L_b\frac{\Delta K}{\Delta S_b}\right)^2 (\Delta S_b)^2 + \left(\frac{\Delta S_b}{\Delta K} + K\frac{\Delta L_b|^K}{\Delta K} + L_b\right)^2 (\Delta K)^2}$$

$$\delta L_b = \sqrt[2]{\left(\frac{1}{K}\left(\frac{\Delta S_b^0|^S}{\Delta S_b} - L_b\frac{\Delta K}{\Delta S_b} - 1\right)\right)^2 (\Delta S_b)^2 + \left(\frac{1}{K}\left(\frac{\Delta S_b^0|^K}{\Delta K} - L_b - \frac{\Delta S_b}{\Delta K}\right)\right)^2 (\Delta K)^2}$$

The above-listed expressions were applied to different flame speed-stretch rate data ranges for all studied operating conditions. The maximum error estimated from the studied conditions was reported as follows:

Uncertainty in unstretched flame speed = ±4.50%

Uncertainty in burned gas Markstein length = ±46.16%

Non-Linear form:

Unstretched flame speed was estimated using the non-linear form as shown below

$$\frac{S_b}{S_b^0}\left(1 + \frac{2L_b}{r} + \frac{4L_b^2}{r^2} + \frac{16L_b^3}{3r^3} + O^4\left(\frac{L_b}{r}\right)\right) = 1$$

Following, the identical procedure used in linear form, absolute errors in S_b^0 and L_b are as follows:

$$\delta S_b^0 = \sqrt[2]{\left([CT1] + [S_b(HT)]\frac{\Delta L_b|^r}{\Delta r}\right)^2 (\Delta r)^2 + \left([CT2] + [S_b(HT)]\frac{\Delta L_b|^S}{\Delta S_b}\right)^2 (\Delta S_b)^2}$$

$$\delta L_b = \sqrt[2]{\left(\frac{\frac{\Delta S_b^0|^r}{\Delta r}\text{-}[CT1]}{[S_b(HT)]}\right)^2 (\Delta r)^2 + \left(\frac{\frac{\Delta S_b^0|^S}{\Delta S_b}\text{-}[CT2]}{[S_b(HT)]}\right)^2 (\Delta S_b)^2}$$

Where, $CT1 = (FT)\frac{\Delta S_b}{\Delta r}\text{-}S_b\left(\frac{L_b}{r}\right)(HT)$, $FT = 1 + 2\left(\frac{L_b}{r}\right) + 4\left(\frac{L_b}{r}\right)^2 + \frac{16}{3}\left(\frac{L_b}{r}\right)^3$, $HT = \left(\frac{2}{r}\right) + 8\left(\frac{L_b}{r^2}\right) + 16\left(\frac{L_b^2}{r^3}\right)$, $CT2 = (FT)\text{-}S_b\left(\frac{L_b}{r}\right)(HT)\frac{\Delta r}{\Delta S_b}$

Above listed expressions were applied to different ranges of flame speed-stretch rate data for all studied operating conditions. The maximum error estimated from the studied conditions was reported as follows:

Uncertainty in unstretched flame speed = ±4.11%

Uncertainty in burned Markstein length = ±55.46%

Uncertainty in unstretched flame speed from Xiouris Model

In this work, Xiouris model was also used.

$$\left[\frac{S_b\text{-}S_b^0}{K}\right]_{Sim} = \left[\frac{S_b\text{-}S_b^0}{K}\right]_{Exp}$$

As the left-hand side was obtained from simulations using GRI-Mech 3.0, there are no uncertainties associated with it. Local linear fit (five neighboring points) between simulated flame speed and stretch rate was used to obtain simulated stretched flame speed identical to that experimental stretch rate data. Error in the fitting was not considered. Then, using the information of errors in flame speed and stretch rate, error in stretched flame speed was estimated.

$$\frac{d_{S_b^0}}{S_b^0} = \sqrt{\left(\frac{d_{S_b}}{S_b}\right)^2 + \left(\frac{d_K}{K}\right)^2}$$

Uncertainty in unstretched flame speed = ±4.39%

Uncertainty in Laminar burning velocity:

Then, unstretched laminar burning velocity was estimated as $S_u^0 = S_b^0\left(\frac{\rho_b^o}{\rho_u}\right)$. As the density ratio was estimated from thermodynamic data and the ideal gas equation, no error is involved. Hence, uncertainty estimated for unstretched flame speed is identical for unstretched laminar burning velocity also.

$$\frac{\Delta S_u^0}{S_u^0} = \frac{\Delta S_b^0}{S_b^0}$$

Uncertainty in unstretched *LBV* from linear stretch extrapolation model= ±4.5%

Uncertainty in unstretched *LBV* from non-linear stretch extrapolation model = ±4.11%

Uncertainty in unstretched *LBV* from Xiouris model = ±4.4%

References:

1. Coleman, Hugh W. and Steele, W. Glenn - Experimentation, validation, and uncertainty analysis for engineers-John Wiley & Sons (2018)

2. Taylor, John R - An Introduction to Error Analysis, The study of uncertainties in physical measurements-2nd Edition-University Science Book (1997)

3. Moffat, R. J. – Using uncertainty analysis in the planning of an experiment – pp: 173-178, vol. 107, Journal of Fluids Engineering, June 1985

4. Mickley, Harold S., Sherwood, Thomas K. and Reed, Charles E. – Applied mathematics in chemical engineering – Tata McGraw-Hill Publishing Company Limited (1975)

Publications

Published (International Journals):

[1] **Muniraja Tippa**; Akash M; Senthilmurugan S; Chockalingam Prathap, A comprehensive study on laminar burning velocity and flame stability of oxy-producer gas mixtures. Part-2: Laminar Burning Velocity and Markstein length analysis. Fuel (2021), 292, 119982, https://doi.org/10.1016/j.fuel.2020.119982

[2] **Muniraja Tippa**; Akash M; Senthilmurugan S; Chockalingam Prathap, A comprehensive study on laminar burning velocity and flame stability of oxy-producer gas mixtures. Part-1: Gas mixture composition and flame stability analysis based on Lewis number, Fuel (2021), 292, 120302, https://doi.org/10.1016/j.fuel.2021.120302

[3] **Muniraja Tippa**; Senthilmurugan S; Chockalingam Prathap, Impact of chamber volume on the measurement of laminar burning velocity using constant volume spherical flame method, Fuel, (2019), 256, 115936, https://doi.org/10.1016/j.fuel.2019.115936

[4] **Muniraja Tippa**; Yaswanthram G; Senthilmurugan S; Chockalingam Prathap, Development of a comprehensive burning velocity and flame instability profile of Refined Producer Gas (H_2:CO:CH_4) – Air mixtures at elevated pressures. (*Accepted, International Journal of Hydrogen Energy under review*).

Published (Scientific meetings/conferences):

[1] **Muniraja Tippa**; Senthilmurugan S; Chockalingam Prathap, Laminar burning velocity and stability study on multi-component premixed producer gas-air mixtures at ambient and elevated initial pressure conditions. 7th Prof. P. J. Paul Memorial Combustion Researchers Meet, 14-15 Feb 2020, IIT Bombay.

Manuscripts (under preparation & review):

[1] **Muniraja Tippa**; Senthilmurugan S; Chockalingam Prathap, Explosion characteristics of Refined Producer Gas (CH_4:CO:H_2)-Air mixtures. (*Under preparation*)

Collaborative research output:

[1] Aswathi Krishna, **T. Muniraja**, C. Prathap, Generation of Homogeneous Isotropic Turbulence Inside Fan Stirred Vessel. National Aerospace Propulsion Conference (NAPC)-2018, 17-19 Dec 2018, IIT Kharagpur.

[2] Yaswanthram G, **Muniraja Tippa**, Senthilmurugan Subbiah, Prathap Chockalingam, A study on data processing techniques of expanding spherical flames at constant pressure conditions. IHMTC-2021, IIT Madras.

Patents:

[1] Energy efficient retort reactor for producing charcoal, oil and gas from biomass and municipal solid wastes. Indian Patent Application No. 202131027584. Date of filing: 20-06-2021. [Patent Pending].

[2] A compact snow melting and purification (S-MAP) system. Indian Patent Application No. 202131019765. Date of filing: 29-04-2021. [Patent Pending].